A Nonlinear River Meandering Model and its Incorporation in a Landscape Evolution Model

by

Stephen Thomas Lancaster

Bachelor of Arts, Cum Laude in General Studies, Harvard
University, Cambridge, Massachusetts (1990)

Submitted to the Department of Civil and Environmental Engineering in
partial fulfillment of the requirements for the degree of

Doctor of Philosophy

at the

MASSACHUSETTS INSTITUTE OF TECHNOLOGY

September 1, 1998

Author ....
Dept. of Civil and Environmental Engineering
September 1, 1998

Certified by ....
Prof. Rafael L. Bras
Dept. of Civil and Environmental Engineering
Thesis Supervisor

Certified by ....
Prof. Kelin X. Whipple
Dept. of Earth, Atmospheric, and Planetary Sciences
Thesis Supervisor

Accepted by ....
Joseph M. Sussman
Chairman, Departmental Committee on Graduate Studies
Dept. of Civil and Environmental Engineering

A Nonlinear River Meandering Model and its Incorporation in a Landscape Evolution Model

by

Stephen Thomas Lancaster

Submitted to the Department of Civil and Environmental Engineering on September 1, 1998, in partial fulfillment of the requirements for the degree of Doctor of Philosophy in Hydrology

Abstract

A topographic steering river meandering (TSRM) model based on continuity of a simplified flow field through bends is developed. The equilibrium coupling between helical flow and sediment transport, as in *Ikeda* [1989] determines downstream variation of transverse bed slope. The model tests the hypothesis that meander development patterns can be captured under the assumptions: (a) bank shear stress arises from forces associated with topographically induced convective accelerations; (b) turbulent boundary layer dissipation of these forces at the banks is sufficiently represented by gaussian smoothing at a parameterized scale; and (c) lateral migration of the channel is proportional to bank shear stress. The resulting TSRM model produces realistic complex meander patterns and scroll bar-like topography. Model compound bend formation is compared to a field case and found to arise from the nonlinear interaction of bank roughness and channel hydraulics scales. When the latter is short relative to the former, maximum bank shear stress occurs early in the bend and leads to compound bend formation. New statistical stream sinuosity and spatial coordinate variation measures are applied to both natural and model streams and reveal secondary sinuosities arising from compound bend formation in both cases. Scroll bar topography and channel bank roughness are studied in the field to compare natural and model mechanisms.

A channel-hillslope integrated landscape development (CHILD) model incorporates the TSRM model. The CHILD model represents the landscape as an irregular, Delaunay triangulated mesh of landscape nodes that may be moved, deleted, or added to accommodate meandering channels that are in general discretized at different spatial resolution than the surrounding landscape. The interactions among meandering, bank erodibility's bank height dependence, and uplift rate in a detachment-limited river valley are examined. An equilibrium landscape adjusts to the onset of meandering and approaches a new dynamic equilibrium. For the detachment-limited case, the hypothesis that meandering is more active when uplift is quiescent is rejected. When bank erodibility's bank height dependence is greater, bend scale sinuosity is smaller, but the tendency toward multi-bend loop formation is reinforced.

Thesis Supervisor: Rafael L. Bras
Title: Chair, Dept. Civil and Environmental Engineering

Thesis Supervisor: Kelin X. Whipple
Title: Professor, Dept. Earth, Atmospheric, and Planetary Sciences

ACKNOWLEDGEMENTS

Table of Contents

List of Figures

List of Tables

Chapter 1

Introduction

The original objective of this study was to model the transport and deposition of sediments in river basins in the context of landscape evolution. The new model would employ techniques developed in previous studies where possible, but new process models would be derived where the techniques of previous models were inadequate: in the treatment of multiple sediment sizes, lateral fluvial erosion, and floodplain deposition. The model study would attempt to answer the following question: given an initial distribution of sediments in space and a climatic forcing in time, what is the structure of deposits after some time interval?

The initial objective of the present study was to develop a landscape evolution model (see review in Chapter 2) that would incorporate the new features listed above. The problem of lateral fluvial erosion, or meandering, would not yield to a solution based on the traditional rectangular grid. Instead, I sought the simplest possible solution that still captured most of the physics of river meandering. The results of the present study are new models of river meandering and landscape evolution. Another member of the research group took up the problem of multiple grain size sediment transport, and the problem of floodplain deposition has not been addressed. I review the landscape evolution modeling literature in Chapter 2.

An understanding of the process of river meandering is basic to an understanding of river processes in general. That general understanding is important for people whose work with rivers covers a broad range of spatial and temporal scales—from the erosion of pasture land from year to year, to the formation of alluvial terraces over millennia, to the evolution of a river basin over the geologic time. I review the river meandering literature in Chapter 2.

From the literature and through studies of rivers from maps and aerial photographs and in the field, I found that important aspects of meandering were not predicted by the state of the art of river meander modeling, nor has the impact of meandering on the landscape received much study. I present a study of natural river meandering in Chapter 3. Field and experimental studies have shown that channel bed topography has a strong effect on the patterns of flow and sediment transport through a bend and, thus, on the meandering process. In Chapter 4, I explain a new model of river meandering based on the hypothesis that "topographic steering" [*Dietrich and Smith*, 1983] is the major physical control on stream bank erosion. I show the model results and draw comparisons with the findings in Chapter 3.

In Chapter 5, I return to the problem of landscape evolution modeling. The aim is to simulate the evolution of valleys and streams as long as several kilometers on the scale of millennia for alluvial streams or millions of years for bedrock streams. I explain a new landscape evolution model that incorporates the meandering model on an irregular, flexible grid and show some synthetic results of the integrated model.

The present work leaves some questions unanswered relative to nature and the two new models. In Chapter 6, I explore the directions of future work and discuss possible improvements to the river meandering model. The landscape evolution model is under active development, and I address the direction of that development and explore some interesting experiments, especially with regard to meandering, that could be done with the fully developed model. I also address the subject of model verification through field studies. Finally, I discuss the implications of the whole study and conclude in Chapter 7.

Chapter 2

Literature Review

This chapter will review previous work on the subjects of landscape evolution and river meandering. In my review of the landscape evolution literature, I will address some of the fundamental processes which remain unaddressed by the models. Specifically, I will address the treatment of geomorphic processes in the context of the fluvial-dominated landscape and review the literature on the subject of river meandering.

2.1 Landscape Evolution

The study of landscape evolution has progressed rapidly within the past decade or so. Landscape evolution models have attained general acceptance only recently and can now model relatively large landscapes relatively quickly, but the suite of modeled processes has not changed much since *Ahnert* [1976], except for a few recent examples which I will highlight in the following review. In this review of landscape evolution modeling, I focus on previous models' capabilities to represent various landscape processes and give less attention to the scientific results of the model studies.

Water, ice, wind, gravity and biogenic activity may all act as agents of, or forces behind, sediment transport and, thus, landscape evolution. Aside from glacial and related processes, ice is responsible for diffusional transport by frost heaving and physical weathering by frost shattering. Wind is responsible for abrasion erosion, soil stripping, loess deposition and diffusional transport on hillslopes by tree throw. The biogenic activity of

burrowing mammals also produces diffusional transport [*Black and Montgomery*, 1991]. Gravity transport in river basins includes soil creep and mass wasting processes such as rockfall [*Carson and Kirkby*, 1972; *McKean et al.*, 1993] and landsliding [*Montgomery and Dietrich*, 1994]. Fresh water transport in river basins may take several distinguishable forms: rainsplash, overland flow, groundwater sapping, and fluvial processes, including channel flow. Overland flow, sapping, and landsliding may cause erosion and initiate a channel [*Dietrich et al.*, 1993; *Montgomery and Dietrich*, 1988, 1989, 1992].

Various studies of sediment transport mirror greatly disparate spatial and temporal scales of sedimentary processes. On the one hand, the finest spatial and temporal scales (< 1mm, < 1 sec.) are required to study the entrainment and motion of sediments in turbulent flow (e.g., *Tetzlaff and Harbaugh*, 1988; *Slingerland, et al.*, 1994). On the other hand, the evolution of fluvial landscapes and sedimentary basins takes place on domains as large as thousands of square kilometers and over periods as long as hundreds of millions of years [*Young and McDougall*, 1993].

Gilbert [1877] recognized that the simultaneous interaction of many processes form a landscape in dynamic equilibrium as opposed to *Davis*'s [1909] geographic cycle of uplift and erosion. *Gilbert* [1909] saw that the local differences in form are due to differing process dominance. For example, he recognized that the change from convexity to concavity in the landscape was due to changes in process dominance from hillslope diffusional to advective fluvial processes. Later, *Hack* [1960] introduced the concept of dynamic equilibrium as a steady state in which uplift exactly balances erosion such that elevations remain constant in time. In this work I use a less restrictive definition of

22

dynamic equilibrium such that elevations at a site may change, but on the scale of the landscape the processes building and eroding the landscape are in equilibrium.

It was not until *Smith and Bretherton* [1972] that the issue of process dominance was addressed in a quantitative model. They found that perturbations of an inclined plane introduced instabilities due to the convergence of flow. This instability allowed advective transport to outpace diffusive transport and, thus, form a channel network. Their work was somewhat flawed, however, in that their results implied an infinite dissection of the landscape.

Kirkby [1971] and *Carson and Kirkby* [1972] introduced a simple profile model of hillslopes in which the sediment flux per unit width is a function of the distance from the divide and the local slope:

$$q_s \propto x^m S^n \tag{2.1}$$

where x is effectively a surrogate for discharge. Later profile studies have built upon the above simple model by adding functions for soil production and considering the effects of spatial and temporal variations in climatic forcing [*Kirkby*, 1989]. Subsequently, three-dimensional landscape evolution models have built upon the above equation by including two basic terms in a sediment flux equation dependent on drainage area (analogous to x above) and local slope, one term for advective transport (m > 0 and n > 0) and one term for diffusive transport (m = 0 and n = 1).

Vanguard among landscape evolution models are *Ahnert* [1976] and *Cordova, et al.* [1982]. *Ahnert* [1976] modeled regolith production and diffusional, mass wasting, and

advective transport processes, and *Cordova, et al.* [1982] modeled explicitly fluvial transport processes, both on a two-dimensional grid. *Ahnert* [1976] modeled transport from a point to all downhill points according to the discharges and slopes in each direction, while *Cordova, et al.* [1982] collected flow and sediment from all upstream points and sent flow and sediment to only the downstream point with the steepest slope. After these works, progress in the modeling of landscape evolution was hindered by the lack of a quantitative, field-based understanding of the processes shaping the landscape and, on a more practical note, sufficient computing power to model landscapes on grids larger than several points per side.

Montgomery and Dietrich* [1988] brought the issue of channel initiation into the general consciousness, and *Montgomery and Dietrich* [1989] followed up on that earlier work with a thorough field study of channel initiation processes, including overland flow, shallow landsliding, and seepage erosion. *Montgomery and Dietrich* [1989] addressed the issue of what defines landscape scale and derived an alternative approach to defining drainage density in terms of channel head source basin length.

Willgoose, et al.* [1989, 1991] developed a landscape evolution model, SIBERIA, in which transport in channels had greater capacity than non-channel transport. Channels were explicitly defined with an activator function. The channel activator was a separate governing partial differential equation which extended the channel network via headward growth according to the value of a threshold criterion dependent on the drainage area and local slope at a point. The latter slope dependence markedly distinguished the activator from the headward growth model of *Howard* [1971]. *Montgomery and Dietrich* [1992]

24

used mapped channel head locations to empirically define a topographic threshold similar in form to the activator function.

Dietrich, et al. [1992] developed a graphical technique to define spatial variation in process dominance and divided the landscape into areas prone to channel instability due to runoff and stable areas dominated by diffusion processes. *Tarboton, et al.* [1991, 1992] developed a similar technique for differentiating channels and hillslopes in digital elevation models (DEMs), but the method was not tested against mapped channels. *Ijjasz-Vasquez, et al.* [1992] used a saturation from below mechanism for channel initiation in the SIBERIA model. *Dietrich, et al.* [1993] addressed the question of whether thresholds for runoff generation or slope failure better defined the locations of known channel heads. They found that a threshold based on a critical shear stress due to saturation overland flow was better than one based on a threshold for landslide initiation at predicting channel head locations when applied to real landscapes. *Montgomery and Dietrich* [1994] derived and tested a model of pore pressure-induced shallow landsliding by combining the infinite slope stability model for shallow soils with a simple expression for subsurface flow in steady state. They were successful in predicting the locations of some mapped landslide scars.

Howard [1994] compared the effects of different hillslope processes, and *Tucker and Bras* [1998] recently incorporated many channel initiation and hillslope processes in a landscape evolution model in order to examine the differences among landscapes produced by the various processes. *Howard* [1998] recently modeled a system in which resistant bedrock is mantled by soft regolith which is in turn covered by resistant vegetation

and investigated gullying in response to disturbances in the vegetation layer. *Moglen and Bras* [1995] investigated the effect of a spatially heterogeneous erodibility and calibrated the model to natural landscapes with a simple detachment-limited advection-diffusion model. They found that heterogeneity led to patterns of drainage aggregation that were more circuitous and more realistic than the model networks produced in the homogeneous case. *Rosenbloom and Anderson* [1994] used a landscape evolution model with diffusion limited by regolith production on hillslopes and detachment limited erosion in channels to model the formation of marine terraces and calibrated the model to a site in California. *Tucker and Slingerland* [1994, 1996, 1997] developed the Geologic, Orographic Landscape Evolution Model (GOLEM) with the above processes and both bedrock and alluvial channels to model escarpments, fold and thrust mountain belts, and the effects of climate change on drainage basins.

Several other landscape evolution models are noteworthy here. *Chase* [1992] developed a "precipiton" model in which parcels of water are placed in random locations, routed downstream, and allowed to erode or deposit sediment along the way. This model is similar to that of *Beaumont, et al.* [1992]. This model is really only valid if the governing equations for sediment transport are linear in discharge because flow cannot aggregate, i.e., only one pixel generates flow during a given iteration. *Beaumont, et al.* [1992] and *Kooi and Beaumont* [1994] also incorporated orogenic influences on rainfall and introduced a reaction length scale such that entrainment and deposition as calculated at a single point are potentially spread over more than one point along the channel. *Braun and Sambridge* [1997] developed a model on a triangulated irregular network (TIN). In this model, points can be added, e.g., to resolve steep slopes, and points can be moved according to

simple rules mimicking tectonic motion. *Gasparini, et al.* [1997] incorporated sediment with multiple grain sizes in a landscape evolution model by combining the sand and gravel transport model of *Wilcock and McArdell* [1993] with *Tucker and Slingerland*'s [1994] GOLEM. They found that even in dynamic equilibrium drainage basins exhibited downstream fining and the changes in texture had a large effect on basin stream profile concavity. This effect was recognized long ago by *Hack* [1957]. *Dunne and Aubrey* [1986] attempted to model the effect of different grain sizes and reported qualitative agreement between model and experiment, but they abandoned the effort because they were unable to reproduce the experimental values of sediment transport due to the sensitivity of the model.

Another group of landscape models takes a more rules-based approach. For example, *Rodriguez-Iturbe, et al.* [1992] evolved topography and stream networks according to optimality criteria. These optimal channel networks, or OCNs, indicate that minimization of total network stream power is sufficient to produce networks resembling natural ones. This approach is essentially statistical mechanics applied to river basins, whereas the present approach addresses the mechanics of specific landscape processes. *Rinaldo, et al.* [1995] used a model with diffusive hillslope transport and detachment-limited advection according to a critical shear stress threshold to study changes in drainage density with climate. They found that a lower threshold and constant diffusion strength led to greater drainage density.

As I will show in later chapters, lateral channel migration is an important factor in the evolution of the landscape, but no landscape model has incorporated this fundamental

process. In fact, no one has even considered the quantitative effects of lateral migration on drainage basin form beyond the recognition that it can widen valley floors and produce characteristic forms such as terraces [*Merritts, et al.*, 1994], bluffs, and slip-off slopes. A model incorporating lateral channel migration, or meandering, is required to address the interaction of meandering and other landscape processes and is the major goal of the present work.

2.2 River Meandering

Schumm, et al. [1987] illuminated some of the conditions necessary for the development of stable meanders. They experimented with meandering in an initially curved, experimental "bedrock" channel. They found that clear water flow incised an inner channel at the inside of the bend. With the admixture of bedload sediment to the incoming flow, however, the channel migrated laterally and incision slowed. They observed that the bedload material formed a transversely sloped point bar which steered the experimental stream's erosive energy toward the outside bank. They concluded that point bar-forming bedload is a necessary condition for meandering in a channel with cohesive banks. *Leopold and Wolman* [1960] noted that meltwater rivulets on ice develop meanders in the absence of bedload, but they did not study the mechanism responsible for this development.

Another set of experiments by *Schumm, et al.* [1987] revealed that an initially straight channel in cohesionless material formed a "meandering thalweg" pattern during a stage prior to the development of a braided pattern. However, when they mixed cohesive material with the inflow to the meandering thalweg channel, the deposition of the cohesive

material stabilized the point bars to form a floodplain, and the meandering thalweg became a stable meandering channel. They concluded that the conditions necessary for the development of a stable meander pattern, whether bedrock or alluvial, were: a) the presence of bedload ample enough to develop a point bar and to redirect a significant portion of the stream's energy toward the outside bank; and b) a mechanism or process providing bank stability, such as cohesive bank material, bank stabilizing vegetation, or a cohesive suspended load to deposit on and stabilize point bars. The recent experimental results of *Smith* [1998] support these conclusions. When the above conditions are met stable point bars may form that steer the high velocity flow to the outside bank. In the case of zero incision, such point bars accrete to form a floodplain which resists the formation of secondary channels or chutes that, in the extreme case, would lead to braiding.

 Dietrich and Smith [1983], *Dietrich and Whiting* [1989], and *Nelson and Smith* [1989b] showed that the flow and boundary shear stress fields in meander bends are strongly affected by the presence of point bars, a phenomenon they called topographic steering. *Dietrich and Smith* [1983] found that "[f]orces arising from topographically induced spatial accelerations are of the same order of magnitude as the downstream boundary shear stress and water surface slope force components." In fact, some of the results of *Dietrich and Whiting* [1989] showed that the forces arising from topographic steering were of greater magnitude than the water surface slope force component. *Nelson and Smith* [1989b] modeled flow and sediment transport in a channel bend with an initially flat bottom. Their modeling experiment showed, with the growth of the point bar, the corresponding development of a region of high boundary shear stress near the outside bank.

Many authors have modeled meandering [*Ikeda, et al.,* 1981; *Parker, et al.,* 1982; *Parker,* 1983; *Parker, et al.,* 1983; *Beck,* 1983; *Blondeaux and Seminara*, 1985; *Johannesson and Parker*, 1985, 1989a, b, c; *Parker and Andrews*, 1986; *Parker and Johannesson*, 1989; *Crosato,* 1990; *Howard*, 1992; *Seminara and Tubino*, 1992; *Garcia, et al.,* 1994] by linearizing the equations of flow and sediment transport such that they afford a tractable solution for the near-bank downstream flow velocity as a function of the downstream coordinate. Higher velocity near the bank corresponds to larger bank shear stress because that shear stress is proportional to the lateral gradient of downstream flow velocity near the bank; higher near-bank velocity means a greater velocity gradient. These models also assume that bank erosion is a detachment-limited process [*Howard*, 1994]. Models of river meandering based on the linearized flow equations (LFE models) produce realistic meander bends [*Howard*, 1992] and have proven useful in predicting channel migration in some cases [*Johannesson and Parker*, 1985] but with mixed results in others [*Garcia, et al.*, 1994]. The models of *Blondeaux and Seminara* [1985] and *Johannesson and Parker* [1989a] revealed the existence of complex feedbacks between flow and bed topography.

Other authors [*Smith and McLean*, 1984; *Nelson and Smith*, 1989a, b] have developed "two-plus"-dimensional channel flow and sediment transport models using depth-averaged equations for the bedload transport and an assumed vertical velocity profile for the suspended load transport. These numerical models are more detailed than LFE models, and, as mentioned above, they show that topographic steering greatly affects flow and sediment transport in bends. *Nelson and Smith* [1989b, p. 350] point out that, to deal with bank erosion and meandering, their model would need to include "both consideration of

the lateral diffusion of momentum [at the bank] by turbulence and the characterization of bank roughness."

Howard [1992] noted four constraints on the rate of bank erosion:

> These constraints are, or may be, sequentially linked, so that the slowest among them controls the overall rate.
>
> (1) The rate of deposition of the point bar.
>
> (2) The ability of the stream to remove the bedload component of the sediment eroded from the bank deposits via a net transport flux divergence.
>
> (3) The ability of the stream to entrain sediment *in situ* or mass-wasted bank deposits.
>
> (4) The rate with which weathering acts to diminish bank sediment cohesion to the point that particles may be entrained by the flow or bank slumping may occur.

Howard [1992] developed an erosion law based on near-bank shear stress and concluded that it was most applicable in the detachment-limited erosion of cohesive banks (constraint 3). Such a law may also be applicable in the case of bedrock, where the global rate of bank erosion may be limited by the weathering rate (constraint 4) which may, in turn, be independent of other channel processes, while the bank erosion at a specific point may be dependent on the relative ability of the near-bank flow to detach bank material.

Howard [1992] used the *Johannesson and Parker* [1989a] model to simulate the long-term evolution of meandering channels and floodplain topography. Following the reasoning of other authors [*Beck,* 1983; *Johannesson and Parker,* 1985; *Crosato,* 1990; *Garcia, et al.,* 1994], *Howard* [1992] expressed the near-bank flow velocity and channel depth in terms of linear perturbations on the mean values; in the model, the rate of bank erosion is proportional to the velocity perturbation, and the initial floodplain elevation is

found from the depth perturbation. *Howard* [1992, 1996] developed this model further by including floodplain deposition as a diffusional process [*Pizzuto,* 1987] and chute formation as a stochastic process [*Howard,* 1996].

The above work has done much to further the understanding of the meandering process, but a key question is left unanswered; that is, how important is the effect of strongly nonlinear topographic steering to meander evolution in light of the success of linear and weakly nonlinear models? The weakly nonlinear approach does address nonlinear effects but only for small curvature and within a small neighborhood of "resonance", or the meander wave number at which the linear solution becomes unbounded. Despite much evidence that topographic effects are strongly nonlinear, almost all models use similar linear or weakly nonlinear approaches. Two recent exceptions are *Droste* [1996] and *Imran and Parker* [1997], but these models are still too computationally slow to model channel evolution over geologic time, especially in the context of an entire landscape.

A new approach combining strong nonlinearity and computational efficiency is called for to address nonlinear effects over long channel courses and times. Strong nonlinearity is required in order that the model's application is not limited to bends with small curvature and, therefore, after short times. Computational efficiency is required to incorporate the model in a landscape-scale model. To meet both of these requirements, I must determine the essential physics required to model meandering. Once the new meandering model is developed, I must address the proper coupling of the meandering channel and the landscape where they meet, at the channel bed and banks. For a full coupling, sediment input to the channel from the surrounding landscape should also be addressed, but a thor-

ough treatment of this issue is beyond the scope of the present work. In order to provide

bases for comparison of both the meandering and coupled models to natural streams and

landscapes, I first investigate the morphology of the latter natural systems.

Chapter 3

River Meandering in Nature

In this chapter I report results and observations from a study of natural meandering rivers. This study was motivated in part by the modeling study presented in the following chapters. I needed to ask the question: How do I judge the success or failure of a new river meandering model and its incorporation in a landscape evolution model; what questions remain unanswered? what phenomena unexplained? Included in this chapter are a field study in Maine and the Ozarks of Arkansas and Missouri and remote studies of the Mississippi floodplain, the Schoharie Creek drainage basin in the Catskills of New York, and Alaskan meandering stream channel planforms.

3.1 Introduction

3.1.1 Meandering and the Landscape

Meandering streams are familiar features of the landscape. Though the valleys of incising meanders may be quite narrow, meandering streams typically occupy relatively flat valley floors, as in the case of Schoharie Creek in New York, shown in figure 3.1. Lateral channel migration may flatten the valley bottom by forming a strath surface if the channel erodes laterally but not vertically. Often meandering streams are characterized by net deposition and aggradation, and these alluvial deposits may partially fill the valley, and their surface may form a relatively flat fill surface.

Meandering streams may also degrade and incise the landscape. If the migration rate is large with respect to the rate of incision, the stream may cut a flat-bottomed swath through the former fill or strath. Cycles of cutting and filling may create a series of cut and fill terraces. Cycles of cutting and strath formation may form a series of strath terraces. Often the two types of terraces are found in the same valley [*Meritts, et al.*, 1994]. If the migration rate is small relative to the incision rate, then the stream forms incising meanders. As opposed to the point bars and cut banks formed on strath and fill surfaces, incising meanders have slip-off slopes and bluffs, respectively, as on the Buffalo River in Arkansas, shown in figure 3.2.
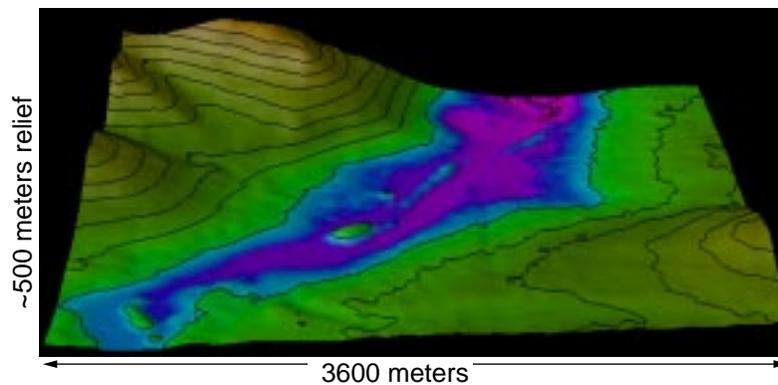
Figure 3.1: Surface with contours at 50 meter intervals of elevation from the 30 meter-horizontal-resolution digital elevation model (DEM) of the Hunter, NY, 7.5' quadrangle. Shown is part of the Schoharie Creek basin along the main channel; view is downstream and to the west.

1 km
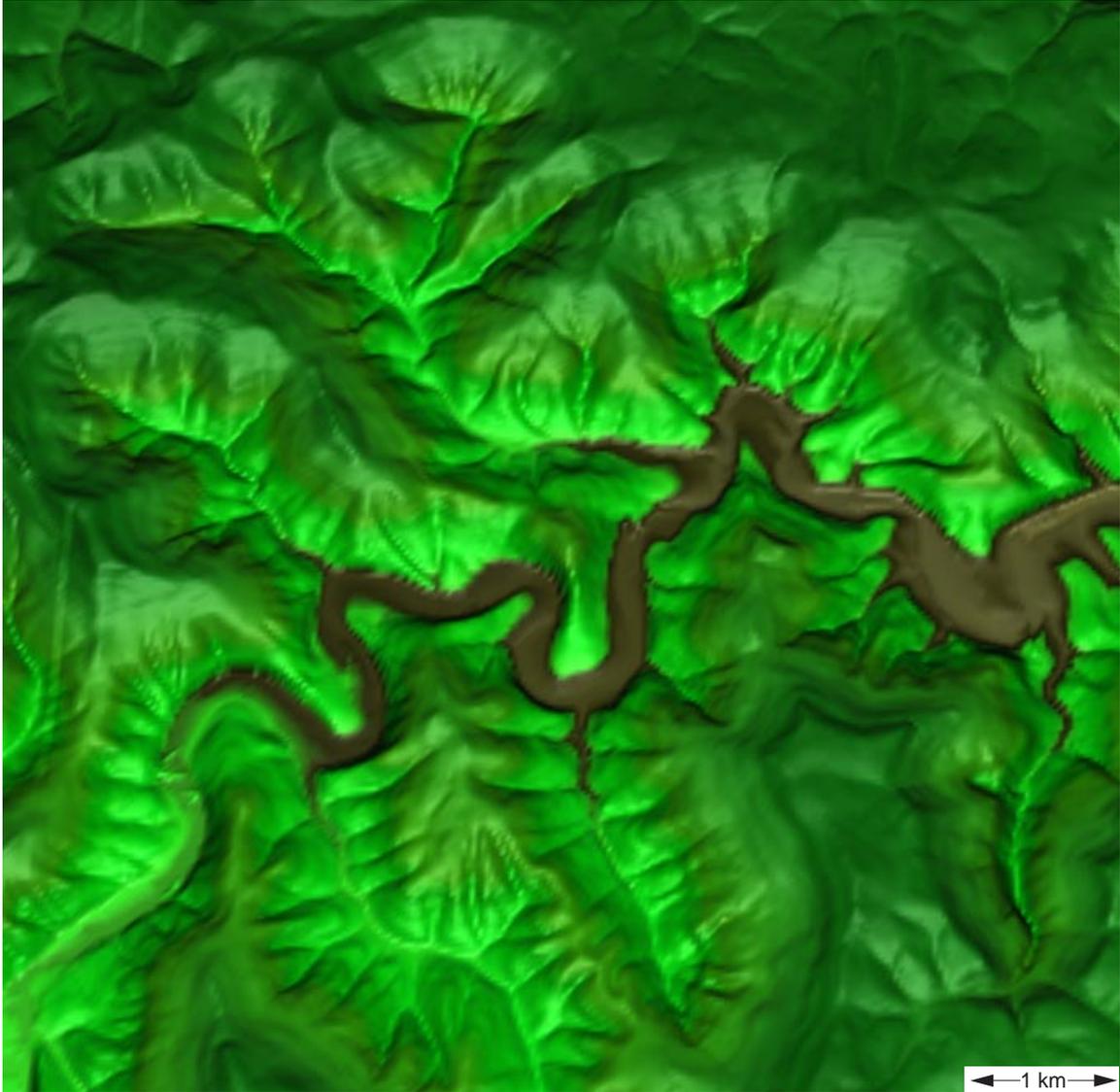
Figure 3.2: Visualization of Ponca, AR, 7.5' DEM. Elevation range of the DEM is 260-739 meters; horizontal resolution is 30 meters.

Even in the absence of terraces, slip-off slopes, and bluffs, meandering streams can form complicated floodplain topographies. As channels erode at the outer banks of bends, they deposit material to form the point bar at the inner banks. Floods deposit not only fine sediments from suspension on the floodplain but also coarser sediments from bedload, often in floodplain channels. Such channels are scoured by flood flow. Thus, floodplain topography is the result of lateral and vertical accretion and scour in floodplain channels.

These floodplain channels may themselves meander. Channels migrate to form meander loops that eventually cut off to form oxbow lakes. Thus, the hydraulics of channel and flood flow can create a complex floodplain topography.

Other features of meandering streams are not as well understood as those described above. Scroll bar topography, or the series of concentric curved ridges and swales on the floodplain, is as ubiquitous as are meander loops and oxbow lakes, but scroll bar topography is not explained by the simple set of processes described above. An example of scroll bar topography on the Mississippi River floodplain is shown in figure 3.3.
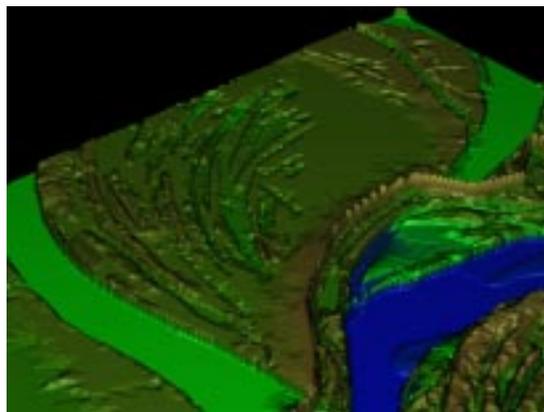
Figure 3.3: Red Leaf, AR, 7.5' quadrangle DEM. Mississippi River (blue) flows toward observer.

Several authors have noted the existence of compound bends, or bends with parts that have opposite curvature (see figure 3.4), as opposed to simple bends that have curvature of the same sign throughout. Compound bends also have familiar, characteristic shapes, such as the bend shown in figure 3.4, and, therefore, are not likely the result of bank heterogeneity or some other stochastic process.

Another important part of the meandering system is the eroding channel bank. The mechanisms of bank failure and the forms created by that failure affect the shape and size

of the meander bend by defining both the channel's migration pattern and the smaller features of the bank.

Finally, I should reexamine the role of meandering in the landscape. Though the characteristic forms of flat valley floors and steep valley sides or slip-off slopes and bluffs are recognized, beyond that qualitative recognition the effect of meandering on the landscape is often ignored in the interpretation of the slope-area relationship, i.e., local slope plotted against contributing area at each point in a discretized drainage basin from a DEM.

Figure 3.4: Photograph from space of a tributary to the Amazon River, flow from top to bottom, channel highlighted.

Also, the mechanism of downstream valley width variation is not well understood. Faster channel migration with respect to the incision rate will lead to a wider, flatter valley bottom. But, what controls these relative rates? Changes in valley width along a stream are commonly observed to correspond to changes in lithology. Valleys may be wider where the valley walls are more erodible because greater bank erodibility will lead to faster migration for the same bank shear stress. It is also possible that changes in lithology may lead to changes in the magnitude of that shear stress. In Chapter 2, I discussed topographic steering, or the role of bedload in forming bars that, in turn, steer the flow toward and, thus, increase the shear stress at the bank. Differences in lithology may correspond to dif-

ferences in bedload, e.g., in the amount or particle size distribution. In turn, different sizes and types of bedload may lead to different bar forms and, thus, magnitudes of topographic steering. An increase in the latter magnitude would increase the lateral channel migration rate and, possibly, the valley width.

In this chapter, I present a study addressing the above issues. The focus is on morphologic, rather than hydraulic, measurements and indicators of meandering process dynamics. The study includes rivers and streams in Alaska, Arkansas, Maine, Missouri, and New York, and uses both remote and field data. The objective is to develop both an understanding of the mechanisms active in meandering streams and a methodology for measuring the morphologic effects of these mechanisms. In later chapters, I draw on the results of this chapter in order to assess the results of the new river meandering and landscape evolution models.

3.1.2 Compound Bend Formation

As noted parenthetically above, I define compound bends as bends that evolve from simple bends to develop a curvature reversal in the course of the bend. *Brice* [1974] documented the formation of compound bends on the White River, Indiana, though the above definition is slightly different from *Brice*'s. He defined a simple meander loop as "[having] one segment of constant curvature whose length exceeds its radius" and a compound loop as "[including] two or more simple loops, whose curvature is commonly directed toward the same side of the river." Both definitions, his and the present one, usually agree and do involve some subjective judgment to distinguish between a compound bend and a series of simple bends. *Brice* [1974] noted that compound loops "demonstrably

40

evolve from simple loops," and the present definition of compound bends follows from this observation.

Two mechanisms, cutting off and compound bend formation (see figure 3.5), are both important for the development of complex meandering stream patterns. Bends are cut off when the channel bypasses the bend by seeking a shorter path across the floodplain. As a result of cutoffs, the meander axis shifts to one side or another at different locations, and the channel course becomes erratic. Cutoffs also produce new smaller bends relative to the larger loops which remain (see figure 3.5(a)).
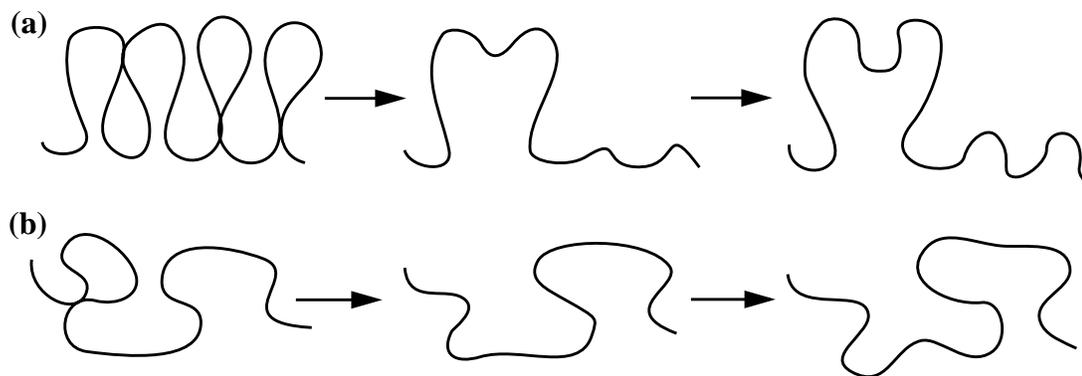
Figure 3.5: Illustration of two mechanisms which influence meander belt complexity: (a) cutoffs and (b) compound bend formation.

As a rule, simple bends that become compound first develop a middle section of low curvature. Such bends might be compound under *Brice*'s [1974] definition, but under the present definition the curvature must actually reverse, or change sign. Some disturbance initiated upstream of the bend, such as that investigated in the following sections, leads to migration that reverses the curvature where it was small (see figure 3.5(b)) and, therefore, makes the bend compound. An example of a typical compound bend shape from the Amazon River basin is shown in figure 3.4. In some cases, the section with reversed curvature may continue migrating in that reverse direction such that the compound bend

separates into three distinct small bends (see figure 3.5(b)). The result of such separations is that the size, shape, and orientation of bends becomes more irregular in general, as in figure 3.5(b). Note that the initial bends in figure 3.5(a) and (b) are differently shaped and that the different shapes are indicative of their different evolution.

The bend separation that often follows from compound bend formation increases the time over which prior conditions are reflected in present forms. In the absence of compound bend formation, bends grow until they cut off, either by chute formation or the breaching of the thin neck connecting the point bar to the rest of floodplain. These mechanisms are known as chute and neck cutoffs, respectively [*Howard*, 1992]. Cutoffs essentially erase the old bend because the new channel bypasses the old bend completely.

However, as explained above, bends may also become compound and separate rather than cutting off, and this process may be repeated in the bends resulting from the initial compound bend formation. In such cases, the shape of the first bend is reflected in the course of a large, multi-bend loop. This loop will eventually cut off, but the initial form will persist over the time it takes for each of the bends to grow and divide, much longer than the time for a single bend to grow and cut off in the absence of compound bend and multi-bend loop formation. If the channel form persists for a longer time, it stands to reason that parts of the floodplain also remain undisturbed more predictably and for a longer time than if the first bend had cut off rather than divided.

Howard and Hemberger [1991] found that their model did not simulate "the compound or cumuliform forms noted by *Brice* [1974] and *Hickin* [1974]" and reasoned that these forms might indicate the operation of "two distinct processes...caused by stream cur-

vature...[and] the formation of alternate bars." It is also possible that compound bend formation is the result of strongly nonlinear dynamics which are not accounted for in their linear model formulation. I will address the latter hypothesis in Chapter 4. This chapter will address the evolution of compound bends from simple bends and the effect of compound bend and multi-bend loop formation on meandering channel planforms over many bends.

3.1.3 Scroll Bar Topography

Scroll bar, or ridge and swale, topography is a familiar feature of meandering river floodplains, but the mechanism responsible for this phenomenon has been studied only rarely, as in *McKenney, et al.*, [1995]. The latter study determined that patterns of vegetation colonization led to observed ridges and swales on gravel bars in the Ozarks of Missouri and Arkansas. However, these gravel bars are not typical of all scroll bar topography. Scroll bar topography is such a common feature of meandering streams in a wide variety of climates that I wish to determine whether it is related to meandering process dynamics and, if so, how.

Several hypotheses for the mechanism forming scroll bar topography exist in the literature. *Parker* [1996] proposes that "highly elongated, partially beached oblique dunes" form observed scroll bars, and this mechanism is consistent with experimental observations [P. Whiting, personal communication, 1996]. I have observed in the field that longitudinal dunes do form ridges on sandy point bars, but the ridges' wavelength is, in general, smaller than that of scroll bars observed on the floodplain, at least at the field sites I have visited.
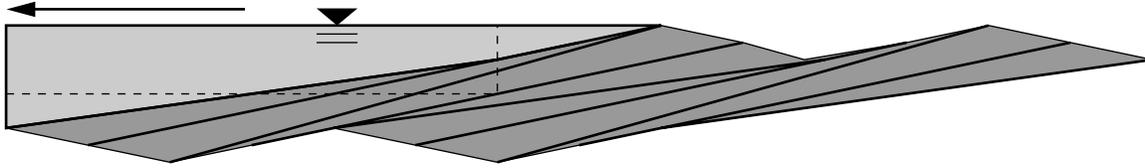
Figure 3.6: Illustration of scroll bar hypothesis. Channel migrates in direction of arrow. Dark gray area with diagonal lines represents point bar deposits with former channel bed surfaces. Light gray area represents present channel cross-section; dashed rectangle represents the rectangular channel cross-section with respect to which the channel bed is sloped.

Another hypothesis is that scroll bar topography is the result of alternating long stable (i.e., channel not migrating) periods during which natural levees form relative topographic maxima and brief unstable (i.e., channel migrating rapidly) periods during which levees do not have time to form and so result in topographic minima. Such a mechanism should produce scroll bars without a characteristic wavelength unless the rapid migration occurs over similar spatial durations from one occurrence to another, though such similarity is not recognized in the literature. A related hypothesis is that episodic bank failure, i.e., a short period of rapid bank migration, leads to episodic point bar accretion. The large sediment load resulting from the bank erosion leads to a large amount of deposition during the point bar accretion such that the elevation of the new accretion is relatively high.

I propose the hypothesis that scroll bar topography is the result of systematic spatiotemporal variations in transverse bed slope, approximately proportional to local channel curvature [*Dietrich and Smith*, 1983; *Ikeda*, 1989]. Downstream variations in transverse bed slope are responsible for point bar-pool topography of meandering stream beds. This hypothesis is illustrated in figure 3.6. *Leopold and Wolman* [1960] observed floodplain stratigraphy in a trench on Watts Branch, MD, and found that their "observations [appeared] to confirm the…hypothesis that point-bar building is the primary process of

flood-plain development in flood plains of this type." According to the present hypothesis, the height of the point bar and, thus, the floodplain surface elevation are determined by the transverse bed slope. When the latter slope is large (or small), the point bar is high (or low), and the pool is deep (or shallow). As the channel migrates the channel curvature and, thus, point bar height may vary. If these variations are oscillatory and periodic or quasi-periodic, then scroll bar topography may result from the lateral accretion of point bars of varying height.

Kinoshita [1987] found stratigraphy resembling that idealized in figure 3.6 in a trench across the Teshio River, Japan, floodplain and perpendicular to the inner bank of the channel. According to *Hasegawa* [1989, pp. 220-221],

> Kinoshita…deduced that a scroll bar may be formed from an embryonic sand bar (at the core of each scroll bar). Each such sand bar is generated by the deposition of suspended sediment swept inward due to the action of large-scale, near-bank separation vortices stretching downstream from the apex of an inner bank.

Unfortunately, the latter study included neither assessments of channel migration rate and curvature where and when the deposits were made nor explanations of how the deposition mechanism was deduced.

In this chapter, I report observations and measurements of natural scroll bar topography. I found the spectral power density of scroll bar topography to determine whether it is periodic or merely quasi-periodic. A finding of periodicity would tend to contradict the hypothesis that scroll bar topography is the result of constant levee deposition and randomly fluctuating migration rates, or vice versa. The scroll bar topography spectra should also allow quantitative comparison of natural scroll bar topography and model results.

McKenney, et al. [1995] found that deposition and scour during floods increased the relief on gravel floodplains of Ozark streams. I examined the stratigraphy of floodplain deposits on a sand-bedded stream to find whether fine flood deposits steepened or smoothened the relief of the deposits from lateral accretion. I also hoped that the stratigraphy might help to reveal the mechanism of scroll bar topography formation. Finally, I measured vegetation stem and trunk diameters to ascertain relative rates of lateral point bar accretion. Detailed examination of scroll bar topography was limited to relatively low-energy, unconfined, single-thread meandering streams, but observations at some of the sites studied by *McKenney, et al.* [1995] were also included to find any similarities or differences between the scroll bar topography on the floodplains of the different stream types.

3.1.4 Bank Failure and Roughness

The mechanism of bank failure can have a large influence on channel planform because different mechanisms can lead to different patterns of bank retreat and, thus, channel migration. Field observations of macro-pores and slump blocks indicate that, in some cases, seepage erosion is the dominant mechanism of bank erosion. This process leads to faster bank retreat not where bank shear stress is greater but, rather, where the groundwater head gradient is greater. Therefore, scour and seepage erosion, respectively, produce dissimilar channel planforms [*Pederson and Cornwall*, 1998]. Some models of meandering (e.g., *Crosato*, 1990) include a bank height-, or near-bank depth-dependent term in the equation for lateral channel migration under the hypothesis that the high banks bordering pools are more subject to seepage-induced failure following decreases in flow stage. However, most models of river meandering assume that the bank migrates as a result of scour, i.e., the pattern of bank migration rate mimics the pattern of bank shear

stress or, in most models, the magnitude of the near-bank velocity, and several studies of bank erosion support this assumption (e.g., *Hasegawa*, 1989; and *Pizzuto and Meckelnburg*, 1989).

The flow affects the form of the bank through scour, and the form of the bank in turn affects the flow through bank roughness. *Thorne and Furbish* [1995] studied the effect of bank roughness on the flow through a meandering channel bend. They found that, after removing vegetation and making the outer bank smooth, the high velocity flow core approached the outside bank more closely and made its closest approach further downstream. They found that bank roughness limited the approach of the core by increasing the width of the rough turbulent flow (RTF) boundary layer. The size of bank roughness elements determines the width of that boundary layer, the rate of turbulent energy dissipation, and the length of bank over which that energy is dissipated through bank shear stress and erosion. In turn, bank erosion and the bank failure mechanism influence bank morphology, bank roughness element size, and meandering channel planform. Therefore, characterizing the bank is integral to understanding the meandering process.

I made observations and measurements of bank roughness elements and the forested bank in general on the outside bank of a meander bend to discover the relationships among bank failure, roughness scale, and their respective mechanisms. For a forested bank, I expected the trees to play an important role but was unsure of the extent and nature of that role. I also made observations and measurements to find the controls on and mechanisms behind an evolving neck cutoff. Partly, the latter observations address whether chute and neck cutoffs are fundamentally different or not. Chutes are formed by floodplain

scour. Are neck cutoffs formed by scouring flood or main channel flow, i.e., are they eroded from the top down or from the sides in? This question leads to another: What controls the lower limit on neck width?

3.1.5 Study Sites

To study compound bend formation, scroll bar topography, and bank roughness elements as part of meandering I studied the meandering process in isolation from other processes and landscape-imposed controls. On the other hand, I also wished to study the interaction of meandering and other landscape processes. For isolation, I studied unconfined, actively meandering streams. These include: the Mississippi River below its confluence with the Arkansas River; the Ellis River, a tributary to the Androscoggin River in western Maine (see location maps, figure 3.7); and several streams in Alaska. I conducted only remote analyses of the Mississippi River and the Alaskan streams and both remote and field studies of the Ellis River.

The Red Leaf, AR, quadrangle, shown in figure 3.3, is on the Mississippi River (in blue in figure 3.3) downstream of its confluence with the Arkansas River and covers part of the point bar surrounded by an oxbow lake formed by a neck cutoff on the Mississippi. The channel is approximately 1000 meters wide. This area is part of the Mississippi River delta and has relief of the same order of magnitude as the channel depth, ~15 meters. The floodplain covered by the Red Leaf, AR, quadrangle has scroll bar topography and some floodplain channels. The part of the floodplain surrounded by the oxbow lake is isolated from the main river channel by a manmade levee system visible in figure 3.3. The scroll bar topography has lower relief, ~5 meters, than the levees, the main channel, and the floodplain channels.
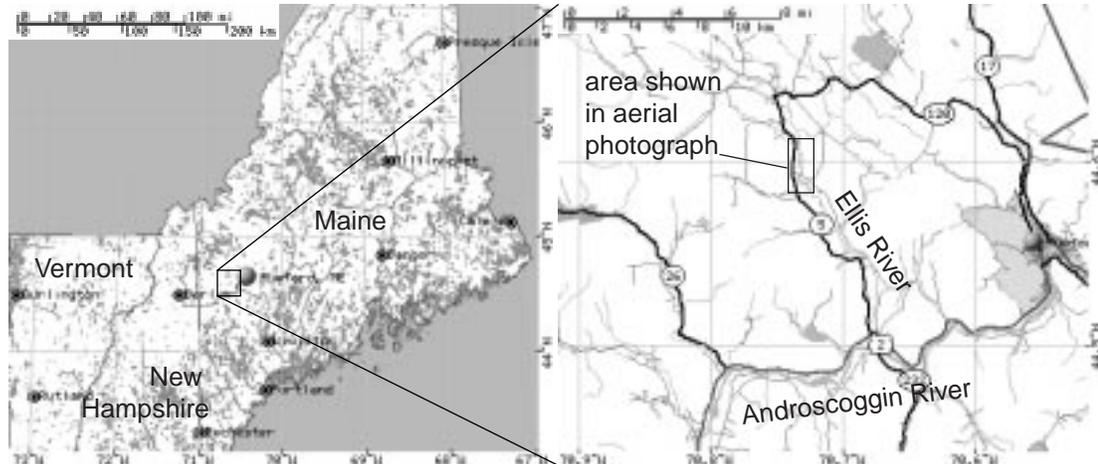
Figure 3.7: Location maps of the Ellis River, ME.

The Ellis River forms both compound bends and multi-bend loops (see figure 3.8). Its valley has a wide, flat bottom and steep sides. Large parts of the floodplain are covered with mostly deciduous forest, though some areas are coniferous. The latter trees are generally on slightly higher ground than the deciduous trees and larger than 20 cm in diameter. The bed material is mostly sand but has some fine gravel, rarely larger than pea-sized. The floodplain has hummocky, ridge-and-swale topography and many oxbows, some of which are connected to the main channel by tie channels. The floodplain surface is composed of silt and fine sand. Observations at the site are consistent with little or no floodplain scour. In the historical record and the field, I observed only neck cutoffs and no chute cutoffs. Bankfull discharge is approximately equal to the discharge with a return period of 1.5 yrs, according to a 20-year gaging station record. This gaging station is located at the covered bridge visible in the photo of figure 3.8 (at the only road crossing the river in the photo). The bankfull hydraulic geometry is shown in table 3.1.

Figure 3.8: 1965 aerial photograph of the Ellis River, Maine.

Table 3.1: Ellis River bankfull hydraulic geometry[a]

parameter	value
discharge	92 m^3/s
cross-sectional area	88 m^2
top width	26 m
average flow depth	3.4 m
average flow velocity	1.0 m/s
channel slope[b]	0.00020 ± 0.00007
valley slope	0.00029 ± 0.00010

a. From USGS discharge measurement of April 4, 1982.
b. Slopes measured from topographic map.

Channel and valley slopes were estimated from a 1:24,000 scale topographic map with a map wheel, though the main reach of the Ellis crosses only one contour. I estimated the elevation at two tributary confluences by assuming the tributaries, each crossing two contours, have constant slope on the valley floor and, thus, calculated two values of channel slope and, by measuring sinuosity over the reach, also valley slope. The channel and valley slopes shown in table 3.1 are the means of the two estimates, and the stated uncertainties are the differences between the estimates. These estimated slopes are not used in the present analysis and are shown only for reference.

The Alaskan streams were digitized from topographic maps. Reaches were selected that are: (a) single-threaded, i.e., not braided; (b) intensely meandering; and (c) unconfined by terraces or valley walls. The streams are listed in table 3.2. I measured channel widths from the maps with the digitizer at many points along each reach and list the means and standard deviations of these measurements in table 3.2.

Table 3.2: Meandering stream reaches

stream reach	quadrangle map(s) (all AK)	mean channel width $\pm \sigma$, meters	reach length, channel widths
Preacher Creek	Ft. Yukon (A-2)	31.2 ± 7.0	1300
Takotna River	Iditarod (C-2)	33.9 ± 12.0	650
N. Fork Kuskokwim River, Mc.	Mt. McKinley (D-6)	38.3 ± 7.4	460
Melozitna River	Melozitna (B-3)	46.2 ± 16.0	990
Teklanika River	Fairbanks (B-5, B-6)	48.0 ± 16.6	1100
Dishna River	Ophir (C-3)	50.4 ± 13.7	510
Birch Creek	Ft. Yukon (A-2)	57.7 ± 14.1	1160
N. Fork Kuskokwim River, Me.	Medfra (B-2, B-3)	95.5 ± 24.1	380
Innoko River	Ophir (C-3)	$113. \pm 18.$	370

The Current River (and Jack's Fork of the Current River) in Missouri, the Buffalo River in Arkansas, and Schoharie Creek in New York serve to illustrate meandering in different settings and in interaction with other landscape processes. The first two streams are located in the Ozarks of Missouri and Arkansas, respectively (see location map, figure 3.9). The present study of these streams is limited to observations in the field and from DEMs and measurements from topographic maps. Schoharie Creek is located in the Catskills of New York. The present study of Schoharie Creek is limited to DEM analysis.
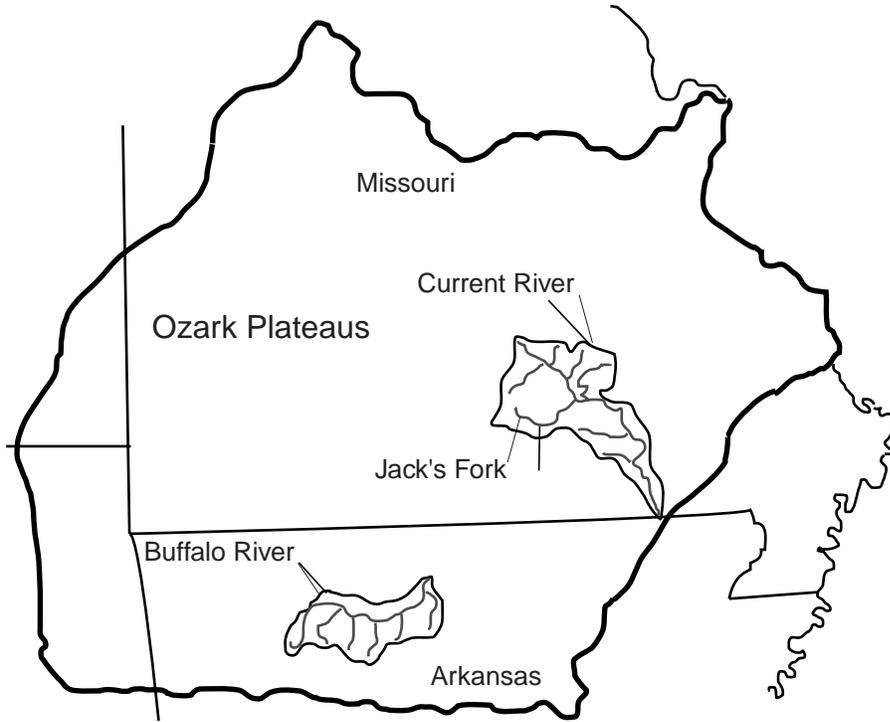
Figure 3.9: Location map of Ozark sites.

The Buffalo River flows west to east in northern Arkansas (see figure 3.9) and is tributary to the White River. The Current River flows northwest to southeast in southern Missouri. Jack's Fork flows west to east, tributary to the Current River. The channels are often confined by bedrock, especially on the Buffalo, but migrate rapidly through alluvial deposits where unconfined. The incising meanders of the Buffalo are relatively sinuous (see figure 3.2). New floodplains on these rivers are mainly gravel and have many flood-plain channels. Some characteristics of Jack's Fork and the Buffalo River are shown in table 3.3.

Schoharie Creek flows west out of the Catskills of New York, then north to its con-fluence with the Mohawk River, tributary to the Hudson River. The headwaters have been captured by the steep gorges of Kaaterskill Creek and other streams flowing east down the Catskill escarpment to the Hudson River. Several studies have examined digital elevation

models of the Schoharie Creek basin, e.g., *Tarboton, et al.* [1991], *Montgomery and Foufoula-Georgiou* [1993], and *Ijjasz-Vasquez and Bras* [1995]

Table 3.3: Characteristics of Jack's Fork at the Burnt Cabin site and the Buffalo River at the Shine-eye site[a]

reach	Jack's Fork	Buffalo River
contributing area, km^2	789	2150
average bankfull channel width, meters	75	100
average bankfull flow depth, meters	1.7	3.0
1.5-year discharge, or bankfull, m^3/s	200	870[b]
channel slope	0.000667	0.00097
valley slope	0.0015	0.0006
geometric mean grain size of bed, mm	21.0	24.6

a. From *McKenney, et al.*, 1995.
b. Estimated assuming same Manning roughness as Jack's Fork.

3.2 Methods

In this section I describe the methods used to study the phenomena and mechanisms described in the Introduction. In general, I studied morphology to infer process dynamics.

3.2.1 Compound Bend Formation

To gain insight into the mechanisms which contribute to compound bend formation, I looked for examples of compound bend formation in the historical migration of the Ellis River by examining aerial photographs spanning the period between 1943 and 1992. I digitized the photos with a scanner, extracted the channels, and super-imposed them to show the time evolution. This exercise revealed two examples of compound bend formation, and observations on the ground at one of the sites corroborate and complement the remote observations.

To measure the importance of compound bend formation on channel planforms over many bends, I analyzed the planforms of the Alaskan streams. The channel center-lines were digitized by hand, and, to eliminate errors and bias, The digitized planforms were corrected by visually comparing the digitized and mapped planforms and moving or deleting points as necessary.

I developed several statistical functions with which to measure the importance and characteristics of compound bend formation in channel planform features such as active meander belt width and channel sinuosity. These measures are generally useful for objective characterization of meandering channel planforms. The statistical functions are based on: (a) the relative width of the active meander belt expressed as the ratio of cross-valley to down-valley standard deviations of the channel centerline coordinates; and (b) sinuosity of the channel centerline. The measurements are made for all possible channel reach lengths and expressed as functions of reach length.

The variances of the x- (down-valley) and y- (cross-valley) components of stream point coordinates are measures of how scattered those points are along each of the axes. The x-axis is parallel to the line fit to the reach's point coordinates by the least-squares method. The expected variances in x and y, respectively, are

$$\sigma_X^2(s') = \left\langle \frac{1}{N(s,\,s+s')-1} \sum_{s_i \,\in\, [s,s+s']} [x(s_i) - \mu_X(s,\,s+s')]^2 \right\rangle \qquad (3.1)$$

$$\sigma_Y^2(s') = \left\langle \frac{1}{N(s,\,s+s')-1} \sum_{s_i \,\in\, [s,s+s']} [y(s_i) - \mu_Y(s,\,s+s')]^2 \right\rangle \qquad (3.2)$$

55

where s' is the reach length; $\mu_X(s, s+s')$ and $\mu_Y(s, s+s')$ are the expected values of x and y, respectively, for points on the channel between s and $s+s'$, inclusive; $N(s, s+s')$ is the number of sampled channel points from s to $s+s'$; and the angle brackets indicate the expected value over all values of s. In practice, for the variances and the other measures defined below, the expected value indicated by the brackets is calculated for a small range of scales about s'. The relative width of the active meander belt is defined as

$$W(s') = \sqrt{\frac{\sigma_Y^2(s')}{\sigma_X^2(s')}} \tag{3.3}$$

If the cross-valley extent of the meander belt decreases relative to the down-valley extent as reach length increases, i.e., the meander belt is longer than it is wide, then the function $W(s')$ will decrease as s' increases. If the mean downstream direction is independent of the down-valley direction, such as over smaller reach lengths, $W(s')$ will be near unity. For longer reach lengths over which the down-valley and mean downstream directions are similar, $W(s')$ will decay and approach zero as valley length approaches infinity. The above measure does have the disadvantage that the orientation of the line fit to the digitized channel points is dependent on the chosen stream reach's length and location.

The above analysis is similar to that of *Matsushita and Ouchi* [1989] and *Ijjasz-Vasquez, et al.* [1993]. These authors used the relative power-law scaling with section length of the *x*- and *y*-variances of detrended sections of contour lines [*Matsushita and Ouchi,* 1989], river basin divides, and river courses [*Ijjasz-Vasquez, et al.,* 1993] to determine fractal self-affinity, or lack of a characteristic scale of fluctuations. The present

method differs from theirs in that the *x*- and *y*-axis orientations are fixed in equations (3.1), (3.2), and (3.3), i.e., the sections are not each detrended.

Sinuosity is a commonly measured characteristic of channel planform and has traditionally been reported as a single value, but that value is not always reproducible. For the same stream, two measurements might yield different values depending on where and over what reach length they were made. *Howard and Hemberger* [1991] recognized that sinuosity could vary according to the reach length and location and divided the total sinuosity into three factors, the full-meander, half-meander and residual sinuosities.

Measurements developed below characterize the distribution of sinuosity measurements as a function of reach length. For a range of stream lengths, I compute the mean and variance of sinuosities measured at that length range. Sinuosity is measured between every pair of points along the reach; the sinuosities for point pairs are binned according to the streamwise distance between the points; and the mean and variance of the measurements in each bin are calculated. Thus, the sinuosity mean and variance are defined as functions of reach length:

$$\mu_S(s') \; = \; \left\langle \frac{s'}{r(s, \, s + s')} \right\rangle \tag{3.4}$$

$$\sigma_S^2(s') \; = \; \left\langle \left(\frac{s'}{r(s, \, s + s')} - \mu_S(s') \right)^2 \right\rangle \tag{3.5}$$

where *s'* is the length of the channel segment; *r(s, s+s')* is the straight-line distance between the segment's end points at *s* and *s+s'*; and the angle brackets indicate the expected value for all values of *s*.

Andrle [1994, 1996] developed the angle measure technique (AMT) to identify characteristic scales and features of meandering channel planforms. Like the measures introduced here, the AMT produces a function of reach length or scale rather than a single number.
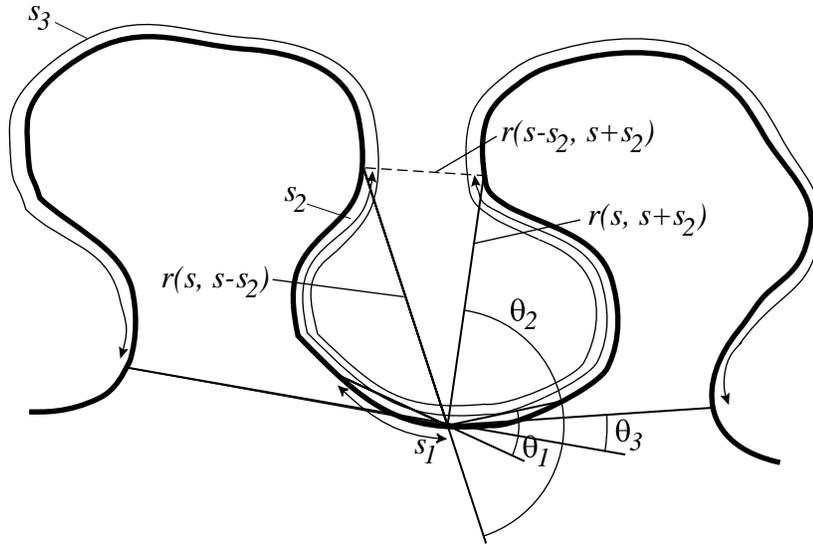
Figure 3.10: Illustration of the angle measure technique of *Andrle* [1994, 1996].

The AMT is essentially a measure of average curvature at different streamwise scales. The method is illustrated in figure 3.10, where, at point s, for the three scales, s_1, s_2, and s_3, the angles are θ_1, θ_2, and θ_3, respectively. For three points at equal intervals along the channel, the streamwise length of that interval is the scale, e.g., s_2 in figure 3.10, at which I measure the angle. I draw two straight lines connecting the first and second and the second and third points, respectively, e.g., $r(s, s-s_2)$ and $r(s, s+s_2)$. The supplement of the angle between those two lines is the angle measure, e.g., θ_2. The smaller the angle between the two lines, the larger the curvature and the angle measure. For example, the angle between the lines, $r(s, s-s_2)$ and $r(s, s+s_2)$, is small, and, therefore, the angle measure, θ_2, at that scale, s_2, is large at point s. The opposite is true for the scales, s_1 and s_3,

such that the angle measures, θ_1 and θ_3, are small at point s. In *Andrle*'s [1994, 1996] original method, for each scale he found the angle measures at 500 points, chosen at random, and averaged those measures to find the mean angle. In a modified version of the AMT, I measured angles for all possible distances between discretized channel points (see figure 3.10) and locations along the channel. The angles were binned according to scale and averaged to find the mean angle as a function of the streamwise scale:

$$\mu_\theta(s') \;=\; \left\langle \pi - \text{acos}\!\left(\frac{r(s, s-s')^2 + r(s, s+s')^2 - r(s-s', s+s')^2}{2r(s, s-s')r(s, s+s')}\right)\right\rangle. \tag{3.6}$$

Andrle [1996] found that, for the meandering streams he tested, the mean angle was peaked at a certain scale. He reasoned that the magnitude of this peak was related to sinuosity and the scale at which it occurred was related to meander wavelength. He also found secondary peaks for manifestly underfit streams, i.e., where stream meanders are smaller than the meander-like valley bends, and inferred that the secondary peaks were indicative of the larger, valley-scale sinuosity.

The streams I measured are not restricted by the valley walls. Therefore, the new measures and *Andrle*'s [1996] should indicate the importance of compound bend formation by revealing the scales of multi-bend loops resulting from compound bend formation. If compound bend formation is absent or does not lead to multi-bend loop formation, then the measures will have only the primary channel planform scale indicators corresponding to the meander bend length and no secondary channel planform scale indicators corresponding to the length of multi-bend loops.

3.2.2 Scroll Bar Topography

At the Buffalo River and the Current River, including Jack's Fork, in the Ozarks of Arkansas and Missouri, respectively (see figure 3.9), I observed the scroll bar-like topography documented by *McKenney, et al.* [1995]. The result of these observations is essentially a corroboration of their results.

For the Ellis and Mississippi Rivers, I calculated power spectra of floodplain cross-sections ("transects"). For the Mississippi River floodplain, I used ERMapper (TM) GIS software to extract several transects of scroll bar topography from the Red Leaf, AR, DEM (see figure 3.3). On the Ellis River floodplain, I surveyed several transects of scroll bar topography on the floodplain, detrended each transect by subtracting from the data a linear least-squares fit to that data, and found the power spectra using the *Lomb* [1976] method [*Press, et al.*, 1997] for spectral analysis of unevenly sampled data. The Mississippi transects are evenly sampled, but the Ellis transects are not, so I chose the Lomb method to use the same method for all transects. The Lomb method produces a normalized periodogram, or spectral power as a function of wave number, and significance levels of the spectral power with respect to the null hypothesis that the data are independent, Gaussian-distributed random values. The significance level of a value is the probability that the value was produced by the above random process. The spectrum is not smoothed.

To examine the stratigraphy of scroll bars on the floodplain, I sampled soil cores to a depth of one meter at some points on the Ellis transects. The cores were taken in six sections. Based on the look and feel of the samples, descriptions of the material in each section of each core were recorded. For example, if the soil could be rolled into balls, then it

was clayey. If it was gritty like sandpaper, then it was sandy. If it was powdery, then it was silty. I assigned each section a grain size class based on the descriptions recorded in the field and, by this method, determined to a reasonable degree of accuracy the relative textures of the sampled materials.

Also on the Ellis, I measured shrub stem and tree trunk diameters along several sections perpendicular to the downstream direction to estimate the relative variation in space of lateral accretion rate on the point bar. The diameter data defines an upper bound on the vegetation age and, by proxy, the point bar age at a point. Where the gradient of diameters is large, the age change per distance is large and indicates a slow migration rate; the opposite is true where the gradient of diameters is small.

3.2.3 Bank Failure and Roughness

I observed and measured bank features to determine the mechanisms and scales of bank erosion and roughness. To find the scale of the bank roughness elements, including slumped blocks and spaces left by slumps and failures, along the outer bank of a bend on the Ellis River, I measured: (a) the bank roughness elements' dimensions in the cross- and downstream directions; (b) the diameters of slumped trees; and (c), where the bank was undercut but had not failed, the depth (cross-stream) of undercutting. Observations included sketches and written descriptions of the bank roughness elements. For scale context, I measured the dimensions of sand dunes on the bed. I also observed and measured the dimensions of a relatively new cutoff on the Ellis.

3.2.4 Meandering and the Landscape

To detect the interactions between the landscape and river meandering, I studied variations in valley width and the relationship between slope and contributing area. I

examined the Schoharie Creek valley as represented by 30-meter horizontal resolution DEMs of the Hunter and Kaaterskill, NY, 7.5' USGS quadrangles. *Tarboton, et al.* [1991] pieced together these DEMs, filled the pits, calculated contributing areas by routing each pixel's contributing area downstream in the steepest single flow direction. The steepest downhill slope for each pixel is plotted against contributing area. I also binned points according to log-area and plotted the average slope of points in each bin against the points' average contributing area.

On the Buffalo, changes in valley width correspond to changes in lithology. The valley is narrow where the channel is on massive, Ordovician sandstone and wide where the channel is on cherty, Mississippian limestone. Conventional wisdom says that, where a valley is wider, the bedrock is weaker, or more erodible. However, it is possible that, in the wider valley, the laterally eroding flow is more erosive by way of a mechanism that is independent of erodibility. Both of these formations can form cliffs, but the Boone limestone has a large chert component which breaks up into relatively fine gravel. The Boone formation also has a well developed Karst system of caves and conduits.

The main channel of a river, such as the Buffalo, that has been actively incising an uplifting plateau for sufficient time should be at or approaching dynamic equilibrium. The fact that the Buffalo River basin has on the order of 300 meters of relief indicates that it has probably been incising for sufficient time to approach dynamic equilibrium. If the controls on channel incision, e.g., either detachment-limited or transport capacity-limited, and the discharge are similar through different lithologies, then channels on more erodible or transportable lithologies will have a lower slope (I address the detachment-limited case in

more detail in Chapter 5). Conversely, less erodible or transportable lithologies will have higher slopes at dynamic equilibrium.

The controls on incision of the Buffalo are not well established, but if I assume, for adjacent reaches through valleys of varying width, that: (a) bank erosion is a detachment-limited process; (b) bank erosion equals lateral channel migration; (c) channel incision is detachment-limited; (d) uplift and channel incision are, at least approximately, in dynamic equilibrium; (e) discharge is approximately constant with respect to distance downstream; and (f) valley width corresponds to rock erodibility; then channel slope should vary with rock erodibility and, therefore, be greater (or smaller) where the valley is narrower (or wider).

To test this hypothesis, I measured channel slopes from 1:24,000-scale topographic maps in the wide valley shown in figure 3.29 and the narrower valleys, i.e., more similar to the topography shown in figure 3.2, up- and downstream of the wide-valley reach. If the rock forming the wide valley has greater erodibility, then, under my assumptions above, the slope through this reach would be lower than in surrounding narrow-valley reaches.

3.3 Results

3.3.1 Compound Bend Formation

Compound bend formation is evident in the historical Ellis River channel plan-forms, extracted from aerial photographs and overlain in figure 3.11. The 1943 (darkest gray) channel appears too wide in a loop, later cut off, at bends 1-7 due to the effect of direct glare in the photograph. Note the existence of multi-bend loops in the vicinity of bends 8-13. These loops indicate that compound bend formation is an active part of the

Ellis' channel planform evolution. In figure 3.12 two examples of compound bend forma-tion on the Ellis River are enlarged to show these cases in greater detail.

In figure 3.12(a) the time sequence illustrates compound bend formation following a cutoff and a subsequent wave of accelerated migration. According to other aerial photos not shown, bend 2 cut off between 1972 and 1981. Subsequently, the "new" bend 2 devel-oped and migrated rapidly downstream. This migration perturbed bend 4 such that it is now compound. Upon inspection of the site, I discovered that the middle, reversed section of bend 4 has a cut bank at the inside and a small point bar at the outside of the bend, fea-tures indicating that this part of the bend has started to migrate in the opposite direction from the migration of the rest of the bend. This reach is unconfined by terraces or bedrock except for the downstream end of bend 7, which is confined by bedrock. The whole area shown is forested.

In figure 3.12(b), the rapid migration of the "new" bend 12 follows a cutoff of the "old" bend 12 before 1943. A wave of channel migration has propagated downstream and led to a curvature reversal in the upstream part or limb of bend 13. The migration of bend 12 may have been further accelerated following the cutoff at bend 8 and the subsequent rapid migration of bends 8-11 after 1965. The reach is wholly unconfined. Cut banks in this reach are generally unforested, though some have a thin line of riparian trees, and bend 10's outside bank is forested at the downstream end.
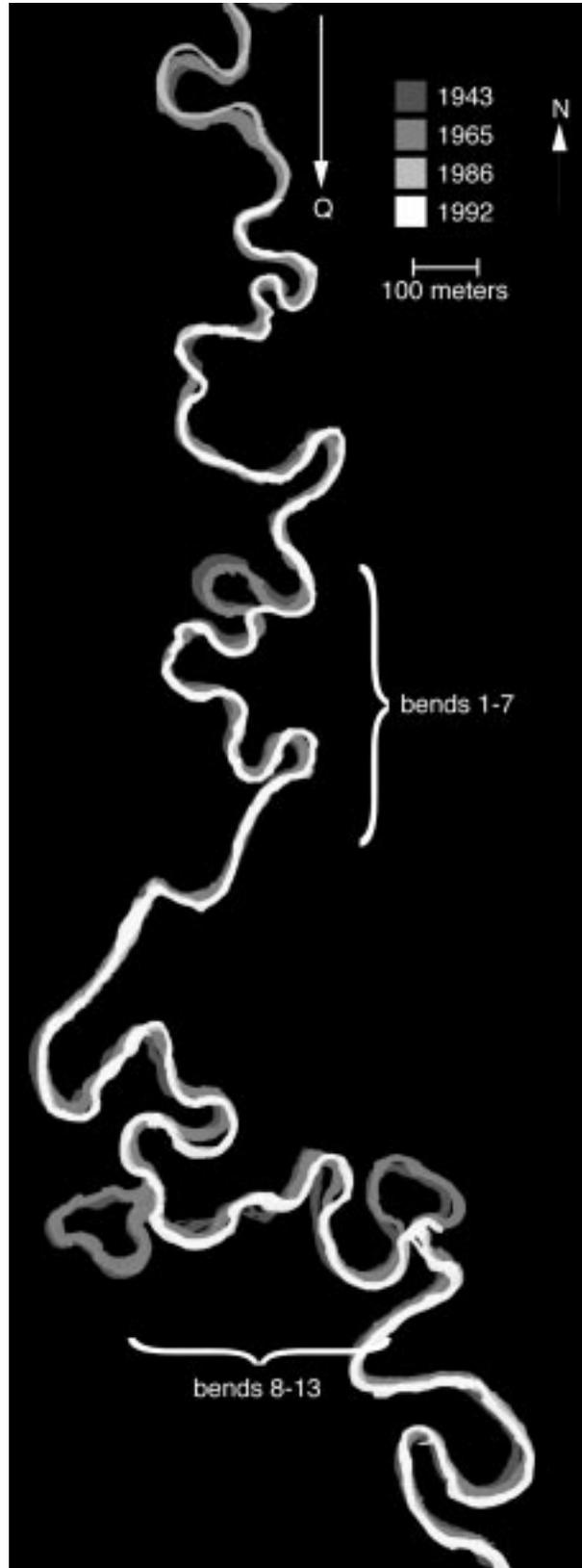
Figure 3.11: Ellis River channels extracted from aerial photos and super-imposed.
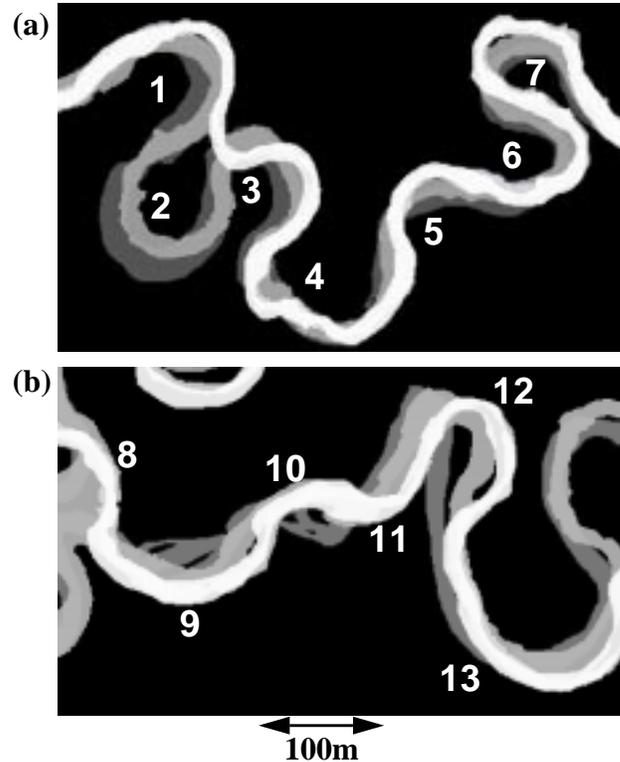
Figure 3.12: Close-ups of Ellis River, ME, channels from figure 3.11. Lighter gray is more recent. Bends are numbered for reference. Flow is from left to right in both (a) (north to south) and (b) (west to east).

To assess the role of compound bend formation in the Alaskan streams, I applied the sinuosity and belt width measures and modified AMT to the planforms of the streams listed in table 3.2. The reaches are shown in figure 3.13. Normalized reach curvature is plotted against normalized downstream distance in figure 3.14. For normalization, curvature is multiplied by the channel width, and downstream distance is divided by channel width. The curvature shown is a moving average of local curvature at three points.

Channel curvature in figure 3.14 is indicative of bend shape. If the channels were sine-generated curves, then the curvature function would be sinusoidal, but, in fact, the wave forms are quite jagged. Bends commonly have two pronounced curvature maxima at the beginning and end of the bend, respectively. In between, the curvature often drops to

nearly zero for a short distance and is nearly constant at an intermediate value for the remainder of the bend's length. In some bends, where the curvature becomes small, it crosses zero, i.e., it reverses sign. Such bends are compound by the present definition, and figure 3.14 indicates that these compound bends are an end member of the continuum of typical bend shapes. As examples, a portion of the curvature plot for Birch Creek is enlarged and inset in figure 3.14, and the part of the channel covered by the inset is out-lined in figure 3.13. The seemingly minor details of bend shape described above are appar-ently indicative of a mechanism that, as shown below, is important on the scale of channel reaches many times longer than a single bend.

The sinuosity mean and variance, relative belt width, and mean angle are plotted against reach length normalized, again, by channel width (see table 3.2) in figure 3.15. The sinuosity means have large breaks in slope that correspond to peaks in the sinuosity variances, changes in slope of the belt width, and peaks in the mean angle. The mean angle peaks are consistently at lower values of reach length than the above features in the other plots. This is explained by referring to figure 3.10, where the large angle θ_2 corresponds to streamwise distance, s_2, and the large sinuosity between the two points $s\text{-}s_2$ and $s\text{+}s_2$ cor-responds to a streamwise distance of $2s_2$. Therefore, features of the sinuosity mean and variance and the belt width occur at a scale apparently twice the scale of the same features of the mean angle. There is no real difference in scale; they are simply measured differ-ently.
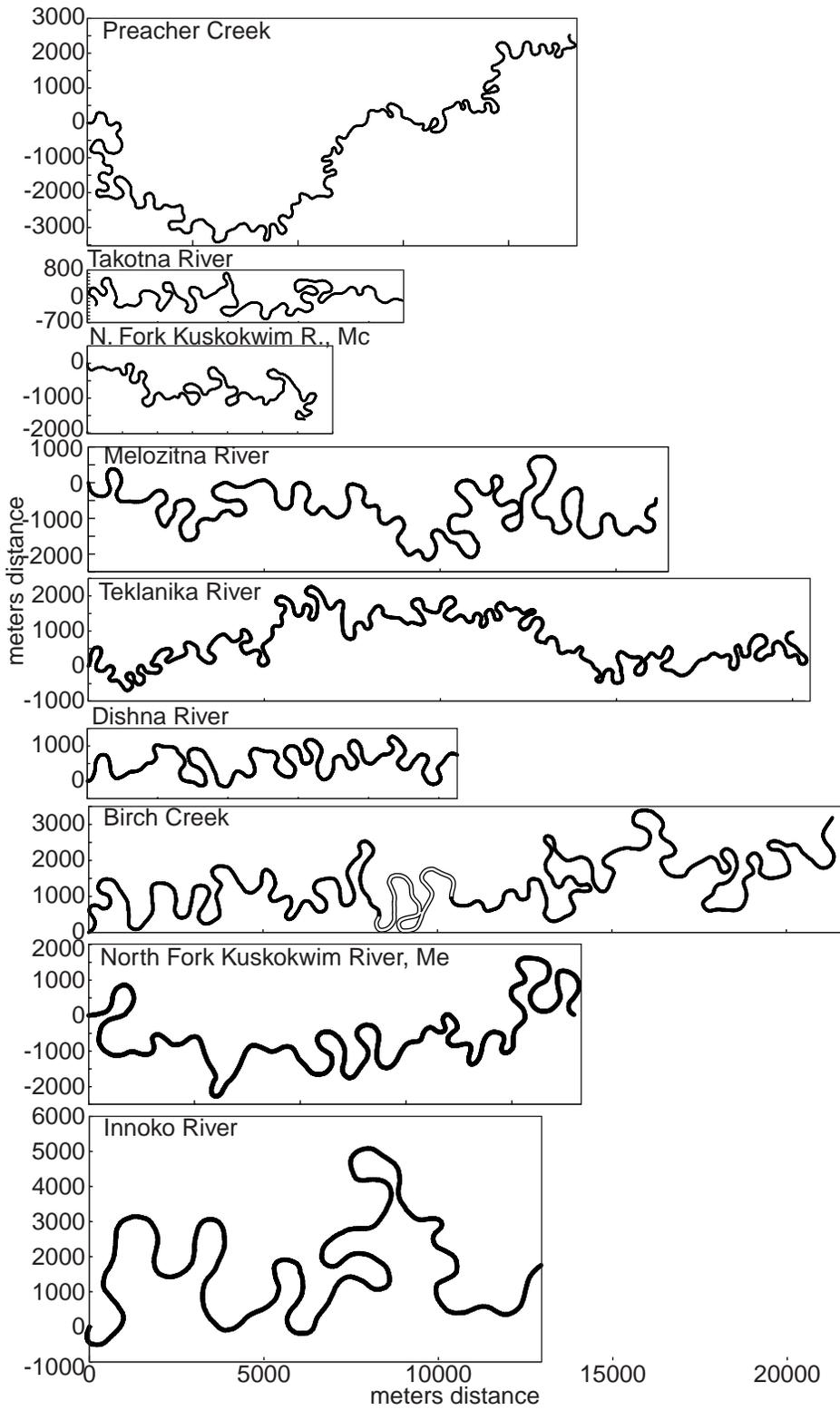
Figure 3.13: Digitized meandering stream reaches from topographic maps. Outlined part of Birch Creek corresponds to inset in figure 3.14.
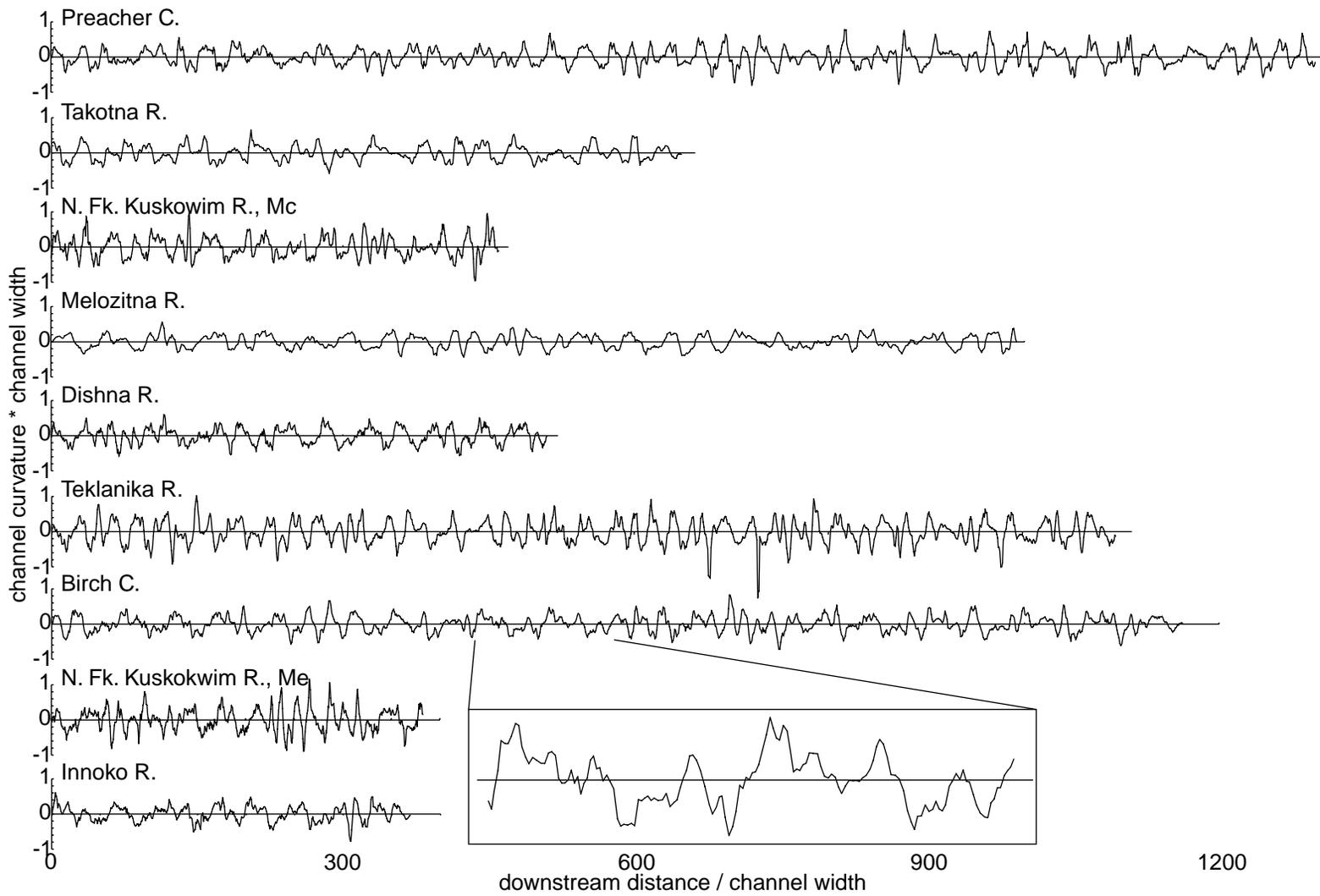
Figure 3.14: Normalized curvature *vs.* normalized downstream distance. Axis scales for inset portion of Birch Creek not shown.
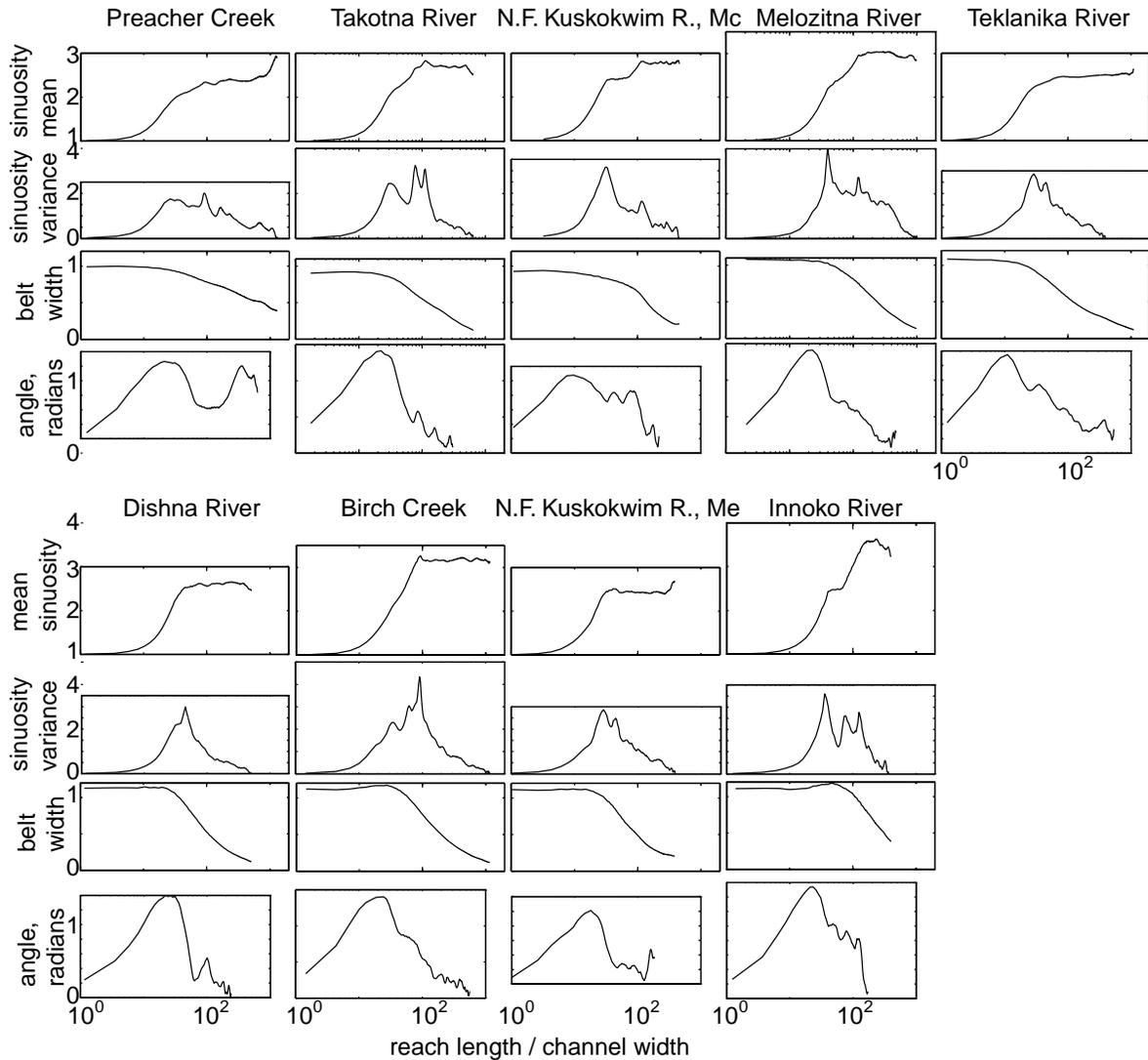
Figure 3.15: Sinuosity mean and variance, relative meander belt width, and mean angle plotted against normalized reach length (i.e., length divided by channel width) for the streams listed in table 3.2 and shown in figure 3.13.

The smallest scale at which μ_S levels off ($\mu_S > 1$), σ_S^2 peaks, W begins to decay, and μ_θ peaks (collectively, channel planform scale indicators) is similar to a meander wavelength, and the level at which μ_S finally levels off is the mean reach sinuosity. The first channel planform scale indicators occur at similar scales for all of the streams, in the range of 20-40 channel widths (20-40 b) for the first three measures. From the curvature

70

plots of figure 3.14, it is apparent that this scale is actually the length of a single meander bend, or half the meander wavelength.

For many of the streams, the sinuosity rises and levels in more than one step corresponding to more than one peak in σ_S^2 and μ_θ and convex or straight-line decay of W (e.g., Takotna, N.F. Kusk. Mc., Melozitna, Innoko, especially). There is even some consistency in the scales of the second peaks in σ_S^2 at ~100 b. Takotna and Innoko have two large peaks bracketing the 100 b scale. These secondary channel planform scale indicators correspond to the scales of multi-bend loops, or the length of several bends. Their exact characteristics may change over time and from stream to stream. For example, on the Ellis River parts of two multi-bend loops cut off between 1965 and 1986, and such changes would be reflected in the magnitudes and scales of secondary channel planform scale indicators.

Multi-bend loops are different among the Alaska streams. On Birch Creek they have irregular shapes, but the multi-bend loops of N.F. Kusk. Mc., Melozitna, and Innoko are more clearly composed of individual, regularly shaped bends. This difference is apparent in the plots of figure 3.15. For the latter group of streams, the secondary channel planform scale indicators are separated from the primary channel planform scale indicators by a significant difference in scale, and μ_S for N.F. Kusk. Mc. and Innoko is flat between the primary and secondary channel planform scale indicators. The separations in scale may indicate that compound bends on these latter streams are more likely to separate into distinct bends. That greater likelihood leads to repeated separations and, thus, multi-bend

loops. In comparison, compound bends on Birch Creek may separate into distinct bends less often.

The measures contain more information than whether compound bend formation is important or not. They reveal the differences in the planforms, even among those where compound bend formation leads to multi-bend loops.

Lateral elongation is apparent in the belt width plots. Most of the W's start at their maximum value, near one, but some rise slightly to a maximum at the first channel plan-form scale indicator before decaying. This rise indicates lateral elongation at the scale of the meander bend length. This effect is strongest in the most sinuous streams, Birch Creek and Innoko River. But, Melozitna is nearly as sinuous as Birch Creek, and the effect is entirely absent. The effect is apparent in Dishna, Birch, N.F. Kusk. Me., and Innoko.

Mean angle is not an exact measure of sinuosity—magnitudes of μ_S and μ_θ are not always consistent. The highest μ_θ is for Innoko, which also has the greatest μ_S, but not at the same scale. Melozitna's μ_θ peak is much greater than N.F. Kusk. Mc.'s, but the latter has the higher first plateau in μ_S. Innoko and N.F. Kusk. Me. have similar first μ_S plateau magnitudes, but Innoko has much greater μ_θ. The magnitudes of the secondary μ_S increase and μ_θ peak are also not similar. For example, compared to Innoko, the secondary increase in μ_S for N.F. Kusk. Mc. is not large, but the secondary peaks in μ_θ for the latter are as large or larger than the secondary μ_θ peaks for Innoko. Peak magnitudes of σ_S^2 and μ_θ are not generally similar either, but I might expect the magnitudes of mean and variance to dif-fer. For μ_θ, the first peak is always the largest; not so, σ_S^2.

The mean angle appears closely related to belt width. Magnitude of μ_θ corresponds to non-concavity of W. Where the angle is large, W is straight or convex; otherwise, W is concave. Comparing the plots for N.F. Kusk. Mc. with those of Melozitna, I find that the shapes of the μ_S and σ_S^2 plots for the two are similar, though σ_S^2 and the maximum μ_S are larger for Melozitna. The W and μ_θ plots are quite different between the two streams, but, for each stream, W and μ_θ are similar: for N.F. Kusk. Mc., the maxima of both are small but relatively level through the secondary channel planform scale indicators; for Melozitna, the maxima of both are large and decay to low values through the secondary channel planform scale indicators. These facts indicate that mean angle is related to both sinuosity and meander belt width but may be more closely related to the latter. Upon inspection of the channel planforms, I find that the apices of the longest bends on N.F. Kusk. Mc. tend to point upstream, and this fact explains the low belt width at the bend scale.

A useful observation derived from these plots is that streams may have both primary and secondary sinuosities corresponding to the single bend and multi-bend loop scales, respectively. The mean sinuosity plots of figure 3.15 show that streams may differ in both the primary and secondary sinuosities and that the magnitude of one does not necessarily indicate the relative magnitude of the other. For example, the primary sinuosity of N.F. Kusk. Mc. is greater than that of Birch Creek, but the secondary sinuosity of the latter is greater than that of the former. Such inconsistencies suggest that mechanisms limiting sinuosity on the bend scale do not necessarily limit sinuosity at the multi-bend loop scale. I will revisit the subject of primary and secondary sinuosities in Chapter 5.

3.3.2 Scroll Bar Topography

The locations of the Mississippi floodplain transects are shown in figure 3.16, and the transects themselves are shown as plots of elevation vs. distance in figure 3.17. The power spectra are shown in figure 3.18. These power spectra characterize the transects' relief in the wave number domain. In some cases, though, the spectra reveal the pitfalls of applying spectral analysis to a non-stationary signal.

All of the spectra have peaks above the 0.1 significance level, i.e., the chance of peaks of that magnitude occurring by a Gaussian random process is one in ten, and many of the spectra have peaks which are significant to a much smaller level. Most of the peaks found in these spectra are listed in table 3.4 with significance level, wave number, and wavelength. The total length of each transect is also shown. Some of the transects have large peaks at wavelengths at the same order of magnitude as the transect length. Such peaks, while large, should be viewed with suspicion because the transect cannot contain more than one or two complete waves.

The transects have different lengths, and some of the transects cover substantially similar parts of other transects, e.g., transects 1, 5, 7, and 8 (see figure 3.16). However, the corresponding spectra are not necessarily similar because some of these transects are not stationary. The periodic forms evident in, e.g., the 0.00257 m^{-1} peak of transect 7 are, upon inspection of the transects, apparent in transect 8, but the latter also contains non-scroll bar topography such as levees and channels that have much greater relief and, therefore, spectral power than the scroll bars. Therefore, the spectrum of transect 8 is dominated by peaks at the lower wave numbers.
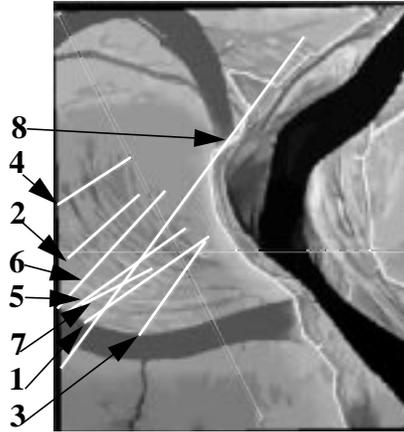
Figure 3.16: Plan view of Mississippi River floodplain on the Red Leaf DEM with elevation in grayscale and showing transect locations by number.
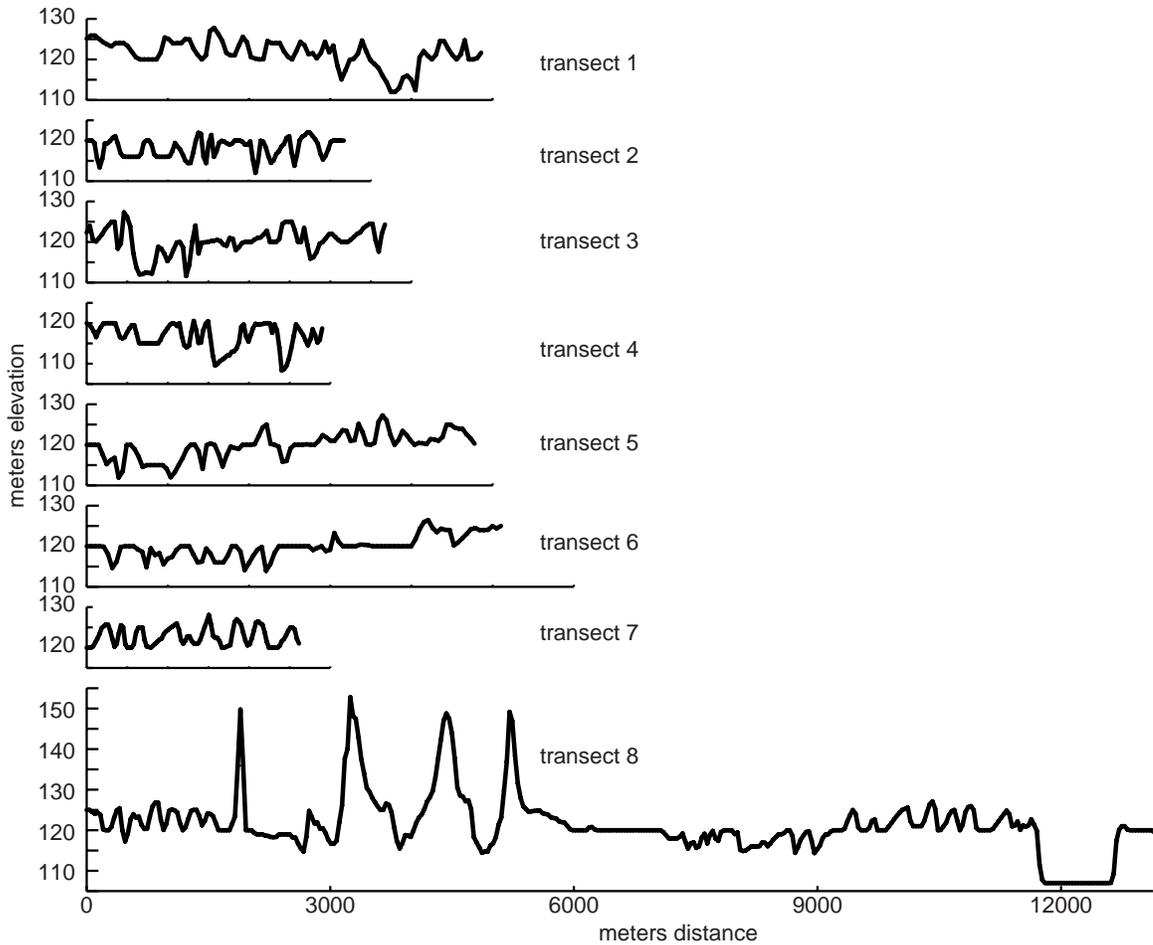
Figure 3.17: Mississippi floodplain transects (see figure 3.16); elevation exaggerated.
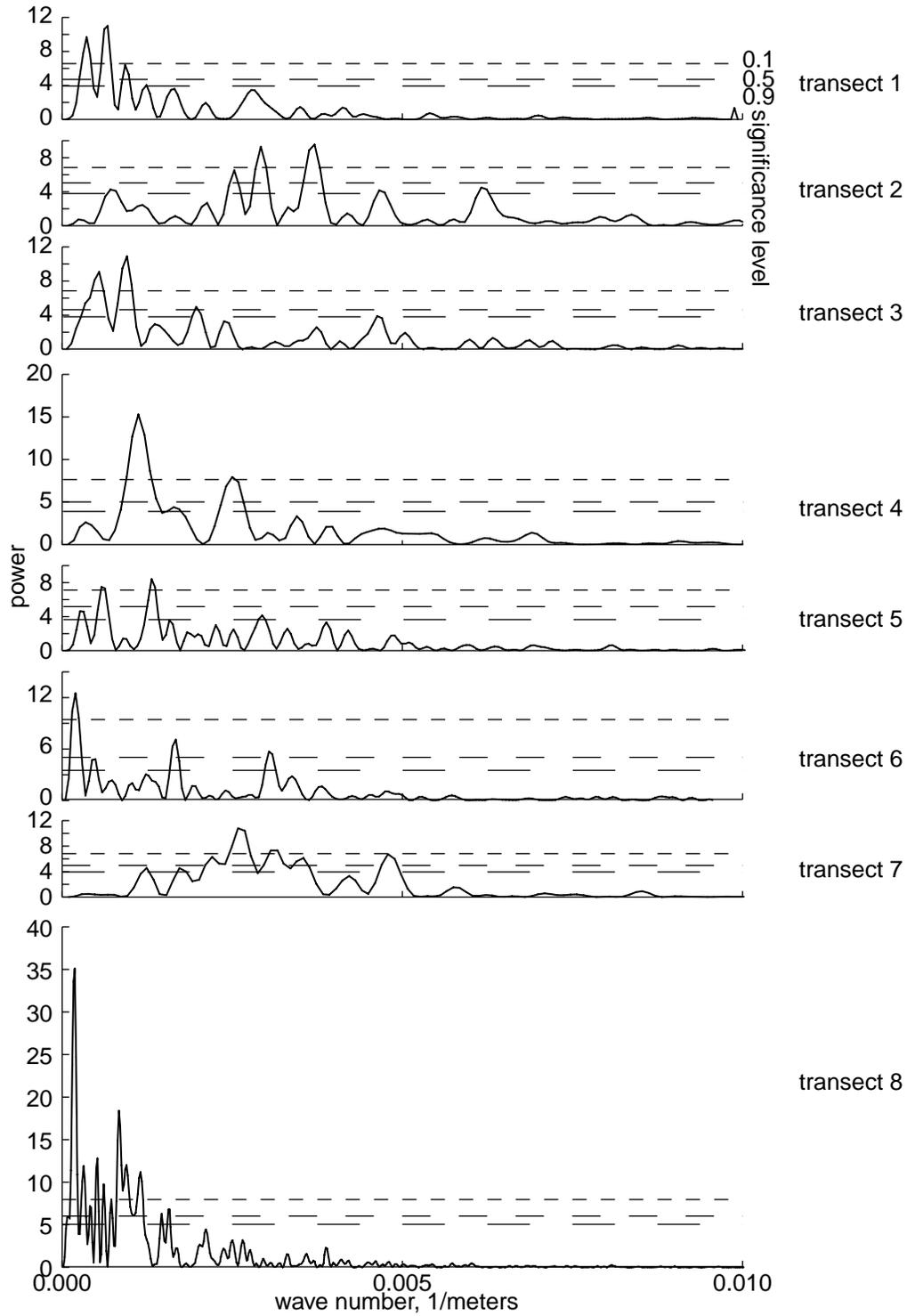
Figure 3.18: Power spectra of detrended Mississippi floodplain transects. Dashed lines indicate significance levels.

Table 3.4: Spectrum peak wave numbers, k (1/meters), wavelengths, L (meters), and significance levels, P, for Mississippi transects, total length shown.

transect 1, 4860 m			transect 2, 3170 m			transect 3, 3680 m			transect 4, 2900 m		
k	L	P	k	L	P	k	L	P	k	L	P
3.60e-4	2780	6e-3	7.09e-4	1410	0.76	5.42e-4	1840	0.01	1.12e-3	893	2e-5
6.71e-4	1490	2e-3	2.52e-3	396	0.14	9.52e-4	1050	2e-3	1.64e-3	611	0.71
9.26e-4	1080	0.15	2.92e-3	342	9e-3	1.97e-3	507	0.49	2.50e-3	400	0.03
1.23e-3	810	0.82	3.71e-3	269	7e-3	4.63e-3	216	0.86			
			4.65e-3	215	0.79						
			6.17e-3	162	0.68						

The scroll bars' signal is especially evident in the spectra of transects 2 and 7. These transects do not extend beyond the area where the scroll bar topography is dominant. Note that the peak wavelength for transect 7 is greater than either of the peak wavelengths of transect 2 because transect 7 is not as nearly perpendicular to the scrolls as is transect 2. Smaller amplitude peaks at similar wavelengths are evident in other transects, but some do not register as significant at even the 0.9 significance level.

Table 3.4: (cont'd.) Spectrum peak wave numbers, k (1/meters), wavelengths, L (meters), and significance levels, P, for Mississippi transects, total length shown.

transect 5, 4780 m			transect 6, 5100 m			transect 7, 2610 m			transect 8, 13,500 m		
k	L	P	k	L	P	k	L	P	k	L	P
2.62e-4	3820	0.62	2.00e-4	5010	4e-4	1.24e-3	805	0.65	1.98e-4	5040	2e-13
5.74e-4	1740	0.05	4.90e-4	2040	0.55	1.72e-3	581	0.65	5.18e-4	1930	1e-3
1.31e-3	764	0.02	1.67e-3	600	0.08	2.20e-3	455	0.17	8.33e-4	1200	4e-6
2.93e-3	341	0.79	3.04e-3	329	0.27	2.58e-3	387	2e-3	1.15e-3	870	6e-3
						3.06e-3	327	0.06	1.57e-3	635	0.37
						3.53e-3	283	0.20			
						4.78e-3	209	0.11			
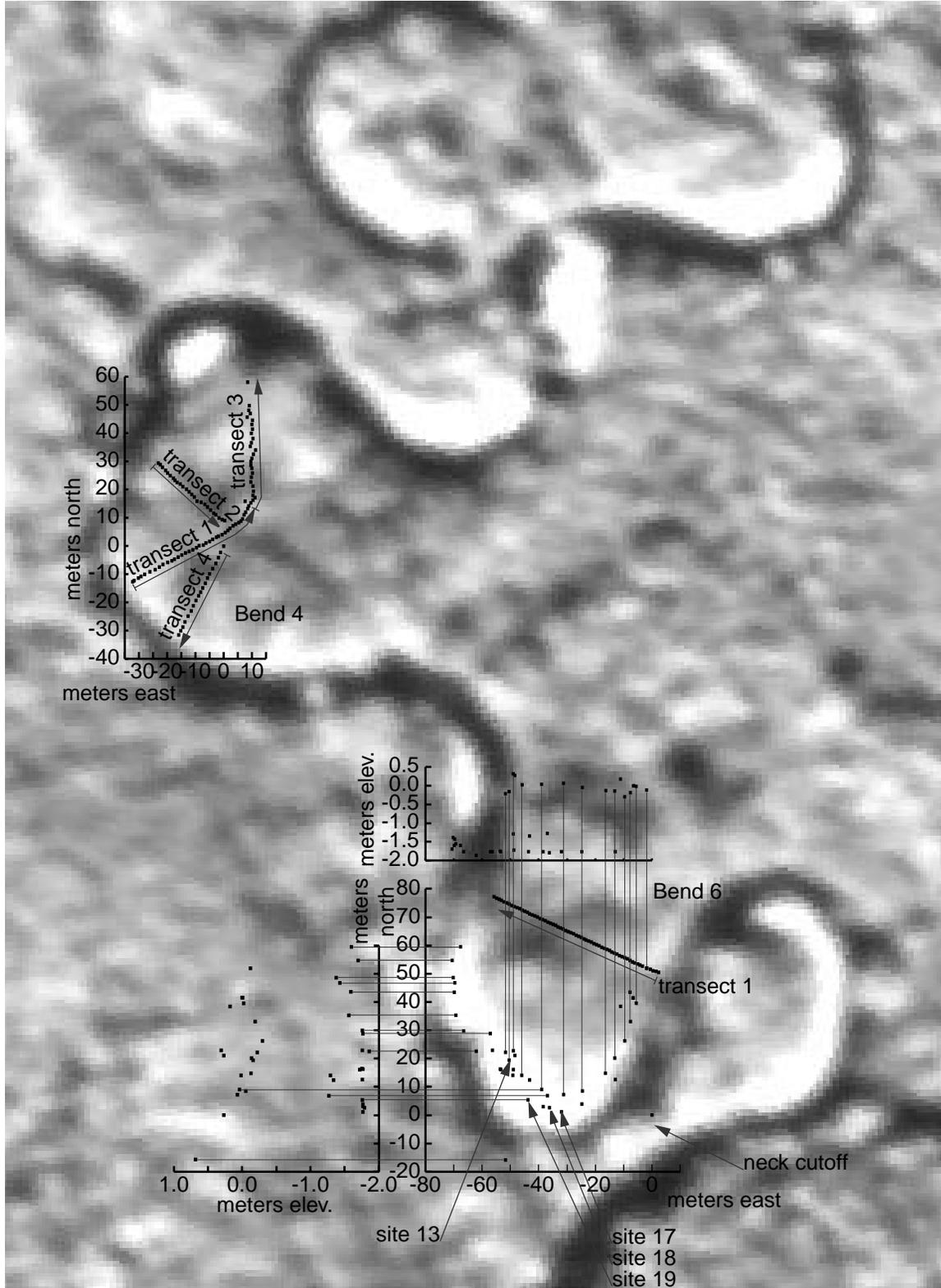
Figure 3.19: Ellis River survey sites super-imposed on 1992 aerial photograph. Non-transect sites on bend 6 are projected onto axes showing their relief, and some sites on the projections are connected by lines to their mapped locations.

78
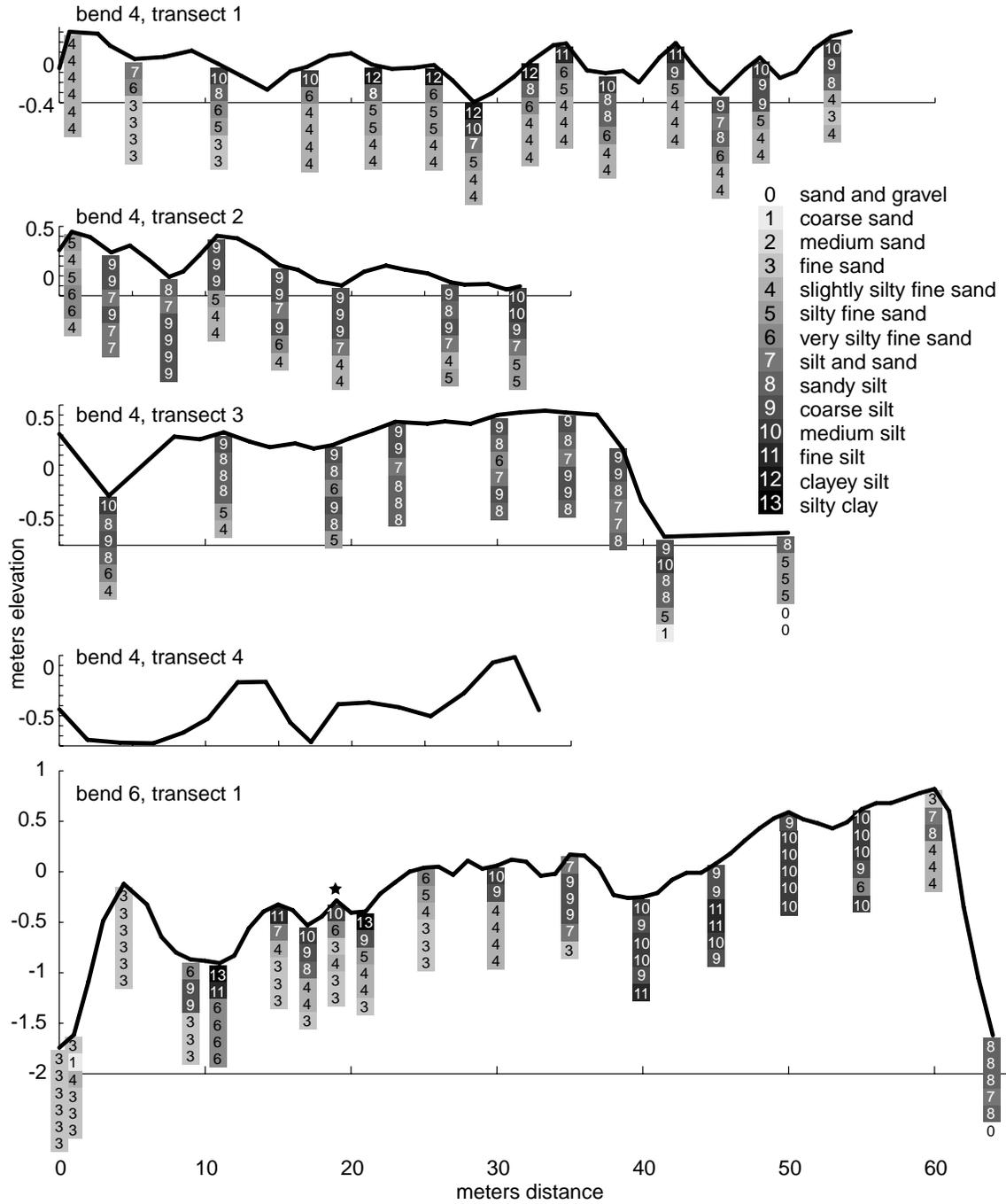
Figure 3.20: Ellis River transects and one-meter soil core samples shown to vertical scale at sampling locations. Vertical scale is exaggerated. Bends 4 and 6 were surveyed with different benchmarks.
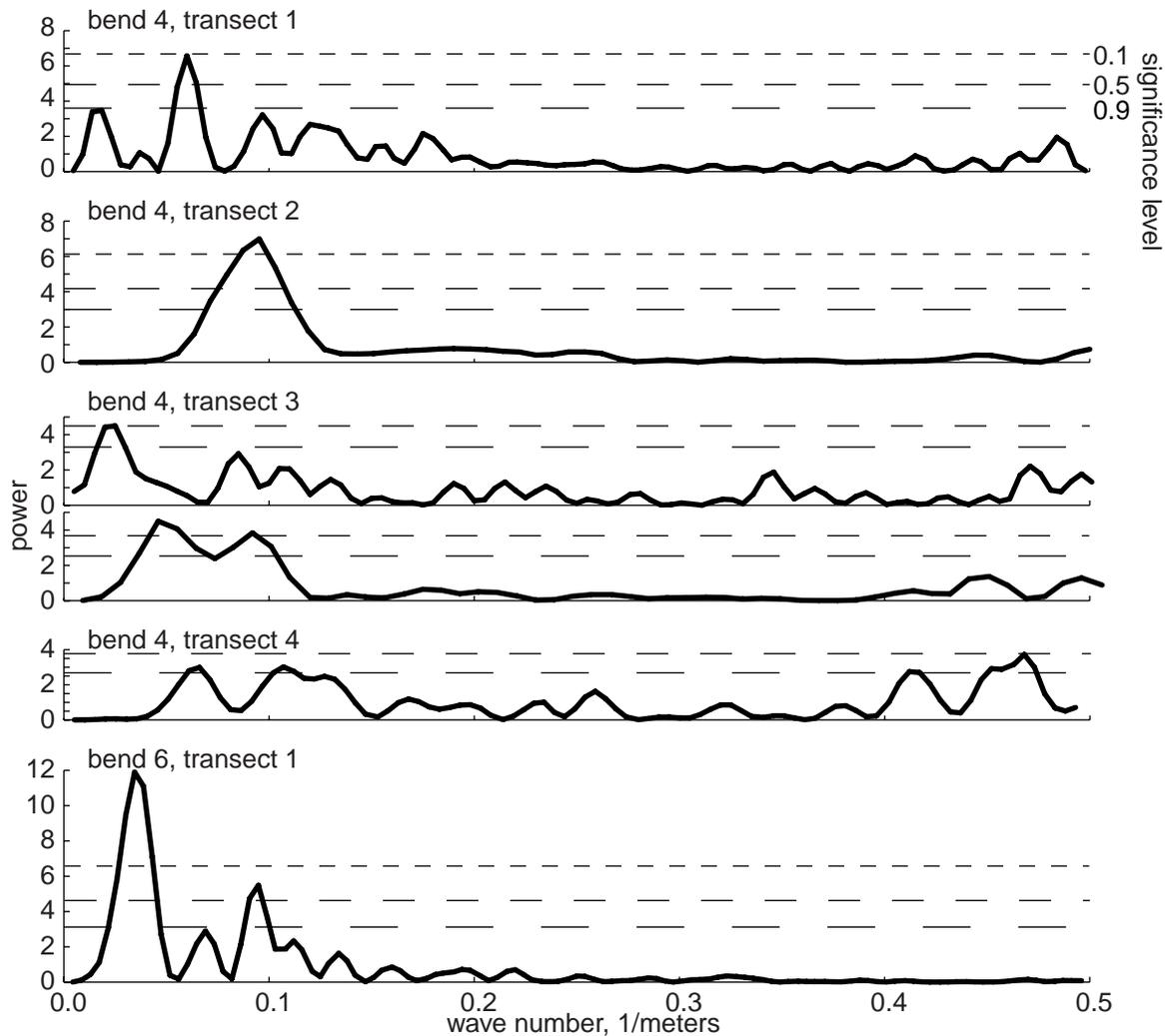
Figure 3.21: Power spectra of detrended Ellis River transects. Significance levels are shown with dashed lines. For bend 4, transect 3, a second spectrum is shown for the portion of the transect between 7 and 41 meters. For bend 6, transect 1, the spectrum is shown for the portion between 2 and 61 meters.

Spectral analysis of the Mississippi floodplain, even when applied to relatively short transects with only scroll bar topography, such as 2 and 7, does not show more than quasi-periodicity. Some transects have peaks that are significant to a small level, but the peaks among the transects do not line up with one another. Furthermore, even for transects 2 and 7, neither of the spectra contain a single, clearly dominant peak.

The survey sites on the Ellis River floodplain and their east-north axes are overlain on the 1992 aerial photograph in figure 3.19. The transects are shown with arrows indicating the (arbitrary) direction of increasing distance in the transect plots of figure 3.20. The soil core data are also shown in figure 3.20.

The transect spectra are shown in figure 3.21, and the wave numbers, wavelengths, and significance levels of spectral peaks are listed in table 3.5. Most of the spectra have peaks with significance levels less than 0.9 at 9-11 meter wavelengths. In general, the spectral peaks for these transects are not significant to as small a level as the Mississippi spectra (see figure 3.18) because the latter transects contained many more scroll bars than the Ellis River transects.

Table 3.5: Spectrum peak wave numbers, k (1/m), wavelengths, L (m), and significance levels, P, for Ellis River transects, total length given.

bend 4, transect 1, 54.2 m			bend 4, transect 2, 31.5 m			bend 4, transect 3, 49.9 m		
k	L	P	k	L	P	k	L	P
0.0599	16.7	0.13	0.0952	10.5	0.04	0.0251	39.9	0.48

I attempted a more general mapping of the point bar of bend 6 to resolve features such as the emergent bar forming a back bar chute shown in figure 3.22 (sites connected by lines to projection on north-elevation axes in figure 3.19) and the first point bar ridge adjacent to the channel (sites connected by lines to projection on east-elevation axes in figure 3.19). It is possible that the morphology shown in figure 3.22 is the pre-cursor to scroll bar topography. Back bar chutes are a common feature of meander bends. In this case, it appears that the colonization of the bar by stabilizing vegetation may allow this morphology to persist and, in time, add another ridge and swale to the point bar. However,

this bar traverses only a minor part of bend 6 at its upstream end, whereas the first point bar ridge borders the channel for most of the bend. Mid-channel bars and, more generally, topographic maxima bordering flat areas on point bars are commonly observed at the upstream ends of meander bends (see, e.g., *Dietrich and Smith*, 1984).

Table 3.5: (cont'd.) Spectrum peak wave numbers, k (1/m), wavelengths, L (m), and significance levels, P, for Ellis River transects, total length given.

bend 4, transect 3, 27.2 m			bend 4, transect 4, 32.8 m			bend 6, transect 1, 58.1 m		
k	L	P	k	L	P	k	L	P
0.0459	21.8	0.28	0.0662	15.1	0.81	0.0344	29.1	4e-4
0.0917	10.9	0.47	0.107	9.37	0.80	0.0952	10.5	0.23
			0.412	2.43	0.88			
			0.467	2.14	0.55			

Figure 3.22: View upstream from bend 6, survey site 13, of bar and back bar chute.

The grain size classes for each core section are shown by a number and a shade of gray according to the key shown in the upper right of figure 3.20. In figure 3.23, I show sections 2-6, still in the coring tool, of the core marked with a star in figure 3.20.
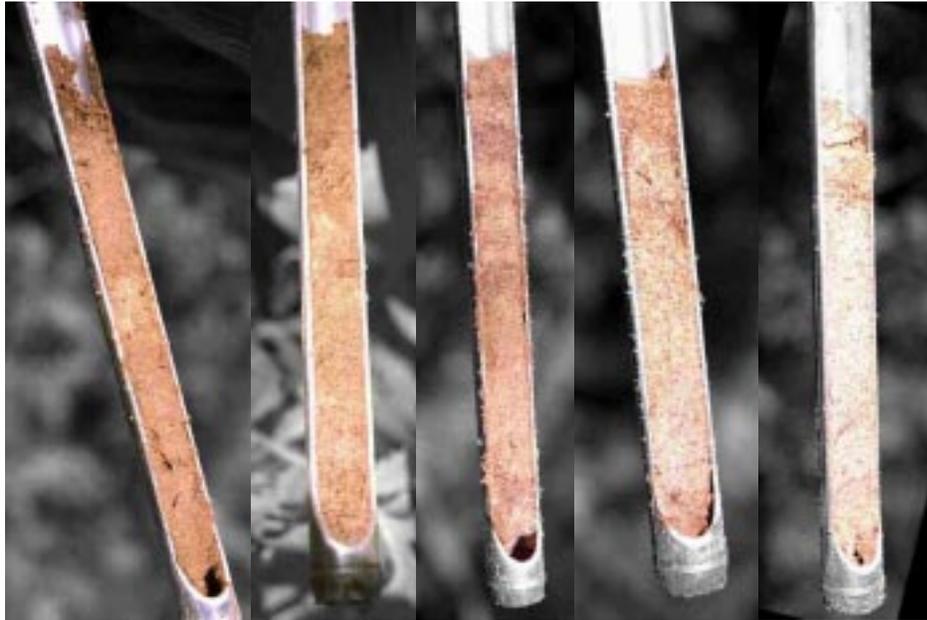
Figure 3.23: Sections 2-6 of core marked with star in figure 3.20.

With few exceptions, I did not find soil classes 0-6 at the surface very far from the present channel, usually not beyond the first point bar ridge. On the floodplain, I typically found classes 7-13 to varying depths above classes 0-6. For bend 4, transects 1 and 3, and bend 6, transect 1, the layer of classes 7-13 is thicker toward the upstream end of the flood-plain, and in parts of these transects, classes 7-13 extend to the full sampling depth of one meter. The layer of finer materials is thicker in the swales than on the ridges.

The coarser classes are more likely laterally accreted point bar deposits, and the finer classes are more likely vertically accreted overbank deposits. Therefore, the interface between the coarser and finer classes likely approximates the elevation of the top of the original point bar. The cores in figure 3.20 show that the elevation of the interface mimics

the topography in that highs and lows along the interface generally correspond to highs and lows on the surface and indicate that the vertical accretion of fines has lowered the relief of the original scroll bar topography. This result is consistent with those of *Leopold and Wolman* [1960].
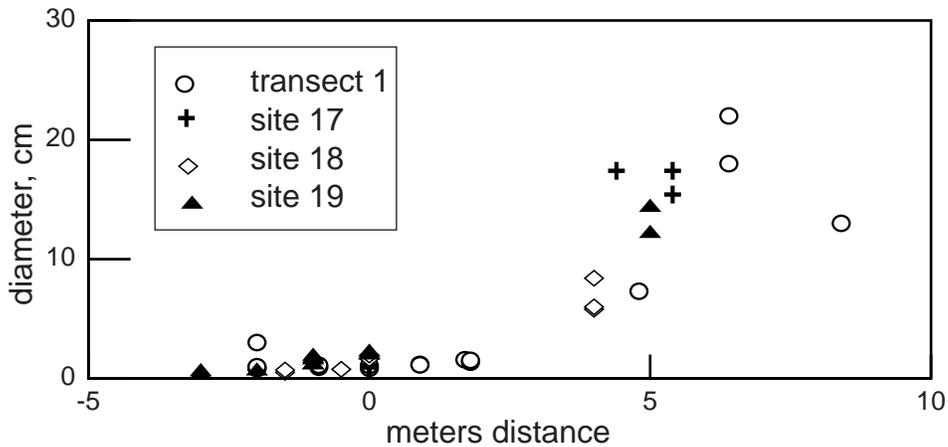
Figure 3.24: Vegetation stem/trunk diameter *vs.* distance from the top of the first point bar ridge, increasing away from the water's edge (site locations shown in figure 3.19).

The vegetation diameter data are shown in figure 3.24. Distance on the horizontal axis of the plot is relative to the location of the top of the first point bar ridge (see figure 3.19). The vegetation on this ridge is rough and relatively homogeneous in size and type (see figure 3.25), though several maple saplings were measured. This rough vegetation is prevalent on the inside banks of bends throughout this reach. The locations of the measurement sites are indicated in figure 3.19. The data are too few and the apparent migration rates too similar to differentiate among the measurement sites. In figure 3.12(a) it appears that the reach bordering these measurements migrated uniformly with respect to the downstream direction between 1965 and 1992. The vegetation diameter data corroborate this observation from the aerial photos.

Figure 3.25: Photo looking upstream from site 19 (bend 6) of flat point bar top and rough vegetation on first point bar ridge. Stadia rod in foreground is marked in tenths of a meter.

The data do indicate differences in migration rate along the distance axis of the plot in figure 3.24. This spatial variation corresponds to temporal variation in migration rate because the data were taken along transects perpendicular to the channel, i.e., parallel to the migration direction. If the data provide adequate resolution, then they indicate that the first point bar ridge accreted more quickly than the swale behind it (in figure 3.20, bend 6, transect 1, the first point bar ridge is at ~4 meters distance, and the swale is at ~10 meters). If these data are typical of scroll bar topography on the floodplain, they indicate that the lateral accretion rate of floodplain ridges is greater than for swales. This result is

contradictory to the hypothesis that scroll bar topography is due to a constant levee deposition rate and variable lateral migration rate. Rather, the data indicate that levee deposition is more rapid when migration rate is greater.

ridges/vegetation bands

Figure 3.26: Bands of willows at the Burnt Cabin site on Jack's Fork of the Current River, Missouri. Flow is from left to right and towards the observer. Vegetation bands are seen end-on.

Figure 3.27: Band of young willows on a gravel bar on the Current River, Missouri. Flow is from left to right and away from the observer.

Figure 3.28: Gravel bar at Shine-Eye site on the Buffalo River, Arkansas. Arrow points to person standing on gravel ridge. Flow is from right to left and toward the observer.

Figure 3.29: Buffalo River at Jamison Creek confluence. Flow is toward the observer.

My observations on the Buffalo and Current Rivers corroborate the conclusions of *McKenney, et al.* [1995]. They found that ridges on the point bar correspond to the locations of bands of same-age vegetation (see figure 3.26). Their conclusion was that the form of the vegetation was due to events of seed deposition along the water line followed by periods lacking flows great enough to remove the seeds or the young vegetation, e.g., the young band shown in figure 3.27. Once the bands of vegetation take hold, they lead to

zones of increased roughness and, therefore enhanced deposition of gravel along those bands. Conversely, flow concentrates in the areas between the bands and leads to enhanced scour there (see figure 3.26). At the Current River sites, these vegetation bands lead to scroll bars, or something very much like them.

The same phenomenon is active on the Buffalo, but, as found by *McKenney, et al.* [1995], the bands tend to be less coherent, bigger, and fewer in number, and the channel is more constrained from lateral migration. The ridge and swale topography shown in figure 3.26 has relief of less than a half-meter. Ridges on the Buffalo, however, can exceed two meters in height (see, e.g., figure 3.28), and multiple bands, such as those in figure 3.26, are rare. Even where the valley is relatively wide, as in figure 3.29, floodplain gravel bars on the Buffalo tend to develop a maze of anabranching channels where the main channel may switch from year to year. An example is shown in figure 3.29 where the main channel changes frequently. As recently as 1992, I observed that the main channel course was in the middle of the vegetated gravel bar in figure 3.29. Now, the main channel is on the right-hand side of the photo. The floodplain channels form the topographic lows, while the spaces between them are vegetated and, in general, form the topographic highs, though these areas are often filigreed with smaller floodplain channels and do not form distinct series of bands similar to those observed on the Current River.

3.3.3 Bank Failure and Roughness

My observations and measurements on the Ellis River indicate that bank failure occurs when the bank is undermined by scour rather than seepage erosion. The measurement data are shown in table 3.6.

I observed that, at an outer bank location without slump blocks (visible in the background of figure 3.22), the roots of the bank vegetation formed a thick (~1 meter, see table 3.6) mat, and these roots were stripped of soil material and scoured such that they were smooth to the touch. This mat was undercut by more than half a meter on average (see table 3.6). There were only small (diameter < 10 cm) trees near the bank at this location.

Table 3.6: Measurements taken on the outside bank of Ellis River bend 6

measurement	mean	standard deviation	number of measurements
embedded log diameter	26 cm	4 cm	3
slumped tree diameter	41 cm	9 cm	4
slump block length (s-dir)	2.8 m	0.4 m	2
slump block width (n-dir)	2.4 m	0.9 m	3
slump block area	5.8 m^2	2.8 m^2	2
scallop length (s-dir)	3.3 m	2.7 m	5
scallop width (n-dir)	1.2 m	1.3 m	5
scallop area	6.4 m	9.5 m	5
depth (n-dir) of undercut	56.7 cm	15.9 cm	7
vegetation mat thickness (z-dir)	90 cm	N/A	1
dune wavelength[a]	1.4 m	N/A	1
dune height	9 cm	N/A	1

a. Dunes not measured at bankfull stage.

In general, where there are large trees on the bank they greatly influence bank, bed and overall channel roughness. Where the root wads of larger trees have been undercut, the bank has slumped in blocks defined by these root wads. The slumps lead to a scalloped bank and, thus, a bank roughness defined by their size (see table 3.6). Often, the trees remain rooted on the slump blocks, even when they have slumped to a horizontal position, and, by remaining in the channel, contribute to bed and channel roughness. In one such

case, the trunk of the tree spanned the pool, and the top of the tree rested on the point bar where it formed a small woody debris jam. A drawing of this slumped tree and a bank scallop is shown in figure 3.30. Trees spanning the pool increase the hydraulic roughness of the channel there, and debris jams increase bed and channel roughness. Other examples of woody debris associated with slumped trees are visible along the outside bank of bend 6 in figure 3.31, "top".

On the channel bed, many dead logs lay partially buried or pinned by other logs, and at least some of them may remain on the bed indefinitely until covered by lateral floodplain accretion and later unearthed by bank erosion, as evidenced by three logs protruding from the bank in bend 6. One such log, visible on the un-slumped bank in the background of figure 3.22, was embedded in the root mat and protruded 1.9 m from the bank. In general, the embedded log diameters were smaller than those of the slumped trees, but, given the observed variability in both groups and the small number of samples, I cannot rule out the hypothesis that the embedded logs are from old slumped trees. Another possible explanation for the embedded logs is that they simply fell in the forest and have been buried by vertical floodplain accretion, but this explanation appears to be possible for only one of the three observed logs that was found at an elevation similar to the lower surveyed floodplain elevations. The other two embedded logs were at elevations lower than any of the surveyed elevations.
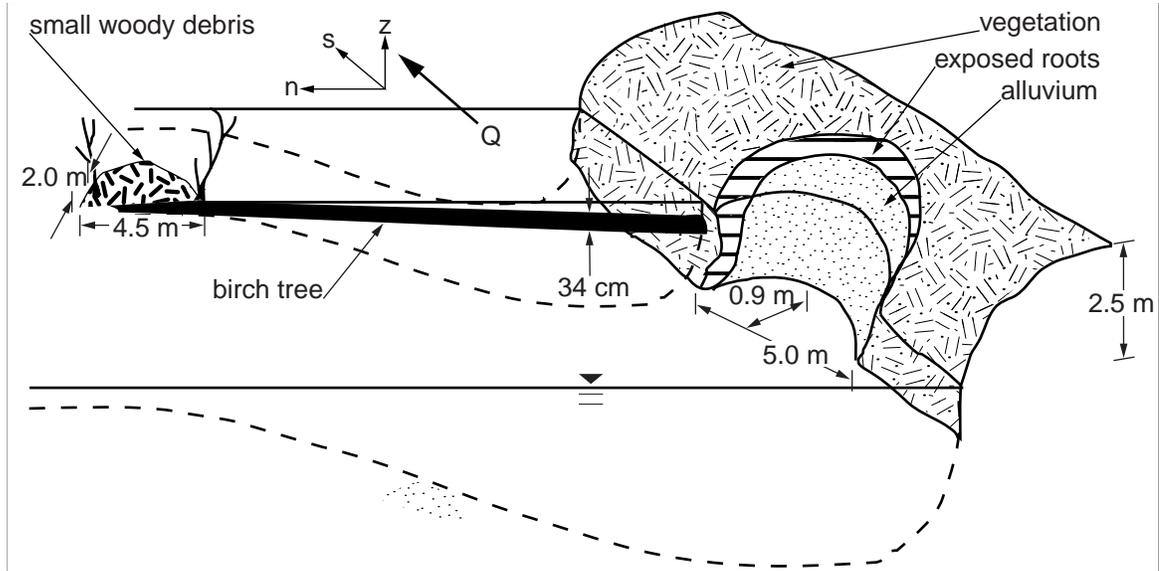
Figure 3.30: Drawing of slumped tree at Ellis River bend 6. At top, *s*-, *n*-, and *z*-directional axes are shown

When slump blocks are removed from the bank a scallop, or an inward undulation, is formed (e.g., see figure 3.30). The depth of the scallop depends on the size and orientation of the slump block prior to removal. If the tree has slumped to a nearly horizontal position, then the scallop depth will be approximately equal to the thickness of the root wad. On the other hand, if the tree is more nearly vertical, then the scallop depth will be approximately equal to the width of the tree's root wad. I observed some slump blocks which were covered only by herbaceous vegetation, and these blocks tend to be smaller than those associated with trees. The sizes of the slump blocks are less variable than the sizes of the scallops, some of which are as long (*s*-direction) as two average sized slump blocks. Some slumped sites had more than one block. Removal of adjacent blocks is likely responsible for the larger observed bank scallops.

Figure 3.31: Neck cutoff of Ellis River bend 7. Top: Flow toward observer on right and away on left. Bend 6 is visible on right. Bottom: Nearly bankfull stage, view from outside bank of downstream limb of bend 7. Flow through cutoff is toward observer. Flow from right to left in foreground. Bend 6 is visible in background.

From the data and observations at the Ellis River, it is apparent that: (a) riparian trees control the bank roughness scale; (b) slumped trees, by spanning the channel and forming small woody debris jams, strongly influence channel and bed roughness; (c) large woody debris tend to accumulate on the bed as more recently slumped trees hold previously deposited trees in place; (d) at least some of the accumulated large woody debris remains in place indefinitely even as the channel migrates; and (e) large woody debris bur-

ied by lateral floodplain accretion may later be unearthed by bank erosion and again contribute to bank and channel roughness.

The mechanism behind and characteristic sizes of bank scallops are closely related to the formation of neck cutoffs. An actively evolving cutoff is shown in figure 3.31. The neck is 7 meters wide at the cutoff. The channel through the cutoff itself is 5 meters wide, except where the slump block visible on the right of the top photo in figure 3.31 constricts the upstream opening to 1.3 meters. That slump block is 3.1 meters long in the *s*-direction by 2.5 meters wide in the *n*-direction, and the slumping tree is 38 cm in diameter. At the flow stage of the top photo, only a small amount of seepage under debris and slump blocks contributes to flow through the cutoff. The debris and slumped bank material fill the bottom of the cutoff such that it is less than 2 meters deep below the neck surface. In the bottom photo, at near bankfull stage, there is substantial flow through the cutoff channel. Between July, 1996, and October, 1997, the times of my first and latest visits to the site, respectively, the cutoff has not changed visibly. This lack of change is likely due to the fact that there is substantial flow through the cutoff only at relatively high and, therefore, infrequent stages.

I observed the clear effects of scouring flood flow on the top of the neck (behind the observer in the top photo of figure 3.31). This scour produced small channels several centimeters wide and deep, and intact tree roots spanned these small channels. The scour channels did not span the entire width of the neck. This neck is the only place I observed incontrovertible evidence of floodplain scour.

The cutoff channel dimensions are consistent with the hypothesis that (a) the cutoff was formed by adjacent slumping events, one on each side of the neck, and (b) the size of slump blocks places a lower limit on the width of necks before they cut off. Furthermore, the data are consistent with the hypothesis that floodplain scour does not form chutes of appreciable size even at the lower limit on neck width imposed by the slumping mechanism: (a) the scoured channels visible on the floodplain surface are too small to undermine trees; (b) the lack of large trees slumped to fall across the cutoff channel indicates that a scoured channel did not lead to slumping of trees of size sufficient to create the cutoff channel opening; and (c) the orientation toward the main channel of an actively slumping large tree with a root wad of size comparable to the cutoff channel dimensions indicates that bank erosion on the main channel by channel flow undermined the trees which slumped to form the cutoff. Subsequent to the cutoff formation, the banks of the cutoff channel have been undermined such that several small trees have slumped toward the center of the cutoff channel (see figure 3.31).

3.3.4 Meandering and the Landscape

The Schoharie Creek valley (see figure 3.1) shows signs that lateral channel migration is or has been active. The valley floor is relatively wide and flat and has visible terraces. These features should have a measurable effect on a plot of slope vs. contributing area.

The slope-area plot for the Schoharie Creek valley is shown in figure 3.32. The average slopes increase with area at low values of the latter, a pattern which is consistent with hillslope diffusional processes. At larger areas, the average slope generally decreases with increasing area, indicative of fluvial processes, but the average slope is level near the

middle range of contributing area. There is a large amount of scatter in the slopes across

the whole range of contributing area, nearly two orders of magnitude at low areas. The

vertical resolution of the DEM is 1 meter such that the smallest non-zero slope possible is

one meter drop per diagonal distance across a pixel, or 0.71 m/30 m. Zero slopes cannot be

plotted on the log-log plot but do contribute to the plotted average. Note the visible dis-

cretization of contributing area at the lower end of the horizontal scale.
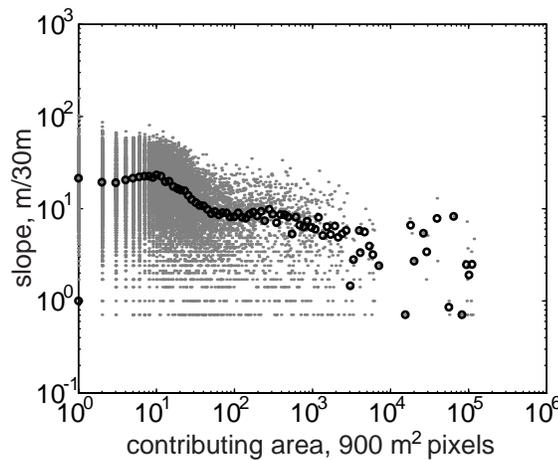
Figure 3.32: Slope vs. contributing area for the part of the Schoharie Creek basin shown in figure 3.1. The data for each pixel are shown with the gray dots. Average slope vs. average contributing area is shown with the dark circles.

The trend of the average slope at areas between 10 and 50 pixels is steeper than at

areas larger than 200 pixels. This steepness indicates that the profiles of these smaller

streams have greater concavity than the larger streams. Such concavity could be the result

of the flattening of the valley floor by meandering. The slopes of streams entering the val-

ley may be affected by that flattening. Such flattening would influence the slopes of

streams over a range of contributing areas such that their slopes would be essentially inde-

pendent of contributing area and could therefore be responsible for the nearly constant

average slope at areas between 50 and 200 pixels. The findings of *Ijjasz-Vasquez and Bras*

[1995] are consistent with the hypothesis that meandering leads to the features I have

noted in the slope-area relationship. *Ijjasz-Vasquez and Bras* [1995] observed this effect in the slope-area plots of many, but not all, river basins, and meandering is a common feature of many, but not all, rivers. I would expect the prominence of the kink in the slope-area relationship to vary with the relative importance of meandering in river basins. These results do not, however, indicate why some rivers meander more, or why some valleys are wider, than others. The modeling study of *Tucker and Bras* [1998] indicates that shallow landsliding may be responsible for the slope-area features described above, but my observations in the field of the Schoharie Creek basin suggest that shallow landsliding is not the dominant hillslope process.

Table 3.7: Measured channel slopes of Buffalo River and corresponding strata[a]

slope	between elevations (feet)	valley	stratum
0.00087	740-720	narrow	Ordovician
0.00082	720-680	narrow	Ordovician
0.0011	680-640	wide	Ordovician, some Boone
0.00093	640-600	wide	Boone
0.00085	600-560	wide	Boone
0.00062	560-540	narrow	Ordovician
0.00061	540-520	narrow	Ordovician
0.00053	520-500	narrow	Ordovician

a. First measurement is just downstream of the confluence with the Little Buffalo River; last two are downstream of the confluence with Bear Creek.

In order to test hypotheses concerning the mechanism of valley widening, I measured Buffalo River channel slopes from topographic maps in the wide valley shown in figure 3.29 and the narrower valleys up- and downstream, e.g., similar to figure 3.2. The results are shown in table 3.7 and show that the channel slope in the wider valley is com-

parable to or greater than slopes through the narrower valleys. If my assumptions of the previous section are valid, then this result contradicts the hypothesis that the valley is wider because the rock is weaker.

3.4 Discussion
3.4.1 Channel Planform Characteristics and Evolution

I examined two cases of compound bend formation on the Ellis River, and both arise from the same mechanism. This mechanism is related to characteristics of bend shape, and the phenomenon is reflected in measurements of channel planform. Plots of bend curvature show that bends often have curvature magnitude maxima at the beginning and end of bends and a curvature magnitude minimum in the middle. The minimum not only approaches zero but also crosses zero, i.e., changes sign, in compound bends. I have shown with the Ellis River study that low-curvature reaches reverse curvature sign when migration rate at the beginning of the bend increases due to the propagation of rapid migration from upstream bends.

I was motivated to find and/or derive measures of channel planform because so few objective measures exist in the literature. Probably the most often quoted measures of meandering channel planforms are sinuosity and meander wavelength [*Leopold and Wolman*, 1960; *Schumm*, 1967]. However, these measures are problematic because they are generally non-reproducible. Both numbers vary according to location, reach length, and method of measurement. For example, *Brice* [1974] showed two sets of measurements of meander wavelength for three reaches of the White River, Indiana, one calculated in his study and the other set from a previous study, and the numbers differed by as much as a

factor of two. *Brice* [1974] also attempted to quantify the meanders of the White River, IN, in terms of bend size and orientation.

Howard and Hemberger [1991] performed a multivariate statistical analysis discriminating among static stream planform data and two models, the disturbed periodic model (DPM) [*Ferguson,* 1976] and the model of *Howard and Knutson* [1984] (HKM). The *Howard and Hemberger* [1991] analysis is objective and quantitative, but this type of analysis is designed to discriminate among given groups of a given data set, i.e., the exact form of the discriminant functions is determined by the data. Interpretation of the resulting functions is not entirely straightforward because so many statistics are combined to produce them. *Howard and Hemberger* [1991] did conclude that (1) the HKM streams were more sinuous than the real ones; (2) the HKM bends were more asymmetric, with the point of maximum curvature near the bend entrance; and (3) "natural streams have higher irregularity of planform at large scales and numerous, low-sinuosity short half-meanders, as well as a wider range of half-meander sizes." Their analysis did not address the issue of compound bend formation and its effect on the channel planform, but compound bend formation could lead to the many short half-meanders observed by *Howard and Hemberger* [1991].

The new measures presented here and *Andrle*'s [1996] show the effect of compound bend formation on the reach scale. A stream with a fully developed but simple meander pattern, i.e., one with no compound bends and a meander axis closely following the down-valley direction, will have a steeply increasing $\mu_S(s')$ for s' smaller than the meander wavelength and a flat $\mu_S(s')$ for s' larger than the meander wavelength.

Compound bend formation leads to the secondary channel planform scale indicators detected in the planform measurements. Repeated compound bend formation forms multi-bend loops observed in the digitized planforms and aerial photos and detected as secondary channel planform scale indicators, such as secondary increases in mean sinuosity, peaks in sinuosity variance, convexity of relative belt width, and secondary peaks in mean angle. Not all of the streams have these secondary features. Specifically, Dishna has one μ_S plateau, one σ_S^2 peak, concave decay of W, and only a low-magnitude second μ_θ peak at 100 *b. Andrle* [1996] found similar low-magnitude secondary peaks for rivers without multi-bend loops and concluded that they were simply an artifact. The lack of prominent secondary channel planform scale indicators indicates the lack of multi-bend loops. The Dishna has many compound bends, but, apparently, either compound bends do not initiate the formation of multi-bend loops or there were multi-bend loops that have cut off. If the former, then the reason some compound bend formation leads to multi-bend loop formation and other compound bend formation does not is a question I cannot answer at this stage. The Dishna is laterally unconstrained, as are all of the digitized channels. The answer must lie elsewhere, with a mechanism not apparent from the topographic maps. Another question I would like to answer is whether multi-bend loop formation is necessary for the channel planform scale indicators observed for the Alaska streams. I know compound bend formation is not sufficient and that multi-bend loop formation is, but I am not certain that a highly sinuous stream with no multi-bend loop formation could not produce secondary channel planform scale indicators. I address the issue of compound bend and multi-bend loop formation with the meandering model in Chapter 4.

The measures reveal other differences among the streams, but I do not know what mechanisms are responsible for the differences. All of the measures give similar values for normalized meander bend length, but the meanders of the different rivers have different characteristics. The measures tend to have distinctive features at similar scales, but they still measure different things. For example, Melozitna has one of the largest μ_θ peaks at a scale corresponding to large σ_S^2 and W but only moderate μ_S. Large W indicates lateral elongation; large σ_S^2 indicates great variation of sinuosity; and large μ_θ indicates large curvature of three points along the stream but not necessarily close proximity of the end-points of the angle-forming segments. Note that large sinuosity of a channel segment requires the endpoints to be close together. The measures all reflect the presence of secondary scales and reveal the various characteristics of the corresponding forms; e.g., N.F. Kusk. Mc. has large secondary μ_θ peaks which correspond to convexity in W, but the secondary rise in μ_S and peak in σ_S^2 are not relatively as great. Clearly, different meandering channels have some similar features which are not, however, universal.

3.4.2 Floodplain Topography

My discussion of floodplain topography addresses the various mechanisms which build the floodplain, including point bar accretion and overbank deposition, and the resulting forms, including scroll bar topography and the floodplain stratigraphy.

I have shown two cases of scroll bar topography, on the Mississippi and Ellis floodplains. Spectra of transects of the scroll bar topography show that there is only a small probability that the elevations are the result of a normally distributed random process. The probability is as small as 0.002 on the Mississippi and 0.04 on the Ellis for

100

wavelengths attributable to scroll bar topography. For the latter, observations on the ground indicate the scroll bar topography is not a product of floodplain scour. Levee formation is a possible mechanism.

Though the scroll bar topography spectra have significant peaks, these spectra often have several significant peaks, and their wavelengths and relative power are not the same among different transects. Some variation of peak wave number among transects is expected because: (a) the transects are drawn at varying angles, not all perpendicular to the scrolls; and (b) wavelength may be related to migration rate such that parts of the bend with different migration rates have scroll bar topography with different wavelengths. The spectra may lack a clearly dominant peak because: (a) some swales may be widened by floodplain scour; or (b) as meander bends themselves have a characteristic scale but vary in length from bend to bend, scroll bar topography also has a characteristic scale, but it is not precisely periodic.

A review of the data: The Mississippi channel is about 1000 m wide; the Ellis channel is about 26 m wide. The Mississippi bend length is approximately 19 b, or 19 times the channel width; the length of bend 4 on the Ellis is approximately 12 b. For the Mississippi, the smallest scroll bar topography wavelength corresponding to a spectral peak with significance level below 0.1 is 269 m (sig. level of 0.007), or 0.27 b and 0.014 of the bend length; for the Ellis, the smallest wavelength with significance level less than 0.1 is 10.5 m (sig. level of 0.04), or 0.40 b and 0.034 of the bend length. In summary, the Mississippi scroll bars tend to have shorter wavelengths as a proportion of both channel width

and bend length than the Ellis scroll bars. As I do not know what the scroll bar topography mechanism is, it is even more difficult to explain this difference in scroll bar size.

From the soil core observations it is apparent that, past the first point bar ridge, the major component of floodplain deposition is from fine particles falling out of suspension as the flood flow crosses the floodplain. Given the decreasing thickness of this fine material with distance from the upstream end of the point bar, the fines probably fall out of suspension at a high rate at the upstream end where the shear stress gradient is negative and large, and that rate decreases downstream as the flow is depleted of fines and the shear stress gradient is smaller. Given the greater thickness of fines in the swales, the fines probably fall out of suspension more quickly there because the increasing depth of flood flow leads to a flow deceleration and, thus, decreasing bottom shear stress from the ridge to the swale.

Because the sandy materials are usually found at the surface only near the channel, it is likely that they are carried primarily by the channel flow. The new accretions to the point bar are colonized by densely stemmed and, therefore, hydraulically rough vegetation [*McKenney, et al.*, 1995]. This vegetation produces a large increase in hydraulic roughness and, therefore, a large negative gradient of shear stress from the main channel flow to the near-bank area such that fine sand is deposited in the area colonized by the vegetation. This deposition may form the observed ridges.

The above reasoning does not adequately explain all of the soil core observations. Sandy material is found below fines in the swales on the floodplain as well as on the

ridges. In all of the transects, the top of the first point bar ridge is the highest level at which sandy material of that coarseness is found on the transect.

The measurements of stem and trunk diameters on the point bar do not yield an absolute lateral accretion rate, but, if the rate of diameter increase is constant in time, then these results do indicate variation of lateral accretion rate over space. Curiously, the trend of the diameters is flat over the point bar ridge and steep in the swale. If the hypothesis is that slow migration equals more deposition per distance and, therefore, leads to a ridge; and fast migration equals less deposition per distance and, therefore, leads to a swale; then the vegetation diameter data contradict the hypothesis because they indicate that the opposite pattern of migration rate applies—fast where high, slow where low. It is possible that the fast migration created a disturbed area ideal for the vegetation colonizing the ridge, and the high roughness of that vegetation led to a high rate of sand deposition. It is also possible that the mechanism behind the accelerated migration is also associated with greater sediment flux. Clearly, bank erosion does input sediment to the channel, but I do not know if sediment from the bank ever enters the system rapidly enough to lead to the observed patterns of deposition.

The formation of the first point bar ridge may be associated with the compound bend formation on bend 4. Aerial photographs indicate that bend 4 became compound between 1981 and 1986 but changed very little between 1986 and 1992 (see figure 3.12(a)). The rapid migration leading to compound bend formation on bend 4 and the corresponding point bar accretion may have created the disturbed point bar surface now colonized by rough, sediment trapping vegetation, and the corresponding rapid bank

erosion may have caused pulses of sediment to move downstream and deposit on that newly accreted point bar to form a ridge.

3.4.3 Bank Failure and Roughness

Measurements of bank roughness elements indicate that the sizes of bank scallops, or inward undulations, covered a wider range than the sizes of slump blocks. Also, the sizes of bank roughness elements are greater than the dune forms on the bed. Note that the size of dunes is stage dependent while the size of bank roughness elements is not. The bank roughness element size is determined by the sizes of trees on the bank and how far they can be undercut before their weight leads to bank failure. The bank has a typical roughness scale whose wavelength and amplitude are controlled by the length and width, respectively, of the slump blocks formed by the trees' root wads (see table 3.6). So, bank roughness elements have a characteristic scale which is largely independent of the bed roughness, though the collapsed trees also contribute to bed and general hydraulic roughness. The trees lead to bed roughness over the point bar and general hydraulic roughness where they span the pool (see figure 3.30).

The slumping mechanism may also control the minimum thickness of meander necks and, to some degree, where they cut off. The neck shown in figure 3.31 is as wide as two slightly larger than average slump block widths, and the channel through the cutoff is as wide as one slightly larger than average slump length. It is apparent, then, that the size of slump blocks controls how thin a neck can get before it is cut off, and the exact location of the cutoff is dependent on the locations of slumps on either side of the neck.

The bank scallops on bend 6 lack vegetation and, therefore, appear to be relatively new. That observation and the fact that many of the slumped trees are still alive may indicate that these slumps and the new cutoff resulted from the same rapid erosion that led to compound bend formation on bend 4 and the high first point bar ridges observed on many point bars, including those of bends 4 and 6.

3.4.4 Landscape-Meandering Interactions

I hypothesize that scatter and deviations from scaling in the slope-area plot for Schoharie Creek may be due to meandering rather than some stochastic process. The DEM clearly shows bend-shaped scarps adjacent to a flat valley bottom. Such forms would surely lead to both steepening and shallowing of slopes relative to the mean behavior. These forms could also be responsible for the observed deviations from mean slope-area scaling. The flattening at moderate slopes apparent in figure 3.32 is often observed (e.g., *Ijjasz-Vasquez and Bras*, 1995; *Tucker and Bras*, 1998), and *Tucker and Bras* [1998] found that using pore-pressure-induced shallow landsliding (e.g., *Montgomery and Dietrich*, 1989, 1994) in a landscape evolution model produced a similar flattening in the slope-area relationship. Given the ubiquity of this flattening, however, it may be polygenetic, and G.E. Tucker does not believe that shallow landsliding is not the cause (personal communication, 1998). It may be that valleys with wider bottoms exhibit this slope-area effect more prominently.

The pertinence to valley width of my measurements of Buffalo River channel slopes is contingent on several assumptions listed in the Methods section. The controls on the Buffalo River's incision, whether detachment- or transport capacity-limited, are not well established. If the assumption of detachment-limited incision does not hold, i.e., if

incision is transport capacity-limited or controls on incision change downstream, then channel slope and rock strength might not be simply related. If the channel is uniformly transport capacity-limited and lithologies with greater transport capacity are also more erodible, then my reasoning still holds. However, if more erodible lithologies are less transportable, or the greater lateral erosion that comes with greater erodibility produces a greater quantity of sediment for the channel to carry, then my reasoning does not hold.

In any case, the mechanism for valley widening is most likely related to what happens to the rock from the valley walls once it is detached. In general, if it breaks up into small-gravel bedload and, therefore, increases the topographic steering effect, the presence of the gravel may tend to make the valley wider by increasing lateral migration. On the other hand, there are at least two other reasons why the slope of the Buffalo, in particular, might become steeper through weaker rock. First, the bedload component of the total sediment load may be relatively larger because of the chert gravel such that the reach is transport-limited rather than detachment-limited. The river's slope may have adjusted to carry the large quantities of gravel bedload, but the valley side walls are not shielded by such bedload and are, therefore, vulnerable to erosion. Second, the river may lose a significant amount of flow to Karst conduits through the limestone, and the slope may have adjusted to compensate for this lost erosive flow.

3.5 Conclusions

Most of my conclusions at this point are really questions. Can I explain compound bend formation and scroll bar topography? Can a new model of river meandering reproduce or explain these phenomena? How may I represent bank roughness in a new model? Can a new model shed light on the interactions between meandering and the landscape? Why

does compound bend formation lead to multi-bend loops in some cases and not in others? What mechanisms are responsible for the differences in the channel planform scale indicators of the Alaskan streams?

I have found that compound bend formation is fundamental to meandering. It is responsible for typical bend shapes and the multi-bend loops observed in the data. Compound bend formation is more active in some streams than others, though the mechanism for this variation is beyond the scope of this chapter.

My studies have raised some interesting questions regarding scroll bar topography. Scroll bar topography on gravel bed streams in the Ozarks is thoroughly explained by *McKenney, et al.* [1995], who determined that vegetation plays the key role. My observations and measurements on the Ellis River are less conclusive. They point to a possible role of vegetation, but an unexplained variation of migration rate may be the missing piece of the puzzle. The data indicate that the newest ridges on the point bar laterally accreted rapidly relative to the lower areas behind these ridges. Therefore, it is unlikely that this topography may be explained by a combination of variable migration and steady deposition rates. Limited possibilities remain:

1. Migration rates are quasi-periodic in space possibly due to episodic rapid migration following upstream cutoffs such as the rapid migration following the cutoff of bend 2. Where the point bar rapidly accretes laterally, rough vegetation colonizes the disturbed area. That roughness leads to a high vertical accretion rate on the newly accreted portion of the point bar such that rapid vertical and lateral accretion coincide. Also, the rapid bank erosion may supply additional sediment to the stream such that the deposition rate on the point bar increases.

2. The height of laterally accreting point bars is quasi-periodic in space due to systematically changing secondary flow hydraulics in migrating channel bends. Vegetation may also play a role by favorably colonizing the higher and, therefore, drier parts of the point bar.

These proposed mechanisms do not explain why the most recent ridge on the Ellis floodplain is the highest and made entirely of sand or why the Mississippi bend has more scrolls on its floodplain than the Ellis, i.e., the wavelengths of the scroll bar topography on the Mississippi are smaller relative to both the channel width and the meander wavelength than the scroll bar topography on the Ellis. The Mississippi is also not as wide relative to the bend length. Are these observations generally the case? What characteristic of the meandering stream determines the scroll bar topography wavelength? The new model developed in the next chapter can simulate floodplain topography only by variations in point bar height. The present study of scroll bar topography indicates that modeling its formation may require a detailed treatment of processes beyond the scope of the modeling in the present work.

I found that the scale of the bank roughness element is independent of the scale of bed forms, though the elements contributing to bank roughness, namely the trees, also contribute to bed and overall hydraulic roughness. It is possible that this vegetative roughness is related to the scroll bar topography wavelength. I have found a likely role of rough, young vegetation in the formation of scroll bar topography, and the scale of this vegetation may also be related to scroll bar topography wavelength. A model of river meandering will likely need to model or parameterize bank and bed roughness independently in order to predict correctly both flow hydraulics and the scale of dissipation of turbulent energy at the bank.

I have not shown conclusively that meandering affects the slope-area relationship. The two things, that the slope-area relationship is stepped and meandering has flattened

the valley bottom and steepened some parts of the valley walls, may be unrelated. However, I believe that they are related, that the flat valley bottom is responsible for the numerous low-slope points at low areas, that the steepened valley wall points are responsible for some of the large slopes at slightly larger areas, and that the flattening of the valley floor is responsible for the mean slopes' lack of area-dependence at even larger areas.

I have drawn into question the hypothesis that wider valleys are due to more erodible valley walls, but, again, the evidence is not conclusive. The limestone walls of the wide valleys of the Buffalo probably are weaker than the sandstone forming the narrow valley walls. The surrounding area may be eroding more quickly and delivering a greater load such that the river has steepened to carry the extra load. But the smaller bedload grain size and larger bedload supply probably do increase the lateral migration rate more than can be explained by the greater erodibility.

The models presented in the following chapters will address some of the issues of compound bend formation, scroll bar topography, bank roughness and failure, and meandering-landscape interaction presented in this chapter. The present chapter addresses some of the morphologic features of meandering streams and their surrounding landscapes. The model development in the next chapter focuses on the physical mechanisms necessary for meandering in general and whether they are sufficient to explain some of the above specific features.

Chapter 4

The Topographic Steering River Meandering Model

In this chapter, I present a simple nonlinear model of river meandering. This new model is based on the phenomenon known as topographic steering introduced in Chapter 2. For comparison with the natural channels of Chapter 3, I use the planform measurements developed there on the results of the new model and compare those results to the natural examples of compound bend formation. I also compare my new model to a meandering model from the literature. The new model simulates meandering with compound bend formation and predicts that the frequency of compound bend formation is sensitive to model parameters. For example, decreasing the mean bedload particle size increases compound bend and multi-bend loop formation frequency.

4.1 Introduction

The review of Chapter 2 suggests that topographic steering plays a key role in bank erosion and meandering. Based on the these results, I reason that a positive feedback, similar to one described by *Dietrich and Smith* [1983], exists between point bar formation and bank erosion: a small point bar develops in a small bend; the small point bar steers the flow such that the outside bank is eroded; this bank migration makes the channel more curved; the point bar grows; and so on. The hypothesis is that this topographically induced lateral transfer of flow momentum provides the major part of the flow momentum lost to bank shear stress. By modeling topographic steering, I can model meandering.

I develop a simple, nonlinear river meandering model to test the topographic steering hypothesis [*Dietrich and Smith*, 1983; *Dietrich and Whiting*, 1989]. The model is not based on a perturbation solution, linear or nonlinear, of the flow equations. Rather, in the topographic steering river meandering (TSRM) model I have sought to simplify the physics of the problem such that it yields a solution which is both nonlinear and computationally efficient. Efficiency is of interest because of the ultimate goal of integrating the meandering model with the landscape evolution model presented in Chapter 5.

4.2 Model

I assume, as a first approximation, that the downstream flow velocity field is constant over a given channel cross-section and given by the Manning equation:

$$U = \frac{R^{2/3}\sqrt{S_f}}{n_m} \tag{4.1}$$

where U is the downstream flow velocity; R is the hydraulic radius; S_f is the downstream friction slope measured over a long distance relative to the channel width; and n_m is the Manning roughness coefficient. I assume that equation (4.1) adequately describes the effects of the total channel roughness and water surface slope on the average flow velocity over a length of several bends. Given U, I consider secondary flows: curvature-induced helical flow; and topographically induced lateral and vertical flows; and derive bed topography and bank shear stress resulting from these secondary flows, respectively. I assume that lateral migration rate is proportional to the bank shear stress.

4.2.1 Transverse Channel Bed Slope

Several authors [*Odgaard*, 1986; *Ikeda*, 1989] have found the transverse bed slope necessary to maintain equilibrium between the opposing forces due to gravity and curva-

ture-induced helical flow. These equilibrium models provide a good approximation of the bed topography, though others (e.g., *Johannesson and Parker*, 1989a; *Nelson and Smith*, 1989a, b; *Blondeaux and Seminara*, 1985; *Seminara and Tubino*, 1989, 1992) provide a more detailed description by coupling the equations of flow and sediment transport to reveal the feedbacks between flow and bed topography.
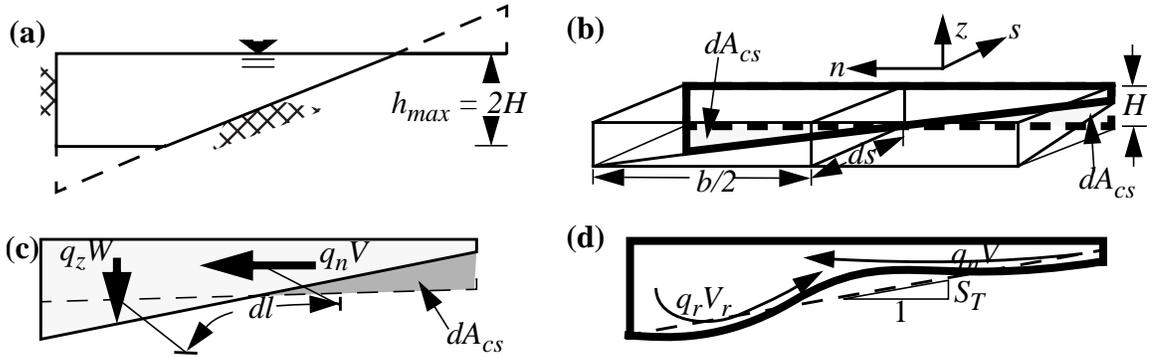
Figure 4.1: (a) Maximum pool depth is *2H*, and the point bar may not break the water surface. (b) Successive channel cross-sections defining directional axes, *s, n,* and *z;* channel width, *b*; average flow depth, *H*; and change in half-section area, dA_{cs}, per change in distance downstream, *ds*. (c) Flow momentum differential over a distance, *dl*, for lateral and vertical flow velocities, *V* and *W*, respectively, and unit discharges q_n and q_z, respectively, due to the change in half-section area, dA_{cs}. (d) Rotational flow momentum, q_rV_r, pushes bed sediment inward while lateral flow momentum, q_nV, pushes sediment outward; the resulting flat-topped point bar is represented by a single transverse bed slope.

The expression presented here is based on *Ikeda*'s [1989] description of bed topography as a function of local curvature and depth of flow. I modify his expression to account for bed form drag from dunes (see Appendix A) and solve for the transverse slope, S_T, at the channel centerline, where I assume that the depth is equal to the average depth, *H*:

$$S_T = KHC \tag{4.2}$$

where *C* is channel centerline curvature; and *K* is described by

$$K = \frac{\Psi'}{\Psi}\sqrt{\frac{\Psi'}{\Psi_{cr}}}\left[0.570\ln\left(\frac{11.0\Psi'H}{\Psi d_{50}}\right) - 0.361\right] \tag{4.3}$$

where Ψ' is dimensionless (Shields) skin friction; Ψ is total Shields stress; Ψ_{cr} is critical Shields stress; and d_{50} is median bed sediment grain size (see Appendix A for derivation).

Limits on the bed topography are necessary such that the pool does not become arbitrarily deep or the point bar arbitrarily high when S_T is large. The maximum possible elevation of the point bar is the water surface elevation (zero depth at the inside bank) and the maximum pool depth is twice the average depth (depth equals *2H* at the outside bank) (see figure 4.1(a)).

Table 4.1: Parameter values used in model simulations

Discharge, width, roughness, grain size, valley slope, and dissipation scale are held constant during the simulation; depth, channel slope, and radius of curvature are given only for reference.

Site:	Muddy Cr., WY
discharge, m³/s	1.6
width, m	5.5
average depth, m	0.5
Manning roughness	0.036
median grain size, mm	0.7
channel slope	0.0014
valley slope	0.0021
radius of curvature, m	8.0
dissipation scale, m	15.

To test the bed topography model, I compare the results of equation (4.2) for the average curvature of a Muddy Creek bend (see table 4.1) to digitized channel sections [*Dietrich and Smith*, 1983; *Dietrich and Whiting*, 1989] (see figure 4.2). The prediction is good, and equation (4.3) is an improvement on *Ikeda*'s [1989], which predicts slopes about twice as large.
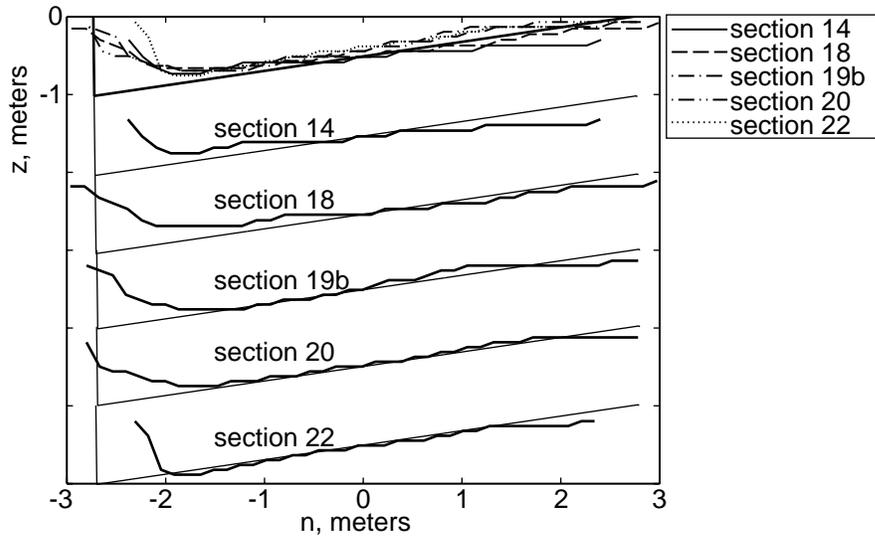
Figure 4.2: Comparison of actual and predicted bed topographies for Muddy Creek. At top the predicted channel section is compared to several actual sections such that the centerlines and water surfaces of the predicted and measured sections coincide. In subsequent views, the actual and predicted sections are adjusted such that the bed topographies overlap at the channel centerline. All of the predicted sections shown are identical.

There is an apparent "phase lag" [*Zhou, et al.*, 1993] between curvature and bed slope in Muddy Creek; the maximum curvature in the bend is at section 14, while the maximum transverse slope is at section 22. *Johannesson and Parker* [1989a, 1989c] used an effective curvature with upstream weighting in their LFE model; however, A.D. Howard (personal communication, 1996) reports that the correction does not have a significant effect on the model results.

4.2.2 Lateral Flow Acceleration

Convective accelerations due to the presence of the point bar cause a lateral displacement of flow and a resulting transfer of momentum from the high velocity core to the outer bank, as described in Chapter 2 and the Introduction. The present approach to estimating the magnitude and spatial pattern of that transfer is based on continuity of mass.

Smith and McLean [1984] solved the continuity equation,

$$\frac{1}{1-nC}\frac{\partial}{\partial s}Uh + \frac{\partial}{\partial n}Vh - \frac{VhC}{1-nC} = 0 \qquad (4.4)$$

where U is the depth-averaged downstream velocity; V is the depth-averaged cross-stream velocity; h is the depth of flow; and s and n are the downstream and lateral coordinates, respectively (see figure 4.1(b)); for the lateral unit discharge,

$$q_n = Vh. \qquad (4.5)$$

Their expression is

$$q_n = -\frac{1}{1-nC}\int_{-\frac{b}{2}}^{n}\left(\frac{\partial}{\partial s}Uh\right)dn. \qquad (4.6)$$

I divide the channel cross-section into two half-sections and assume that the downstream flow velocity is uniform with respect to s and n, to solve equation (4.6) for the lateral flow at the channel centerline, $n = 0$:

$$q_n = -U\frac{\partial A_{cs}}{\partial s} \qquad (4.7)$$

where A_{cs} is the cross-sectional area of the inside half channel, between the bank at $n=-b/2$ and the centerline at $n=0$. I calculate A_{cs} from the bed geometry derived in the previous section; except for very large curvatures (see figure 4.1(a)), $\partial A_{cs}/\partial s$ is proportional to $\partial S_T/\partial s$ and, therefore, $\partial C/\partial s$. For the planar bed described by equation (4.2), the vertical unit discharge averaged over the outside half-channel, between $n=0$ and $n=b/2$, is approximately equal in magnitude to the lateral unit discharge at $n=0$, or

$$q_z = W\frac{b}{2} = -q_n \qquad (4.8)$$

where q_z is the vertical unit discharge averaged over half the channel width; and W is the vertical flow velocity, also averaged over half the channel width. Using equations (4.5), (4.7) and (4.8), I solve for the lateral and vertical flow velocities at the channel centerline, $n=0$, and in the outside half-channel, respectively:

$$V = -\frac{U}{H}\frac{\partial A_{cs}}{\partial s} \qquad (4.9)$$

$$W = U\frac{2}{b}\frac{\partial A_{cs}}{\partial s} \qquad (4.10)$$

where h in equation (4.5) has been replaced by H, the average depth and, for the simplified bed topography, the depth at the channel centerline.

At a bend entrance, the increasing channel curvature implies an increase in transverse bed slope. Therefore, the cross-sectional area of the inside half-channel ($n<0$) decreases, while the cross-sectional area of the outside half-channel ($n>0$) increases. Thus, flow is displaced away from the point bar (across the channel) and down into the pool. The unit discharges, q_n and q_z, are the volume discharges per downstream distance; therefore, the magnitudes of the vertical and lateral discharges are

$$|Q_z| = |Q_n| = U\left|\frac{\partial A_{cs}}{\partial s}\right|ds. \qquad (4.11)$$

I hypothesize that the momentum transferred to the channel bank as shear stress is the difference between the lateral and downward discharge momenta [*Chow*, 1959], or the change in momentum along the path in figure 4.1(c):

$$dF_n = \rho(|Q_n V| - |Q_z W|) \qquad (4.12)$$

where ρ is water density. The lateral discharge momentum is greater than the vertical for half-width greater than depth (see equations (4.9) and (4.10)). Substituting equations (4.9), (4.10), and (4.11) in equation (4.12) yields

$$dF_n = \rho U^2 \left(\frac{1}{H} - \frac{2}{b}\right)\left(\frac{\partial A_{cs}}{\partial s}\right)^2 ds \qquad (4.13)$$

where dF_n has units of force. It is the incremental lateral transfer of flow momentum due to topographic steering and dissipated by bank friction. I refer to dF_n as the "lateral momentum transfer" or "bank shear force increment". Note that this "force" is felt at the bank as shear stress, not as a normal force.

In the model, the convective acceleration described by equation (4.13) is calculated only where the point bar is rising, i.e., the inside half-section area (A_{cs}) is decreasing downstream ($\partial A_{cs}/\partial s < 0$), and not where the pool is becoming shallower. The lateral momentum transfer, dF_n, is largest at the bend entrance. Because $\partial A_{cs}/\partial s$ is proportional to $\partial C/\partial s$ (usually; see figure 4.1(a)), $dF_n \propto (\partial C/\partial s)^2$. Terms with similar dependence on $\partial C/\partial s$ may be derived from the scaled, depth-averaged flow momentum equations under the assumption, based on the results of *Dietrich and Whiting* [1989], that changes in the downstream (*s*) and lateral (*n*) directions are of similar magnitude and occur over similar distances (see Appendix B).

In Appendix C, I show that, for the special case of a sine-generated channel centerline, dF_n and the integrated bottom shear stress are of similar magnitude. For maximum flow direction angles, with respect to the down-valley direction, greater than 1.0 radian,

the lateral force is somewhat larger than the bottom shear (see Appendix C). This result is consistent with the findings of *Dietrich and Smith* [1983].

I have made several simplifying assumptions that influence the accuracy of equation (4.13). I assumed uniform downstream velocity with respect to the downstream and cross-stream directions. *Dietrich and Smith* [1983] showed that flow over the point bar decelerates as the high velocity core moves to the outside bank. Therefore, this assumption may lead to underprediction of lateral discharge. I assumed uniform transverse bed slope: using different slopes across the channel has an insignificant effect on the magnitude of the lateral momentum transfer. I decouple the bed topography from the bed shear stresses associated with topographic steering; i.e., bed topography is determined by helical flow only (see figure 4.1(d)). My model, therefore, does not represent overdeepening and resonance [*Parker and Johannesson*, 1989; *Blondeaux and Seminara*, 1985] and, according to figure 4.2, may overpredict the transverse bed slope and, therefore, the lateral flow near the bend entrance. The errors due to flow deceleration and overprediction of transverse bed slope near the bend entrance will tend to cancel each other. I have neglected in equation (4.13) the effect of curvature on the vertical discharge. With large curvature, the outside half-channel has more volume per downstream increment (at the centerline) than the inside half-channel, and vertical discharge is increased relative to lateral discharge such that dF_n is decreased. In the numerical model, I make a correction that decreases the effective dF_n in sharper bends by selecting the component of dF_n perpendicular to the flow direction at the downstream end of a discrete channel segment (see figure 4.3(a)). An earlier version of the model omitted this correction with little difference in model results.
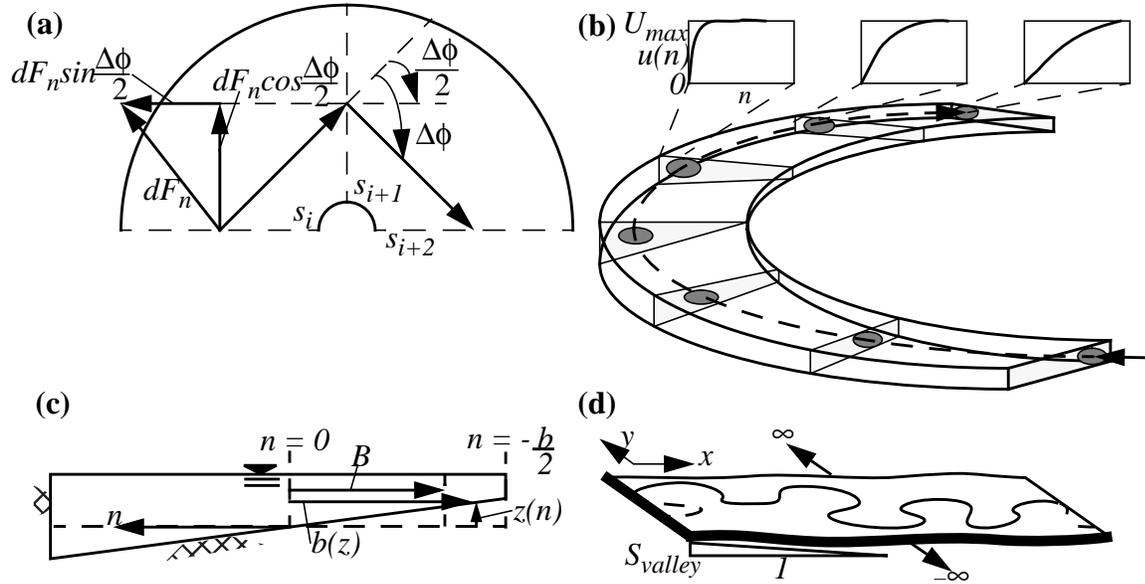
Figure 4.3: (a) The lateral momentum transfer, dF_n, is adjusted to account for the difference in downstream direction angle between successive points. (b) Conceptual diagram of lateral acceleration of the high velocity core and the resulting lateral profiles of near-bank downstream flow velocity; the profile is steep where the core reaches the bank but becomes less steep downstream, though the position of the core is nearly constant. (c) The width, B, used in the lag function, L, is the distance between the inner and outer banks at a depth of $H/2$. (d) The valley is conceptually infinite in the $+$ and $-$ y-directions and "falls off" at set values of x at either end of the valley; channels are cut off when they cross the end boundaries.

4.2.3 Bank Shear Stress

The bank shear stress associated with the lateral momentum transfer is felt downstream, where the high-velocity flow core reaches the bank (see figure 4.3(b)). I derive a simple expression to describe this downstream "lag".

Neglecting curvature in the continuity equation (4.4), substituting with equation (4.5), and letting

$$q_s = Uh \tag{4.14}$$

I get

$$\frac{\partial q_n}{\partial n} = -\frac{\partial q_s}{\partial s}.$$

(4.15)

I simplify equation (4.15) further to derive an estimate of the downstream distance between the convective acceleration of equation (4.13) over the point bar and shear stress on the opposite bank. If I ignore changes in depth and integrate, equation (4.15) reduces to

$$s = -\frac{U\partial n}{\partial V}.$$

(4.16)

I replace ∂n with B, the effective, "depth-averaged" channel width (see figure 4.3(c)):

$$B = \frac{1}{H}\int_{z(0)}^{z\left(-\frac{b}{2}\right)} b(z)dz$$

(4.17)

and ∂V with V and write the downstream lag as

$$L = \frac{UB}{V}.$$

(4.18)

The lag in equation (4.18) is analogous to a translation of a shear force increment from the point bar to the opposite bank downstream and laterally at the downstream and lateral flow velocities, respectively. The lag between lateral acceleration at the bend entrance and bank shear stress clearly exists, otherwise bends would migrate upstream.

One possible improvement over equation (4.18) might be to follow the incremental progress of the high-velocity core across the channel. Such a calculation could amount to solving the nonlinear flow equations for the cross-stream variation of downstream flow velocity and would complicate the model considerably and unnecessarily.

The bank shear stress is proportional to the large lateral gradient of downstream flow velocity that is created where the high velocity core approaches the outside bank. That gradient increases as the core approaches the bank and decreases downstream due to bank friction and the development of a rough turbulent flow boundary layer between the core and bank (see figure 4.3(b)). I parameterize this downstream boundary layer development with a Gaussian bank shear stress function. The bank roughness is parameterized by a constant dissipation scale. The bank shear stress is the integral over upstream points of the Gaussian-weighted and lag-offset dF_n's:

$$\tau_w(s) = \frac{\int\limits_{s'} \exp\left[\frac{-(s-(s'+L(s')))^2}{2\lambda^2}\right] dF_n(s')}{\lambda\sqrt{2\pi}h_o(s)} \tag{4.19}$$

where s' is a dummy variable indicating points upstream of s where the dF_n's are generated; λ is the dissipation scale; and $h_o(s)$ is the depth at the deepest part of the channel section.

In LFE models, dissipation of turbulent energy in the downstream direction is modeled by an exponential decay term (see Appendix D), and the rate of decay is governed by the bed friction factor, C_f. *Johannesson and Parker* [1985] used C_f as the calibration parameter and found that the calibrated values were larger than the calculated values. It is likely that the larger calibrated C_f reflects bank friction.

Similarly, the dissipation scale, λ, is the calibration parameter for the TSRM model. The value of λ is not well constrained by theory or existing data. This scale is related to the scale of bank roughness elements, such as fallen trees or herbaceous vegeta-

tion clumps, but I have not attempted a derivation of the value of λ from observations of bank roughness such as those in Chapter 3. In general, greater relative bank roughness should result in smaller values of λ and, therefore, shorter meander bends.

In equation (4.19) I have parameterized the frictional dissipation of the bank shear stress at the bank, but, as the flow depths are different over the point bar and in the pool, the effect of bed friction is also different near the different banks. The effect of bed friction is likely small where the channel is deep but may be large over the point bar where the channel is shallow. Therefore, an effective "bank" area parameter lumping the effects of bed and bank friction would be large not only in the pool, where the actual bank area is large, but also over the point bar, where the effect of bed friction becomes large though the actual bank area is small. This parameter would have a minimum at intermediate values of actual bank height, i.e., where the channel is approximately rectangular. In the present model, this parameter is $h_o(s)$ (see equation (4.19)), the outside bank depth. Using the outside bank depth where the channel is actually shallow reflects the larger bed friction there.

4.2.4 Implementation

In the model, bank migration rate, ζ, is proportional to bank shear stress, τ_w (positive on the left bank, negative on the right), and perpendicular to the downstream flow direction:

$$\zeta = (E \cdot \tau_w)\bar{n} \tag{4.20}$$

where E is the bank erodibility coefficient; and $\bar{n}$ is the lateral unit vector (see figure 4.1(b)).

The expression for bank shear stress, equation (4.19), does not yield an analytical solution. Instead I discretize the equations and solve them numerically at points along a discretized channel. The model results may be sensitive to the scale of that discretization (as in, e.g., numerical solutions of the diffusion equation) because of the dependence of dF_n on the downstream rate of change of channel curvature and, thus, the inverse of the downstream distance increment. I assume that cross- and downstream changes occur over comparable distances and, therefore, use a default channel discretization which yields an average of $\Delta s=b$; i.e., one channel width. When two adjacent channel points are farther apart than twice the default Δs, a new point is added between them.

In the simulations of this chapter, the model's initial condition is a noisy straight line (see *Howard and Knutson*, 1984, or *Howard*, 1992). The model boundary conditions represent an infinitely wide valley floor with a uniform slope and truncated at both the upstream and downstream ends (see figure 4.3(d)). Neck cutoffs occur when two channel segments come close enough to one another that the channel cross-sections would overlap. I do not model chute cutoffs.

To visualize the model's evolution, the channel is super-imposed on a regular grid discretized at one-third of the channel width. Before each iteration, grid points at the outside bank, channel centerline, and inside bank are set to the bed elevations corresponding to those locations, respectively. After channel movement, all channel grid point elevations are reset to the average bed elevation. Pixels that are abandoned by the channel during the iteration retain their previously set elevations. Finally, I may impose "uplift" or "incision" by adding elevation to all grid elevations except for channel points. Thus, as a channel

124

erodes at the outside bank (next to the pool), a floodplain is built by abandonment of points at the inside bank (next to the point bar). Inside bank pixels are assigned a deposit thickness, h_{dep}:

$$h_{dep} = z_{pb} - z_{cl} \qquad (4.21)$$

where z_{pb} is the elevation of the point bar at the inside bank; and z_{cl} is the elevation of the bed at the channel centerline, or the average bed elevation for the channel section; and h_{dep} is restricted to positive or zero values ($h_{dep} \geq 0$). I must emphasize that in these rules "erosion" and "deposition" are only conceptual and are not governed by mass balance calculation.

4.3 Results

In the following sections, I report the results of two groups of simulations with the Muddy Creek parameters (see table 4.1). I simulate streams in spatial domains much longer than the length of a single bend ($L_{valley} > 100 \times L_{bend}$) and streams and topography over a shorter domain ($L_{valley} > 10 \times L_{bend}$) to visualize the model results in three dimensions. First, I briefly explain the model parameter set. Next, I break up the results into three sections focusing on the forms and evolution of meander bends, the floodplain, and the meander belt, respectively. These sections progress from details to the bigger picture to show how the former is reflected in the latter. Inevitably, there is some overlap of themes among sections. For comparison with the Topographic Steering River Meandering (TSRM) model, I draw on both examples from the field (see Chapter 3) and results from a model

based on *Johannesson and Parker's* [1989c] LFE model (see Appendix D). Finally, I

investigate the TSRM model's parameter sensitivities.

4.3.1 Parameters

Parameters were obtained from published data, shown in table 4.1 [*Dietrich and*

Smith, 1983; *Dietrich and Whiting,* 1989].

The dissipation scale was varied to calibrate the model channel bend size to the

size of the Muddy Creek bend studied by *Dietrich and Smith* [1983] (the "study bend").

Also, from *Dietrich and Smith*'s [1983] detailed map of the study bend, I measured the

distance from the locus of maximum bank erosion to the ends, both upstream and down-

stream, of the cut bank on that bend. Both cut bank measurements and the calibrated value

of λ (see table 4.1) are all approximately equal.

4.3.2 Meander Bends
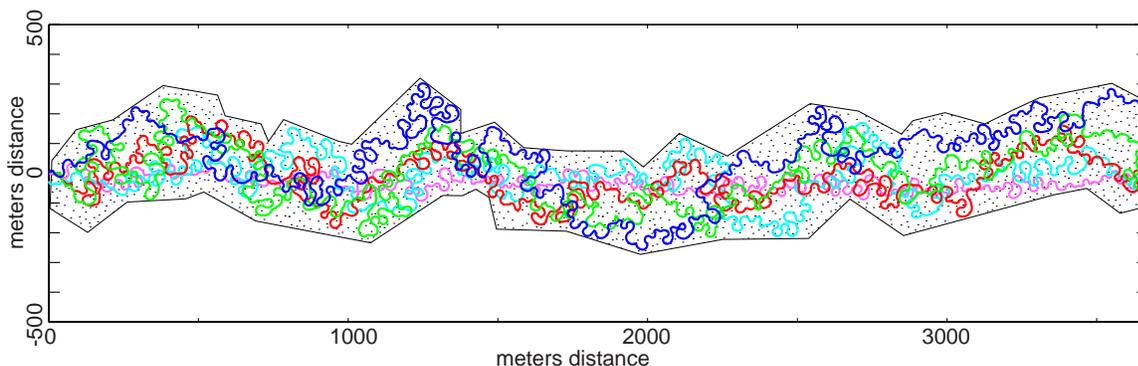
Figure 4.4: Meander model evolution over long domain with Muddy Creek parameters. Display every t = 5000 arbitrary model time units, except magenta, at t = 250 units; cyan is at t = 5500. units; red is at t = 10,500 units; green is at t = 15,500 units; blue is at t = 20,500 units. The meander belt, or the area swept by the channel in all time slices, including many not shown, prior to and including t = 15,500 units is outlined and filled with a speckled pattern. There is little transgression from this area during the last 5000 units.

Several time slices from the long domain TSRM model simulations are shown in

figure 4.4. The model produces realistic, complicated meander patterns. Individual bend

126

forms vary among many "typical" shapes, and the great variety of these shapes gives the appearance of irregularity. In figure 4.5, I compare a short section of model channel from the simulation of figure 4.4 to a digitized natural river channel, the Kuskokwim River, Alaska (see figure 3.13).
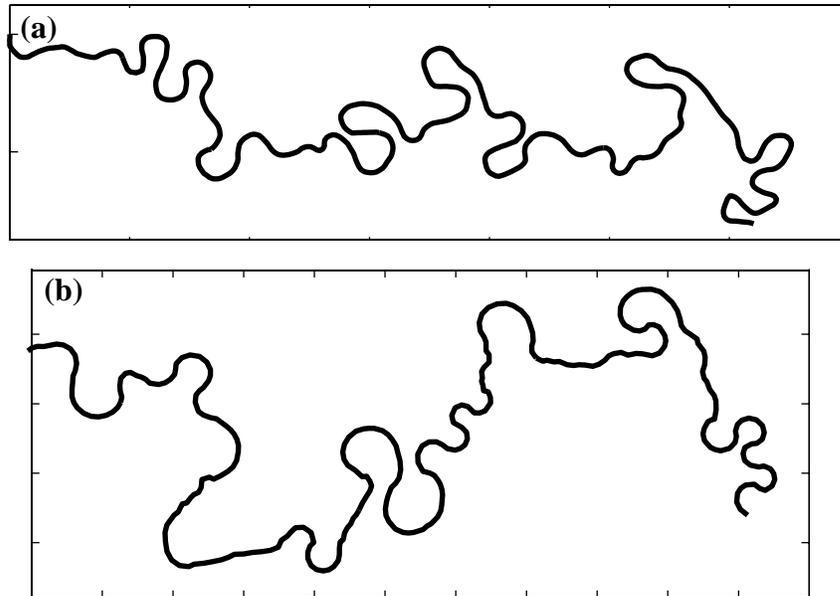
Figure 4.5: Comparison of Kuskokwim River, AK, and a TSRM model channel. (a) Digitized natural channel centerline (see Chapter 3). (b) Model channel segment from the simulation of figure 4.4.

The channel segments shown in figure 4.5 illustrate some of the similarities and differences between natural and TSRM model channels. The comparison illustrates that the model reproduces many of the types of forms found in real channels, such as compound bends, loops that point upstream, relatively straight reaches, and some peculiar yet characteristic forms which defy nomenclature. Some of the natural shapes are irregular in comparison with the ideal shapes simulated by the model. In other cases, the natural shapes are even smoother than the simulated.
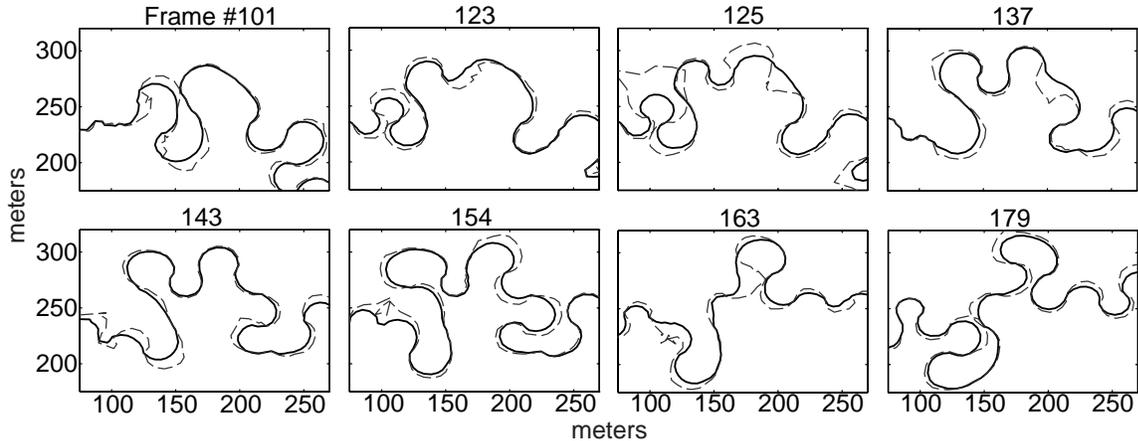
Figure 4.6: Model channels (drawn in solid black) superimposed with the predicted bank shear stress (drawn in dashed gray at a distance proportional to its magnitude from and perpendicular to the corresponding channel segment) to show evolution. Flow is from left to right. Frame numbers are from an animation of the channel evolution where frames are drawn every t = 10.0 units.

A TSRM model time series from a short domain simulation that illustrates some of the possible channel forms and how they evolve over time is shown in figure 4.6. Note that the frames in figure 4.6 are not chosen at equal time intervals but are, rather, chosen to exhibit the details of the model evolution. An interesting result shown in figure 4.6 is the model's formation of compound bends. Frame #101 shows the channel prior to an imminent cutoff at x=150m. In frame #123 the cutoff has developed into a new, downstream migrating bend. In frame #125 the latter bend has "pushed" into the downstream bend and led to an instability and large shear stress on the inner bank of the bend at x=200m; the latter bend is now compound, defined as such by the small curvature reversal at x=200m. In frame #137 the compound bend has separated into three "daughter" bends; the middle of the three is migrating quickly and eroding into the inner bank of the third; the migration of the latter, in turn, has led to compound bend formation at x=225m; the bend at x=100m has recently cut off. In frame #143 the bends at x=200m and 225m have become relatively stable; the compound bend at x=225m has not separated to form daughter bends; and, the

128

new bend at x=100m has initiated another "wave" of rapid channel migration downstream. In frame #154, as a result of that wave, a bend at x=150m is now compound and the bends downstream have changed. In frame #163 two more cutoffs, at x=150m and 225m, have initiated two waves, respectively, of accelerated channel migration. Finally, in frame #179 the bend at x=100m has formed a series of bends resembling the "daughter" bends at x=200m in frame #154, though the two mechanisms are different. These frames show that, in general, bends first migrate downstream when they are small, grow laterally when they are of medium length, and finally grow upstream when they are long. This result is consistent with the decreasing "phase shift" with increasing bend length found by *Odgaard* [1987] and predicted by *Furbish* [1991].

The model produces compound bends similar, both in form and evolution, to those observed in the field. The "dog-leg" bend at the bottom of frame #154, at x=150m is characteristic of a shape often produced by the model and found in nature. I showed an example from the Amazon River basin in figure 3.4. In figure 3.12 I showed two examples of compound bend formation on the Ellis River, ME, which formed by a mechanism similar to that described above and shown in figure 4.6.

4.3.3 The Floodplain

I emphasize again: in these "floodplain" results I do not calculate the sediment mass balance. Thus, when, in the context of the model visualization, I use terms such as deposition, incision, and uplift, I mean them figuratively.

Two time slices of the figure 4.6 simulation with uniform uplift are shown in figure 4.7, one slice at an early stage of the simulation and the other slice at a time

(between frames #137 and #143 of figure 4.6) much greater than the time for the channel to rework most of the meander belt. Both elevation and alluvial thickness shadings are shown. If there were no uplift in the simulation, the surfaces with non-zero deposit thicknesses (alluvial shading other than white) would be floodplain surfaces higher than the average channel bed elevation.

The time of figure 4.7(c) and (d) is chosen to show the early development of the compound bend at the center of the domain; this is the same compound bend as that shown in frame #123 of figure 4.6. The blue shading of the new point bar indicates that the bend is growing rapidly compared to bends without blue-shaded point bars. As shown above, waves of accelerated migration, such as often follow cutoffs, lead to a punctuated evolution of alternating slow and rapid channel migration. This punctuated evolution is evident from the variations in topographic slope on the modeled point bars (detail shown in figure 4.7(e) and (f)). The uplift rate is constant; therefore, topography will be steeper when channel migration is slower. Flatter surfaces indicate locations of more rapid channel migration.

Sloughs (see *Howard,* 1992) form on the point bars of bends (marked by arrows in figure 4.7) which are short enough that the lateral momentum transfer at the bend entrance leads to shear stress which carries over into the next bend (e.g., see frame #137 in figure 4.6) and erodes the point bar of that downstream bend. Where the point bar is eroded, the channel moves away from the pool, rather than from the point bar as is more usual, and points which were last occupied by the pool form a slough which resembles those observed in the field and in the modeling of *Howard* [1992].
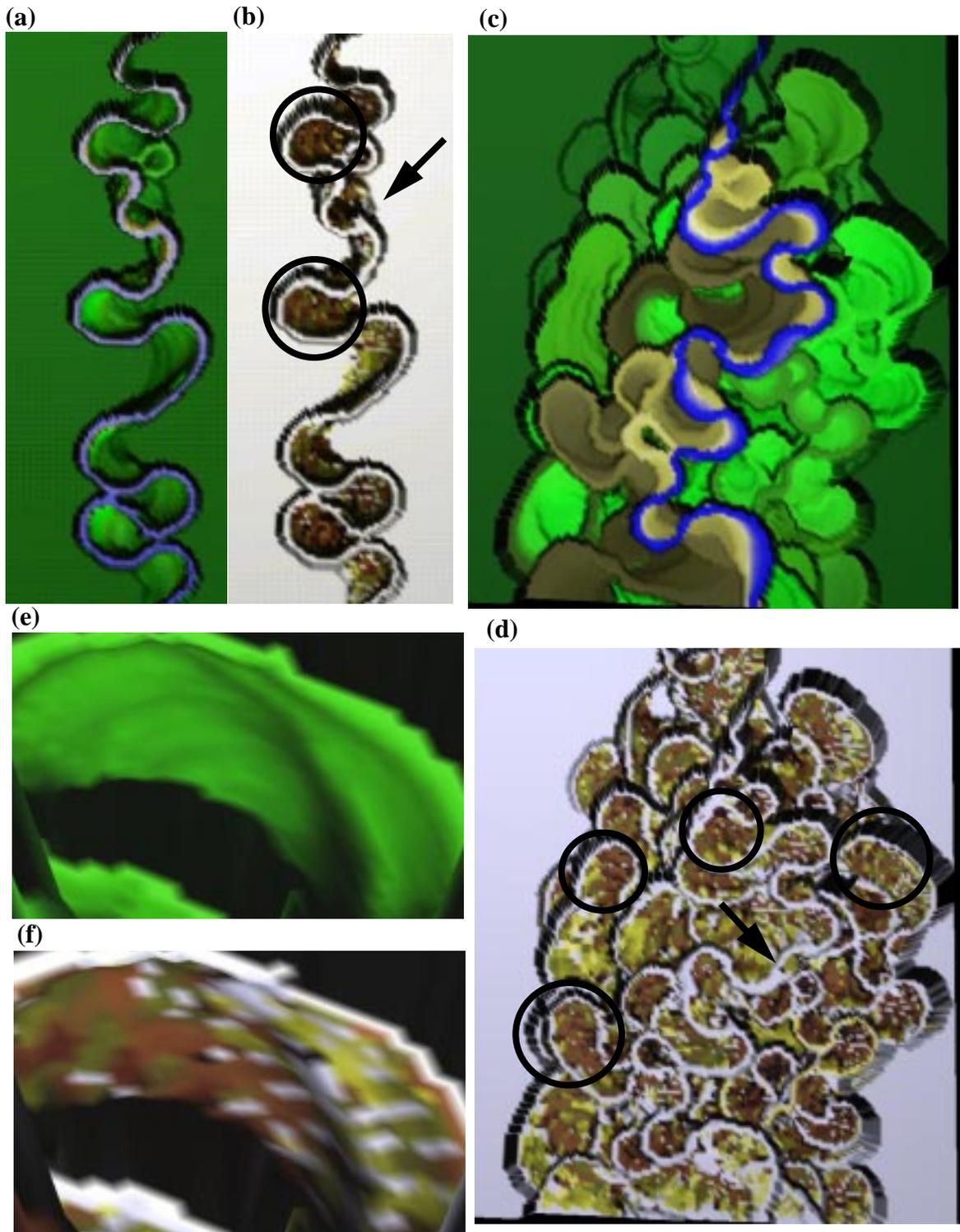
Figure 4.7: Visualizations of "incised" meanders. (a), (b) Time = 300 units. (c), (d), (e), (f) Time = 12,490 units. (a), (c), and (e) Elevation shading, low to high: blue, tan, brown, light and dark greens; stretched at low elevations. (b), (d), (f) Alluvial shading, ~0-0.5 meters: white; yellow; yellow, green and dark grays; light and dark browns. (e), (f) Detail of point bar, (e) elevation and (f) alluvial shading.
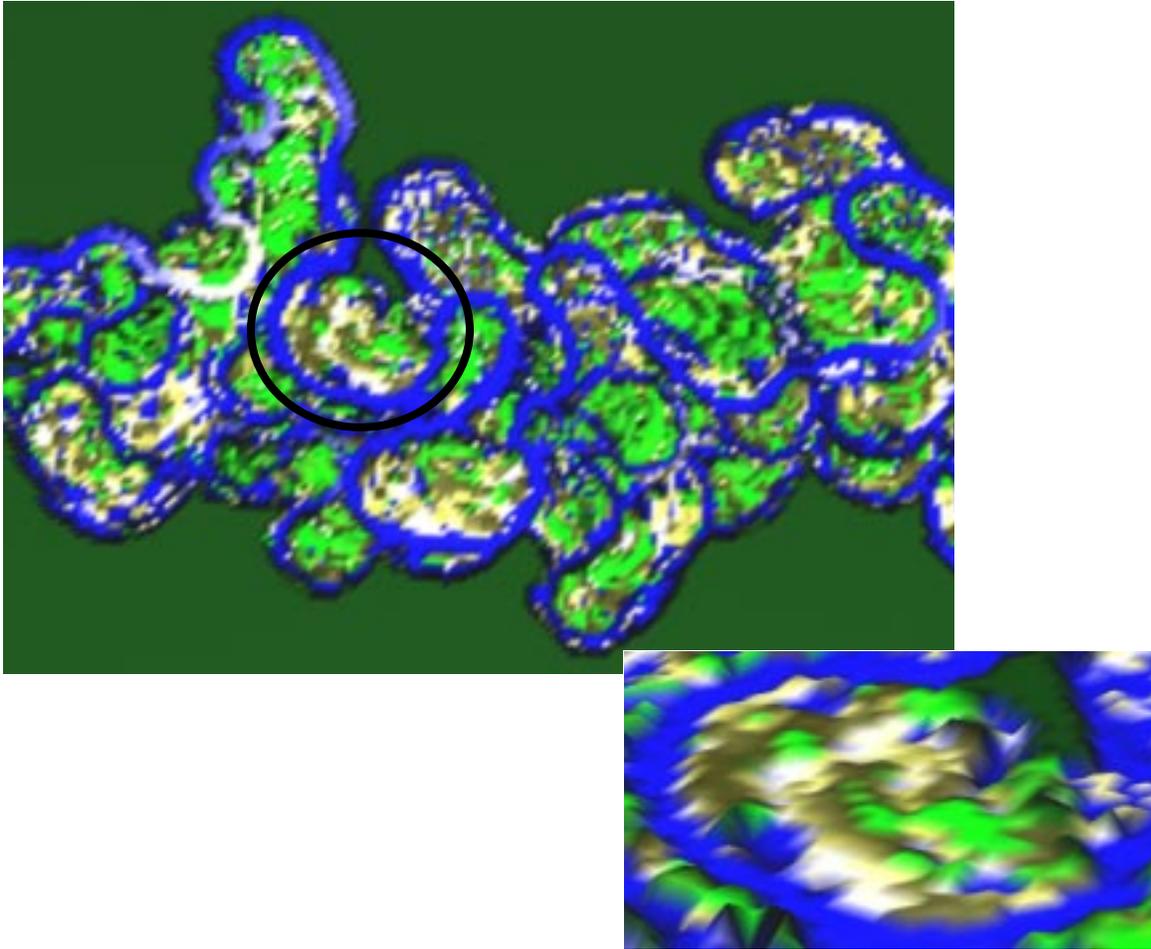
Figure 4.8: Visualization of model evolution without uplift to show floodplain topography. Elevation shading is similar to that of figure 4.7 except that here greater elevations are stretched to show scroll bar topography. A close-up perspective view of the circled area is inset. Flow is from left to right, and I have removed the valley's downward elevation trend.

Deposit thicknesses appear as bands of alternating light and dark in many locations (some examples are circled in figure 4.7). These bands of contrasting deposit thickness are similar to scroll bars observed in the field (see figures 3.3 and 3.16) and are not formed by other models (e.g. *Howard,* 1992). In the simulation without uplift, shown in figure 4.8, the scroll bar-like topography is more evident. These model scroll bars are the result of oscillating channel curvature—which determines point bar height through equations (4.2) and (4.21)—during the evolution of the meandering channel.

To better understand this mechanism and others, it is useful to compare TSRM and LFE model bends. In figure 4.9, I plot the shape, curvature, and shear stress for bends typical of each model: small bends and the same bends just prior to cutoff. Note that no LFE model parameters were calibrated. The plots of curvature and bank shear stress as functions of downstream distance are normalized by the maximum curvatures and shear stresses and the bend lengths, respectively, for the small bends. These normalization values are listed in table 4.2, along with the similar quantities from the Muddy Creek study bend.

Table 4.2: Bend characteristics for both models and Muddy Creek study bend

	LFE model	TSRM model	Muddy Creek
bend length, m	42.1	25.2	25.2
max. curvature, m^{-1}	0.0902	0.136	0.13

From equation (4.20), the bank migration rate, $\zeta = 40\ cm/yr$, measured at the Muddy Creek study bend, and the TSRM model-predicted maximum bank shear stress, $\tau_w = 1.1\ N/m^2$, the bank erodibility predicted by the TSRM model is

$$E = \zeta/\tau_w = 0.36\ m^3/N \cdot yr.$$

Shear stress distributions in the small bends are fairly similar, but subtle differences become more pronounced in the long bends. The different mechanisms driving bank shear stress in the two models are evident in the different bend shapes and shear stress distributions. The reader should refer to figure 4.9 in the following explanatory paragraphs.
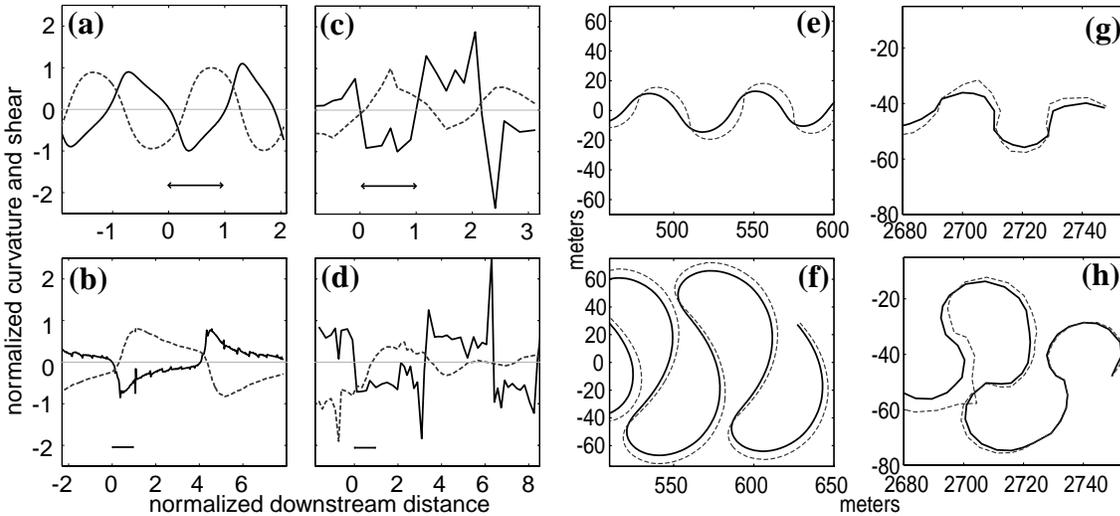
Figure 4.9: Comparison of the LFE and TSRM models. (a), (b), (c), and (d) plot channel centerline curvature (solid black) with bank shear (dashed gray); (e), (f), (g), and (h) show the channel planforms (solid black) with bank shear (dashed gray), where its magnitude is proportional to the perpendicular distance from the channel. (a) and (e) show small bends from the LFE model, and (b) and (f) show the same bends near cutoff. Similarly, (c) and (g) show small bends from the TSRM model, and (d) and (h) show the same bends near cutoff. The curvature and shear plots, (a), (b), (c), and (d), have normalized axes; the horizontal axes are normalized by the lengths of the small bends (arrows) of each model; the vertical axes are normalized by the maximum values of curvature and shear in the same small bends. Both cases use the Muddy Creek parameter set.

In the LFE model, the effective bank shear stress is linearly dependent on a weighted integral of local and upstream curvature (see equation (D.0.1)). The curvature function peaks shortly downstream of the crossover between bends and decays through the bend, and the bank shear stress function has a similar shape peaked downstream of the curvature. The curvature and shear stress functions and channel planforms are quite regular from bend to bend, and the curvature changes gradually through the bend. The bends tend to "lean" upstream but continue to elongate laterally because the loci of maximum shear stress are at the bend apices.

In the TSRM model, bank shear stress is nonlinearly dependent on the downstream rate of change of curvature. Curvature peaks twice, at the beginning and end of each bend.

In between, the curvature is nearly constant for much of the bend and, for a small part near the end of the long bends, approaches zero. These curvature changes occur over short distances. The model bend curvature is strikingly similar to some of the natural channels' curvature plotted in figure 3.14.

The bank shear stress function peaks early in the bend, downstream of the first peak in the curvature function, and may drop to nearly zero due to the nearly constant or decreasing curvature through the middle of the bend. Thus, the direction of maximum channel migration shifts away from the down-valley or lateral directions toward the up-valley direction. This tendency for long bends to "point" upstream limits the bend's lateral elongation and is commonly observed in the field (see, e.g., figures 4.5(a) and 3.4). Bank shear stress due to the second curvature peak carries into the next bend and somewhat counteracts the shear stress from the opposite lateral momentum transfer at the beginning of that next bend. Note that I do not explicitly model the flow field; that said, the latter counteraction effect is similar to what happens to the flow field in the transition between bends. At a bend entrance, if the high velocity core is accelerating toward the inside bank, it takes some force to reverse that acceleration and steer it towards the opposite bank, force which might otherwise be expended as shear stress.

The spatiotemporal coevolution of curvature and bank shear stress forms scroll bars, as shown in figures 4.7 and 4.8. This phenomenon bears some discussion here. In the two long bends in figure 4.9(d) and (h), smaller curvature peaks at the crossover and beginning of the first bend lead to a longer downstream lag than in the second bend, where the curvature peaks are larger. In the latter bend, bank shear stress is concentrated in a rel-

atively high curvature reach such that high points are left behind by the migrating channel; in the former bend, bank shear stress is peaked where curvature is small such that low points are left behind as the channel migrates. Such differences in the downstream lag exist among bends and over time in the same bend. As the lag changes over time, the step-like nature of the curvature function leads to similarly abrupt differences in floodplain elevation. Two other simple mechanisms also come into play: (a) where bank migration is localized, curvature at that locus increases; and (b), in loci of less bank migration, local curvature decreases.

I further examine the model scroll bars by repeating the spectral analysis of Chapter 3 for transects extracted by scan line conversion of line segments between specified endpoints onto the model grid (see figure 4.10). This is the same method used to superimpose the TSRM model channel segments onto the grids in figures 4.7 and 4.8. The numbered transects from figure 4.10 are shown in figure 4.11.

I employed the same spectral technique used for the natural channels in Chapter 3 to find the power spectra of the transects (see figure 4.12). Many of the transect spectra do not have peaks with confidence levels smaller than 0.5, and none of the spectral peaks have confidence levels smaller than 0.1 (see table 4.3). This result indicates that the model scroll bar topography is only quasi-periodic, though many of the spectra have peaks at similar wave numbers. The mean peak wavelength, excluding transects 4, 15, and 20, is 9.6 m. The results of the model spectral analysis are not dissimilar to the results of the Ellis River spectral analysis (see Chapter 3, especially figure 3.21) which also did not have many peaks at confidence levels smaller than 0.1. Neither the Ellis nor the model transects

are long enough to contain many oscillations at the peak wavelength because their point bars contain few scrolls, but even the Mississippi scroll bars analyzed in Chapter 3 were only quasi-periodic.

Some of the peak wavelengths are close to twice the channel discretization. Animations of the formation of these scroll features indicate that some of them result from the channel discretization where the channel runs perpendicular to the ridges. Much of the model scroll bar topography, however, is indeed produced as the curvature through several channel points oscillates as the bend migrates. Note that transects 4 and 12 are practically on top of one another but have different maximal peaks, testimony to the lack of a dominant periodicity in the model topography.
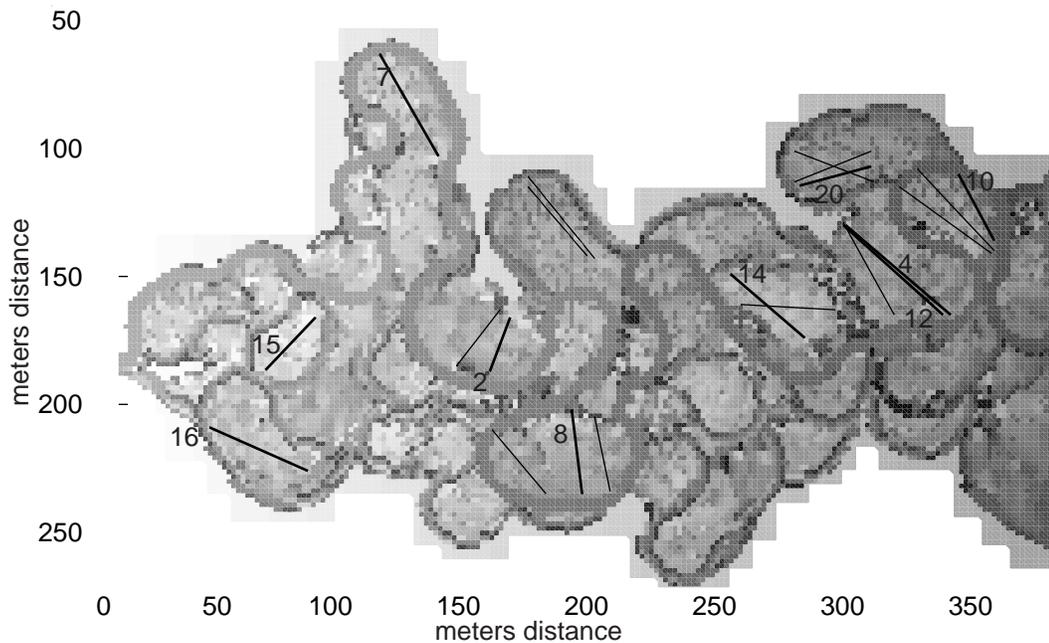
Figure 4.10: Gray scale image of the model simulation of figure 4.8 with locations of transects. Numbered transects are drawn with a thicker line than the rest.
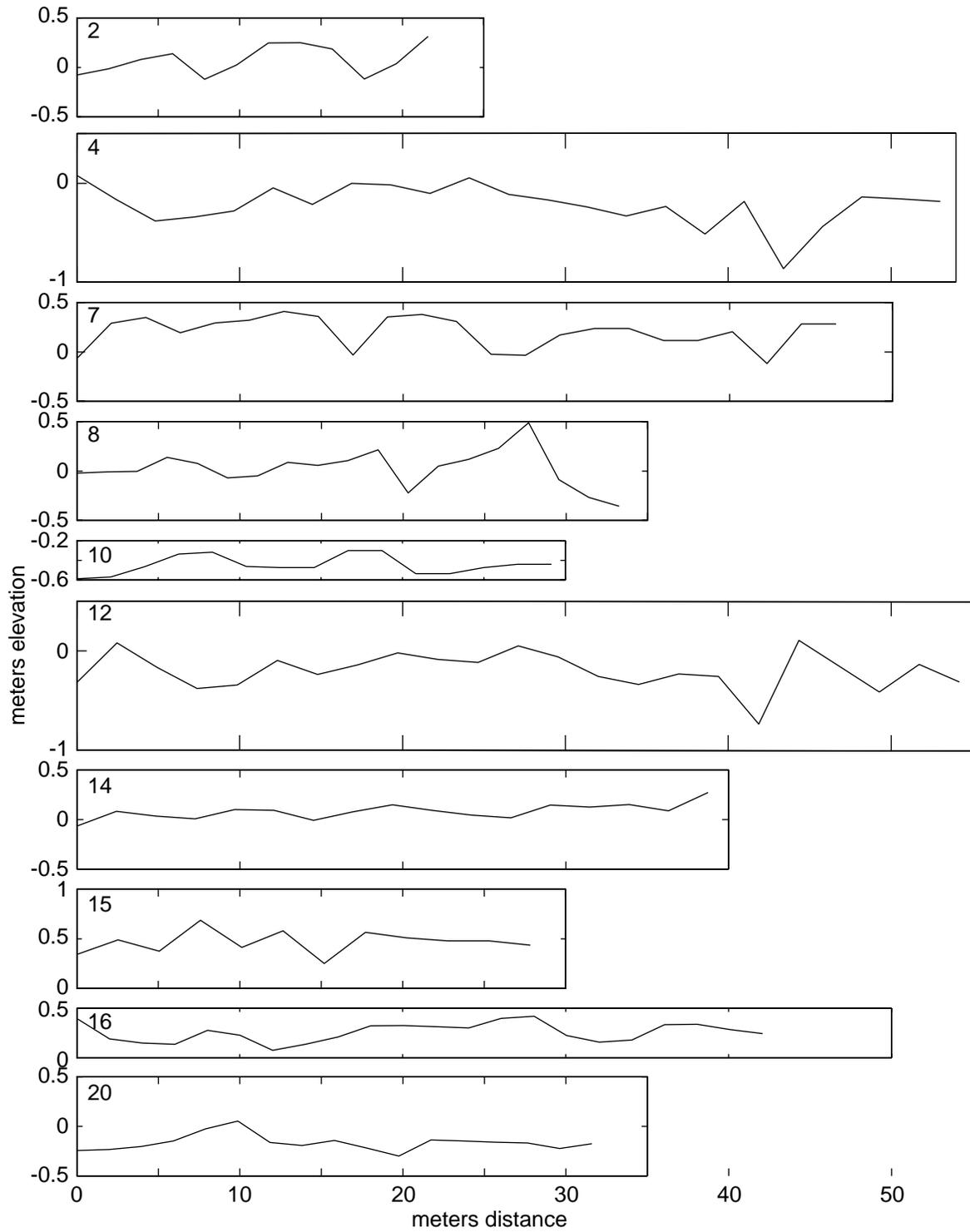
Figure 4.11: Elevation plotted vs. distance for the numbered transects shown in figure 4.10. Note that the grid point spacing is 1.83 meters in both the *x*- and *y*-directions. Therefore, the minimum possible transect increment is 1.83 m.
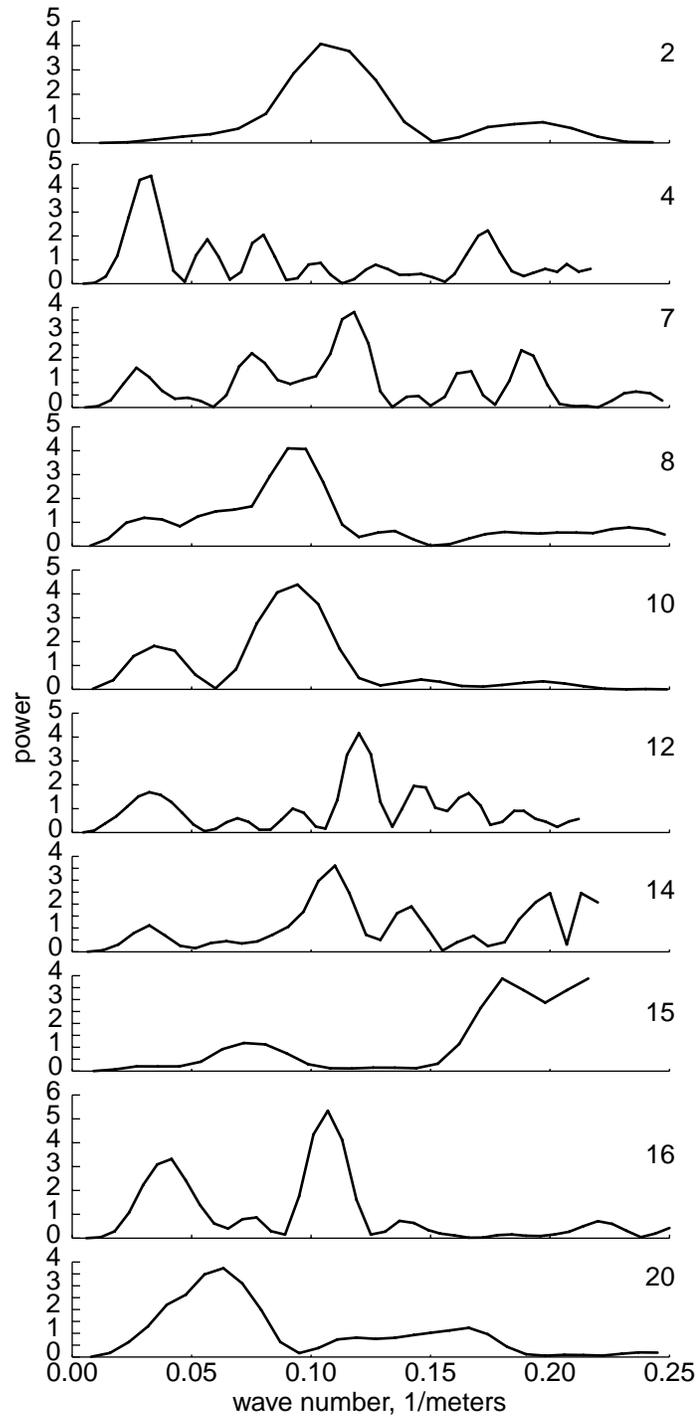
Figure 4.12: Power spectra of the numbered transects shown in figures 4.10 and 4.11. The plots show power vs. wave number. Only those spectra with maximum power above the 0.50 confidence level are shown. The confidence levels of the maxima are as follows: 0.19, 0.20, 0.40, 0.27, 0.17, 0.30, 0.37, 0.22, 0.10, and 0.33 for spectra of transects 2, 4, 7, 8, 10, 12, 14, 15, 16, and 20, respectively.

Table 4.3: Confidence levels of spectral peaks[a]

transect	peak wave number, m^{-1}	peak wavelength, m	confidence level
2	0.10	9.6	0.19
4	0.033	30.	0.20
7	0.12	8.5	0.40
8	0.091	11.	0.27
10	0.091	11.	0.17
12	0.12	8.3	0.30
14	0.11	9.1	0.37
15	0.18	5.6	0.22
16	0.11	9.4	0.10
20	0.063	16.	0.33

a. Grid discretization is 1.83 m; channel discretization is variable, on average 5.5 m, or one channel width.

4.3.4 The Meander Belt

The meander belt according to one definition is drawn in figure 4.4. In figures 4.7 and 4.8, the meander belt consists of points visited at least once by the channel. Areas completely surrounded by "visited" points could also qualify and are visible in figures 4.7 and 4.8 but are not represented in the following statistics. When past channel location is not recorded, the meander belt is defined by the present channel.

Cumulative distribution functions (CDFs) of meander belt age and the time development of meander belt width are shown in figure 4.13 for the simulation of figure 4.7. The CDFs show that most of the material in the meander belt is relatively new; i.e., the channel reworks ~70% of the meander belt every ~3000 model time units. But the distribution has a tail which grows longer through time and indicates that the probability of finding older surfaces remains relatively high for times much longer than 3000 units; e.g., after 13,100 units, the probability of finding a surface older than 10,000 units is greater

than 10% (see figure 4.13). The meander belt reaches a stable maximum width (figure 4.13(b)) after 3000-5000 time units, though the channel often approaches the belt edges (see figure 4.7). *Lathrap* [1968] found the oldest of his archaeological sites on the Rio Ucayali, Peru, on the edge of the meander belt.
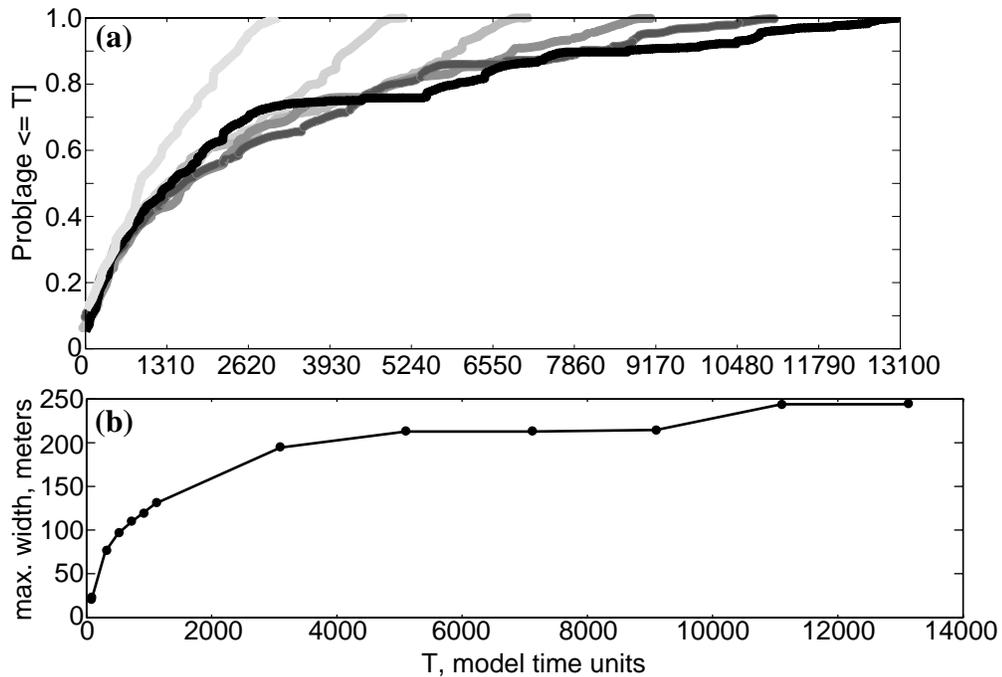
Figure 4.13: Cumulative distributions of floodplain age and maximum meander belt width. Time (horizontal) axes are of approximately equivalent scale. Results are from the simulation shown in figure 4.7. (a) Cumulative distributions of ages of meander belt material are shown for several times after meander belt widening has nearly ceased; only locations which have been visited at least once by the channel are included in the distributions. (b) Maximum meander belt width *vs.* time. Maximum meander belt width is defined by the longest row (i.e., cross-valley) of grid points which have been visited by the channel (see figure 4.7).

Meander belt stability is also illustrated in figure 4.14, where the normalized probability density and non-normalized frequency distributions of the *y*-coordinate values of channel points are shown for the long domain simulation time slices of figure 4.4. Between the first and second times, the number of points and the meander belt width increase dramatically; after t = 5500. units, the number of points and the meander belt

width increase little, but the likelihood of a channel point lying near the edge of the mean-

der belt increases greatly. The last time slice in figure 4.14 shows that the channel pattern

eventually loses its "memory" of the initial channel location and that, in so doing, the *y*-

coordinate values of disparate parts of the meander belt become uncorrelated. This de-cor-

relation leads to the bimodal distribution of *y*-coordinate values for the last time slice in

figure 4.14. But, even as different sections of the channel occupy different regions on the

y-axis, the major part of the channel remains within a range whose width is relatively con-

stant throughout the simulated channel's evolution. Note that these plots are not meant to

predict patterns of deposition, which could affect meander belt location, width and stabil-

ity. The finding that meander belt width remains nearly constant after some time contrasts

with *Howard*'s [1996] finding that his meander model produced logarithmic growth of the

meander belt width with time.
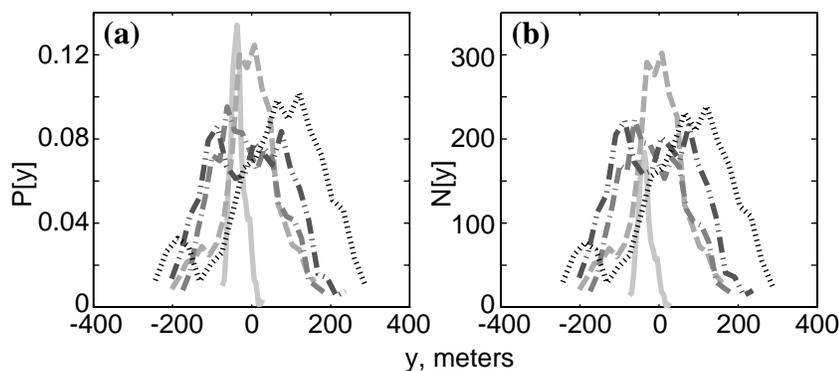
Figure 4.14: Distributions of *y*-coordinates of simulated channels from figure 4.4. Solid light gray, t = 250. units; dashed light medium gray, t = 5500. units; dot-dashed dark medium gray, t = 10,500. units.; dot-dot-dashed dark gray, t = 15,500. units; dotted black, t = 20, 500. units. (a) Normalized sample distributions of probability of finding a channel point at a given *y*-coordinate; (b) non-normalized sample distributions.

In figure 4.15, I show the results of applying the measures (sinuosity mean and

variance, meander belt width, and mean angle) developed in Chapter 3 to the model chan-

nels at several times during the simulation of figure 4.4. First, note that the characteristic

features change over time. The first slice has a single plateau and single peak in μ_S and

σ_S^2, respectively. W decreases monotonically with a convexo-concave profile; convex at

the peak of σ_S^2 and where μ_S is increasing, concave where μ_S is level. μ_θ has a single

peak, though a subtle bump is apparent after the peak. In all subsequent time slices, σ_S^2

has more than one peak corresponding to more than one step in μ_S and convexity of W.

Correspondence to peaks in μ_θ is also apparent though less consistent. The number of

channel planform scale indicators is not monotonically increasing through time, and the

primary sinuosity remains nearly constant. The secondary sinuosity, however, varies. If

secondary features correspond to large multi-bend loops, then the cutoff of such forms

will eliminate corresponding channel planform scale indicators. Apparently, there was at

least one major cutoff event between times 5450 and 10,450. Similar forms have become

reestablished as of time 15,450. The scale of the primary channel planform scale indica-

tors is nearly constant in time at ~20-30 *b*. Secondary channel planform scale indicators

are also at similar scales over time, at ~100 *b*. These characteristics and scales are similar

to those of the natural channels in Chapter 3.

For comparison, I show several time slices from the LFE model simulation over a

domain the same length as the TSRM model simulation of figure 4.4 in figure 4.16 and the

results of my planform measures in figure 4.17. I have already pointed out some of the dif-

ferences in form in figure 4.9. Note the different model times bearing no correspondence

to times of the TSRM model simulations shown. The LFE model simulation has complex

forms but lacks multi-bend loops and other forms typical of compound bend formation,

such as that in figure 3.4. Computation time for the simulation shown was an order of

magnitude longer than that of figure 4.4, and the LFE simulation time corresponds to much less time than in figure 4.4 in terms of the lifetime of a simple bend. This version of the LFE model needed a much finer discretization than the TSRM model, and the correspondingly greater number of channel points led to much of that longer computation time. Others, e.g., *Howard* [1992] use a channel discretization comparable to that used here for the TSRM model.
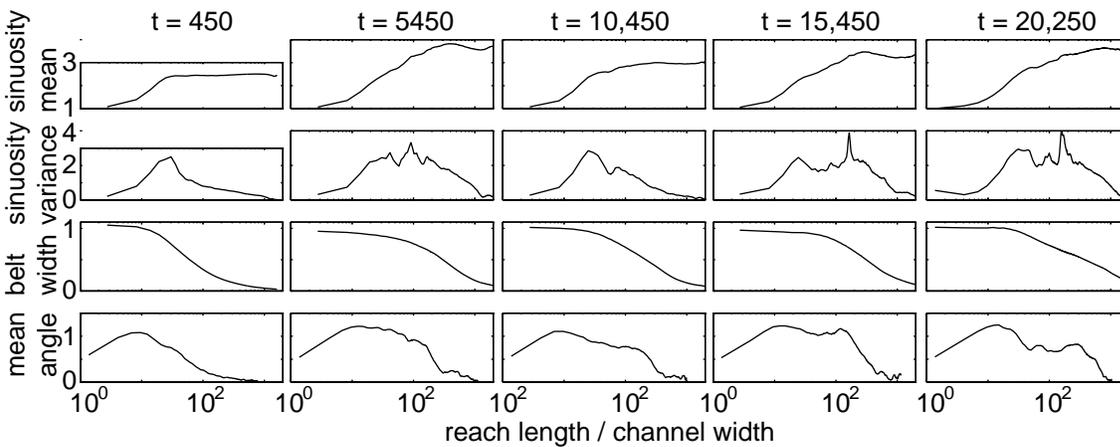
Figure 4.15: Sinuosity mean and variance, relative meander belt width, and mean angle vs. normalized reach length for the TSRM model simulation of figure 4.4.
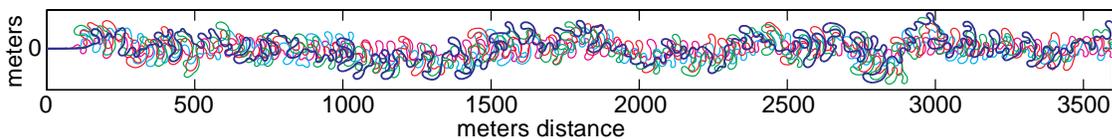
Figure 4.16: Meandering channels simulated with the LFE model and shown at several times. Magenta, cyan, red, green, and blue are after 20, 40, 60, 80, and 100 time units, respectively.

There are some interesting differences in the planform measures of the LFE model simulations. The shapes of the σ_S^2's are most strikingly different. The integral or mass of σ_S^2 for the LFE model simulation is smaller and more closely distributed around the peak value. There are secondary peaks, but they are limited to spikes, i.e., they are not associated with much of the σ_S^2 mass, and they look more like noise. Similarly, μ_S does not have

distinct secondary steps. Peak values of *W* are larger than for either natural or TSRM

model streams. Two slices (excluding noise) are not monotonically decreasing and are

peaked at the scale of the peak in $\sigma_S{}^2$. I observed this peak in *W* for TSRM model simula-

tions not shown, but it appears to be less common and may vary with parameters. There

are no significant secondary μ_θ peaks. The scale of channel planform scale indicators is

approximately constant over time at ~20-40 *b*, though there is some increase over time

which may or may not be significant. I observed that LFE model bend growth is bounded

only by spatial limitations, whereas the TSRM model bends tend to become compound.

By the last time slice, the maximum *W* has decreased to a value similar to that typical of

the TSRM model.
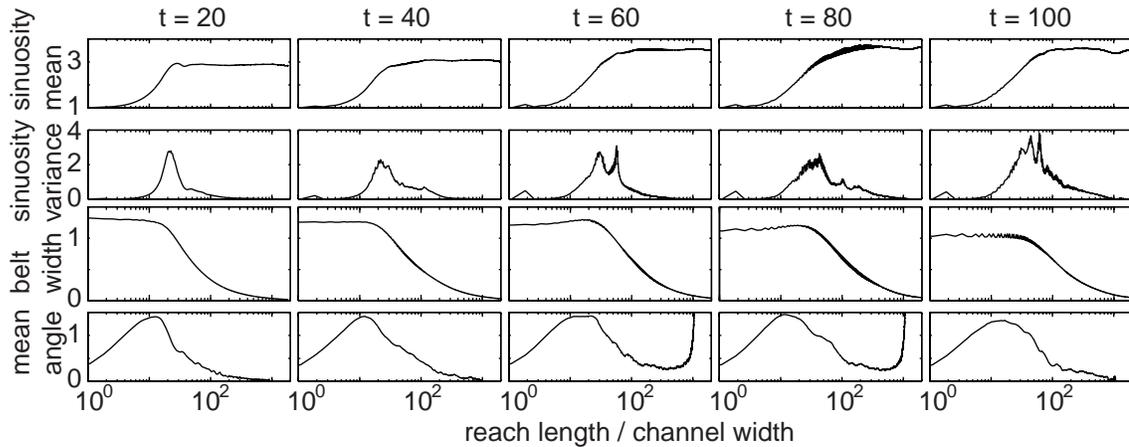
Figure 4.17: Sinuosity mean and variance, relative meander belt width, and mean angle vs. normalized reach length for the LFE model simulation of figure 4.16. The steep rises in mean angle for scales approaching 1000 channel widths at t = 60 and t = 80 are artifacts of the measure.

4.3.5 Model Sensitivity to Parameters

I have analyzed the model's sensitivities by running simulations varying each

parameter, and I show some of the more interesting cases in this section. Parameter

changes can have complicated effects due to the interplay among the various model components described in the previous section.

The dissipation scale is the major control on the size of the simulated meander bends. Smaller (or larger) dissipation scales lead to smaller (or larger) bends. The relationship between dissipation scale and bend length is linear. The dissipation scale was the calibration parameter because it most directly controls meander bend length.

Parameter changes that increase the difference between the lateral and vertical momenta in equation (4.12) usually result in increased migration rate. Such changes include increasing channel width (see figure 4.18) and slope and, counter-intuitively, decreasing discharge; when channel width is held constant, a decrease in discharge also decreases the depth such that the width-to-depth ratio and, therefore, the difference between the lateral and vertical momenta, also increase (see equation (4.13)). However, discharge and width do not, in general, vary independently in natural channels.
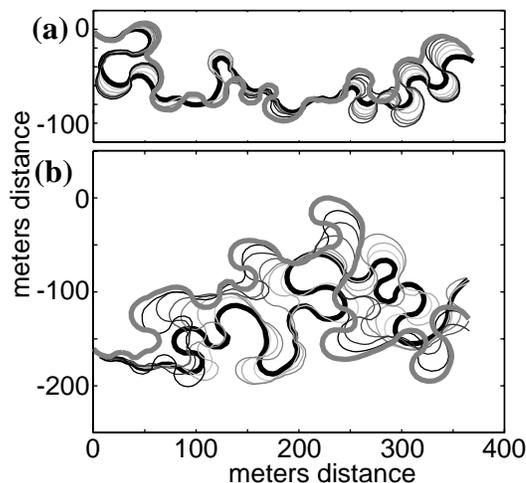
Figure 4.18: Illustration of the model's sensitivity to channel width. In (a), simulation with default channel width, $b = 5.5$ m; in (b), simulation with $b = 10.$ m. Both simulations are shown after and for equal times. Earliest times shown in bold black; latest times in bold medium gray; intervening times, from early to late, shown in thin light gray to black.
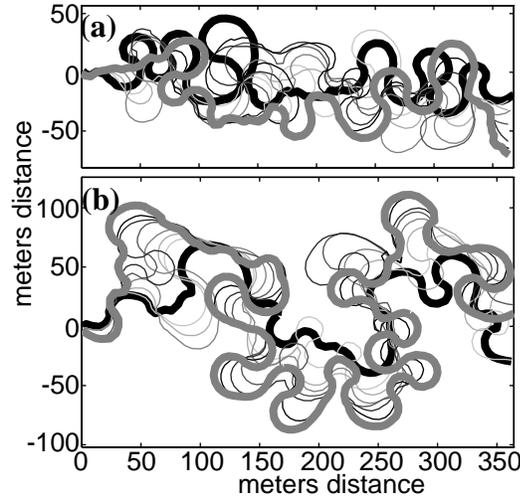
Figure 4.19: Illustration of the model's sensitivity to median grain diameter. In (a), simulation with $d_{50} = 2$ mm; in (b), simulation with $d_{50} = 0.4$ mm. Both simulations are shown after and for equal times. Earliest times shown in bold black; latest times in bold medium gray; intervening times, from early to late, shown in thin light gray to black.

Changes in grain size affect both the rate and style of channel migration (see figure 4.19). Decreasing the grain size can have a dramatic effect because of the transverse bed slope's dependence on grain size (see equation (4.3) and equations (A.1.4) and (A.2.10)). Smaller grain size corresponds to greater transverse bed slope and, thus, larger $\partial A_{cs}/\partial s$. The lateral momentum transfer increases as $(\partial A_{cs}/\partial s)^2$ (see equation (4.13)), and the downstream lag decreases as the inverse of $\partial A_{cs}/\partial s$ (see equation (4.18)). Migration rate increases with lateral momentum transfer. Shorter downstream lags, relative to the dissipation scale, promote more compound bend formation, such as in the run of figure 4.19(b), because the bank shear stress is applied earlier in the course of the bend. I showed in Chapter 3 that bends of the Ellis River became compound when the channel at the beginning of the bend migrated rapidly (Aside: note the marked similarity, in both shape and evolution, between the bend at the bottom of figure 4.19(b), at $x = 250$ meters, and the Ellis River bend #13 in figure 3.12(b).). Thus, parts of the channel migrate in the

same direction as, and elaborate on the patterns of, earlier bends to form sinuous, "puzzle-piece" patterns. This type of pattern is prevalent, for example, on the Melozitna and Innoko Rivers, Alaska (see figure 3.13).

4.4 Discussion

The model suggests answers to some of the past riddles concerning the evolution of meandering channels and the effect of that meandering on floodplain and meander belt geomorphology.

4.4.1 Conditions for meandering and channel stability

It has been suggested [*Schumm, et al.,* 1987; *Howard*, 1992] that cohesive bank material and mobile bedload are necessary for meandering. My model supports the necessity of the latter and, implicitly, the former conditions.

Without stabilization by cohesive materials and vegetation, the floodplain and channel banks are eroded until the stream is fully braided, as shown in the experiments of *Schumm, et al.* [1987] and my own field observations in the Missouri Ozarks (see Chapter 3). The TSRM model assumes that the channel banks and floodplain are stabilized by some mechanism though I do not model that mechanism explicitly. The bed topography model assumes that the bed is composed of mobile bedload material. Therefore, mobile bedload is necessary in the TSRM model, and experimental observations also support the necessity of bedload for meandering [*Schumm, et al.*, 1987; *Smith*, 1998].

Bend migration may become small under several conditions, as indicated in the results. The model predicts a punctuated evolution, fast when bends are small and slow when bends are either long or "incoherent", i.e., lacking a consistent scale, such as in the

period just following a cutoff. The latter phenomenon is apparent from the long time between the first two frames of figure 4.6. Changes in bedload material may also affect channel stability, as shown in figure 4.19. If the bedload source for a meandering channel were to coarsen and that coarsening were the only change, then, according to the model, the channel migration rate would decrease as transverse bed slopes and, thus, lateral momentum transfers became smaller. Deeper, narrower channels should also migrate less quickly.

On the other hand, I have shown several situations in which migration rate is particularly large. Of course, increases in parameters which reflect the available energy, such as discharge and valley slope, lead to increases in migration rate. This sensitivity to slope is consistent with *Schumm*'s [1993] observations and *Schumm, et al.*'s [1987] experimental results. But, the model also predicts some less obvious sensitivities. In the model, wider channels with smaller bedload migrate more rapidly, as shown in figures 4.18 and 4.19, and small bends migrate quickly and lead to rapid migration in bends downstream.

I, and others, have observed that meandering channels occur only in valleys of low slope. According to equations (4.3) and (4.13), migration should be more rapid when valley slope is larger because larger bottom shear stress due to the slope increase leads to greater transverse bed slope. However, flow on the floodplain will also be swifter, and deposition of stabilizing fines and seeding of stabilizing vegetation will be less likely. Therefore, such streams are more often braided, as per the discussion above.

Dietrich and others (personal communication, 1995), *Howard* [1992], and *Smith* [1998] have observed that some sinuous, low-slope channels do not migrate at all. As

noted above, my model suggests that migration should decrease with lower channel slope. If there is a critical shear stress for bank erosion, migration could cease entirely when channel slope is small enough. I experimented with a critical shear stress for bank erosion and modeled some cases in which migration stopped after the sinuosity increased, and thus the channel slope decreased, beyond a threshold value.

4.4.2 Meander bend shape and evolution

The present results indicate that details of meander bend shape may have profound implications for the meander belt as a whole. Most of the differences in bend shape between the TSRM and LFE models are due to their dissimilar dependencies on channel curvature, as explained in the results section.

In the LFE model, the channel migration rate's linear dependence on channel curvature discourages, and may even disallow, compound bend formation. *Howard* [1992] noted the absence of compound bends in his LFE model simulations. In the LFE model, bends remain stable with respect to variations in curvature as long as the curvature does not change sign, even as these bends become quite long. Such bends never develop more than one pronounced curvature maximum (see figure 4.9). *Howard* [1992] conjectured that un-modeled secondary processes, such as migrating alternate bars, or conditions, such as heterogeneous bank erodibility, are responsible for compound bend formation.

Seminara and Tubino [1992] reasoned "that strongly nonlinear effects may play a non-negligible role for fairly small values of channel curvature." The TSRM model is strongly nonlinear, and this nonlinearity plays an important role in meander evolution. In the results, I showed how bank shear stress may approach zero (see figure 4.9) in longer

150

bends. In such cases, the model's nonlinearity promotes planform instability due to relatively small variations in curvature. The bank shear stress dissipation scale determines the length over which such variations are smoothed out and bends remain stable. For bends longer than that stable length, small increases in curvature promote instability which in turn promote the formation of compound bends. The lateral momentum transfer's nonlinear dependence on changing curvature is both necessary and sufficient for compound bend formation.

The sensitivity analysis suggests, and I have observed, that compound bend formation is more likely when the downstream lag is small relative to the dissipation parameter, λ. The lag is smaller with smaller channel width (see equation (4.18)) and greater lateral flow velocity relative to the downstream velocity (see equation (4.9)). Greater lateral flow velocity is generally due to greater transverse bed slope, e.g., for small grain diameter. Greater downstream slope leads to an increase in transverse bed slope, a decrease in flow depth, and, therefore, a disproportionate increase in lateral flow velocity relative to downstream flow velocity ($V \sim S_f^{0.65}$, $U \sim S_f^{0.3}$) because lateral velocity increases with both transverse bed slope and the inverse of flow depth (see equation (4.9)), the latter decreasing with greater channel slope (see equation (4.1)). Therefore, the lag decreases with increasing slope ($L \sim S_f^{-0.35}$), and the lateral momentum transfer increases linearly with slope ($dF_n \sim S_f$).

4.4.3 Meander belt and floodplain evolution

It is apparent from the model results that the style or mechanism of bend evolution has a significant impact on the meander belt as a whole. Compound bend formation pro-

motes planform complexity, which is reflected in stream sinuosity. When bends cut off, a simpler, less sinuous channel pattern replaces the original. When bends divide, however, a more complex and sinuous channel pattern replaces the original.

This type of complexity enhances system memory, defined as the time over and extent to which current form reflects prior conditions, as discussed in Chapter 3. As shown in the Results, compound bend formation leads to puzzle piece channel planforms. These puzzle pieces enclose significant areas of the meander belt without encroaching on them. Such areas may contain remnants of the point bar of the original bend on which the puzzle piece is an elaboration. In this case, the lifetime of that point bar remnant is extended by the several bend lifetimes over which the original bend has divided and re-divided. This lifetime extension is one mechanism by which floodplain surface remnants may persist for times much greater than the time the channel takes to re-work most of the floodplain, as evident in the long tails of the CDFs of floodplain age shown in figure 4.13 and by the unvisited surface remnant visible in figure 4.7(c).

This result is consistent with field observations. T. Abbe [personal communication, 1996] has found trees whose age greatly exceeds the estimated, or expected, period between channel occupations on alluviated floodplains in the Queets River watershed on the Olympic Peninsula of Washington.

The relative importance to the planform of compound bend formation is apparent in the planform measures as secondary channel planform scale indicators. Both the natural channels from Chapter 3 and the TSRM model channels exhibit these secondary channel planform scale indicators, but the LFE model, which lacks compound bend formation,

also lacks secondary channel planform scale indicators, though the LFE and TSRM model channels have similar total sinuosity at the last times measured (see figures 4.15 and 4.17). Thus, not only does the new model reproduce a natural phenomenon not captured by previous models, but also the new statistical measures of channel planform distinguish between the presence and absence of that phenomenon in model and natural channels.

The model results have implications with respect to the meander belt width. Model bends develop such that their apices point more nearly upstream/up-valley as they grow longer, e.g., in the last frame of figure 4.6. This detail of bend development implies that, in the absence of net aggradation, which could cause the channel to avulse, the meander belt width may be self-limiting and, thus, narrower in the TSRM model than in, e.g., the LFE model, where bends are more laterally elongated. However, one implication of enhanced system memory from compound bend formation is that channels will continue to migrate in the direction of a prior bend. Such migration tends to increase the meander belt width (see figure 4.19). In aggrading systems, channel avulsions may also widen the meander belt.

The most surprising model result is the formation of scroll bar-like topography. Traditionally, scroll bars have been thought to result from alternating periods of slow levee formation and rapid bank erosion. Such a mechanism is consistent with the experimental observations of C.E. Smith [personal communication, 1998], who developed non-dune, unvegetated scroll bars under experimental, steady flow conditions. As shown in the present results, the TSRM model channels do not evolve at a steady rate, and the alternating periods of slower and faster migration are visible as bands of steeper and more gradual

slope, respectively, in figure 4.7(a), (c), and (e). Migration rate and deposit depth at a point are not correlated, but, given that the locus of bank erosion is distal from the point of lateral momentum transfer, this lack of correlation does not necessarily imply independence.

My observations and analyses of natural channels and point bars do not rule out the hypothesis that scroll bar topography is produced by a mechanism similar to that of the model scroll bars. Like the natural scroll bar topography, the model scroll bar topography is only quasi-periodic. Many of the model transects have a maximum peak at a wavelength that is close to a multiple of the average channel discretization, and I cannot rule out a grid effect as the mechanism responsible for the model scroll bar topography in some cases.

From the field investigation of scroll bar topography on the Ellis River in Chapter 3, I favor the hypothesis that scroll bar topography is related to episodic rapid channel migration due to the occurrence of upstream cutoffs. The TSRM model channel migration is characterized by episodic rapid channel migration. From figure 4.6 and an animation of the model, it is evident that the episodic migration in the TSRM model is due to the occurrence of cutoffs.

4.4.4 Other Model Verification Methods

Some authors (e.g., *Johannesson and Parker*, 1985; *Garcia, et al.*, 1994; *Howard and Knutson*, 1984) have evaluated the capability of models to predict observed channel evolution. Others (e.g., *Johannesson and Parker*, 1989a; *Nelson and Smith*, 1989a, b) have compared details of the flow and bed topography of models and nature. *Howard and Hemberger* [1991] developed a multivariate statistical channel planform analysis.

It is nearly impossible to use the model to predict specific, observed migration from an observed initial condition because the TSRM model is strongly nonlinear and sensitive to initial conditions. The stability of LFE models may allow them to better predict short-term channel migration. As noted previously, the TSRM model is not designed to predict details of flow and bed topography. I have, however, shown striking similarities between model and natural channel planform and evolution styles.

4.5 Conclusions

The TSRM model simulates meandering channel evolution and produces realistic channel patterns and floodplain topography, including scroll bars and sloughs. The model's successful simulation of meandering supports the topographic steering hypothesis, i.e., that bank shear stress arises mainly from forces associated with topographically induced convective accelerations. More generally, the bank shear stress' dependence on the downstream rate of channel curvature change is probably sufficient to produce meandering. The nonlinearity of that dependence is certainly sufficient and may be necessary for compound bend formation.

I have derived an expression for transverse bed slope of sand-bedded channels. The modification of *Ikeda*'s [1989] formula permits accuracy in sand-bedded channels because the modified version accounts for the effect of form drag associated with dunes.

Unlike most models of river meandering, the TSRM model is strongly nonlinear, as noted above. The simplified physics makes such nonlinearity approachable not only conceptually but also computationally. The model's computational efficiency allows observation of the long-term, complex, and often surprising model results in great detail over short valley domains, as in the incising meander simulations, and less detail over long

domains. The model formulation's conceptual "modularity" allows ready identification of modeled phenomena and their attribution to specific mechanisms.

The present approach apparently captures physics that other models do not. Unlike most meander models, the TSRM model forms compound bends and allows prediction of the sensitivity of compound bend formation frequency to model parameters that affect the transverse bed slope. Specifically, the model predicts that, all other parameters remaining constant, a decrease in bed material grain size increases not only the rate of channel migration but also the prevalence of compound bend formation. With greater migration rate, the rate at which the meander belt widens is, of course, greater. I have also shown that a meander belt with more compound bend formation is wider than one with less compound bend formation. Thus, a decrease in grain size has a disproportionate effect on the rate of valley widening. Another result of more compound bend formation is the increased likelihood that parts of the valley floor will remain untouched for longer periods of time. This result may have profound implications for archaeology in alluvial valleys. The model's sensitivity to grain size also suggests a mechanism for observed downstream changes in valley width on the Buffalo River. The valley is wider where the river crosses a cherty limestone unit that produces relatively small gravel bedload; the valley is narrower where the river crosses a massive sandstone unit that produces cobble-size bedload.

The model predicts a heretofore unrecognized mechanism behind the formation of scroll bar topography. As the model channel migrates, curvature and, thus, point bar height change. These changes are sudden and systematic in space and time such that, as a meander bend evolves, the varying point bar heights form ridges and swales, or scroll bars. I

have not verified this prediction, but neither do my studies of natural channels falsify it. The model results are consistent with another scroll bar formation theory based on the episodic nature of channel migration. TSRM model channel migration rate fluctuates, visible in the "incising" meanders (see figure 4.7) as banded areas of alternating gradual and steep slope reflecting fast and slow migration, respectively. These bands are consistent with the Ellis River measurements indicating that alternating periods of fast and slow lateral point bar accretion correspond to fast and slow vertical point bar accretion, respectively. Also, given a constant rate of levee deposition, this bandedness would be expressed as ridge and swale topography.

The new quantitative channel planform analytical methods can detect that the natural and TSRM model channels form compound bends and the LFE model channels do not. These measures also detect variations in the prevalence of multi-bend loops in the evolving planform over time. Such time variations could be responsible for the lack of secondary channel planform scale indicators for channels which do have many visible compound bends.

The TSRM model is incorporated in a new channel-hillslope integrated landscape development (CHILD) model in Chapter 5. The TSRM model is efficient enough to keep the larger computational burden of the coupled models well within the range of feasibility.

Chapter 5

The Channel-Hillslope Integrated Landscape Development Model

In this chapter, I present the channel-hillslope integrated landscape development (CHILD) model. The model integrates the TSRM model from Chapter 4 and a landscape evolution model including hillslope and channel sediment transport. The integrated model is the result of a team effort including Nicole Gasparini, Gregory Tucker, and Rafael Bras. We have developed the model so that it may be used for a wide variety of applications, including distributed hydrologic and plate tectonic modeling.

5.1 Introduction

The model simulates landscape evolution, but its components are flexible enough to serve a number of ends. The CHILD model is written in the C++ computer language, and we have attempted to take advantage of its features, including data hiding, the use of template and inherited classes, and a fully object-oriented design. We sought a new approach to enable modeling of the interaction of a variety of processes. In this chapter I show the development of the model to examine, among other things, the interactions between a laterally migrating channel and the surrounding landscape. The CHILD model was designed, in a group effort, to address a wider range of issues than I can address in the present work, and I will describe some of those wider capabilities even though their application is beyond the present scope.

5.1.1 Channel-Hillslope Interaction

I reviewed some approaches to modeling the coupled system of channels and hillslopes in the landscape in Chapter 2. Such approaches are, however, limited to channels that do not migrate laterally. In Chapter 3, I showed that lateral channel migration affects topographic slopes outside of the main channel. Also in Chapter 3, I discussed the ways that lithologic properties might control lateral channel migration and, in Chapter 4, showed the effect of different bedload grain sizes and controls on channel width and discussed the effects of varying slope and other factors. In Chapter 3 I discussed the possible effects of the interactions between the channel and the surrounding landscape on channel transport regimes and slope.

The CHILD model was designed to model all of the above effects, but a full treatment of all of them is beyond the scope of this chapter. Here, I have focussed on the interactions among uplift, bank (or bluff) height, and lateral channel migration because even these relatively simple interactions have not been addressed in previous studies and must be addressed before more complicated cases. As reviewed in Chapter 2, *Howard* [1992] discussed the constraints on bank erodibility and modeled the effect of confining valley walls by super-imposing the meandering model channel and a grid with two possible values of bank erodibility, one "floodplain" value for pixels previously visited by the channel and another, higher "valley wall" value for unvisited pixels. In the long term, however, the interaction of the migrating stream and the valley walls will depend on both the uplift rate and the bank erodibility's bank height dependence. The latter, as discussed by *Howard* [1992], is a complicated problem in itself, and the present model includes only a simple parameterization of bank erodibility's bank height dependence. This parameterization

should be sufficient to test the hypothesis that meandering is more active during periods of quiescent uplift. More specifically, I will test this hypothesis for the case of meandering stream incision in a detachment-limited system. In Chapter 4 I showed that the channel slope and the shear force increment have an approximately linear relationship. This result indicates that, if larger channel slopes result from greater uplift, then the latter may actually increase the lateral migration rate if the effect is not cancelled out or reversed by the effect of uplift on bank height.

Also, the valley form should be affected by compound bend formation. The valleys simulated by *Howard* [1992] were, relatively, straight and of constant width. In Chapters 3 and 4 that greater frequency of compound bend and multi-bend loop formation led to channels with a large secondary sinuosity. In an incising system multi-bend loop formation might lead to a sinuous valley formation because, as discussed in Chapter 3, multi-bend loop formation tends to leave some parts of the floodplain for longer times between visits by the migrating channel. If the stream is incising, then these less frequently visited points would be uplifted for a longer time between channel visits. If the bank erodibility is dependent on bank height, then these uplifted areas would tend to resist lateral channel migration and reinforce the tendency for the channel to form sinuous valleys. Depending on the exact form those valleys took, the multi-bend loop formation might even cause such streams to appear to be underfit, i.e., appear to have valley bends that were formed in the past when flows were greater and the channel was larger. In Chapter 4 I showed that the channel slope and the downstream lag between shear force increment generation and bank shear stress are inversely, though weakly, related ($L \sim S_f^{-0.35}$, where L is downstream lag

and S_f is channel slope). That smaller downstream lag leads to greater frequency of compound bend and multi-bend loop formation. The model experiments in this chapter should allow examination of the role of compound bend and multi-bend loop formation in incising river valley formation.

5.1.2 Model Requirements

Most previous landscape evolution models have mapped elevations—and other properties—on a rectangular grid (e.g., *Ahnert*, 1976; *Kirkby*, 1986; *Willgoose, et al.*, 1989; *Chase*, 1992; *Howard*, 1994; *Tucker and Slingerland*, 1994; *Moglen and Bras*, 1995; *Tucker and Bras*, 1998). Such a grid is similar to that used in DEMs, sufficient to represent the modeled processes, and convenient for programming. We were, therefore, reluctant to abandon this format. However, in order to incorporate the TSRM model, the new model needed the capability to represent: (a) channel point locations with real-number coordinates; (b) lateral channel migration; and (c) different landscape processes at their appropriate, often different scales. Superimposing the meandering model on a rectangular grid, as in Chapter 4, was a possible approach. *Howard* [1996] used a grid of erodibilities to represent meandering in a confining valley and with resistant clay plugs, and the latter situation was modeled by *Sun, et al.* [1996] using a similar but more finely discretized grid. The latter grid is much too finely discretized to be practical for modeling an entire landscape and would not be suitable for simultaneously modeling channels of widely varying size because the necessary discretization is dependent on the size of the channel. *Howard*'s [1992] coarser grid discretization was also dependent on channel size and would, therefore, be similarly problematic.

In order to represent channel point locations, it was necessary to model the landscape on an irregular mesh. *Braun and Sambridge* [1997] developed a landscape evolution model using a Delaunay triangulated irregular network (TIN) of points. The Delaunay triangulation is the unique set of triangles that connect a given set of points such that a circle passing through the three points of any triangle contains no other points. Though the *Braun and Sambridge* [1997] model has the capability of adding and moving points in the landscape, their model was not sufficient for the CHILD model. Their model typically adds points to resolve steep slopes, and their rules for movement of points were designed to model the tectonic motion of crustal plates, where moving landscape "nodes" will tend to deflect one another. The CHILD model needed to represent channel migration such that nodes are deleted from the eroding bank and added to the accreting point bar.

We were also concerned that the model's useful lifetime should not end with the completion of the current project. Therefore, we designed the model as a set of objects, or classes—in C++ an object is the set of data and functions which define a particular thing, e.g., a "window" exists to the computer as a something with properties, like height and width, and functionality, like opening and closing. Some of the objects written for the CHILD model are general enough to be used in any application which uses a network of points in two-dimensional space, e.g., distributed hydrologic or plate tectonic modeling. This object-oriented approach enables the CHILD model to function as a modeling tool box in which the individual objects are the tools which may be used as needed by the individual user.

In this chapter I present the CHILD model development and capabilities and the model objects, or algorithms and data structures, as logical outcomes of the model's conceptual parts. I then describe a set of simulations to address uplift-bank-meandering interactions. These simulations specifically address the landscape-scale importance of bank erodibility's bank height dependence at the channel scale and compound bend/multi-bend loop formation at the bend scale. Beyond the visible morphologic features, the relationships between topographic slope and contributing area for the simulated landscapes enable comparisons to the Schoharie Creek valley studied in Chapter 3.

5.2 Model Conceptualization

The CHILD model design allows simulation of any combination of a large number of geomorphic and hydrologic processes, mechanisms, and influences, including:

1. stochastic rainfall;
2. runoff generation;
3. flow routing;
4. fluvial erosion and deposition (vertical);
5. transport and stratigraphic representation of multiple sediment clasts;
6. lateral channel migration, or meandering;
7. floodplain deposition;
8. diffusive and other hillslope transport processes;
9. weathering/soil development;
10. vegetation; and
11. uplift.
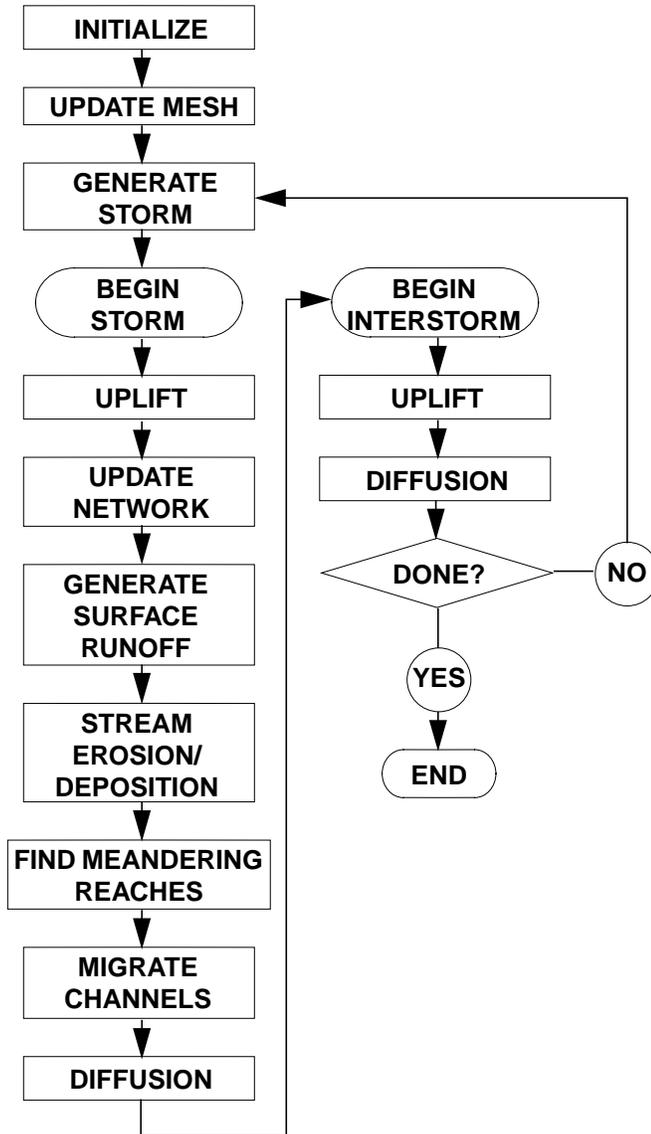
Figure 5.1: Flow chart showing the implementation of the basic processes in the CHILD model. In the chart, "diffusion" might include other hillslope processes.

Implementation of the more basic processes is shown as a flow chart in figure 5.1; this chart leaves out some of the processes enumerated above.

5.2.1 The Grid

The grid is the basic infrastructure of the model. In the CHILD model, what I call a grid is actually a triangulated irregular network (TIN) of points, or nodes, at which model

processes are calculated. The nodes are connected by edges which define the connectivity

of and distances between points on the grid for finite difference calculations (see

figure 5.2). With a standard rectangular grid, the distances are uniform, and finite differ-

ences are calculated for a standard set of neighbors, e.g., the eight neighbors of a grid cell.

With a TIN, the nodes are, in general, irregularly spaced and located, and the edges are, in

general, unique. The connectivity of the irregular mesh is non-trivial and is only known

after finding the Delaunay triangulation. With a rectangular grid, the area associated with

each node is rectangular, and its determination is, again, trivial. With the TIN, the area

associated with each node is defined by the mesh's Voronoi diagram, the inverse of the

Delaunay triangulation (see figure 5.2). Hereafter, I will often refer to the TIN as the grid.
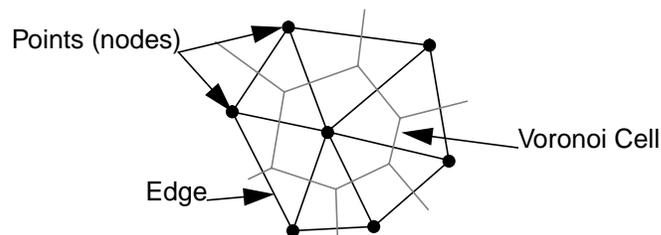
Figure 5.2: Schematic illustration of model grid components.

A Voronoi diagram defines the Voronoi areas, or nearest neighborhoods, of each

node in the grid. The Voronoi area of a node is the locus of points in two-dimensional

space which are closest to that node. For a set of rain gauges, the Voronoi diagram is the

same as the Thiessen diagram [*Bras*, 1990]. The Voronoi area of a node is the intersection

of the half-spaces defined by the perpendicular bisectors of the spoke edges. This area is a

polygon whose sides are connected by the vertices at the intersections of those bisectors

or, equivalently, the circumcenters of the triangles defined by the node and its neighbors.

The Voronoi diagram is the inverse of the Delaunay triangulation.

5.2.2 Hydrology

Hydrology in the model includes storm and runoff generation and flow routing. As in most landscape evolution models, the CHILD model may use uniform rainfall and run-off generation. But, unlike most other models (a recent exception is *Tucker and Bras*, 1998), the CHILD model has the capability of using more complex hydrology.

The model has the capability of generating storms stochastically according to the *Eagleson* [1978] model. In this model, rainfall intensity, storm duration, and time between storms are all exponentially distributed random variables.

For uniform runoff generation, runoff is simply the difference between the rainfall and infiltration rates. Discharge at a point is calculated by multiplying the point's drainage area, or the area for which that point is the outlet for flow, by the runoff rate. The model may also generate saturation overland flow, also known as partial-area runoff to distinguish it from uniform runoff (*Beven and Kirkby*, 1979; *O'Loughlin*, 1986). In this model, accumulated flow at a point is compared to the capacity of the soil layer to transmit that flow. If the accumulated flow exceeds that capacity, then the excess flow contributes to surface runoff or discharge:

$$Q = \begin{pmatrix} PA - Tb_v S, \, PA > Tb_v S \\ 0, \, PA \leq Tb_v S \end{pmatrix} \tag{5.1}$$

where P is precipitation rate; A is area contributing to flow; T is transmissivity; and b_v is the length of the Voronoi cell edge associated with the flow edge. This method allows spatio-temporal variations in soil layer material properties and depths to be reflected in runoff generation through the transmissivity, the product of hydraulic conductivity and depth.

5.2.3 Vertical Erosion and Deposition

The model is designed for both erosion and deposition of multiple sediment clasts, although the capability for handling multiple grain sizes is still under development by another group member at this writing. In general, the time rate of change of elevations is described by the sum of uplift and the sediment flux divergence:

$$\frac{\partial z}{\partial t} \; = \; U + \nabla q_s \tag{5.2}$$

where U is uplift with dimensions of L/T (T is time, L is length); and q_s is unit sediment flux with dimensions of L^2/T. The model uses a combination of detachment-limited erosion and capacity-limited transport similar to that of *Howard* [1994], *Tucker and Slingerland* [1994, 1996, 1997], and *Lancaster and Bras* [1995]. I prefer the term "capacity-limited" to the more traditional term "transport-limited" because the former is more precise in denoting the limitation on the sediment carrying capacity of the transporting medium.

Many models treat all materials as cohesionless and model erosion and deposition as the result of capacity-limited sediment transport, often as bedload. Such an approach has two major problems. First, in general, all materials present some resistance to erosion, whether due to cementation, cohesion, vegetation, or some other mechanism. Second, the treatment of all material as bedload ignores that, in many situations, bedload is a minor component of the total volume excavated by erosion, and suspended load is the major component. A significant portion of the load may also be material in solution.

In this study, the model simulates only detachment-limited erosion of a homogeneous substrate, i.e., everything that is eroded, or detached, is carried out of the system by flow with enough capacity to carry anything that is detached. The following equation for the time rate of elevation change represents these processes:

$$\frac{\partial z}{\partial t} = -K_B Q^m S^n + K_D \nabla^2 z + U, \, K_D \nabla^2 z \leq 0 \tag{5.3}$$

where K_B is the erodibility coefficient with dimensions of T^{m-1}/L^{3m-1}; Q is water volume discharge with dimensions of L^3/T; S is the greatest downward-positive slope of the spoke edges and is dimensionless; K_D is the diffusion constant with dimensions of L^2/T; and z is elevation. The model described by equation (5.3) is essentially identical to that of *Moglen and Bras* [1994, 1995] except that the latter had spatially heterogeneous erodibility and diffusion coefficients. The first term on the right-hand side of equation (5.3) describes erosion by running water both on hillslopes and in channels. The second term describes diffusive hillslope processes such as transport by tree throw, burrowing animals [*Black and Montgomery*, 1991], frost heave, and soil creep. This diffusion is detachment-limited in the sense that, in equation (5.3), it is assumed that any diffusive infilling, e.g., of valleys and channels, is carried away by advective processes such that positive changes in elevation by diffusion are disallowed [*Moglen and Bras*, 1994]. The third term describes the input of material at a point by uplift, assumed positive and constant. The detachment-limited model is well suited to modeling stream incision into bedrock in a landscape undergoing active uplift, which enables the stream to reach whatever slope is necessary to erode the material input by that uplift. *Howard* [1994] noted that a detachment-limited model is most appropriate to clayey badlands topography.

5.2.4 Meandering

The CHILD model uses an irregular, dynamic grid in order to incorporate lateral channel migration. Otherwise, the model could employ a regular, static grid. To adequately represent meandering, nodes must be removed from the eroding channel bank, moved with the migrating channel, and added to the accreting point bar.

Moving nodes is complicated because of the complicated connectivity of nodes in the grid and the nature of the thing being moved. Our model may be a successor to the *Braun and Sambridge* [1994, 1997] (BS) model, but the latter dealt only with relatively simple point movement issues. In the BS model, a moving node represented a part of the earth's crust in tectonic motion, and, when that node approached another, the two repelled one another as in a strike-slip fault. In the CHILD model the movement of a node does not represent movement of the land itself but, rather, the location of the channel moving over that land, eroding its banks, and leaving behind a point bar. Recording stratigraphy is not necessary n the detachment-limited version of the CHILD model. More complicated model cases, however, will require that, when a channel moves, the channel node acquires the subsurface characteristics of the location to which it is moving and leaves behind nodes with the subsurface characteristics of the location it is leaving.

Removing nodes where the channel is eroding the bank is complicated by consideration of not only the moving nodes but also the moving channels, i.e., the edges between channel nodes. A bank node's proximity to moving nodes, as in *Braun and Sambridge* [1994], is not a sufficient criterion for removal. Rather, proximity to the channel, i.e., the channel nodes and the edge between them, is the proper criterion because, otherwise, the

bank node could slip between migrating channel nodes and escape removal as if a piece of the bank were to escape erosion as the channel passed. Other issues, such as the preservation of the channel edge and Delaunay-ness when it is close to a bank node, have also become apparent in the process of model development, and, in general, the model must be designed to deal with all potential, even unlikely, scenarios.

The addition of nodes presents its own suite of issues in terms of not only the addition of a node to the grid but also the characteristics of the added node and the time and place of addition. The BS model added nodes to increase the resolution of steep slopes, but adding those nodes was not strictly necessary. The CHILD model, on the other hand, must add nodes to represent the channel at the fine discretization required by the TSRM model and not leave gaps in the mesh as the channel migrates.

Only grid nodes with discharge greater than a critical value are subject to the meandering process. Granted, meandering may be active over a broad range of scales including some excluded by the discharge threshold criterion. Practically, however, models cannot resolve every process to the smallest level and must, therefore, employ some size cutoff criterion.

The TSRM model is described in detail in Chapter 4. Here, I address only the issue specific to the incorporation of the TSRM model into the CHILD model, the issue of bank erodibility. As explained in Chapter 4, a TSRM model channel point's migration is proportional to the shear stress on the bank and the bank's erodibility (see equation (4.20)), but the absence of a surrounding landscape precluded further examination of the role of bank erodibility because the landscape's characteristics determine the bank's erodibility.

Bank erodibility is dependent on bank material properties and, possibly, bank height. In the most simple case, all banks have similar material properties, bank erosion is purely detachment-limited, and all undermined bank material is also detached by that undermining (see *Howard*, 1992, section 2.2, and figure 5.3(a)). In this case, channel migration rate is simply proportional to bank shear stress because bank erodibility is independent of bank height.
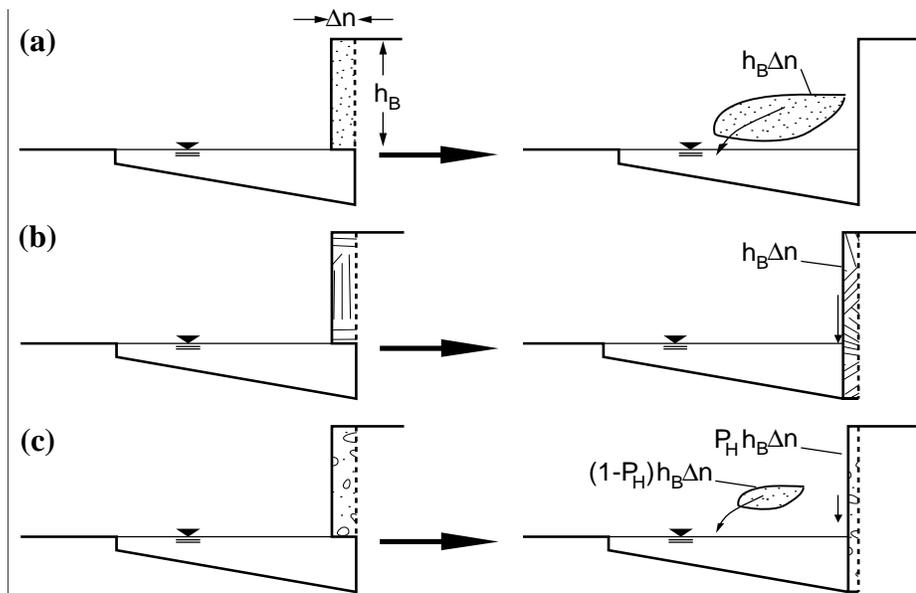
Figure 5.3: Conceptual drawing of spectrum of bank erodibility's dependence on bank height. (a) Bank erodibility is independent of bank height. (b) Bank erodibility is fully dependent on bank height. (c) Bank erodibility is partially dependent on bank height.

On the other end of the spectrum, none of the undermined material is detached (see figure 5.3(b)). The volume rate of material excavated per unit distance downstream is

$$\eta = E_0 \tau_w H \tag{5.4}$$

where E_0 is the nominal bank material erodibility; τ_w is the bank shear stress; and H is the average channel depth. If h_B is the height of the bank above water level, then the bank migration rate is

$$\zeta = \frac{\eta}{H + h_B},$$ (5.5)

and the bank height-dependent erodibility is

$$E_B = \left(\frac{H}{H + h_B}\right) E_0, \, h_B > 0$$ (5.6)

$$= E_0, \, h_B \leq 0$$

where enforcing a minimum erodibility of the nominal value ensures that E_B does not become arbitrarily large.

The situation in most natural systems where seepage-induced failure is not an important mechanism is probably somewhere between these two extremes, as illustrated in figure 5.3(c) where part of the undermined material is detached. The size of that part is determined in the model by a parameter, P_H, such that the effective bank erodibility is a weighted average of the two extreme cases:

$$E_{eff} = P_H E_B + (1 - P_H) E_0, \, 0 \leq P_H \leq 1$$ (5.7)

where P_H is the fraction of bank material that does not behave as detachment-limited. Substituting with equation (5.6), equation (5.7) reduces to

$$E_{eff} = E_0\left(1 - \frac{P_H h_B}{H + h_B}\right), \, h_B > 0$$ (5.8)

$$= E_0, \, h_B \leq 0.$$

Finally, the nominal bank and bed erodibilities may not be the same even for identical materials. Even in a detachment-limited system, bedload may often shield the bed from erosion. The bank, on the other hand, is never shielded. Therefore, the bank's effec-

tive erodibility will be larger. To address this issue I have introduced a parameter, f_{lat}, that

is the ratio of the bank and bed erodibilities. This parameter allows control of the relative

strengths of lateral erosion and vertical incision.

5.3 Model Implementation

In this section I describe the data structures and algorithms used to implement the con-

cepts of the previous section. Except where noted, that implementation is new and origi-

nal.

5.3.1 The Grid Object

The model grid exists as both a conceptual geometric entity and a C++ object. The

object consists of three linked lists of nodes, edges, and triangles, respectively, and a set of

functions used to construct, change, and determine the properties of the grid. The nodes

are the basic landscape units and contain data pertaining to location coordinates, Voronoi

area, geomorphic characteristics, and connectivity. The major issue addressed by the grid's

data structure is the connectivity of its parts.

The first basic issue is the connectivity of a particular node to other nodes on the

grid. This connectivity is stored as a linked list of edges which are dual and directed; i.e.,

for each line segment connecting two nodes there are two edges, one pointing from the

first node to the second, the other pointing from the second to the first (see figure 5.4).

This dual edge data structure is derived from the QuadEdge data structure of *Guibas and

Stolfi* [1985]. Each node is explicitly associated with a set of edges that originate at that

node and connect it to its neighbors.

174

(a)

C
B
b
A
a
D
Voronoi Cell

A.edge = AB
AB.ccwedge = AC
AB.vvertex = a

(b)

C
B
b
A
a
D

B.edge = BA
BA.ccwedge = BD
BA.vvertex = b
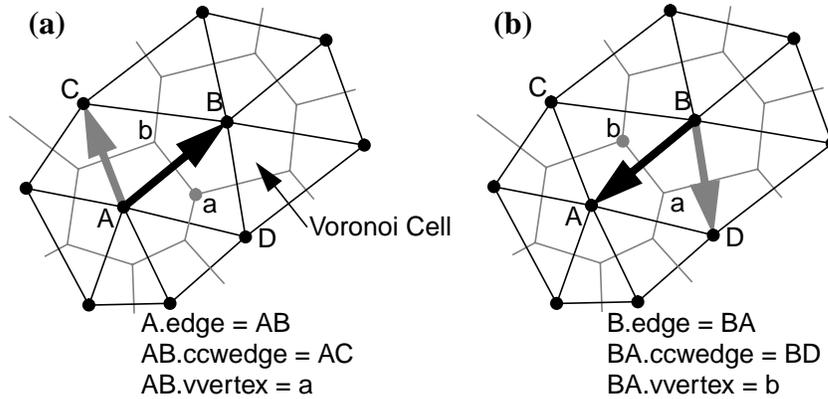
Figure 5.4: Illustration of the dual edge data structure, showing triangular lattice (black) and corresponding Voronoi diagram (gray). (a) Directed edge **AB**, its right-hand Voronoi vertex **a**, next counterclockwise edge **AC**, and its right-hand Voronoi vertex **b**. (b) Complementary directed edge **BA**, its right-hand Voronoi vertex **b**, next counterclockwise edge **BD**, and its right-hand Voronoi vertex **a**.

In order to accommodate different programming styles, this connectivity is accomplished in two ways. First, each node contains as a data member a spoke list, a linked list of pointers to the edges originating at the node in counter-clockwise order. The spoke list takes advantage of the generic linked pointer list class' functionality for navigation, manipulation, and data protection. Second, each node contains the first edge pointer of the spoke list, and each edge contains a pointer to the next counter-clockwise edge. This structure uses less memory but does not have the built in functionality of the generic linked pointer list. A regular grid would not require explicit inclusion of edges in the data structure because the connectivity is trivial.

As explained in the previous section, the vertices of the Voronoi diagram are defined by the circumcenters of the triangles. In the data structure, each directed edge holds the coordinates of the Voronoi vertex on its right-hand side (see figure 5.4). As the spoke edges around a node are accessed in counter-clockwise order, the Voronoi edge

crossing that spoke edge is defined by the right-hand vertex coordinates held by that spoke and the next. The Voronoi vertices' positions are calculated in the context of the triangles. For each triangle, the circumcenter is found and assigned to each of the clockwise edges of the triangle (see figure 5.5). As mentioned in the previous section, these circumcenters are the vertices of the Voronoi diagram.
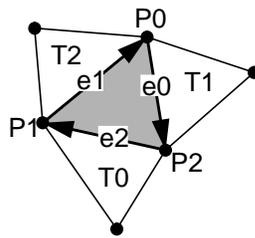
Figure 5.5: Illustration of triangle data structure, including numbering of nodes, adjacent triangles, and clockwise edges. Nodes and edges are listed in counter-clockwise order; triangles are listed in clockwise order and correspond to node at opposite vertex.

The triangle data structure is also used to locate on the grid an arbitrary point in space. In order to add a node at a particular location, an algorithm finds the nodes to which the new node will be connected. The CHILD model employs a directed search algorithm, shown in figures 5.6 and 5.7, similar to that of *Braun and Sambridge* [1997]. For each triangle checked, the algorithm loops through its edges and finds whether the point lies on the right- or left-hand side of each edge. If the point lies on the left-hand side of the edge, the algorithm proceeds to check the neighbor triangle on the other side of that edge; e.g., in figure 5.5, if the algorithm checks edge **e0** and finds that the point is on its left side, the algorithm will next search the neighbor triangle **T1**.
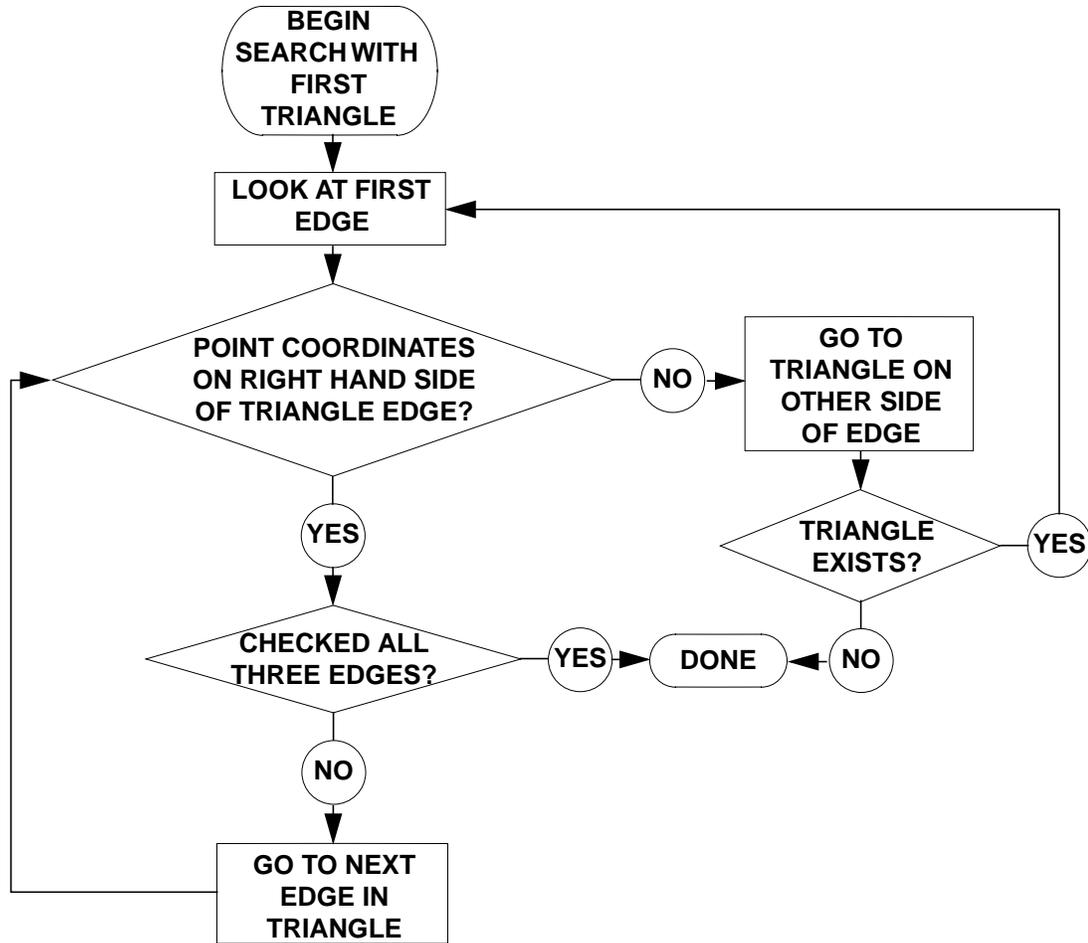
Figure 5.6: Flow chart of the directed search algorithm, which returns either a pointer to a triangle or a null value. The latter indicates that the point lies outside the grid.
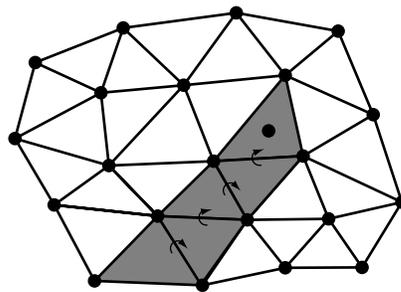
Figure 5.7: Illustration of the sequence of triangles checked by the directed search algorithm.

Whenever a node is moved, added, or removed, the triangulation must be checked and, if necessary, corrected. The Delaunay triangulation of the mesh is maintained by

exploiting the fact that, by definition, if each triangle is locally Delaunay, i.e., Delaunay with respect to its neighbor triangles, then the mesh is globally Delaunay by the definition stated in the Introduction. A triangle's Delaunay-ness is ensured by checking whether any of the edges between the triangle and its neighbors need to be flipped to satisfy the Delaunay condition (see figure 5.8). The criterion for flipping is from *Du* [1996] and is illustrated in figure 5.8.
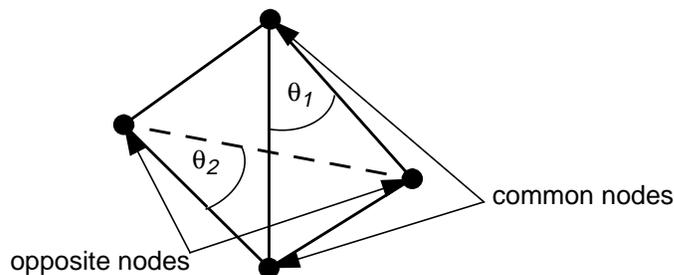
Figure 5.8: Illustration of flip-checking between two triangles. The edge between the common nodes is flipped to connect the opposite nodes if $\theta_2 > \theta_1$ [*Du*, 1996]. This criterion is equivalent to checking whether the node associated with θ_2 in the left-hand triangle falls within the circle defined by the nodes of the right-hand triangle.

The flip-checking algorithm is similar to that used by *Braun and Sambridge* [1994], but our implementation of the algorithm is new. In this algorithm (see figure 5.9), triangles to check, e.g., the new triangles created by the addition of a node or triangles containing moving nodes, are added to a temporary list. Each triangle is removed from the front of the temporary list and checked for local Delaunay-ness (flip-checked) against each of its neighbors. If this check results in an edge-flip, the two triangles on either side of the edge and the edge pair are deleted from the main list, two new triangles and an edge pair connecting the formerly opposite nodes are added to the main list, and the two new triangles are added to the end of the temporary list. The procedure repeats until no triangles remain on the temporary list. This procedure guarantees local and, by definition, glo-

bal Delaunay-ness, and using a list eliminates the need for recursion or repeated scans of

the triangle list, as in *Braun and Sambridge* [1994].
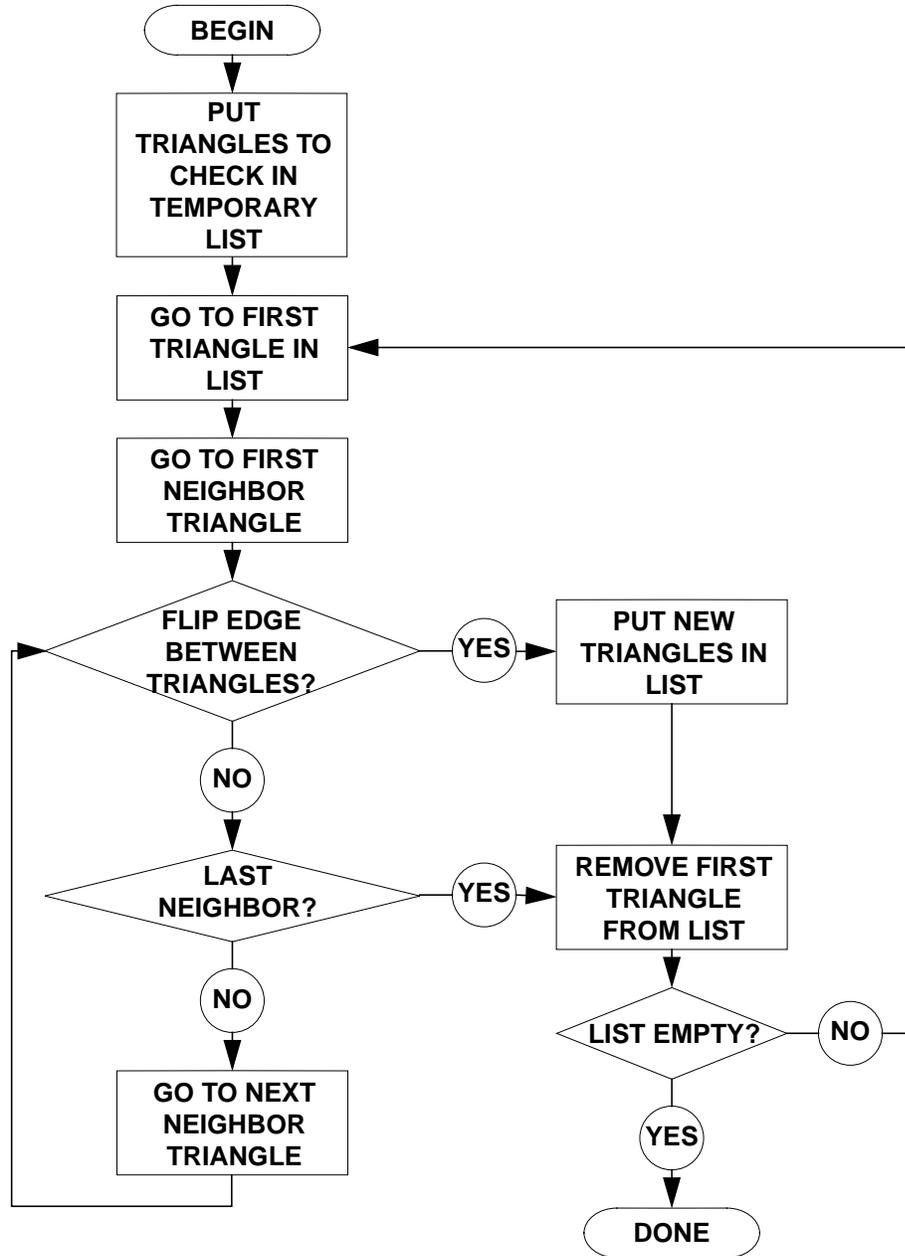
Figure 5.9: Flow chart showing the iterative flip-checking algorithm.

Both the directed search and flip-checking algorithms are used when a node is

added to the grid. When adding a node, the triangle in which it falls is located with the

directed search algorithm. That triangle is deleted, and three new triangles and edge pairs are added connecting the new node to the three vertices of the old triangle (see figure 5.10(a)). Then, the new triangles are given to the flip-checking algorithm.
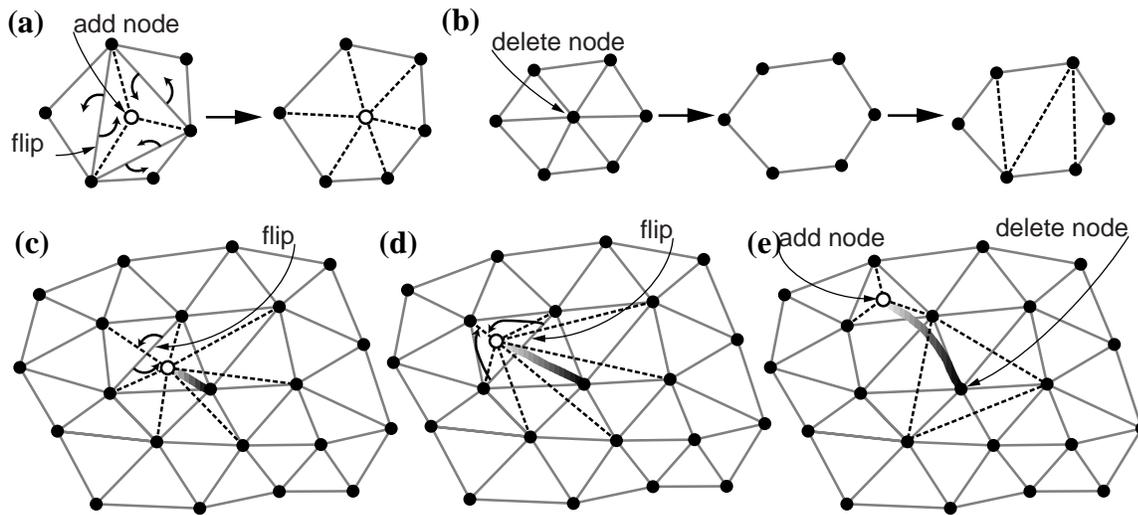
Figure 5.10: Illustrations of (a) point addition and edge flipping; (b) point deletion; (c) point movement within local polygon; (d) point movement to neighboring triangle; and (e) point movement outside of local neighborhood. The small arrows on either side of an edge indicate the edge is to be flipped in the direction indicated by the arrows.

Node deletion is conceptually simple and uses some of the same basic routines as node addition. The node to be removed and all of the edges connecting it to its neighbors are deleted, and the resulting hole in the mesh is filled with new Delaunay triangles (see figure 5.10(b)) that are, in turn, given to the flip-checking routine. However, implicit in both addition and deletion of nodes is not only the addition and deletion of edges and triangles but also the adjustment of the various relationships among data members (see figures 5.4 and 5.5). These relationships are the key to the functionality of the model. When a node is deleted, edges and triangles must also be deleted in order to extricate the node from the grid data structure. The procedure is shown as a flow chart in figure 5.11. This procedure may be entered at any of the "begin" points, and the extrication and deletion

routines below that point in the flow chart are called from the higher routine to ensure the integrity of the data structure. Thus, a node cannot be deleted without also deleting the associated edges, and the edges may not be deleted without also deleting the associated triangles.

Node movement may result in three possible scenarios, shown in figure 5.10(c), (d), and (e) in order of increasing computational cost. In the first, the node moves within the polygon defined by the node's neighbors, and the flip-checking algorithm is sufficient to maintain the mesh. In the second, the node leaves that polygon but falls within one of the triangles neighboring the polygon, and the side between the polygon and the neighboring triangle is flipped before the mesh is flip-checked. In the third case, the node leaves the polygon and does not fall within one of the neighbor triangles, and the node is deleted and added again in its new location before flip-checking the mesh. *Braun and Sambridge* [1994] considered only the first scenario.

Any time the mesh is changed, whether by addition, deletion, or movement, the basic characteristics of the mesh must be updated (see figure 5.1). This procedure, illustrated in figure 5.12, corrects each node's neighborhood properties, i.e., the distance to the node's neighbors and its Voronoi area.
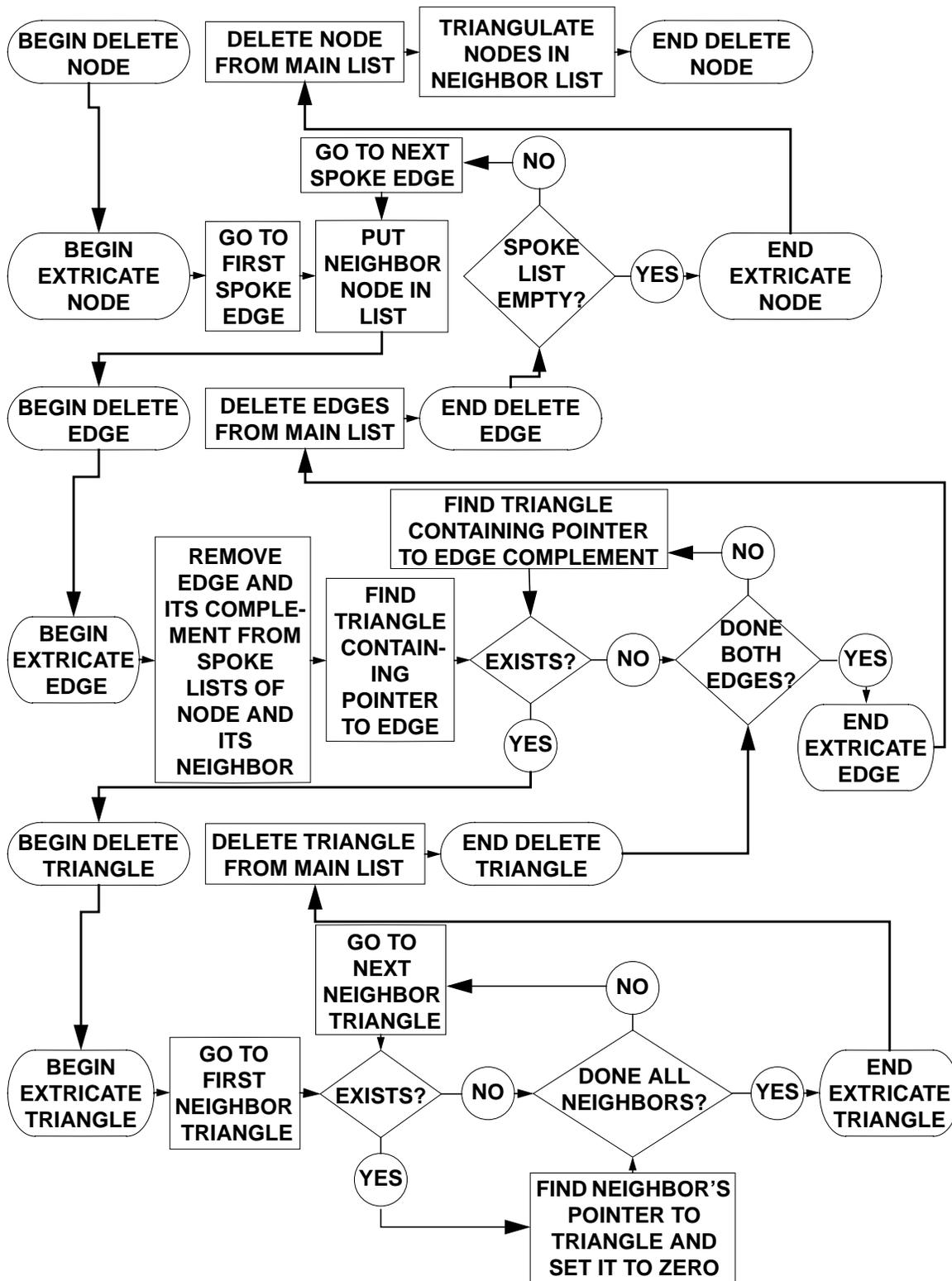
Figure 5.11: Flow chart illustrating the node deletion procedure.
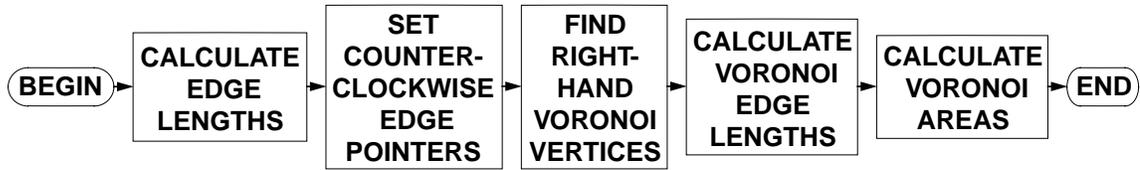
Figure 5.12: Flow chart illustrating the mesh updating procedure.

5.3.2 The Storm and Stream Network Objects

The storm object generates storms as defined by precipitation intensity and duration and interstorm duration, or the time until the next storm. These quantities can be either constant or stochastically generated. In the stochastic option, all three quantities are exponentially distributed [*Eagleson*, 1978], though the object could be modified to accommodate any probability distribution. The storm object could also be modified to read storm information from data.

The storm information is used to define the stream network properties. The stream network in the model is an object consisting mainly of functions for runoff generation and flow routing but also pointers to the grid and storm objects and runoff parameters, such as the transmissivity for equation (5.1). The functions are generally called together to update the network after the grid has changed. This updating procedure is shown as a flow chart in figure 5.13.
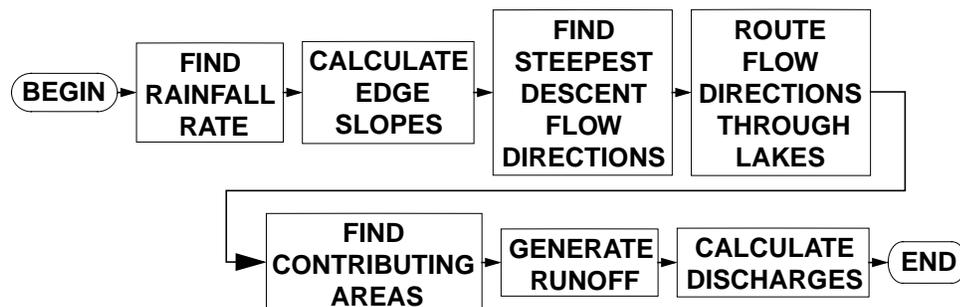
Figure 5.13: Flow chart showing the stream network updating procedure.

The surface discharge at each node is computed as a function of the upstream contributing area and the runoff at each of those contributing nodes. Each node is assigned a drainage direction along the steepest downhill slope (edge) toward one of its neighboring nodes. The area contributing flow to a node is the sum of the Voronoi areas of all nodes whose paths to the outlet pass through that node and the Voronoi area of the node itself.

In some cases a node may form a local depression, with no neighbors lower than itself. This case can be handled in one of two ways in the model. The simplest method assumes that all water entering a "sink" evaporates at that point and forms a discontinuity in the network, i.e., not all nodes contribute flow to an outlet. Alternatively, an outlet can be found for each sink using the "lake filling" algorithm. The lake filling algorithm starts by creating a list of contiguous flooded nodes that initially contains just the sink itself. The perimeter of the flooded region ("lake") is then iteratively searched to identify the lowest node along the perimeter. If this node can drain downhill to a location other than the lake itself, it is flagged as the outlet point for all nodes in the list. If not, it is added to the list. If a node is encountered that is part of a pre-existing lake (one initiated at a different sink), it is also added to the list. Finally, flow directions are arbitrarily assigned to the lake nodes such that each node in the grid "drains" to one of its neighbors. Except for this final step, the lake filling algorithm is essentially identical to that employed in the model of *Tucker and Slingerland* [1994]. The algorithm is robust enough to handle any arbitrary initial condition and is useful for modeling a rising base level or the damming of water and sediment behind an uplifting block.

For a mesh with numerous sinks, the lake filling algorithm is probably slower than the "cascade" algorithm of *Braun and Sambridge* [1997]. However, in the more typical case of a few isolated sinks, the lake filling algorithm is probably faster than the cascade algorithm. The number of iterations needed by the lake filling algorithm depends on the number of flooded points, whereas the cascade algorithm requires a number of iterations equal to the maximum number of segments along any continuous stream regardless of the number or depth of sinks. Typically, the lake filling algorithm is employed to route flow past a low or high point along the main channel, where these anomalies usually arise from numerical instability.

The simulations shown later in this chapter use only a subset of the model's hydrologic capabilities: uniform, steady rainfall; uniform runoff production; and lake filling.

5.3.3 The Sediment Transport and Uplift Objects

These objects together calculate the finite-difference solution to equation (5.3) for "vertically acting" processes: stream erosion, hillslope diffusion, and uplift. In this study I use detachment-limited erosion, but the sediment transport object also contains options for capacity-limited erosion/deposition and the combined detachment- and capacity-limited transport described in the previous section.

The advective erosion term, the first term on the right-hand side of equation (5.3), contains a channel slope dependence, but this erosion term applies to the landscape scale, i.e., over channel reaches long enough that water surface slope is adequately represented by topographic slope. This approximation is reasonable over a distance of many channel widths but, of course, breaks down over smaller distances approaching a single channel

width. But, some channels will be discretized at approximately one channel width to satisfy the TSRM model's requirements. This scale discrepancy is resolved by averaging the slope for finely discretized channels over a distance of ten channel widths (flow directions are still determined by slopes to nearest neighbors).

5.3.4 The Stream Meandering Object
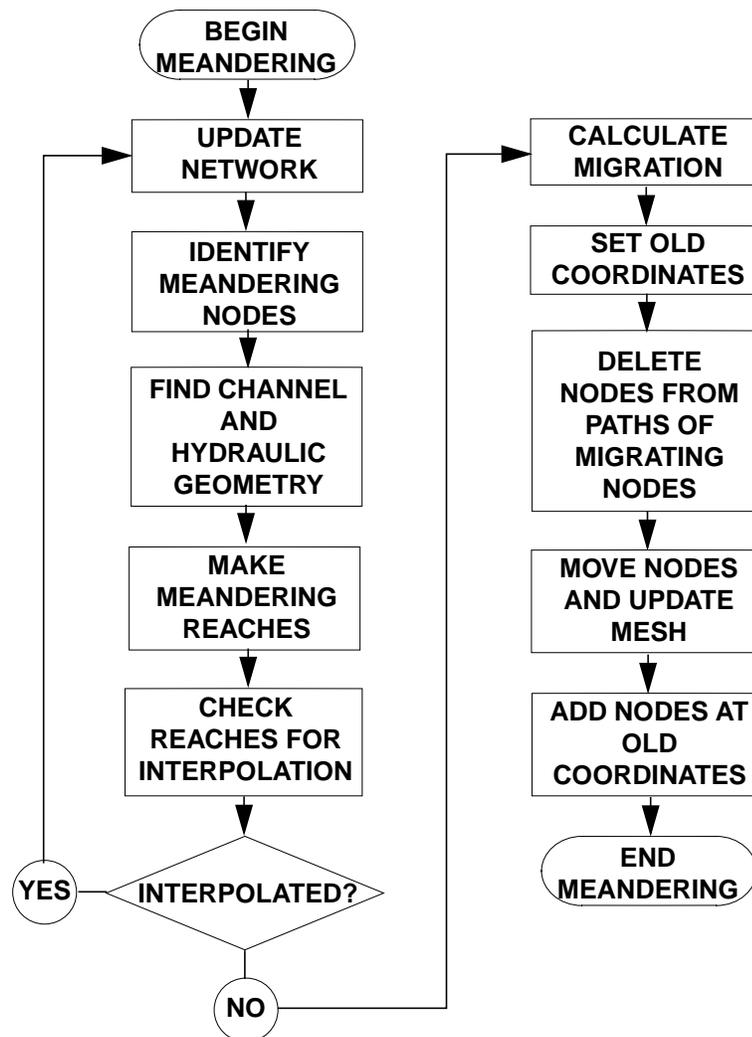
Figure 5.14: Flow chart showing the implementation of meandering.

In figure 5.14 shows a flow chart of the CHILD model's implementation of the TSRM model in the stream meandering object. First, the network is updated (see

186

figure 5.13). Then, the meandering nodes are identified. A node is designated as a meandering node if it: (a) has discharge greater than a critical value; (b) is not "flooded", i.e., in a lake; and (c) is not a boundary node.

5.3.4.1 Meandering Channel Reaches

Meandering nodes are next organized as meandering reaches (see figure 5.15) because the meandering model requires a list of points along the channel ordered from upstream to downstream (see section 4.2.4, "Implementation", on page 123). For each meandering node, if none of the neighbors flowing to it are also meandering nodes, then the node is a reach "head", i.e., the node is at the upstream-most extent of a meandering stream reach. For each reach head, if the node downstream is: (a) a meandering node; and (b) not already a member of a reach; then the downstream node is added to the present reach and marked as a "reach member", and these criteria are applied iteratively downstream until they fail. At the downstream end of each reach, if the downstream nodes are also meandering nodes, then nodes for a distance of ten of the last reach node's channel widths are added to the reach as "tail" nodes. Recall from Chapter 4 that the bank shear stress at a point is generally generated by lateral momentum transfers at points upstream. Thus, bank shear increments generated at the end of a reach will be applied as bank shear stress at points in the downstream reach. The distance of ten channel widths is arbitrary.
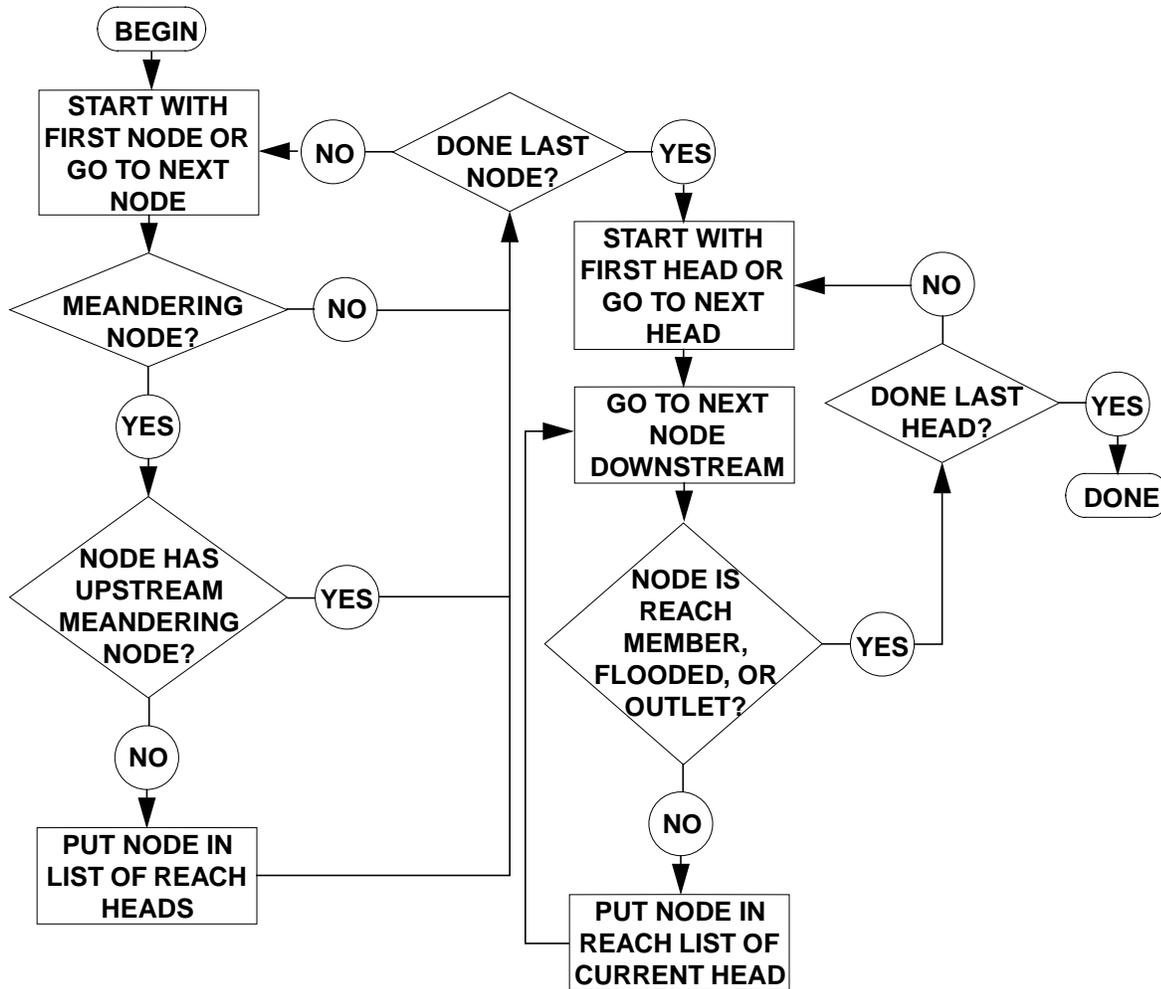
Figure 5.15: Flow chart illustrating meandering reach construction.

Once the reaches have been defined, distances between reach nodes are compared to a nominal downstream increment on the order of one channel width, the discretization required by the meandering model. If any distance is greater than twice that nominal increment, the reach segment is interpolated by adding one node or, if the distance is larger than three times the nominal increment, two or more nodes at intervals approximately equal to the nominal increment. In order to avoid exact colinearity, which can cause the triangulation algorithm to fail, a small amount of noise is added to the interpolation. In the case of

adding more than one node, the nodes are added by generating a random walk with uniform spacing along the original channel segment and random steps perpendicular to the line:

$$n_i = n_{i-1} + \Delta n_i \tag{5.9}$$

where Δn_i is

$$\Delta n_i = Axe^{-(n_{i-1}x)}\Delta s_0 \tag{5.10}$$

where x is uniformly distributed from -0.5 to 0.5 ($x \sim U[-0.5, 0.5]$); A is some small number; and Δs_0 is the nominal increment for the uniform spacing parallel to the line. The nominal increment is used to scale the amplitude of the noise to the discretization scale of particular channel.

The inverse exponential ensures, or at least makes it likely, that the random walk's deviation from the original line will not become arbitrarily large at any point and, most importantly, at the last interpolation point. A large deviation at that point could, in effect, reinforce the original grid spacing by adding a large step and, therefore, high curvature, at the regular intervals of the original uninterpolated mesh. Note that equation (5.10) does not result in exponentially distributed random steps but, rather, represents a random walk through a potential energy well in which steps away from the line become more damped and steps toward the line more amplified when the step originates at a greater distance from the line and the step magnitude is greater. Conversely, small steps close to the line are damped and amplified by only a small amount.
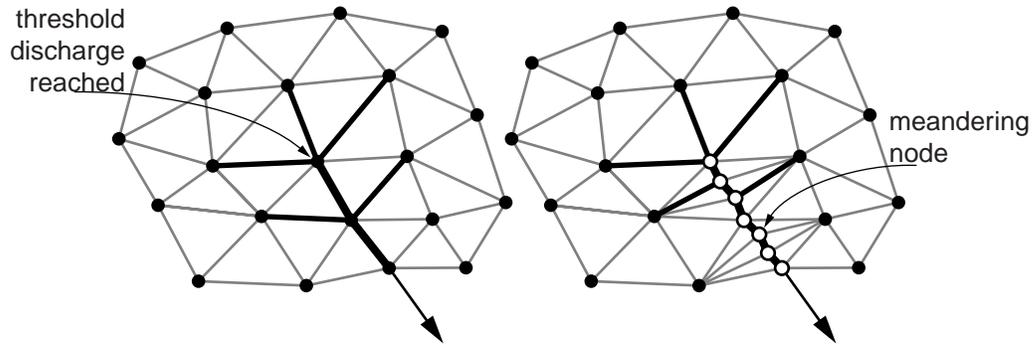
Figure 5.16: Illustration of meandering channel interpolation. Note that two tributary channels take a shorter route to the main channel after interpolation.

As shown in figure 5.15, after the discretization of the initial reaches is checked, if any interpolated nodes are added, then the procedure iterates: it updates the network (see figure 5.16), redefines the meandering nodes, constructs new reaches, and again checks the discretization. The iteration of this loop proceeds until the discretization check results in no addition of nodes. Several iterations may be required the first time the procedure is called to add many points to a coarse mesh (see figure 5.16), but subsequent calls should require interpolation infrequently and, then, only to add one point between two channel points that have spread apart as the channel has lengthened and become more sinuous, as in Chapter 4.

When the reaches are complete, the CHILD model, written in C++, must call the TSRM model, written in Fortran, to calculate the lateral migration of the channel nodes.The CHILD model calls the TSRM model as a function/subroutine through a "wrapper" function. The meandering reaches are constructed as a list of lists of pointers to meandering nodes. As evident from above, nodes in each of the latter pointer lists are arranged in upstream-to-downstream order. The wrapper function takes each pointer list in turn and constructs one-dimensional arrays for each node data member required by the

TSRM model, e.g., arrays for *x*-coordinates, *y*-coordinates, discharge, channel slope and

bank erodibilities. The TSRM model passes back arrays of displacements which are sub-

sequently scaled by the time step determined in the wrapper function. This time step is set

such that the greatest displacement does not exceed an arbitrary fraction of the channel

width, typically one-tenth, for stability.

5.3.4.2 Channel Bank Erodibility

To find the bank erodibility at a particular channel node, the bank nodes must be

identified. The identification procedure is illustrated in figure 5.17. With respect to the line

perpendicular to the channel node's flow edge, the line remainder and perpendicular dis-

tance are calculated for each channel node neighbor's position. For example, for a point at

(x_0, y_0) and a line defined by $ax + by + c = 0$, the remainder, R_{line}, is

$$R_{line} = ax_0 + by_0 + c \tag{5.11}$$

and has opposite sign for points on opposite sides of the line. Starting with the channel

node's downstream neighbor, the algorithm proceeds through the neighbors in counter-

clockwise order and finds the two pairs of consecutive neighbors which have remainders

of opposite sign, i.e., the neighbors in a pair are on opposite sides of the line. The first pair

found constitute the left bank and the second pair constitute the right bank. In figure 5.17,

node **A**'s right bank nodes are nodes **C** and **D** at distances d_1 and d_2, respectively, from the

line perpendicular to node **A**'s flow edge, edge **AB**. The effective erodibility of each node

is found with equation (5.8), and the erodibility of that bank is an average, weighted by

distance, of the two nodes' erodibilities:

$$E_{bank} = \frac{E_1 d_2 + E_2 d_1}{d_1 + d_2} \quad\quad (5.12)$$

where E_1 and E_2 are the effective erodibilities of the two neighbor nodes, respectively.
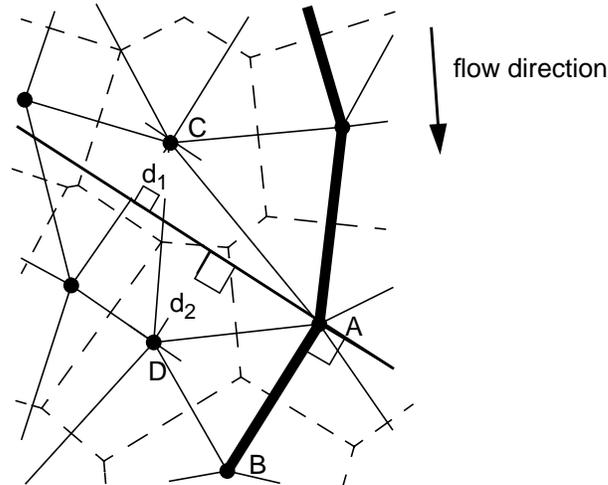
Figure 5.17: Illustration of right bank erodibility determination for node **A**. **C** and **D** are right bank nodes of **A** at distances d_1 and d_2 from the line perpendicular to **A**'s flow edge, **AB**. Delaunay triangulation is in thin lines; Voronoi diagram is in dashed lines; and flow edges are in heavy black.

As the channel approaches the grid boundary, the bank erodibility is set to zero. Thus, the boundary presents an inerodible barrier such that a channel node may not approach to within one-half channel width of a boundary edge.

5.3.4.3 Channel Bank Erosion

Once the new positions of the channel nodes are known, the triangulation must be prepared for the change by removing nodes from the channel's projected path, i.e., nodes that have been eroded by the migrating channel. The criteria for removalI are illustrated in figure 5.18.
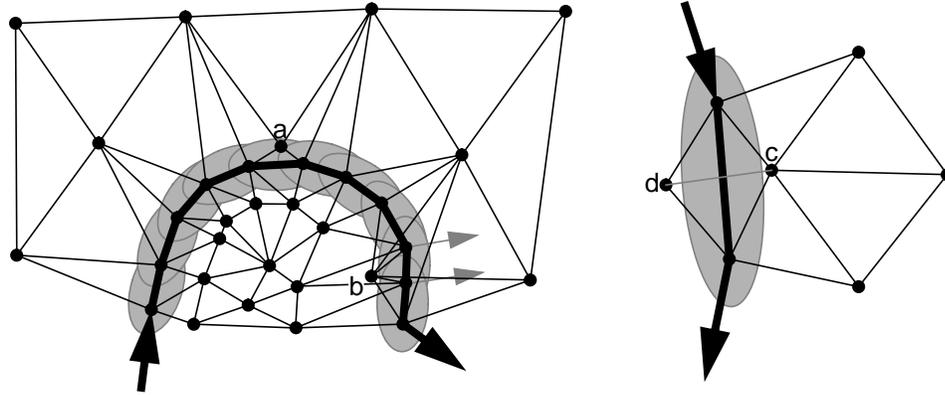
Figure 5.18: Illustrations of criteria for removing points from the path of the migrating channel. Heavy lines are flow edges; heavy black arrows are flow directions; gray ovals are channel segment neighborhoods; letters **a**, **b**, and **c** are nodes to be deleted.

First, a bank node is deleted if it falls within a channel segment's neighborhood, defined by an ellipse with foci at the ends of the segment and perpendicular distance from the segment at the upstream node of one-half the hydraulic width; i.e., for a given node, the sum of the distances to the segment endpoints, D, must satisfy

$$D \geq \sqrt{\Delta s^2 + \frac{1}{2}b^2 + b\sqrt{\Delta s^2 + \frac{1}{4}b^2}}$$

(5.13)

where Δs is the length of the channel segment. In figure 5.18, point **a** falls within the neighborhood of a channel segment.

The latter criterion, equation (5.13), should prevent most potential problems. However, to ensure the robustness of the channel migration under any and all conditions, nodes are tested to eliminate the possibility of two more scenarios.

First, nodes are deleted if they have been crossed by a channel segment, e.g., if two channel nodes moved distances greater than one hydraulic width in an iteration, that channel segment could pass over a point such that its distance from the channel would satisfy

equation (5.13) both before and after the movement (e.g., node **b** in figure 5.18) even though, conceptually, the node should have been eroded by the channel. If, after movement, any triangle's nodes are clockwise and two vertices are connected by a flow edge, and either a spoke of the third vertex intersects the flow edge or more than one neighbor triangle has also become clockwise, then the third vertex node is deleted if it is neither: (a) a meandering node with greater discharge than either of the other two vertex nodes; nor (b) a boundary node. Failing the latter condition, then either or both of the other two nodes are returned to their original coordinates, i.e., before movement, if their new coordinates were outside the mesh. Failing the former condition, then the more upstream of the other two nodes is deleted instead. In figure 5.18, node **b** has been crossed by the migrating channel segment indicated by the gray arrows denoting the approximate direction of migration in the previous step. The triangle formed by node **b** and its two meandering neighbors has become clockwise, and one of node **b**'s spoke edges intersects the flow edge. Node **b** is neither a meandering node nor a boundary node and will, therefore, be deleted.

The final test for node removal ensures that the integrity of the flow edges between meandering nodes is preserved. That integrity could be compromised if a point were close enough to the flow edge that, under flip-checking, the flow edge would be flipped. In figure 5.18, node **c** would be deleted to preserve the flow edge separating nodes **c** and **d** where, to satisfy Delaunay-ness, the flow edge would be flipped to connect nodes **c** and **d**; deleting the closer node, **c**, allows the flow edge to remain intact following re-triangulation.

5.3.4.4 Point Bar Accretion

As the channel migrates and nodes are removed from its path to simulate bank ero-
sion, nodes are left in the channel's wake to resolve the point bar, as in the simulations
superimposed on the regular grid in Chapter 4. The algorithm used to "drop" new points is
illustrated in figure 5.19. In summary, this algorithm essentially keeps track of a channel
node's location where it last dropped a node. When the channel node is half of a hydraulic
width away from these old coordinates, the algorithm updates them by finding the exact
position on the bed at the water's edge on that side of the channel, i.e., the point on the bed
at half of a hydraulic width away and on the line perpendicular to the flow edge. Depend-
ing on the desired discretization, the algorithm either immediately places a new point at
the determined coordinates or waits to do so until the channel node has moved some addi-
tional distance. In the latter case, the algorithm checks to make sure the old coordinates
have remained on the same side of the channel and do not fall within any channel seg-
ments as defined by equation (5.13).

In more detail, each meandering node contains a four-member array with coordi-
nates in three dimensions and a flag indicating the side of the channel, right or left, where
those coordinates lie. When a node is recognized as a meandering node, its x and y coordi-
nates are stored in the array as the "old" coordinates; the value of z is left undetermined
and the fourth member of the array is set to zero as a flag to signify that the old coordinates
have not been finally determined.
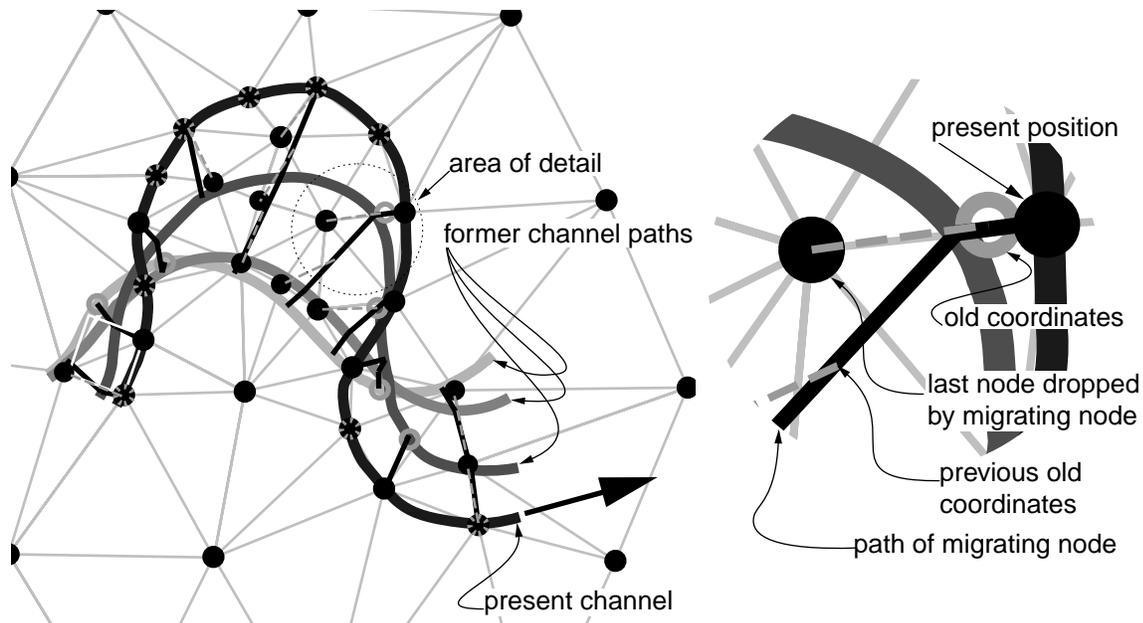
Figure 5.19: Schematic diagram illustrating the point-dropping algorithm. The nodes with dashed gray boundaries presently occupy the "old" coordinates, i.e., the old coordinates are initialized to the present coordinates.

Before migrating nodes are moved, if the flag is zero, the distance to the old coordinates is measured. If that distance equals or exceeds half the hydraulic width, the algorithm determines the side of the channel where the old x and y coordinates lie and updates the old coordinates to the position of the bank on that side. The elevation of the bed at that bank is recorded as the old z coordinate. The channel side determined above is recorded as plus or minus one for the left or right sides of the channel, respectively.

After node migration, the horizontal distance to the old coordinates is measured again. If that distance exceeds a set fraction (or multiple) of the hydraulic width and the old coordinates are (a) not in the channel, and (b) still on the same side of the channel, then a node is added at the old coordinates. The above fraction of the width must be greater than or equal to half the hydraulic width; in figure 5.19, the value equals half the hydraulic width, and nodes are dropped as soon as the final old x, y, and z values are deter-

mined. In figure 5.19, this final determination is signified by the dashed gray lines drawn perpendicular to the node's flow direction at the time of the determination. Note that these coordinates at which the new nodes are dropped do not necessarily lie in the migrating node's path because they are the coordinates at the bank, whereas the node's coordinates are on the channel centerline. Implicit in the procedure described above is that the discretization of the point bar is limited by the hydraulic width, i.e., the procedure would not allow a discretization finer than half the hydraulic width, coarser than the regular grid used in Chapter 4.

5.4 Simulations

With the CHILD model, I ran simulations of meandering in landscapes with varying strengths of bank erodibility's bank height dependence and rates of uplift to examine the effects of these variations both on the meandering and the landscape. The simulations reported here are relatively simple because, in working with the potentially complicated CHILD model, it is necessary to understand the simplest case before consideration of more complex cases. I began with a vertically incising river flowing through a valley. At one end of the domain is a single inlet, and at the other end the whole side is an open boundary. I ran the model with detachment limited erosion until the valley was at dynamic equilibrium and, then, turned on meandering. These simulations show the effects of meandering with the different parameter sets on the same initial valley.

The case of dynamic equilibrium is a particularly useful reference because I know what the channel slope should be. For $\partial z / \partial t = 0$, discharge proportional to contributing area, or $Q = PA$, and where advective channel processes are dominant over diffusive processes, equation (5.3) reduces to the following expression for channel slope:

$$S = \left(\frac{U}{K_B P^m}\right)^{1/n} A^{-m/n}.$$

(5.14)

After the incising channel reached dynamic equilibrium, meandering started with f_{lat} = 100 and ran for thirty thousand years. The result is the initial condition for the remaining simulations. For the latter simulations, I increased the relative strength of meandering by using f_{lat} = 1000. Each simulation ran for ten thousand years and another 100,000 years for examination of the transient and long term responses, respectively, of the landscape to the meandering. In the long term, the system as a whole may approach dynamic equilibrium, though the simple idea of no elevations changing at any point cannot apply because of the laterally migrating channel. The simulations and their parameters are listed in table 5.1. Note that the times are model years, which are uncalibrated with respect to real time. Because discharge in the advective erosion term of equation (5.3) is usually expressed in units of volume per second, the conversion to elevation change per year is contained in K_B (see, e.g., table 5.1).

The first task was to address the issue of bank height and erodibility for an incising stream. The dependence of bank erodibility on bank height is a first order problem which is not well understood, in part, because no landscape evolution model has incorporated meandering. This incorporation is necessary in order to examine the interactions between the migrating, incising river and the surrounding landscape.

In the simulations listed in table 5.1, the main purpose was to address the responses to varying both bank erodibility's bank height dependence, P_H, and uplift, U, after the onset of meandering. I also show the short term effect of varying median grain

diameter, d_{50}, but this is more of a parameter adjustment than a sensitivity analysis. The sensitivity of the TSRM model to d_{50} was addressed in Chapter 4.

Table 5.1: Simulations and variable parameter values[a]

simulation	initial condition	d_{50} (cm)	U (m/yr)	P_H	f_{lat}	t_{Total} (k-yrs)
A	noise	NA	0.001	NA	NA	320[b]
B	A	0.5	"	0.0	100	30
C	B	"	"	"	1000	10
D	B	1.0	"	"	"	10
E	B	"	"	0.5	"	10
F	E	"	"	"	"	100
G	B	"	"	1.0	"	10
H	G	"	"	"	"	100
I	B	"	0.002	0.5	"	10
J	I	"	"	"	"	100
K	B	"	"	1.0	"	10
L	K	"	"	"	"	100

a. Other parameters are constant: $A_{inlet}=10^8$ m^2; $P=10^{-6}$ m/s; $K_B=0.0316$ m$^{3/2}$ s$^{1/2}$/yr.; $m_B=0.5$; $n_B=1.0$; $K_D=0.01$ m^2/yr.
b. Landscape is at dynamic equilibrium.

All simulations employed the lake filling algorithm and used a minimum discharge for meandering such that only nodes downstream of the inlet, i.e., points along the main channel, were meandering nodes.

The initial condition for simulation **A** was a flat plane with minor elevation perturbations. The nodes were arranged in offset rows such that the polygon around each node is a hexagon, as is the Voronoi area. Nodes on the same row were spaced 100 meters apart.

5.5 Results

The results reveal dramatic differences between the transient and long term responses of

the model meandering river valley and the landscapes resulting from different strengths of bank erodibility's bank height dependence as well as subtle but important differences due to the different uplift rates. These results also reveal the important, varying roles of compound bend and multi-bend loop formation in the model river valley forms.

For each of the simulations listed in table 5.1, figures 5.20-5.31 each show three perspective views of the simulated landscape. The first view maps color according to elevation and shows the landscape as a surface at a low enough angle to appreciate the shape of the relief. The second view uses the same elevation color map as the first and shows a "wire" mesh of the model grid at a large viewing angle in order to show all of the nodes, edges, and triangles. The third view maps color according to discharge and shows the landscape as a surface at a large viewing angle in order to best show the model stream network and, especially, the main channel down the center of the valley.

Plots of slope vs. contributing area are shown in figure 5.32. The slopes of the individual nodes are plotted vs. area as gray dots. Also on the slope-area plots I have drawn lines described by equation (5.14); in the simulations with increased uplift, the original dynamic equilibrium line is solid gray and the new dynamic equilibrium is dashed gray. I binned slope according to increments of log-area and plotted bin average slope vs. bin average area. These average slopes are shown with black rectangles. Note that each node in the mesh has one point in the slope-area plot, but the nodes do not have equal Voronoi areas. Therefore, nodes with smaller areas are effectively over-weighted in the averages because the averages are not weighted by Voronoi area.
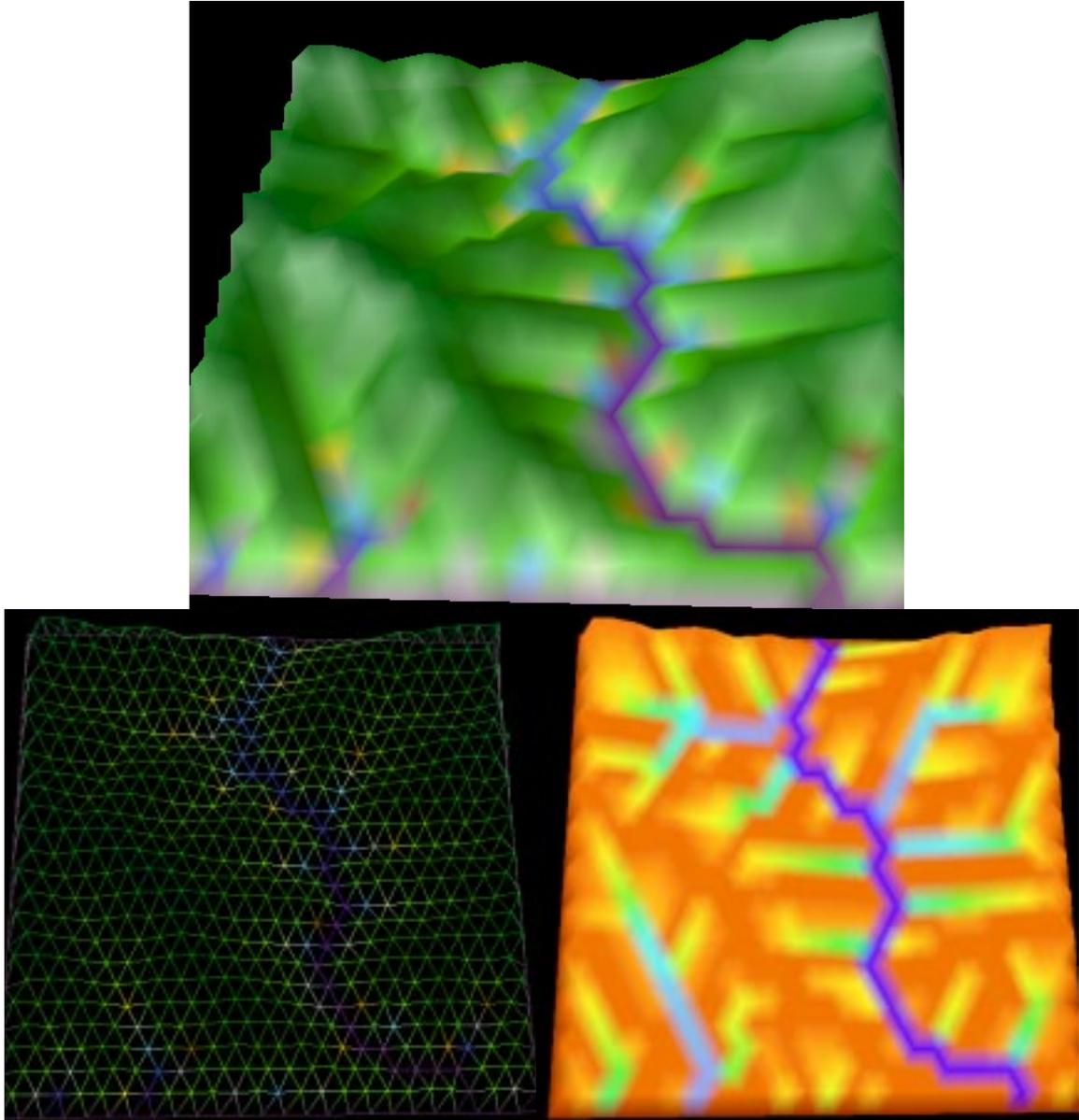
Figure 5.20: Perspective views at end of simulation **A**.

The slope-area plots allow a quantitative assessment of the effect of meandering on slopes in the landscape. The fact that meandering, by steepening valley walls and flattening the valley bottom, creates topographic slopes independent of contributing area should be visible in the plots in figure 5.32.
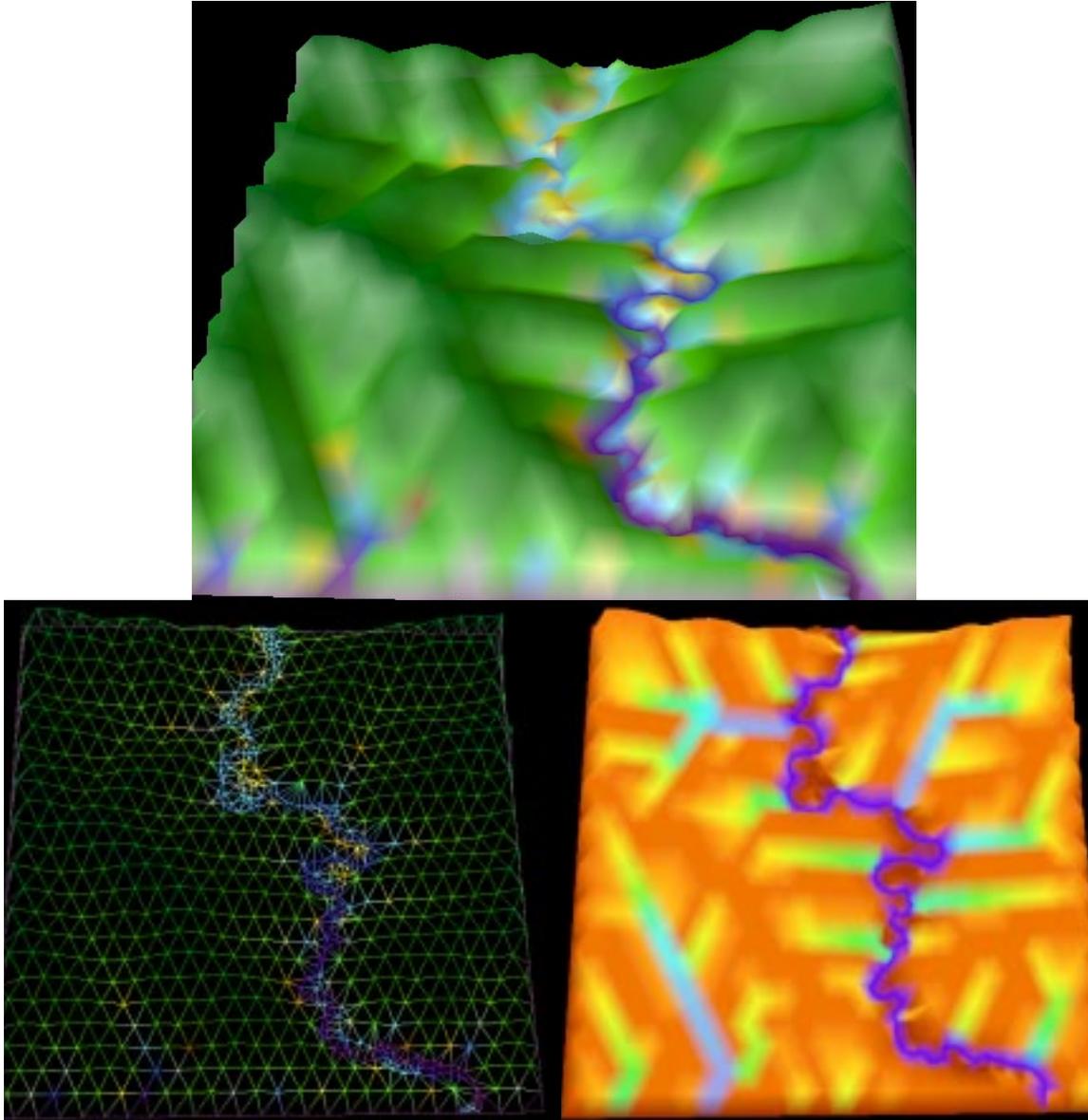
Figure 5.21: Simulation **B**.

Areas of the grid which have been visited by the channel are more finely discretized than the nominal discretization. This is visible as a dense mesh in the wire plots and darker reds in the discharge map—only these nodes with small Voronoi areas can have discharge values low enough to reach into the dark red end of the color map. The migrating nodes drop new nodes when they are $0.7\ b$ (seven-tenths of a channel width) from the old coordinates. The channel is 30 meters wide.

The valley at dynamic equilibrium, or simulation **A**, is shown in figure 5.20. The channels, constrained to follow the regular network of edges, have an unrealistic, angular appearance, an effect common to most landscape evolution models. The points in the slope-area plot (see figure 5.32) closely follow the power law describing dynamic equilibrium (see equation (5.14)).

Simulation **A** was the initial condition for simulation **B**. The latter ran with relatively weak meandering, or f_{lat} much lower than for the following simulations, until the initial channel lost its angularity and formed meander loops, and the simulation ended before any major cutoffs occurred. The resulting landscape is shown in figure 5.21. The weak meandering produced some scatter in the slope-area plot and added a number of nodes with contributing area smaller than any of the nodes in simulation **A** and many more channel nodes with large contributing area because of the channel interpolation (see figure 5.32). For the latter channel nodes, slopes are quite scattered. For the meandering nodes the slopes plotted were averaged over a distance of ten channel widths, and the points along the channel are spaced at approximately one channel width (in these simulations with constant rainfall, the channel and hydraulic widths are identical). Note that slopes have been scattered both ways: some slopes are steeper, e.g., nodes along the outer bank of meander bends, while some slopes are more gradual. Most of the latter have small contributing areas and, therefore, must lie in the area of the main valley swept by the migrating channel. Mean slopes at lower contributing areas, below about $5 \times 10^4 \, \text{m}^2$, reflect the influence of meandering and are nearly independent of area. The result of simulation **B** was the initial condition for simulations **C**, **D**, **E**, **G**, **I**, and **K**, while simulations **F**, **H**, **J**, and **L** are continuations of **E**, **G**, **I**, and **K**, respectively.

Simulations **C** and **D**, shown in figures 5.22 and 5.23, simulate meandering with $P_H = 0$ and varying d_{50}. I did not run long simulations with $P_H = 0$ because it would not have been very interesting because of the minimal interaction between the migration of the channel with the surrounding topography, but they are interesting as transients. The valley width is more variable for the larger grain size, and the total area visited by the channel is larger for the smaller grain size. Both of these results may be due to the larger lateral migration rates associated with smaller grain size. The valley for the larger grain size widened appreciably only at the location of a sharp bend in the initial condition. The major result of these first runs is that the model grid represents meandering as intended, i.e., that bank nodes are deleted and point bar nodes added. Note the several isolated nodes which were not eroded by the main channel.

Not surprisingly, the slope-area plots (see figure 5.32) show that a large number of nodes, those on the valley floor, have slopes much lower than they would at dynamic equilibrium and some nodes, those on the valley sides, have steeper slopes. These slope changes have dramatically changed the mean slope trends. The effect for smaller areas is similar to, though more pronounced than, the effect noted above for simulation **B**. For larger areas, the mean channel concavity is greater, especially for simulation **C**, because the slopes of tributaries close to the main channel were determined by the migrating channel such that the mean slope near 10^6 m^2 is nearly identical to the slope of the main channel.
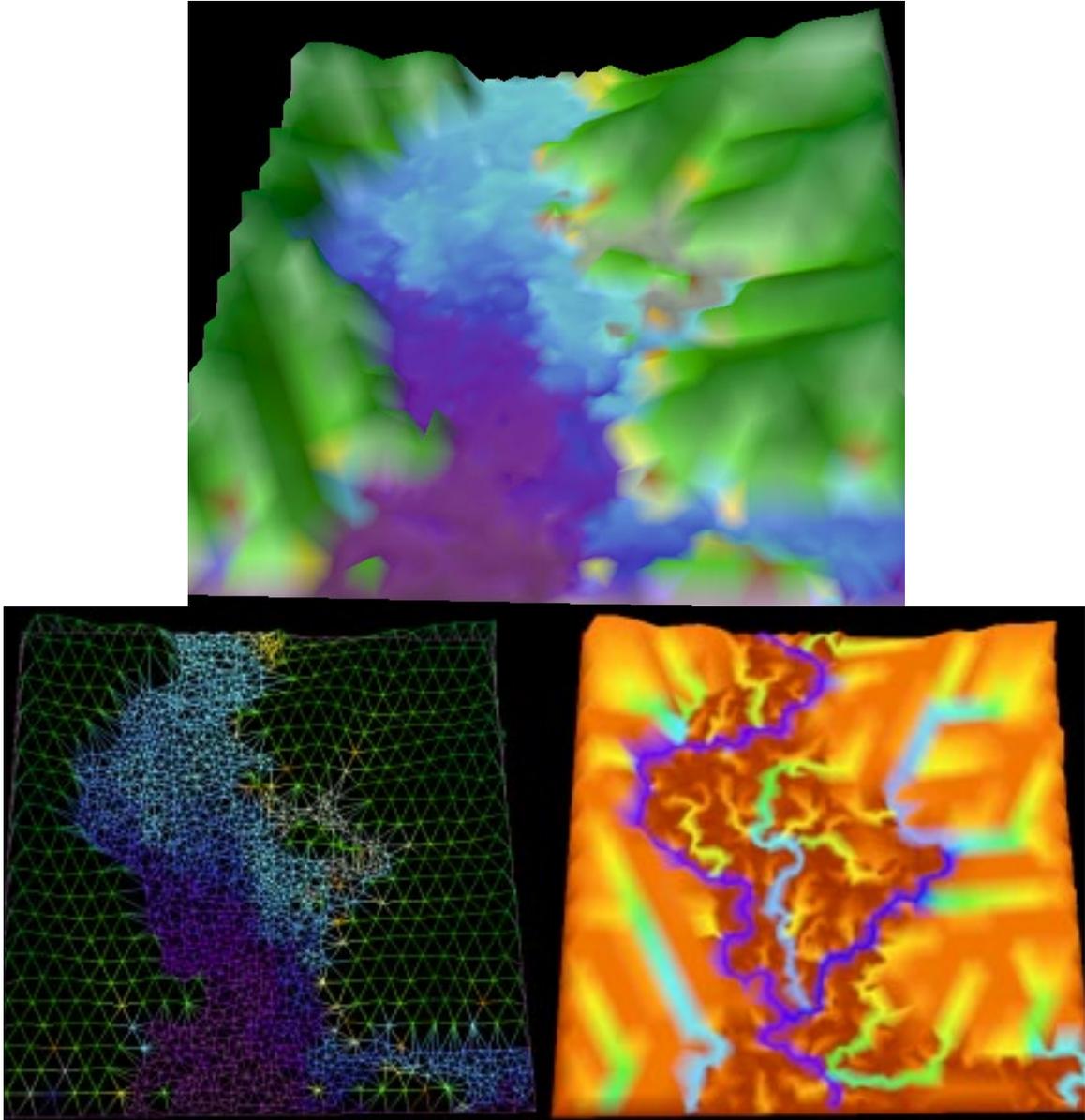
Figure 5.22: Simulation C.
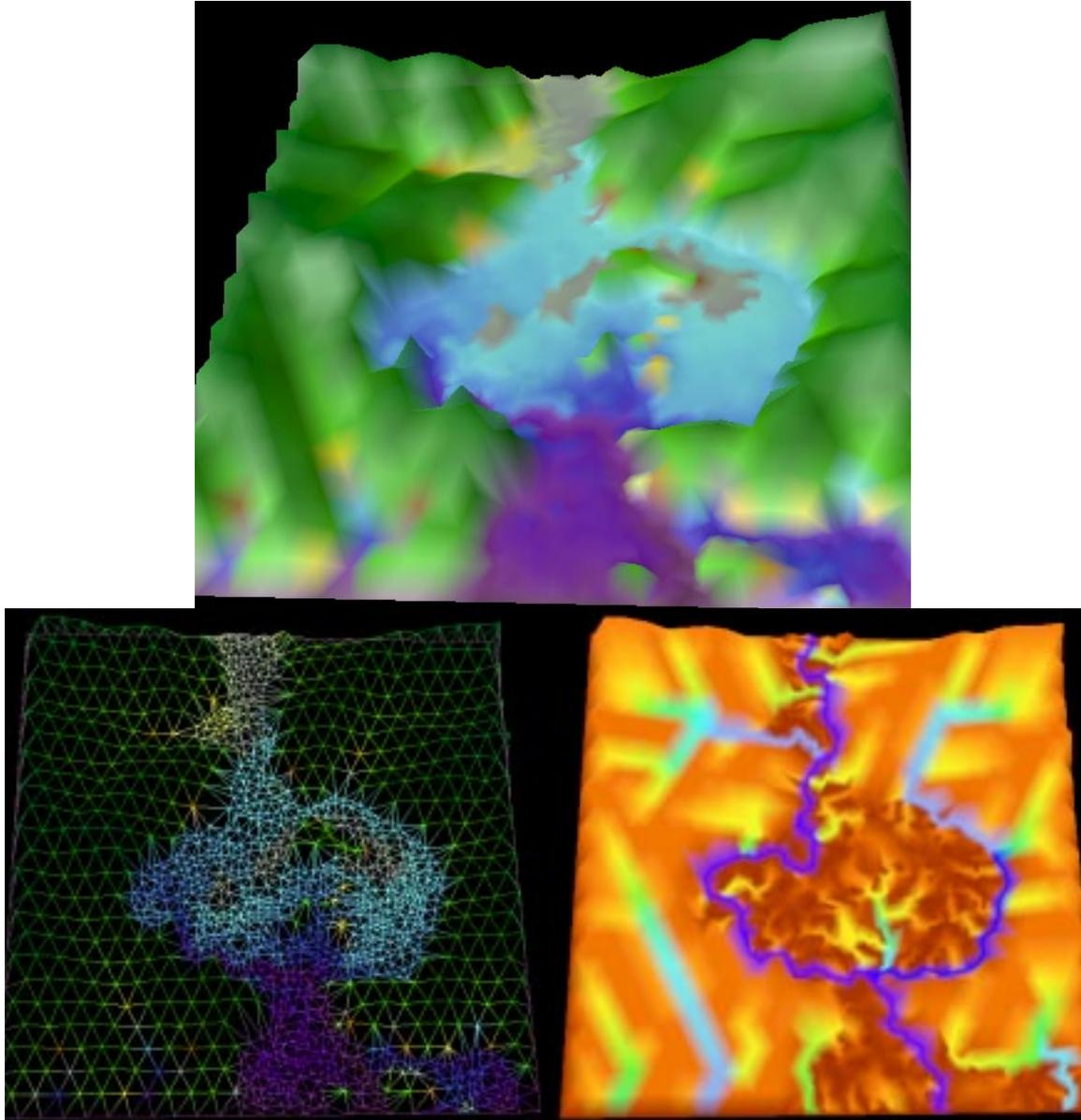
Figure 5.23: Simulation **D**.

The remaining simulations form a more controlled and systematic experiment examining the four possible combinations of two different values for each of two parameters, uplift, U, and the bank erodibility's bank height dependence, P_H (see table 5.1).

In figure 5.24 I show simulation **E**, the result of setting $P_H = 0.5$ and running for 10,000 model years. The migrating channel swept out a relatively flat valley floor, but, at

its widest, the valley floor is significantly narrower than the widest parts of the valley floor

in simulations **C** and **D** (see figures 5.22 and 5.23) due to the non-zero P_H. The slope-area

plot for simulation **E** is quite similar to that of simulation **D** (see figure 5.32): the initial

increase in mean slope is due not to the transition from diffusion to advection dominance

but, rather, to the low valley floor slopes at the smallest areas and the steep valley wall

slopes at slightly greater areas. This effect is common to all of the transient cases.
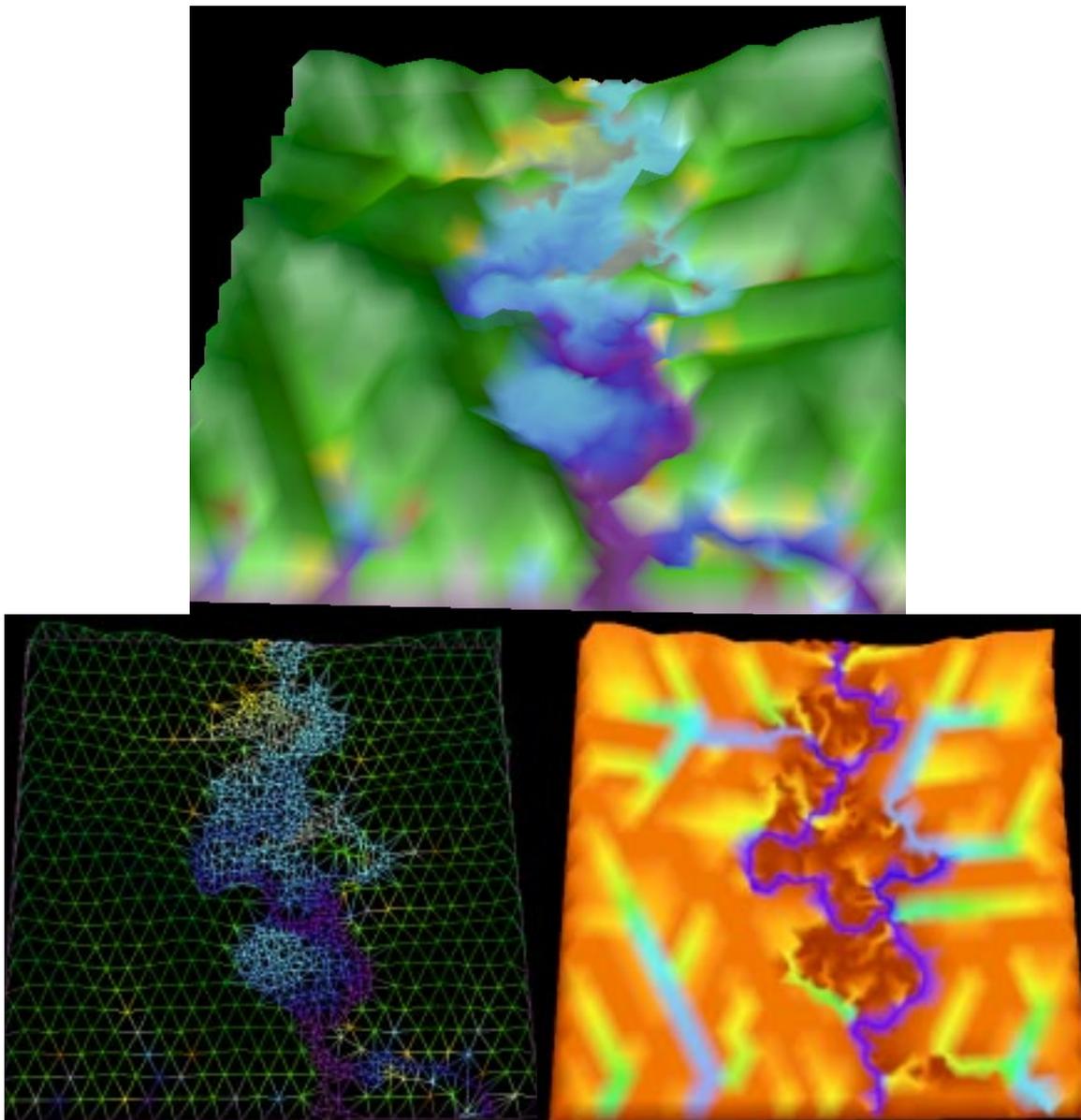
Figure 5.24: Simulation **E**.

The results of simulation **F**, the continuation of simulation **E,** are shown in figure 5.25. Roughly half of the model domain was visited by the migrating channel and is, therefore, finely discretized. The main valley narrowed considerably since the time of simulation **E**. Nodes once visited by the channel are now on hillslopes or in small tributaries. The point bars in simulation **F** have greater slope and relief than in simulation **E**. This greater slope indicates that the channel migrated more slowly at the time of simulation **F**.
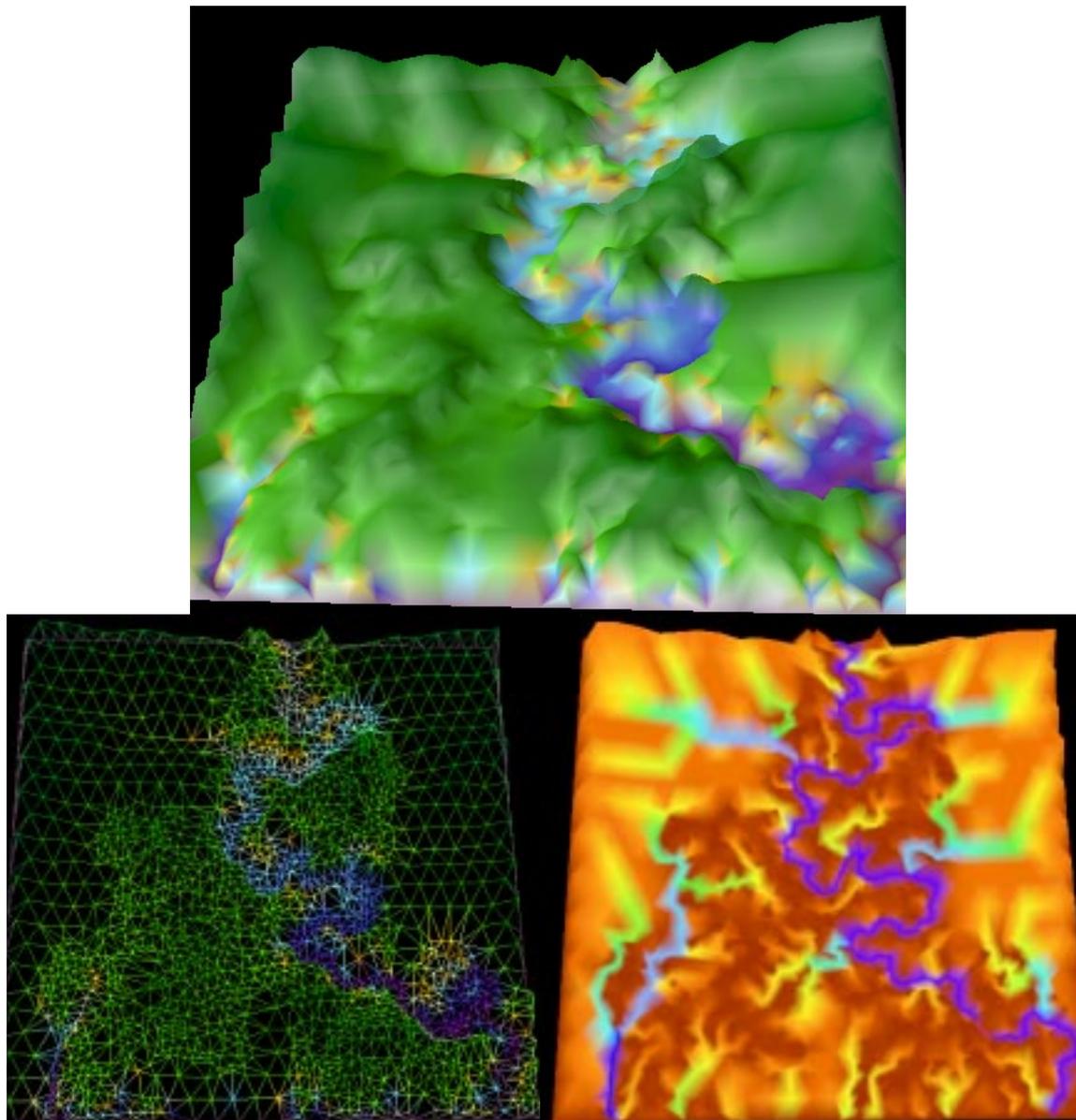
Figure 5.25: Simulation **F**.

Recall from the "incising" stream simulations with the TSRM model on a rectangular grid in Chapter 4 that a grid cell's topographic slope indicated the migration rate at the time the channel left that cell (see section 4.3.3, "The Floodplain", on page 129). Slope is similarly indicative here, though CHILD model nodes, once left by the migrating channel, are modified by not only uplift but also diffusive and erosive processes.
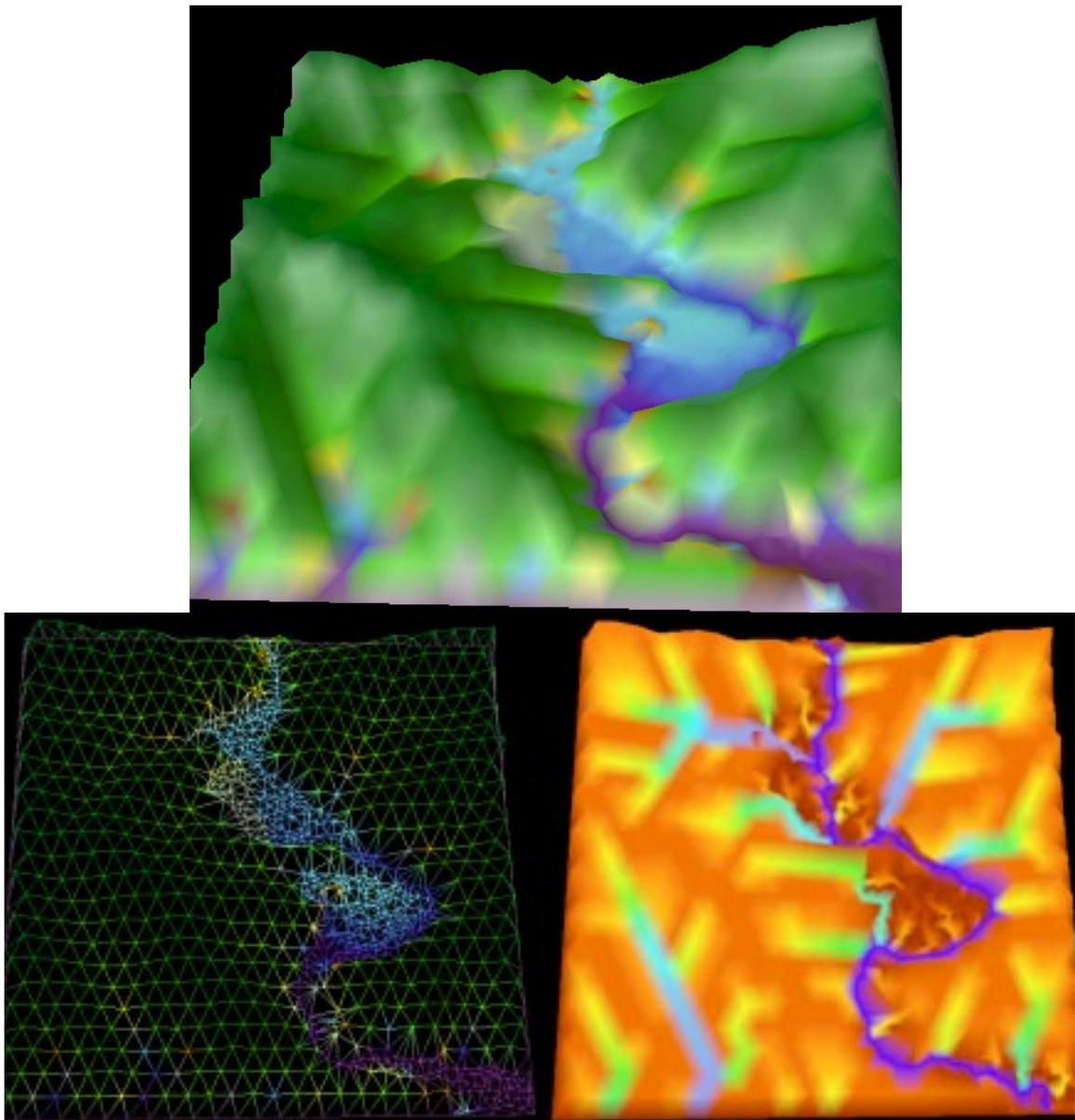
Figure 5.26: Simulation **G**.
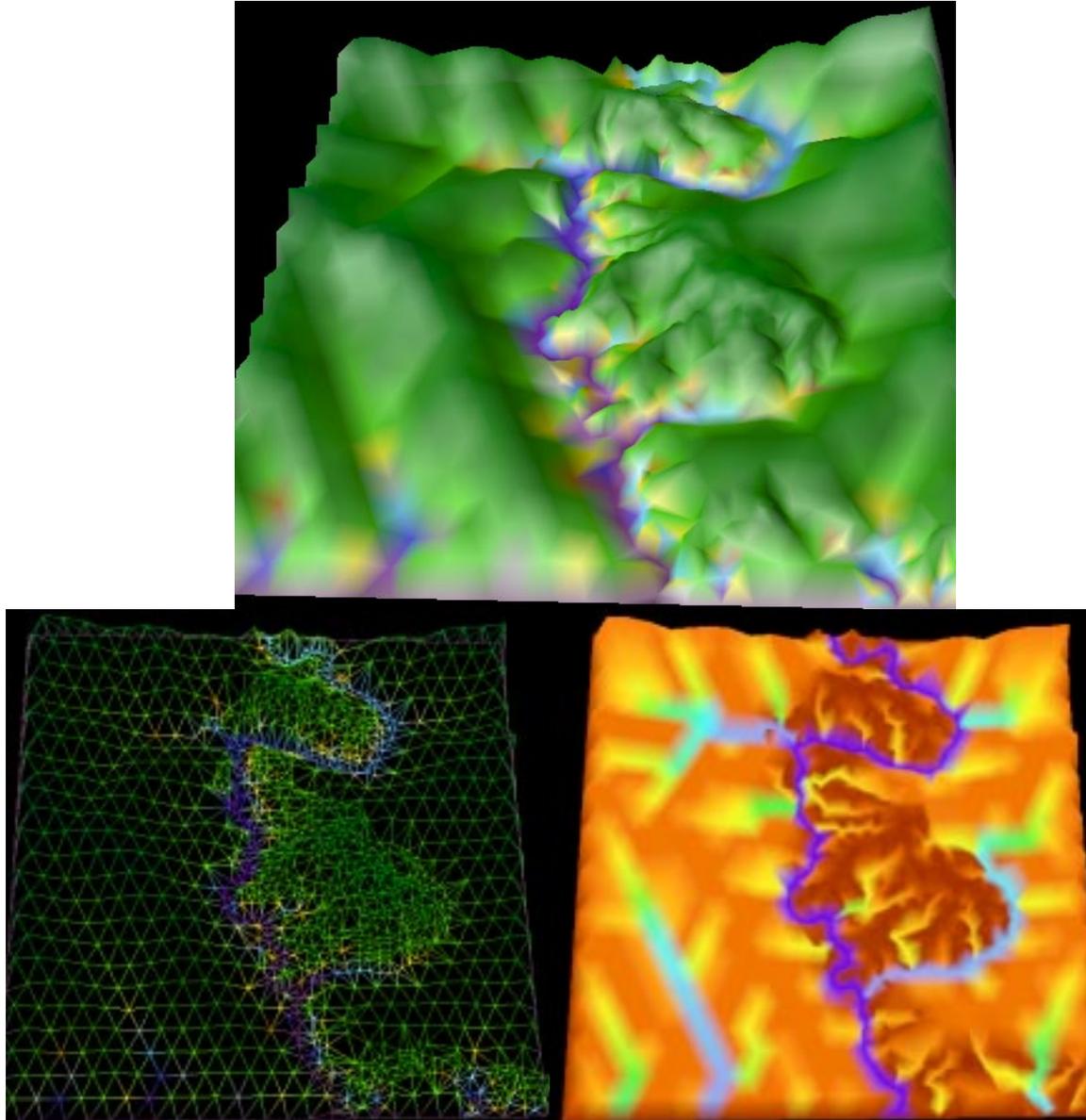
Figure 5.27: Simulation **H**.

The slope-area plot for simulation **F** confirms that a lower proportion of the nodes have shallow slopes. The plot more closely resembles what I would expect in the absence of lateral migration, though the points are still relatively scattered. The number of nodes with over-steepened slopes is not markedly different than in simulation **E**. The mean slope falls below the fluvial equilibrium line for contributing areas less than approximately

2×10^5 m^2. In simulation **A** the slopes at only the lowest areas fall just below the line due to the influence of diffusion at these points. Therefore, discounting the effect of meandering on slopes in this basin and considering only the processes in equation (5.3) to be important, I would overestimate the strength of diffusion.

The results of simulation **G**, identical to simulation **E** except that $P_H = 1.0$ in the former, are shown in figure 5.26. Many of the results of simulation **G** are similar to those of simulation **E**. The valley is, on average, narrower than the valley of simulation **E** due to the larger P_H in **G**. As in **D** and **E**, the valley width varies greatly and in places is nearly indistinguishable from the valley without lateral channel migration.

The slope-area plot for simulation **G** is quite interesting. The initial increasing mean slope trend, evident in the other transient cases, is particularly steep in simulation **G**. And, at areas between 10^4 and 10^5 m^2 there is essentially no mean slope trend with increasing area because of the numerous shallow, valley bottom slopes and few steep, valley wall slopes. Meandering, in this transient case, altered slopes such that the mean slope-area relationship resembles that of Schoharie Creek (see figure 3.32) in that both have a region of nearly constant mean slope at areas larger than that of the peak mean slope.

Simulation **H**, in figure 5.27, is the continuation of simulation **G**. As in the latter, the greater P_H led to less channel migration than in the simulation, **F**, with lower P_H. As in **F**, the valley narrowed considerably and migration slowed during the time after **G** as the system adjusted to the meandering.

The slope-area plot is even less scattered than that of **F** and, thus, reflects the greater ability of the system to adjust due to the greater coupling between migration and topography through greater P_H. Only a few nodes outside the main channel have slopes lower than about 0.05. Fewer nodes have over-steep slopes, and those few have lower slopes than in **F**. In **F**, there are many points with slopes greater than 1.0, but, in **H**, only two nodes have slopes greater than 1.0. The mean slopes in **H** fall below the dynamic equilibrium line only for contributing areas less than 10^4 m^2, but a kink in the mean slopes is visible at that area. The higher mean slopes at areas above 10^4 m^2 reflect a greater balance between the numbers of lowered and steepened slopes, respectively, in simulation **H**. As opposed to **F**, fewer small channels in **H** follow former main channel courses left by cutoffs. Partly the lack of cutoffs in **H** is due to the lower migration rate, but the more fundamental mechanism is the difference in forms taken by multi-bend loops in the two cases. Multi-bend loops in **F** more closely resemble those in the unconfined meanders of Chapter 4, whereas the multi-bend loops in **H** are larger and less sinuous at the bend scale.

The results of simulation **I**, where $P_H = 0.5$, and uplift has doubled, from 0.001 m/yr at dynamic equilibrium to 0.002 m/yr. (see table 5.1), are shown after 10 ka in figure 5.28. The valley floor is relatively flat in the sense that points across the valley have similar elevations, but the valley is steeper in the downstream direction, as shown by the wider range of colors along the main valley in the views with color mapped to elevation. This wide valley bottom is similar to, but wider than, that of simulation **E** ($P_H = 0.5$, $U = 0.001$ m/yr). The channel of **I** visited a greater portion of the model domain.
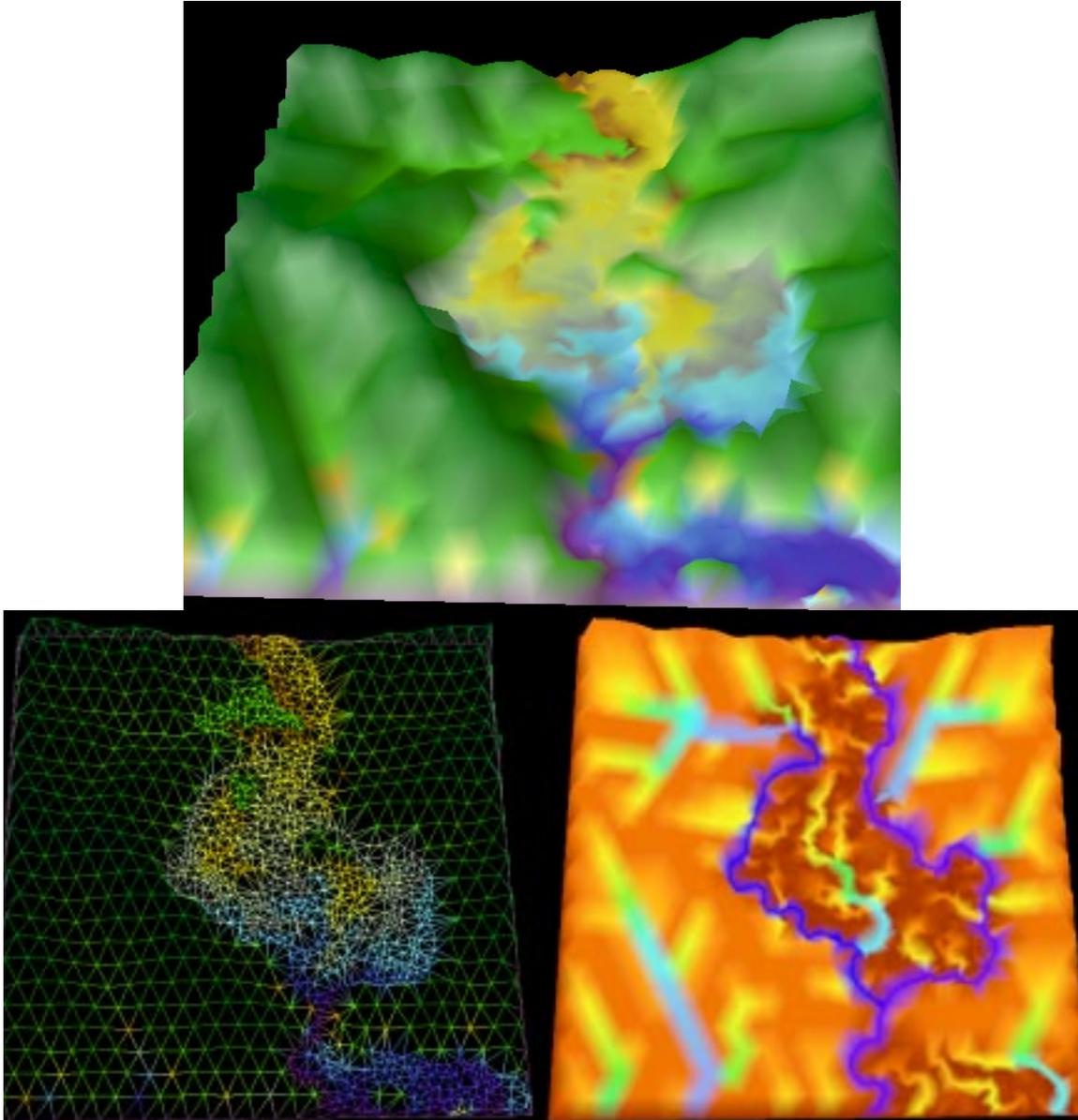
Figure 5.28: Simulation **I**.

The slope-area plot is similar to that of **E** but has greater scatter in the slopes. Some of that additional scatter is from slopes steepening due to the increase in uplift. This plot resembles that of Schoharie Creek more closely than does that of **G** in that both Schoharie Creek and **I** have a low-area dip in mean slope before the peak in mean slope at, in the case of **I**, 10^4 m^2.
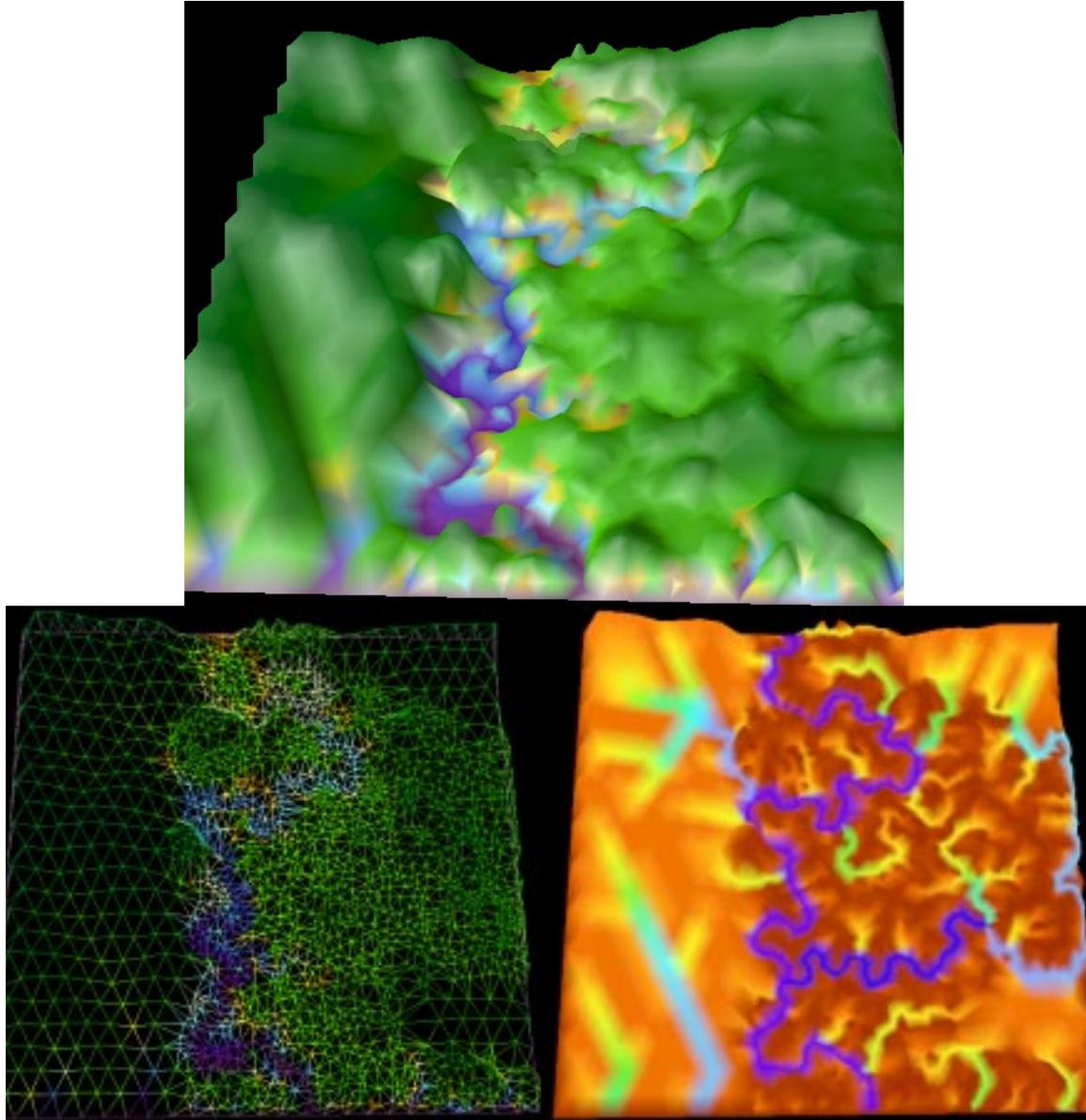
Figure 5.29: Simulation **J**.

The results of simulation **J**, the continuation of simulation **I**, are shown after 100 ka in figure 5.29. It appears that meandering affected this landscape more than any of the others. The channel visited most of the right two-thirds of the domain, and the left one-third was not visited at all. This tendency to migrate in one direction is characteristic of channels with greater frequencies of compound bend and multi-bend loop formation, as

shown in Chapter 4. The channel also visited a somewhat greater portion of the model

domain than the channel in simulation **F**. It appears, then, that some of the effects of

increased uplift nearly cancelled each other, that the increase in bank shear stresses due to

the greater channel slope was partially damped by greater valley wall steepening.
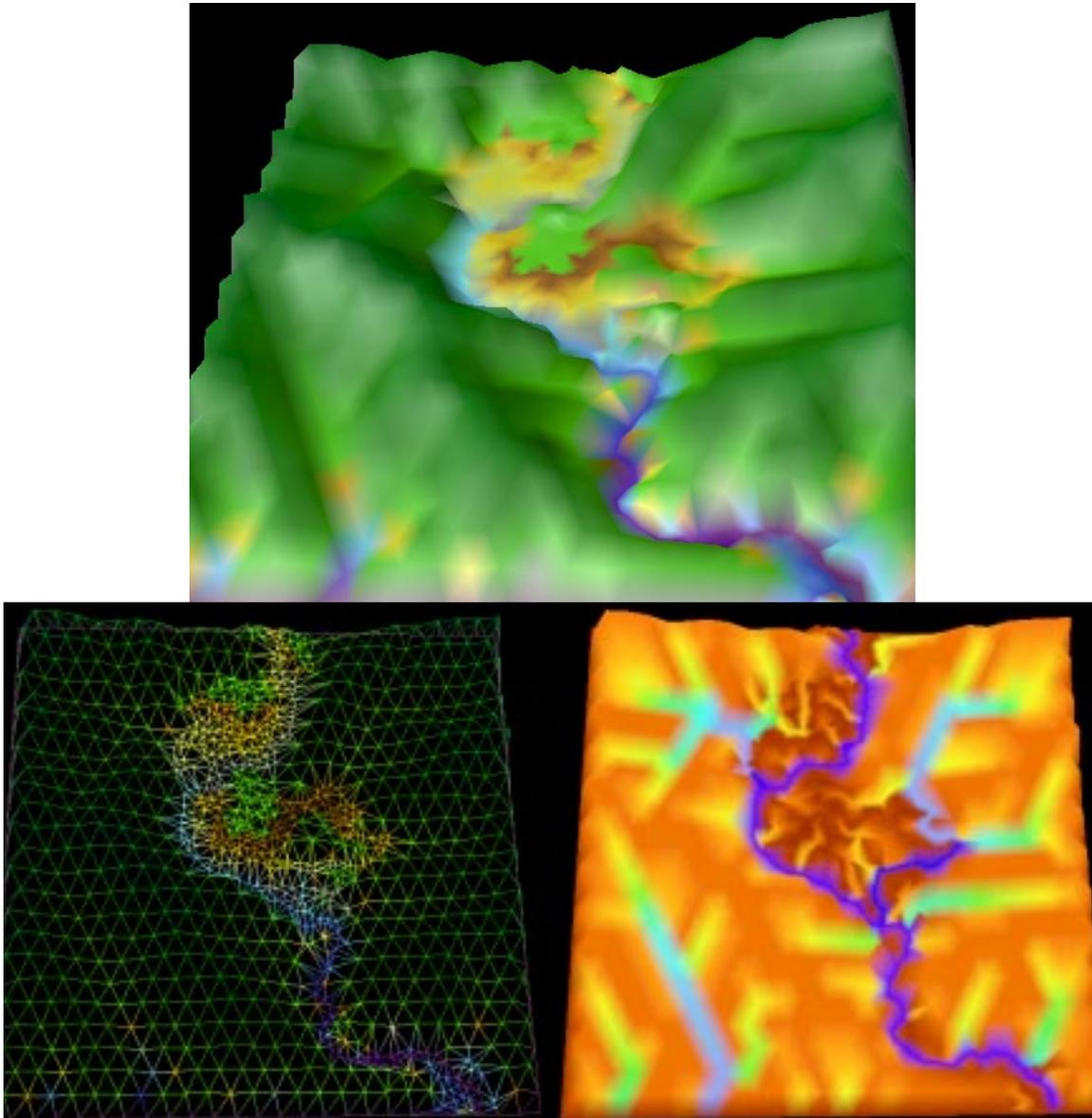
Figure 5.30: Simulation **K**.

On the other hand, the increase in compound bend/multi-bend loop formation fre-quency due to greater channel slope is readily apparent. Parts of the landscape visited by the channel look fundamentally different than unvisited areas. Examination of the dis-charge color map reveals clearly the persistence of cut off meander loops now occupied by tributaries, as in simulation **F**, but the effect is even more pronounced in **J** than in **F**. Note that none of these tributary channels were meandering at the end of the simulation because their flow was too low.

In the slope-area plot for **J**, the points are more scattered than for simulation **F** (smaller uplift), and many slopes have increased to fall on the new dynamic equilibrium power law, where slopes are greater by a factor of two for the same area. As in **F**, mean slopes in **J** tend to fall below the line of dynamic equilibrium.

The results of simulation **K**, where $P_H = 1.0$ and uplift has been increased as in simulations **I** and **J**, are shown in figure 5.30. Points visited by the channel in simulation **K** have greater relief than visited points in any of the other 10 ka simulations. Small parts of the valley are flat, but the channel evidently became entrenched more quickly than in the other simulations. Even so, the channel visited a larger part of the domain than the channel of simulation **G**. The latter fact and the early entrenchment indicate that migration at the beginning of the simulation was much faster than in simulation **G** due to the increased channel slope from greater uplift but that the same greater uplift led to a faster adjustment to the migration by the valley system.
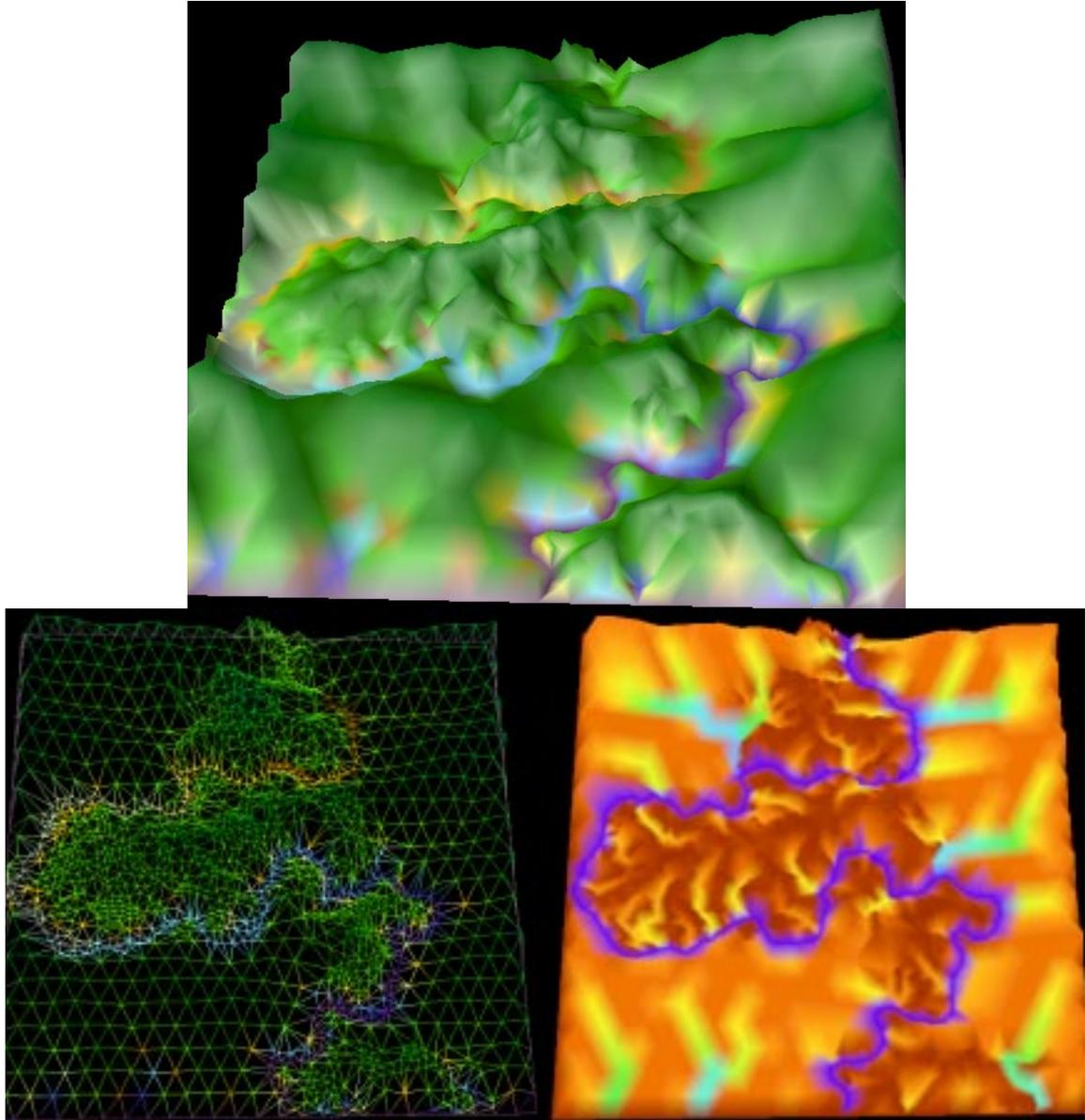
Figure 5.31: Simulation **L**.

The slope-area plot reflects the channel entrenchment in that the lowest mean slopes at the smallest areas are greater than for simulation **G**. In simulations **C**, **D**, **E**, **G**, and, to a limited extent, **I**, there is a visible separation between the cluster of low slope and area points and point near the line of the power law, but this separation is not apparent in

the slope-area plot of **G**. Also unlike the other 10 ka simulations, mean slopes at areas between 10^4 and 10^5 m^2 have a clearly decreasing trend.
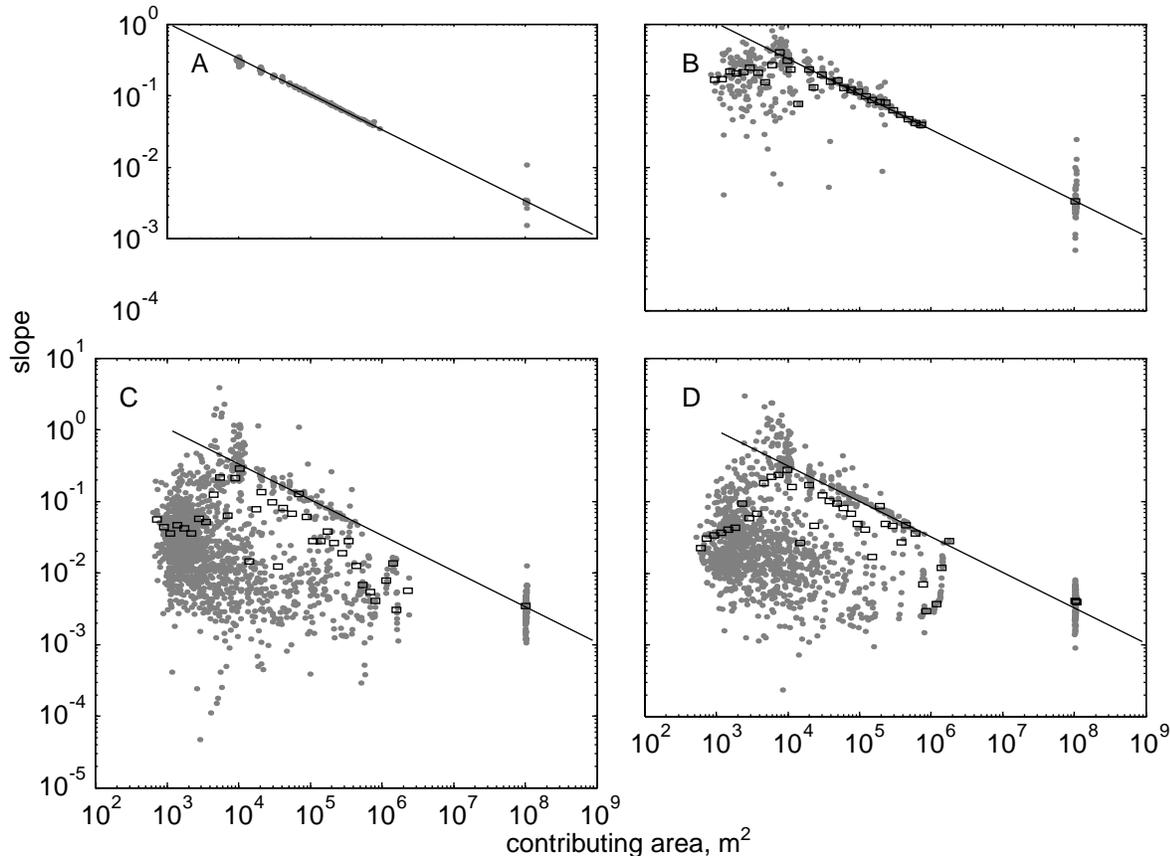
Figure 5.32: Slope vs. contributing area for the simulations listed in table 5.1. The gray lines indicate the fluvial dynamic equilibrium power law, equation (5.14).

Finally, the results of simulation **L**, the continuation of simulation **K** for 100 ka, are shown in figure 5.31. In simulation **L**, the effect of meandering on the landscape is clear and dramatic. This simulation is striking for the large multi-bend loop in the center of the domain and, thus, also shows the clear effect of multi-bend loop formation. The channel visited a greater part of the domain than the channel of **H** but, unlike the channel in **H**, did not cut off. The channel of simulation **L** also has greater sinuosity on the bend scale than **H**'s.
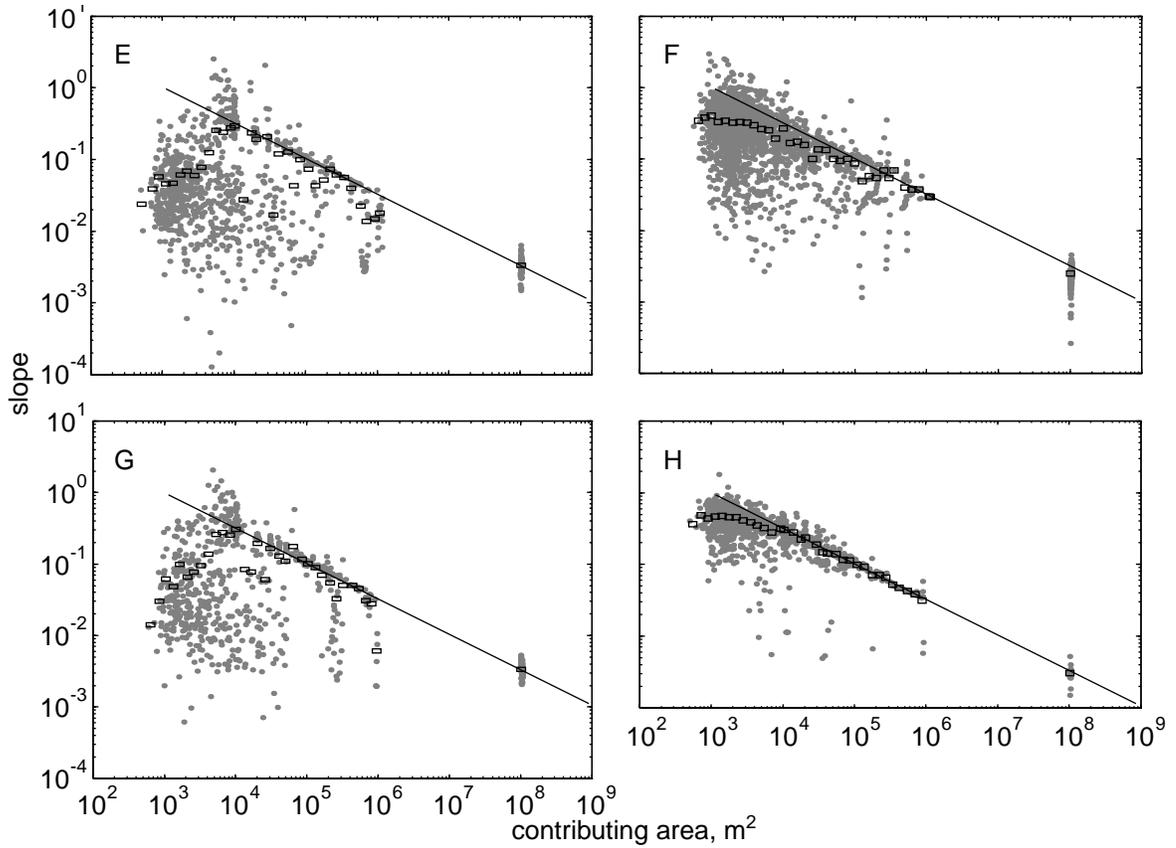
Figure 5.32: (Continued.) Slope vs. contributing area for the simulations listed in table 5.1.

As in simulation **H**, the slope-area plot is less scattered than at the time of simulation **K**, and it has a shape similar to the plot for **H**. As in **J**, the line has moved up to reflect the increased uplift. The plot has more scatter than that of **H**, both above and below the line, but exhibits similar balance between scatter above and below the dynamic equilibrium line.
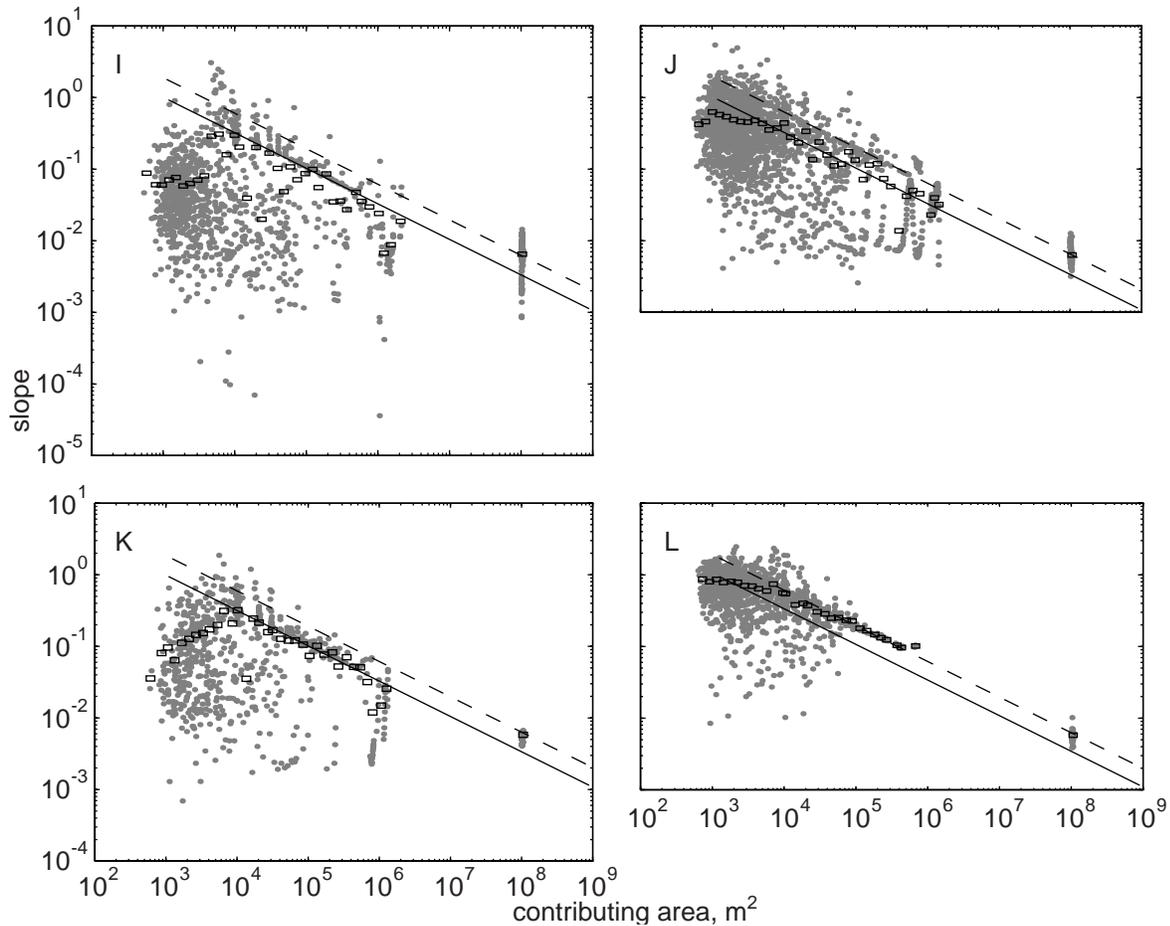
Figure 5.32: (Continued.) Slope vs. contributing area for the simulations listed in table 5.1. The dashed gray line indicates fluvial dynamic equilibrium with the greater uplift.

5.6 Discussion

The results touch on a number of areas, and I discuss them in turn: (a) the general interaction of meandering and the landscape in the model; (b) the quite different results of the transient and long term cases; (c) the role of bank erodibility's bank height dependence in the meandering patterns and landscape forms; and (d) the effect of uplift on the incising meandering stream.

5.6.1 Meandering and the Landscape

The CHILD model represents the first opportunity to study the interaction of two systems with complex dynamics. The model results should give some clue as to how to

interpret landscape forms resulting from incising meandering streams. The slope-area relationship allows quantitative comparison of the simulated valleys in this chapter and the natural valley in Chapter 3.

Points scattered toward greater slopes and slightly smaller areas have been eroded by the migrating channel. As the channel erodes part of a bank node's Voronoi cell, that node's contributing area decreases slightly by the amount eroded, and the slope to the channel becomes steeper as the latter approaches the node's coordinates. These nodes on the valley wall belong to the original, regular grid and are, therefore, still clustered according to contributing area at multiples of 10^4 m^2. Similar over-steepened points persist even at later times as long as some of these original, previously unvisited points remain.

In several of the slope-area plots in figure 5.32, especially those for the transient cases, many nodes with low contributing areas have been added in the valley, and these new nodes are responsible for the trend of increasing mean slope at low areas in the slope-area plot. Previous studies have assumed that similar trends in plots from DEMs are due to the convexity of the hillslopes (e.g., *Tarboton, et al*, 1991, 1992), but the results of the present study call this assumption into question. From visual inspection of the Schoharie Creek DEM (see figure 3.1), it appears that most of the points with the smallest slopes are in the flat valley bottom rather than at the tops of hillslopes. In the slope-area plots for the transient cases in figure 5.32, mean slope increases sharply from the shallow valley bottom slopes at low contributing areas to the steepened valley wall points, decreases sharply, levels briefly, then continues on the line of dynamic equilibrium. This is a subtle effect, but it does resemble the slope-area plot for Schoharie Creek in this mean behavior (see

figure 3.32) and does raise the possibility that meandering is responsible for some of the observed trends in slope *vs.* area, though some of the specific features of the Schoharie Creek slope-area relationship may arise from effects not present in the simulations, such as the alluviated valley floor and the capture of its headwaters by tributaries to the Hudson River. The hypothesis that the observed slope-area trends described above are due to meandering, as illustrated in figure 5.33, is supported by *Tucker*'s [1996] finding that, for a small watershed in Pennsylvania, the low-area increasing, decreasing, and level trends in slope *vs.* area as derived from a high-resolution DEM correspond to contributing areas smaller than those of the channel heads observed in the field.
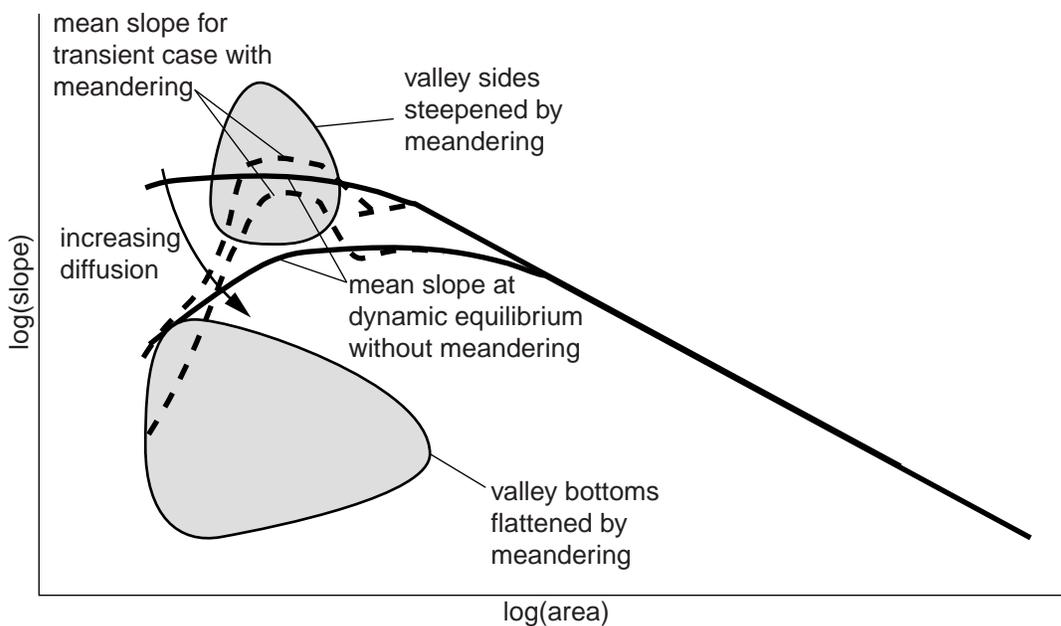
Figure 5.33: Illustration of possible effect of meandering on slope-area relationship.

5.6.2 Time Scales

I did not expect such a dramatic difference between the transient and long-term responses. At the onset of meandering, or, more precisely, after meandering had been running for some time but an order of magnitude more slowly (I will not make this lengthy

caveat from here on), the channels migrated at a great rate and carved out relatively flat valleys. But, later on, the valleys became narrow again. It is also interesting that the channel in many of the 10 ka simulations carved valleys of highly variable width, from relatively wide to gorge-like. If one were to observe this topography in the field, one would likely suspect that lithologic variations were responsible for the variations in valley width. But, the model domains are homogeneous.

At the end of simulation **B**, the spurs and tributaries encounter the main channel at a relatively low slope such that the banks are relatively low and allow the channel to migrate rapidly. After some time, the sides of the valley become much steeper and confine the channel more effectively. This adjustment is apparent from the reverting of points to a tight cluster in the slope-area plots for the 100 ka simulations. This effect also leads to variable valley width because the channels preferentially migrate up the tributary mouths and into the basins draining into the main channel.

In the transient cases, the lower slopes at small contributing areas are comparable to the slope of the main channel. These points are distinctly grouped apart from the points lying on or near the line. This cluster also appears to have, on average, decreasing slopes with increasing area; i.e., the longitudinal profiles of these channels are, on average, concave. Points in this lower cluster are new, valley bottom points. Therefore, they are either former channel points, i.e., oxbows, or points left in the wake of the channel on the slip-off slope. The oxbows become tributary channels with low-slope, weakly concave longitudinal profiles. Points on the slip-off slope have low contributing area because they are small and disconnected from the network, and their slope is controlled more by the lateral

migration rate, relative to the uplift rate, than by diffusion or fluvial erosion. With time, all of these points move up to steeper slopes on the slope-area plots and join the main point cluster as their slopes adjust to their small discharge.

At longer times, the lateral migration rate decreases from its initially large value. The landscape has adjusted such that migration is smaller relative to uplift/incision and, thus, the slip-off slopes now fall closer to the line of dynamic equilibrium. The first rapid stage of lateral migration exploits the tributary confluences because of their low relative elevation and, therefore, high erodibility. Eventually, as the channel migrates further into the tributary basins it encounters valley walls of increasing height and, in some cases, the domain boundary, and the migrations slows or, at the boundary, stops. With slower migration relative to uplift, steeper slip-off slopes are formed. Thus, the uplifting system adjusts toward dynamic equilibrium even with lateral channel migration because the bank erodibility is dependent on bank height, which can grow through uplift. The larger tributaries in the adjusted system typically have narrower valleys and steeper valley walls adjacent to the main stream than the tributaries in simulation **A** such that the tributary mouth is narrower and, therefore, affects the erodibility of a smaller part of the bank.

The model simulations represent an idealized case in which there is no alluvium in the valley. Natural streams are likely to have some alluvial deposits in the valley, and these deposits have a greater erodibility than the bedrock valley walls

5.6.3 Bank Erodibility's Bank Height Dependence

The different values of P_H produce quite different landscapes. The simulations with $P_H = 1.0$ look more realistic or, at least, more like the Buffalo River DEM (see

figure 3.2). One question I might ask about the Buffalo is, how long has the incising mean-dering process combination been active with respect to typical lateral migration rates? Does the Buffalo more closely resemble simulation **B**, where meandering has been active only a short time, or simulations **H** and **L**, where meandering has been active much longer? An interesting result of this modeling is that, given the system's adjustment to meandering, the only obvious difference between simulations **B** and, e.g., **H** is due to the finer discretization of some areas in simulation **H**. The slope-area plots are also similar (see figure 5.32).

The larger tributaries tend to skirt the areas visited by the channel in the long term simulations with $P_H = 1$, i.e., simulations **H** and **L**. The new points tend to slip off toward the valley walls because that is how the migrating channel has left them. So, especially where there has been a major cutoff, the middle of the valley has been left at relatively high elevations such that the tributaries tend to flow between these new topographic highs and the steep valley walls. These locations also correspond to the position of the channel before it was cut off.

The long term simulations with $P_H = 0.5$, i.e., simulations **F** and **J**, produced land-scapes that are quite different from those landscapes produced by simulations with $P_H = 1$, i.e., simulations **H** and **L**. In the simulations with $P_H = 0.5$, the system does not adjust as quickly or, possibly, as well because the migration rate is less dependent on the topogra-phy and, therefore, less influenced by adjustment through uplift. The channel, therefore, migrates more quickly, sweeps out a greater area, and cuts off more often. As a result, sev-

eral cutoffs are left with much less flow than before, and the resulting channels have an abnormally low slope where they follow the old cutoffs.

One reason for the different appearances of landscapes simulated with different P_H's is the greater primary sinuosity of the streams with low P_H and the similarity of the the bend and drainage spacing scales. Where primary sinuosity is large, meandering is the dominant influence on hillslope form because the slip-off slopes form in hillslope units too small to be dissected: their size is similar to the spacing of small tributaries along the main stream. Where primary sinuosity is small, however, the slip-off slopes form in hillslope units the size of the multi-loop bends, and these slopes are then large enough to undergo significant dissection by small tributaries.

5.6.4 Uplift and Meandering

Increasing bank erodibility's bank height dependence, P_H, slows lateral migration because the channel must erode more to move the same distance laterally. Increasing the uplift rate leads to greater channel and valley slopes, but the effects on the meandering are less clear. I might expect that greater uplift would lead to greater main channel slope and, therefore, lateral erosivity (see section 4.4.2, "Meander bend shape and evolution", on page 150). Conversely, I might also expect that greater uplift would allow the system to adjust more quickly to the channel migration, i.e., faster uplift leads to faster steepening of the valley walls. In the simulations, it appears that the total area swept out by the channel was slightly larger in the cases with greater uplift but much less than the two-fold increase that would be expected from the increase in lateral erosivity alone. So, greater uplift

should lead to only slightly greater lateral migration rate of an incising stream because the greater lateral erosivity is partially balanced by valley wall steepening.

The effect of the slope increase on the frequency of compound bend/multi-bend loop formation is marked. In the long term simulations with greater uplift, the channels migrate all the way to the boundary as they form multi-bend loops. Compound bend/ multi-bend loop formation is not inhibited by the steepening banks.

5.7 Conclusions

The CHILD model described in this chapter succeeds in coupling models of channel meandering and landscape evolution. Because the CHILD model is the first to achieve it, this coupling represents a major advance in the state of the art of landscape evolution modeling.

This chapter's results may be summarized as follows:

1. Coupling channel migration to the landscape through bank erodibility's bank height dependence, P_H, allows the system to adjust toward a new dynamic equilibrium.

2. Increased uplift leads to steepening channel slope and, therefore, greater bank shear stresses, but the effect on migration rate is muted because increased uplift also leads to steeper channel banks.

3. Steepening channel slope also leads to more compound bend/multi-bend loop formation, and this effect is not muted by the steeper banks.

4. Larger P_H leads to lower primary sinuosity and slower migration such that the simulated landscapes with greater P_H's are less chaotic in appearance because the hillslope-scale landscape features are shaped mainly by "vertical" processes.

5. Large uplift and P_H combine to increase multi-bend loop formation and decrease bend-scale sinuosity, respectively, such that the channel course resembles that of an "underfit" stream.

6. The simulations with $P_H = 1$ have a more realistic appearance than those with $P_H = 0.5$. This result may indicate that $P_H = 1$ is a more realistic value for channels incising into bedrock, though the similar scales of the bend length and the incisional hollow spacing may lead to the unrealistic appearance of the simulations with $P_H = 0.5$.

The modeling experiments in this chapter are the first to address the combined interactions of channel migration, bank erodibility's bank height dependence, and uplift. The results of increasing uplift call into question the conventional hypothesis that meandering is more active during periods of quiescent uplift (e.g., from *Lobeck* [1939, p. 227]: "Young rivers actively cutting downward do not meander."). The simulations produced the opposite result: meandering is more active when the uplift rate is greater because greater uplift leads to greater slopes and, therefore, greater lateral accelerations in channel bends. Of course, I have not considered other changes possibly resulting from greater uplift. It is possible that greater uplift could increase the channel slope enough to significantly reduce the residence time of the point bar-forming bedload required to produce lateral accelerations and migration. In that case, the lateral migration rate might be reduced. Also, I have not considered the effect of alluvial deposits and the contrasts in bank erodibility such deposits would cause. The model results are consistent with *Schumm*'s [1993] and *Schumm et al.*'s [1987] findings in the field and from experiments, respectively, that increased valley slope led to increased sinuosity in meandering alluvial channels.

The model results suggest a new hypothesis concerning observed slope-area relationships from DEMs. It is possible that the prevalence of a flat part in the slope-area relationship, as discussed above, is due to the prevalence of meandering in natural streams. If this hypothesis is true, then I would only need to increase the relative strength of diffusive processes in the model to see the effect more clearly in the simulations' slope-area relationships. The model results presented here have relatively weak diffusion and could correspond to the upper set of curves in figure 5.33.

Chapter 6

Future Directions

At the conclusion of this study, many questions remain unanswered, many areas unexplored. The TSRM model takes a fundamentally different approach to the meandering problem and opens up a whole range of new modeling possibilities. Similarly, I have only begun to explore the CHILD model's capabilities, some of which I introduced in Chapter 5 but did not employ. My investigations of meandering in the field served to narrow the range of possible answers to some questions, but more thorough studies are needed in order to satisfactorily answer these questions. Also, there are several loose ends left by the present work, and I discuss how I might resolve them.

6.1 TSRM Model Extensions

I am aware that the assumptions, approximations, and parameterizations inherent to the TSRM model are somewhat limiting, and I discuss ways in which the model could be improved. The TSRM model is different from other models of stream behavior. It is more rules-based than most LFE models (e.g., *Johannesson and Parker*, 1989a) and two-dimensional flow models (e.g., *Nelson and Smith*, 1989a) tend to be, but it is more physically and mathematically based than some rules-based models, such as the cellular braided stream model of *Murray and Paola* [1994]. Many variations on the TSRM model are possible with my approach. Also, I have not thoroughly examined the model's parameter space, e.g., with some kind of Monte Carlo scheme.

It would be interesting to more fully explore the model parameter space and to see the effect in the measures I introduced in Chapter 3. For example, I saw that compound bends show up as prominent secondary channel planform scale indicators; if I make grain size smaller and, thus, increase the frequency of compound bend formation, do the secondary channel planform scale indicators become more prominent? Can I eliminate the secondary channel planform scale indicators by increasing the grain size? One problem with investigating the model's parameter space is that there are so many parameters. Some parameter combinations are unrealistic and could be excluded, but defining the criteria for such exclusions is not straightforward. Another problem is that I lack simple measurements with which to characterize the model's performance as a function of some independent variable. For example, how do I characterize the prevalence and importance of compound bend formation? For example, I could design an algorithm to look for secondary peaks in $\sigma_S{}^2$, but it would be difficult to distinguish important, thick peaks from the noisy, thin peaks I see for the LFE model.

The bank shear stress smoothing is perhaps the most parameterized aspect of the model, and it would be useful to investigate alternatives. I could try other functions, e.g., exponential and gamma functions. I could allow shape to vary with lag, where the front end of the function is tied to the point of lateral momentum transfer, and spread is still a constant parameter, i.e., if lag is zero, the function is exponential, longer it is gamma, even longer gamma approaches a normal distribution.

I should explore the physical basis for the smoothing function. My measurements of bank roughness elements on the Ellis River are a first step in this direction. Does the

physics tell me what the smoothing function should be? Can I use my bank measurements to calculate a bank drag coefficient in a way similar to *Hopson and Smith* [1997]?

The model behavior becomes problematic with some parameter sets. For example, if the lag is long relative to the roughness scale, forces in one direction may not be counteracted by the next forcing in the opposite direction. Instead, the first force will be applied as shear stress downstream of the second forcing and before the shear stress from the latter forcing. Clearly, this phenomenon is not physical and represents a case where the model's assumptions and approximations are not valid. Is there a better, still simple way to model the lag mechanism? What can I get from the flow equations? Alternatively, is there a simple way to track the position of the flow core such that the above phenomenon cannot occur?

Some of the details of the lateral momentum transfer formulation bear some scrutiny. Can I use special cases of the scaled flow equations (see appendix B) to get a better, still simple expression? Could the same equations also yield a simple solution, i.e., another way to derive a simple, fast, nonlinear model, as was my goal with the TSRM model?

I would like to investigate further the conditions necessary for compound bend and multi-bend loop formation. Under what conditions do compound bends become multi-bend loops, and why?

6.2 CHILD Model Extensions

I have dealt with only a small part of the CHILD model's present and near-future capabilities. Unfortunately, I was unable to address many of the issues of channel-landscape inter-

action, such as the issue of varying valley width, that I discussed in Chapter 3. Here, I outline some possible future model experiments.

The first next step is to try out more of the model's existing capabilities, listed in Chapter 5. The most basic next step is to run the meandering model with capacity-limited or detachment- and capacity-limited sediment transport. Then, investigate the more advanced runoff generation mechanisms, e.g., saturation overland flow. Next, investigate the different erosion limitations with stochastic rainfall and advanced hydrology. These experiments could be done with the valley scenario presented in Chapter 5, but I should also look at meandering and the other processes mentioned above in the context of a drainage basin. Even for the detachment-limited case with uniform runoff, it would be interesting to examine the effect of meandering on the stream network. Lateral migration could have something like an optimization effect on the network similar to evolving a network with the optimal channel network (OCN) model [*Rodriguez-Iturbe, et al.*, 1992]*,* where the network is optimized by randomly changing the paths of network links and keeping only the changes which reduce the network's energy dissipation. Over the long term, lateral channel migration could produce a similar result by providing the mechanism by which network links might change their course. The process dynamics and interactions, rather than an optimization rule, would create the criteria for "keeping" the changes.

As I showed in Chapter 4, the meandering model is sensitive to bed material grain size. In the TSRM model sensitivity analysis of Chapter 4and the CHILD model simulations of Chapter 5, grain size is a free parameter. However, to effectively test process interactions in a drainage basin the grain size should be determined by the system dynamics. The most important incomplete CHILD model component is the capability to erode, trans-

port, and deposit sediment with multiple grain sizes. I will not deal with all of the issues here; *Gasparini, et al.* [1997, 1998] combined a multiple grain size transport model [*Wilcock and McArdell*, 1993] and a sediment layering scheme with GOLEM, the rectangular-grid landscape evolution model by *Tucker* [1996] (see also: *Tucker and Slingerland*, 1994, 1996, 1997; and *Tucker and Bras*, 1998). In the CHILD model, treatment of multiple grain sizes must include source materials, transport, and layered deposits in the context of a moving channel on a dynamic, irregular grid.

In Chapter 3, I raised the question of the effect of different source materials on the rate of lateral channel migration for the Buffalo River, AR. I proposed the hypothesis that changes in source material texture, rather than rock strength, could be the mechanism behind the corresponding valley width and lithology changes. In Chapters 4 and 5 I showed that modeled rate and style of lateral channel migration is sensitive to bed material grain size, and the mechanism by which this happens is physically reasonable. The latter findings tend to support the above hypothesis, but it could be more thoroughly tested with the CHILD model with meandering and multiple grain sizes.

Gasparini, et al. [1997, 1998] showed that climate change can have a dramatic effect on channel bed material texture throughout a drainage basin, especially in the short term. Specifically, they found that, following an increase in rainfall rate, a "wave" of fining propagated from the source areas through the channel system before the bed material throughout the basin became generally coarser. I showed in Chapter 5 the dramatic transient effect of "turning on" meandering in a river valley previously in dynamic equilibrium. A similar change might occur given a fining of bed material or an increased rate of

bar-forming sediment input. I could examine the dynamics of these interactions with the complete CHILD model.

The CHILD model was designed, in part, to examine hillslope-channel interaction and possible feedbacks in that interaction. For example, does the channel have a positive or negative feedback effect on hillslope erosion? If the latter increases, do the actions of the former act to moderate and dampen or aggravate and force further hillslope erosion? An argument for a dampening effect is the following: hillslope erosion increases sediment delivery to the channels which respond with aggradation which increases the base level of the hillslopes and decreases their slope and, therefore, their erosion rate. An argument for a forcing effect is: hillslope erosion increases sediment delivery to the channels which respond by forming point bars and increasing their lateral erosion rate which erodes the toes of and, therefore, steepens the hillslopes and leads to greater hillslope erosion.

In Chapter 5 I raised the question: Does greater lateral channel migration accompany periods of quiescent or active uplift? Conventional wisdom says the former (e.g., *Lobeck*, 1939), but my results say that increasing the uplift rate also increases the lateral migration rate. However, I noted that my modeling did not account for the effect of uplift on bed material. Streams with a higher incision rate are more likely to flow on bedrock, while slower incision may lead to aggradation, the formation of point bars, and, thus, increased lateral migration. On the other hand, accelerated incision would likely increase channel slope, therefore, bedload sediment flux, and, as the nickpoint moves upstream, hillslope erosion. The resulting increase of bedload sediment could promote the formation

of point bars even as the increase in channel slope increases its erosive energy, and the two effects could combine to increase lateral migration rates.

The CHILD model should include a mechanism for overbank deposition. *Howard* [1992] modeled overbank deposition rate as a function of elevation and distance from the channel:

$$\phi = (z_{max} - z)\left[\nu + \mu\exp\left(-\frac{r}{\lambda_d}\right)\right]$$ (6.1)

where z_{max} is the upper elevation limit on overbank deposition; ν is the position independent fine sediment deposition rate; μ is the deposition rate of coarser sediment by overbank diffusion; r is the shortest distance to the channel; and λ_d is the length scale of the deposition rate decay with distance from the channel [*Pizzuto*, 1987]. *Howard* [1996] pointed out that the choice of z_{max} was arbitrary and proposed a modified form of the equation with exponential elevation dependence. He argued that such a form was better for modeling the cumulative effect of all flood events. In the CHILD model, I may stochastically generate storms whose magnitude is exponentially distributed. Once I figure out how to determine maximum flood stage, z_{max}, based on discharge magnitude, the cumulative effect of equation (6.1) with stochastically generated storms may be similar to the modified expression of *Howard* [1996].

The recent work of *Mertes* [1997], my results from the Ellis River, and other field studies (R. Jacobson, personal communication, 1995) indicate that such a model may be too simple to produce realistic floodplain deposition. For example, my Ellis River floodplain coring shows that the thickness of fine deposits generally increases toward the

upstream end of individual point bars on the floodplain (see figure 3.20). The *Howard* [1992] model may produce similar patterns in some cases, but I must wonder whether it does so for the right reasons. Nevertheless, a model along the lines of equation (6.1) provides at least a first approximation of the overbank deposition process.

Finally, I call attention to some of the loose ends in the CHILD modeling study. In the slope-area plots, I should weight the slopes in the bin averages by the Voronoi areas of the corresponding points in order to get a more accurate picture of the trends in mean slope. I should examine the CHILD model channels with the planform measures introduced in Chapter 3 and investigate the sensitivity of the model results to parameter changes through these measures.

6.3 Studies of Natural Streams

The field studies of Chapter 3 serve to illuminate how many questions are unanswered. In that chapter, I scratched the surface of what needs to be done in order to begin verifying the modeling of this work.

I would like to conduct a more thorough study of scroll bar topography in order to determine its mechanism. Issues include the following:

1. What are the scaling properties of scroll bars in terms of their wavelength, amplitude, curvature, and length relative to channel properties such as width, depth, meander wavelength, and migration rate?

2. What is the role of vegetation? Are only some scroll bars formed as a result of systematic variations in vegetation roughness? If so, how do different forms relate to different mechanisms?

3. Is elevation on the floodplain correlated with migration rate at the time of lateral accretion? If so, are topographic highs associated with fast or slow migration rates? My Ellis River study suggests that highs are associated with fast rates; is this a spurious result?

4. Is elevation on the floodplain correlated with channel curvature at the time of accretion as in the TSRM model?

I would like to study the effects on lateral channel migration of gravel inputs, sudden changes in bed texture or grain size, and changes from bedrock to alluvial streams. I may be able to conduct such a study in the Oregon Coast Range. A large storm event in 1996 initiated a large number of landslides, and, thus, large quantities of sediment were introduced into the channel network. Much of that sediment has since moved through the system, but its movement has been slowed at some locations and created gravelly alluvial reaches. Does this gravel initiate lateral channel migration? On Knowles Creek in the Oregon Coast Range I observed a site where the gravel has formed what appear to be small point bars, and there is evidence of lateral erosion in the form of undercut banks. These observations lend support to the topographic steering hypothesis. Further monitoring and study at this site might reveal whether this lateral migration initiates a positive feedback effect in which bank failures maintain the gravel supply such that the migration continues; or whether the gravel eventually gets flushed from the system such that the long term effect is small.

Can I determine in the field what P_H is for a particular site? Is it a function of material, rate, or both? P_H could simply be a function of the fraction of coarse material in the bank material, where fine materials are detachment-limited and coarse materials must be re-eroded. Or it could be the other way around. If the migration rate is slow enough that the input of sediment from bank erosion is small relative to the sediment flux in the channel, then coarse materials which lack cohesion may behave as detachment-limited because they crumble when undermined and represent an insignificant addition to the channel's bedload. Fine, cohesive materials, on the other hand, remain intact as slump blocks when undermined and must be eroded directly by the channel flow. If the migration rate is fast

enough that the input of sediment from bank erosion is large relative to the sediment flux in the channel, then the removal of coarse materials from the bank may be limited by the transport capacity of the channel flow. Fine materials, if their proportion is small may simply wash away.

I should be able to quantify bank roughness in terms of dissipation of turbulent energy through boundary layer development. In the case of the Ellis River, bend 6, I was able to find the average dimensions of the bank roughness elements. Such information should enable me to calculate a bank drag coefficient and, thus, turbulent energy dissipation rate and scale; i.e., calculate the TSRM model bank roughness scale, λ.

My work on the Ellis River brought the role of large woody debris (LWD) to my attention. Does LWD simply enhance channel roughness? Is it more important on the bank or the bed? Does it behave differently in meandering and non-meandering channels? I found evidence on the Ellis River that the LWD may stay in place and be covered over by the accreting point bar. If so, then there would be a limit to how much could accumulate in the channel. In a non-meandering channel, LWD accumulates and stays in the channel until it is transported out, whereas LWD in the meandering channel may just get covered up after a time. How old were the logs I saw in the Ellis River channel? Were they all from relatively recent bank failure, or were some of them left over from the last time the channel migrated through that area and uncovered by recent channel migration? If the latter, then the accumulation of LWD might eventually reach some critical state in which it is either moved or dams up the reach. Or, the LWD may just eventually rot underground. Or it may not, in general, get covered over after all but, rather, be transported relatively

quickly. In the case of streams in the Oregon Coast Range, does the LWD characteristic of old growth roughen the channel such that the residence time of gravel and, thus, the activity of lateral erosion is greater? Does the absence of old growth fundamentally change patterns of process dominance and dynamics?

One advantage of the *Howard and Hemberger* [1991] analysis is the ability to place many streams, both model and natural, together on a plot. It would be useful if I could use my own measurements to compare different channel planforms on the same plot, as in *Howard and Hemberger* [1991]; e.g., does the first plateau in mean sinuosity correlate meaningfully with relative meander belt width at the lower length scale of that plateau? By plotting the streams together, I could see the ranges of characteristics of natural and model streams and the relative effects of model parameter changes. It is not clear at this time how I could use the present measurements to create such a plot. Its development might require the derivation of additional new measures.

Murray and Paola [1996] developed a dynamical systems approach to measuring the behavior of braided streams. Their method utilized measurements of total channel width and is, therefore, not directly applicable to the TSRM model, which assumes a constant width. However, I might be able to use another variable, such as flow direction or curvature, to develop a similar "state-space" plot characterizing meandering streams.

For the measures that already exist, I need to better understand what they reveal about channel planform. One way to gain such understanding would be to apply the measures to idealized planforms in order to infer what the measures of natural planforms mean.

There are several loose ends remaining with respect to the signature of the meandering process in the slope-area relationship. I should map pixels on the DEM, and even nodes on the CHILD model mesh, to points on the slope-area plot in order to ascertain the impact of the various valley features on the plot. How does DEM pit filling affect the slope-area relationship in the valley? If the artifacts of pit filling are significant, it might be useful to obtain a high-resolution DEM of a meandering channel valley in order to find the slope-area relationship more accurately. I should also look at the slope-area relationship for different meandering streams, such as the Buffalo River, to see how the plots are affected by valley width and form.

Another issue brought up in my examination of Buffalo River valley width is the following: How can I tell whether specific reaches are capacity- or detachment-limited? Does the presence of bedload always imply capacity limitation? I may ultimately find that these cases are merely end members.

Chapter 7

Discussion and Conclusion

This chapter summarizes the previous chapters and discusses some implications of the broader work that were addressed in those chapters. Finally, I draw some specific conclusions.

Chapter 2 introduced the topic of landscape evolution modeling. The main thrust of the review was to motivate the inclusion of processes usually ignored in these models and, in particular, lateral channel migration. Chapter 2 also introduced the topic of river meandering and the importance of topographic steering in that process.

Chapter 3 addressed meandering in natural streams and, specifically, compound bend formation, scroll bar topography, bank failure and roughness, and meandering-landscape interaction. A major finding was that compound bends on the Ellis River, Maine, develop from simple bends during periods of rapid channel migration initiated by upstream cutoffs and that compound bends sometimes separate to form multi-bend loops. I developed several measures of meandering channel planform which can and did detect the presence and importance of multi-bend loop formation in channel planforms of meandering Alaskan streams.

On the Ellis River, lateral accretion of the point bar was fast where the ridges had formed and slow in the swales. It follows that the rapid migration following a cutoff led

not only to the formation of a compound bend but also to the rapid accretion of these new-est ridges. I concluded that rough vegetation on the point bar probably contributed to the ridge formation by trapping sediment. In this respect, vegetation plays similar roles on the Ellis River and on the Current River, Missouri. Spectral analysis showed that the scroll bar topography on the Ellis and Mississippi River floodplains was not clearly periodic but only quasi-periodic.

On the Ellis River, I found that banks were undermined by scour and failed in clumps defined by tree root wads. The typical size of these root wads also places a lower limit on the width of a meander loop's neck before it cuts off.

I examined the role of meandering in the landscape by looking at the slope-area relationship for Schoharie Creek, New York, and the relationships among valley width, lithology, and channel slope on the Buffalo River, Arkansas. For the Schoharie Creek val-ley, low slopes on flat valley bottoms and high slopes on valley sides are independent of contributing area and may lead to a commonly observed but previously not understood feature of natural slope-area relationships. For the Buffalo River, valley width is probably dependent on the size of bedload particles and their amount as much as or more than the strength of the rock forming the valley walls. It may be that, in this case, bedrock incision is transport- rather than detachment-limited.

Chapter 4 introduced the topographic steering river meandering (TSRM) model. This model takes a different approach to the problem of river meandering. In this approach, some of the physics may appear relatively crude compared to the mathemati-cally precise derivations of LFE models but really only represent a different way of

approximating the behavior of the active physical processes. Within the constraints imposed by the model assumptions, such approximations may not be any less accurate than those made in LFE models. In fact, the TSRM model approach captures important physics and mechanisms, particularly compound bend formation, that other models lack. The approach was immersion in the literature of field and experimental studies of meandering, breaking the process physics down into simple, easily understood pieces, and putting those pieces back together in a new model. I determined the importance of various processes and mechanisms based on empirical evidence. The studies at Muddy Creek by W.E. Dietrich and his co-authors in particular provided much of the information needed to determine what the pieces were and which to include. Along the separate but complimentary line of investigation taken by J.D. Smith and co-authors, I eventually found that scaling the flow equations according to a slightly different set of assumptions yielded terms resembling my expression for lateral momentum transfer (see Appendix B).

Perhaps the most important lesson from the TSRM model is the answer to this question: What must a meandering model include to reasonably, approximately describe the meandering process? Evidence from the literature indicates the importance of the bed topography and that a reasonable assumption is that the topography is due solely to the curvature-induced, helical part of the secondary flow. This assumption is further supported by the finding that, in the special case of large but gradually changing curvature, the scaled flow equations reduce to two terms, both in the lateral momentum equation: the lateral shear stress at the bed and the curvature-induced lateral flow acceleration (see Appendix B, equation (B.5.4)). So, both empirical and theoretical evidence indicates that the assumptions concerning bed topography are reasonable.

The topographic steering calculation does not describe how and where the shear stress is applied to the bank. The topographic steering effect is strongest where curvature is changing most rapidly, at the bend entrance, but meander bends, at least small ones, migrate downstream. In simplifying the problem, I had not described how a force at the bend entrance leads to shear stress on the bank downstream. The simplest way to project the effect of the force downstream worked well—better, in fact, than the more complicated methods devised later and discarded. Numerical stability and common sense said that this force would not all be spent at one point, that I needed to describe the turbulent dissipation of that force along the bank as shear stress. A simple Gaussian smoothing was a sufficient parameterization of that turbulent dissipation.

Topographic steering is of sufficient magnitude to cause the bank shear stress, and this expression, in combination with the other parts of the model, produces realistic results and simulates the previously unexplained phenomenon of compound bend formation. The magnitude of the predicted topographic steering force is similar to that of the total bed shear stress, and this result is in line with observations. In the special case of small but quickly changing curvature in the scaled flow equations, the topographic steering terms are dominant (see Appendix B, equations (B.5.1), (B.5.2), and (B.5.3)). So, again, both empirical and theoretical results support the formulation, though I acknowledge that the derivation of topographic steering is far from perfect and might bear some modification guided by the scaled flow equations.

The model yielded results pertinent to the findings of Chapter 3. The model produced compound bends much as they were formed on the Ellis River and multi-bend loops

that produced both primary and secondary channel planform scale indicators, as found for the Alaskan streams in Chapter 3. Also, the frequency of compound bend formation was sensitive to model parameters that affected the location in the bend of maximum bank shear stress. Parameter changes, such as decreasing median bedload grain diameter or increasing channel slope, that caused that location to shift toward the beginning of the bend produced more compound bend and multi-bend loop formation. More multi-bend loop formation leads to wider valleys and greater variation in valley floor age. The landscape is, of course, the source of discharge and bedload and determines channel slope. Thus, characteristics of the landscape influence compound bend and multi-bend loop formation and, in turn, determine the effect of meandering on that landscape. Also, bank roughness and compound bend formation are related. The bank roughness parameter is the major control on bend size, and its size relative to the downstream lag influences bend shape and compound bend formation. For example, decreasing the bank roughness corresponds to increasing the smoothing scale and the bend size with respect to the downstream lag; smaller downstream lag with respect to the bend size increases the frequency of compound bend formation; therefore, decreasing bank roughness would lead to a greater frequency of compound bend formation.

The model also formed floodplain topography resembling scroll bar topography through the spatio-temporal variation of channel curvature, proportional to point bar height in the model. This model scroll bar topography was, like the Ellis and Mississippi scroll bar topography, quasi-periodic. The model also formed bands of alternating fast and slow channel migration related to the occurrence of upstream cutoffs. This mechanism is more likely related to the mechanism forming scroll bar topography in nature.

Chapter 5 introduced the channel-hillslope integrated landscape development (CHILD) model. Building the CHILD model required devising a new way to represent the migration of a channel in the landscape and a new set of rules to govern and describe that migration. The CHILD model uses a dynamic, irregular mesh to represent the landscape and incorporates the TSRM model as a component landscape process. The development of this model involved some additional conceptual modeling, such as the parameterization of bank erodibility's bank height dependence, but for the most part presented implementation problems related to the data structure and the movement of channel nodes in the model landscape mesh. Specifically, I developed new algorithms and rules to deal with finding bank nodes, removal of nodes from eroding banks, and addition of nodes to accreting point bars.

The landscape and channel forms produced by the model were quite sensitive to the magnitude of bank erodibility's bank height dependence. As expected, the latter affects the channel's migration rate. Larger bank height dependence leads to greater interaction between the channel and the landscape and, thus, faster and more thorough adjustment of the system toward a new dynamic equilibrium through valley wall steepening. Prior to this adjustment, the initially low banks led to transient states in which the valley floor was flattened by rapid lateral channel migration. Migrating channels for which bank erodibility's bank height dependence is larger have lower bend-scale sinuosity but still form multi-bend loops. The slope-area relationships of the transient cases were affected by meandering such that the plots are similar to the slope-area plot for the Schoharie Creek valley in Chapter 3 and, thus, support the hypothesis that, in nature, meandering is responsible for the "step" in the mean slope's trend.

Increasing the uplift rate led to both greater bank shear stress by increasing channel slope and lower bank erodibility by increasing bank height such that migration rate increased by a small amount. Thus, the channel migration rate is only weakly sensitive to uplift rate. The frequency of compound bend and multi-bend loop formation increased with greater uplift and, therefore, channel slope. The steepening of the valley sides may even reinforce the tendency to form multi-bend loops.

The CHILD model will allow investigation of many aspects of river basin evolution. In the present work, I have focussed on the interaction between a meandering channel and its valley, but future studies will address the interaction between landsliding and channel evolution.

In conclusion, the modeling studies benefited greatly from previous field studies and, in turn, motivated new field studies by making testable predictions. I expect future work to involve a similar close coupling of modeling and field studies.

I cannot rule out the possibility that scroll bar topography is associated with changing channel curvature, but the data from the Ellis River suggest that scroll bars are associated with large variations in channel migration rate.

Compound bend formation is an integral and important part of the meandering process. It leads to multi-bend loo formation and, thus a secondary sinuosity. The models reproduce this effect to a degree that is sinsitive to model parameters such as bed material grain size, channel slope, and bank roughness. Unlike migration rate, this effect is not suppressed byb steeper banks when uplift rate increases.

Channel banks are an important part of the coupling between channel migration and the landscape. By their roughness, they influence the size of meander bends and the frequency of compound bend formation. By their height, they influence bank erodibility and, thus, the channel migration rate such that the steepening banks associated with more rapid uplift dampen the effect of increasing bank shear stresses associated with the corresponding increase in channel slope. Variations in bank erodibility's bank height dependence affect the appearance of the landscape when the bend length and channel spacing are of similar magnitude. Channel bank steepening is the mechanism by which the drainage system adjusts to the onset of meandering and approaches a new dynamic equilibrium.

Appendix A

Derivation of the Transverse Bed Slope

A.1 Neglecting Bedforms

This derivation is similar to that of *Ikeda* [1989]; the reader is referred to that work for explanation of some of the assumptions and reasoning implicit in the following derivation.

The lateral force balance for a bed grain particle is

$$D_r + (M - m)g\sin\phi - \frac{\mu[(M - m)g\cos\phi - L_f]V_{pr}}{V_p} = 0 \tag{A.1.1}$$

where M is the particle mass; m is the fluid mass; ϕ is the transverse bed slope angle; μ is the dynamic Coulomb friction coefficient; L_f is the lift force; V_p is the particle velocity; V_{pr} is the radial component of the particle velocity; and D_r is the radial component of the drag force:

$$D_r = \frac{D(U_{br} - V_{pr})}{U_b - V_p} \tag{A.1.2}$$

where D is the total drag force on the particle; U_b is the fluid velocity at the bed; and U_{br} is the radial component of the fluid velocity at the bed. In this derivation I simplify the assumptions made by *Ikeda* [1989] and extrapolate my simplified result to apply under the more complicated set of assumptions. Specifically, in the following derivation I assume that, at the equilibrium bed slope, the radial component of the particle velocity is zero ($V_{pr} = 0$). Under this assumption, I get

$$\sin\phi = -\left(\frac{r}{R}\right)^2 \frac{h}{r}\sqrt{\Psi}\left(\frac{2.6}{\sqrt{C_f}} - 2.2\right) \tag{A.1.3}$$

249

where Ψ is the dimensionless shear stress, or "Shields stress",

$$\Psi = \frac{\tau}{\rho(s-1)gd} \tag{A.1.4}$$

Ikeda's formula accounting for the critical shear stress for the initiation of particle motion is

$$\frac{dh}{dr} = \left(\frac{r}{R}\right)^2 \frac{h}{r} \sqrt{\frac{\Psi}{\Psi_{cr}}} \left(\frac{0.2278}{\sqrt{C_f}} - 0.3606\right) \tag{A.1.5}$$

which is the solution when the total shear stress, form drag plus skin friction, determines the transverse bed slope. I have skipped many steps in the derivation of equation (A.1.3) because a more complete derivation exists in the literature [*Ikeda*, 1989] and it is similar the derivation which follows below.

A.2 Including Bedforms

To find the transverse bed slope caused by skin friction, I need to take the derivation a step further because the radial component of the near-bed velocity at the sand grains is less than what I have derived for the total shear. Let U_{br} be the radial component of the flow velocity at the top of the form drag roughness layer and U' be the average velocity within that roughness layer; i.e., the average velocity in the layer affected by skin friction. I assume that the wavelength of the bedforms is related to the depth of flow:

$$\lambda_{bf} = 2\pi h \tag{A.2.1}$$

and let the height of the dunes, h_d, be related to the bedform wavelength, λ_{bf}, by

$$h_d = \frac{1}{10}\pi h \tag{A.2.2}$$

   The skin friction drag force (see equation (A.1.1)) is

$$D' = \frac{1}{8}\rho C_d \pi d^2 (U_b' - V_p)^2 \tag{A.2.3}$$

and its radial component is

$$D_r' = \frac{D'(U_{br}' - V_{pr})}{U_b' - V_p} \tag{A.2.4}$$

Assuming a log-profile for flow velocity and the Nikuradse equivalent sand grain roughness equal to the particle diameter, I solve for the average velocity between the bed and the dune height, h_d, as the velocity at height h_d/e:

$$U' = \frac{1}{\kappa}\sqrt{\frac{\tau'}{\rho}}\ln\left(\frac{11.0 h_d}{d}\right) \tag{A.2.5}$$

where τ' is the skin friction [Ole Madsen, class notes, 1996].

If I assume that the near-bottom boundary-layer radial velocity is related to the average boundary-layer velocity in a way similar to the relation neglecting the effect of skin friction (see *Ikeda*, 1989), then I can solve for the skin friction factor,

$$C_f' = \frac{\kappa^2}{\ln\left(11.0\dfrac{h_d}{d}\right)^2} \tag{A.2.6}$$

and the radial component of the near-bed (elevation above the bed goes to zero) skin friction roughness layer velocity:

$$U_{br}' = 0.349\frac{\sqrt{\dfrac{\tau}{\rho}}\,rh\left[-1.00 + 3.00\ln\left(11.0\dfrac{h_d}{d}\right)\right]}{\kappa^2 R^2} \tag{A.2.7}$$

The relationship between the near-bed velocity, U_b', and the particle velocity is [*Ikeda*, 1989]:

$$U_b{}' = V_p + \frac{2\sqrt{3}}{3}\sqrt{\frac{\mu(s-1)gd}{C_d(1+\alpha\mu)}} \tag{A.2.8}$$

Substituting for D', U_{br}', V_{pr}, U_b', and V_p, I get

$$D_r{}' = \sqrt{3}\pi\frac{\rho d^3\mu(s-1)g\sqrt{\frac{\tau}{\rho}}rh\left[-1+3\ln\left(11.0\frac{h_d}{d}\right)\right]}{(1+\alpha\mu)\kappa^2R^2\sqrt{\frac{\mu(s-1)gd}{C_d(1+\alpha\mu)}}} \tag{A.2.9}$$

Finally, I define the dimensionless skin friction as

$$\Psi' = \frac{\tau'}{\rho(s-1)gd}. \tag{A.2.10}$$

Table A.1: Transverse bedslope dimensionless parameters

parameter	symbol	value
drag coefficient	C_d	0.4
dynamic Coulomb friction coefficient	μ	0.43
ratio of lift and drag coefficients	α	0.85
von Karman's constant	κ	0.4
particle sphericity	β	1.0
ratio of sediment and water densities	s	2.65

Let θ be the transverse bed slope angle due to skin friction. I solve the force balance (equation (A.1.1) with "primes") for

$$\sin\theta = \frac{\sqrt{\mu C_d}}{\kappa^2\beta\sqrt{1+\alpha\mu}}\left(\frac{r}{R}\right)^2\frac{h}{r}\sqrt{\Psi'}\left[-0.91\ln\left(\frac{h}{d}\right)-0.83\right] \tag{A.2.11}$$

Or, from table A.1, equation (A.2.6), and equation (A.2.2),

$$\sin\theta = -\left(\frac{r}{R}\right)^2\frac{h}{r}\sqrt{\Psi'}\frac{h_d}{h}\left(\frac{2.6}{\sqrt{C_f'}}-2.2\right) \tag{A.2.12}$$

which is nearly identical to equation (A.1.3) except for dependence on the skin friction

Shields parameter and friction factor and the ratio of skin friction roughness layer depth to

total depth, which is just

$$\frac{h_d}{h} = \frac{\Psi'}{\Psi} \tag{A.2.13}$$

Assuming that the necessary modification of equation (A.2.12) to account for the thresh-

old of particle motion is similar to the modification of equation (A.1.3) to get

equation (A.1.5) and using table A.1 and equation (A.2.13), I have

$$\frac{dh}{dr} = \left(\frac{r}{R}\right)^2 \frac{h}{r} \frac{\Psi'}{\Psi} \sqrt{\frac{\Psi'}{\Psi_{cr}}} \left[\frac{0.2278}{\kappa} \ln\left(11\frac{h}{d}\frac{\Psi'}{\Psi}\right) - 0.3606\right] \tag{A.2.14}$$

I define the transverse slope, S_T, as equation (A.2.14) evaluated at the channel centerline,

where $r=R$ and $h=H$. The radius of curvature, R, is just the inverse of the curvature, C. So,

I have

$$S_T = KHC \tag{A.2.15}$$

$$K = \frac{\Psi'}{\Psi} \sqrt{\frac{\Psi'}{\Psi_{cr}}} \left[0.5695 \ln\left(11\frac{H}{d}\frac{\Psi'}{\Psi}\right) - 0.3606\right] \tag{A.2.16}$$

which is identical to equation (4.3). In the above derivation I assume that all references to

grain diameter, d, refer to the median grain size, d_{50}. The appropriate quantile of grain size

in equation (A.2.5) is actually d_{65}, but, because this term is inside the logarithm, the use of

d_{50} does not introduce much error.

Appendix B

Scaling the Depth-Averaged Flow Equations

B.1 Scaling Parameters for Nondimensionalization

I begin by identifying the spatial scales I am interested in. Other authors (e.g., *Johannesson and Parker*, 1989) have typically used the meander wavelength to scale downstream distances though they are modeling accelerations over much shorter distances.

Dietrich and Whiting [1989] showed that strong convective accelerations may occur over downstream distances much shorter than the meander wavelength and even shorter than the channel width. Therefore, it is appropriate to scale down- and cross-stream distances with the same value, in this case the channel width. I scale vertical distances by the average channel depth. Thus I define the non-dimensional coordinates,

$$\hat{s} = \frac{s}{b} \tag{B.1.1}$$

$$\hat{n} = \frac{n}{b} \tag{B.1.2}$$

$$\hat{z} = \frac{z}{H} \tag{B.1.3}$$

where s, n, and z are the downstream, cross-stream, and vertical directions, respectively; b is the channel width; and H is the average channel depth. Likewise, I scale curvature, flow depth, and bed elevation:

$$\hat{C} = Cb \tag{B.1.4}$$

$$\hat{h} = \frac{h}{H} \tag{B.1.5}$$

$$\hat{\eta} \; = \; \frac{\eta}{H} \qquad \qquad \text{(B.1.6)}$$

I have scaled the curvature with the channel width, similar to the inverse of down-stream and cross-stream coordinates. However, terms proportional to curvature will gener-ally be smaller than terms proportional to $1/\partial s$ and $1/\partial n$ because, while $1/\partial s$ and $1/\partial n$ are usually greater than the channel width, b, curvature, C, is always less than b. In places where curvature is small, terms proportional to curvature will be much smaller than terms proportional to $1/\partial s$ and $1/\partial n$ as long as the downstream rate of change of curva-ture, $\partial C/\partial s$, is large.

Dietrich and Smith [1983] found that lateral flow velocities may be comparable to downstream velocity over short distances. Therefore, I scale both downstream and lateral velocities by the average downstream velocity, U_0:

$$\hat{U} \; = \; \frac{U}{U_0} \qquad \qquad \text{(B.1.7)}$$

$$\hat{V} \; = \; \frac{V}{U_0} \qquad \qquad \text{(B.1.8)}$$

Though I am not directly concerned with vertical velocity, I will need it to scale shear stresses:

$$\hat{w} \; = \; \frac{w}{W} \qquad \qquad \text{(B.1.9)}$$

where W is a typical vertical velocity, where $W<<U_0$.

Changes in water surface elevation are generally not comparable to those in water depth and bed elevation. The average water surface slope is related to the friction factor and flow velocity:

$$\frac{gH}{b}\frac{\partial E}{\partial \hat{s}} \sim C_f U_0^2 \tag{B.1.10}$$

$$\partial E \sim C_f U_0^2 \frac{b}{gH} \tag{B.1.11}$$

And I define the non-dimensional water surface elevation:

$$\hat{E} = E\frac{gH}{C_f U_0^2 b} \tag{B.1.12}$$

B.2 Downstream Momentum Conservation Equation

I use the depth averaged equations used by *Smith and McLean* [1984]. In the downstream, or *s*, direction, I write:

$$\frac{\rho}{1-nC}\frac{\partial}{\partial s}U^2 h + \rho\frac{\partial}{\partial n}UVh - 2\frac{\rho}{1-nC}UVhC = \frac{\rho gh}{1-nC}\frac{\partial}{\partial s}E + \frac{1}{1-nC}\frac{\partial}{\partial s}\tau_{ss}h$$

$$\ldots + \frac{\partial}{\partial n}\tau_{ns}h - \frac{2}{1-nC}\tau_{ns}hC + \frac{1}{1-nC}\tau_{ss}\Big|_{\eta}\frac{\partial\eta}{\partial s} + \tau_{ns}\Big|_{\eta}\frac{\partial\eta}{\partial n} - \tau_{zs}\Big|_{\eta} \tag{B.2.1}$$

Applying the scaling relations of the previous section and canceling like terms, I have:

$$\frac{1}{1-\hat{n}\hat{C}}\frac{H}{b}\frac{\partial}{\partial \hat{s}}\hat{U}^2\hat{h} + \frac{H}{b}\frac{\partial}{\partial \hat{n}}\hat{U}\hat{V}\hat{h} - \frac{2}{1-\hat{n}\hat{C}}\frac{H}{b}\hat{U}\hat{V}\hat{h}\hat{C} = \frac{1}{1-\hat{n}\hat{C}}C_f\hat{h}\frac{\partial}{\partial s}\hat{E}$$

$$\ldots + \frac{1}{1-\hat{n}\hat{C}}\frac{H^2}{b^2}\frac{\partial}{\partial s}\hat{\tau}_{ss}\hat{h} + \frac{H^2}{b^2}\frac{\partial}{\partial \hat{n}}\hat{\tau}_{ns}\hat{h} - \frac{2}{1-\hat{n}\hat{C}}\frac{H^2}{b^2}\hat{\tau}_{ns}\hat{h}\hat{C}$$

$$\ldots + \frac{1}{1-\hat{n}\hat{C}}\frac{H^2}{b^2}\hat{\tau}_{ss}\Big|_{\eta}\frac{\partial}{\partial \hat{s}}\hat{\eta} + \frac{H^2}{b^2}\hat{\tau}_{ns}\Big|_{\eta}\frac{\partial}{\partial \hat{n}}\hat{\eta} - \hat{\tau}_{zs}\Big|_{\eta} \tag{B.2.2}$$

I now assign values of ε to small numbers of $O(1/10)$:

$$\varepsilon = \{\frac{H}{b}, \sqrt{C_f}\} \tag{B.2.3}$$

Substituting ε in equation (B.2.3), dropping terms of $O(\varepsilon)$, and switching back to dimensional terms, I have:

$$\frac{\rho}{1-nC}\frac{\partial}{\partial s}U^2h + \rho\frac{\partial}{\partial n}UVh - 2\frac{\rho}{1-nC}UVhC = -\tau_{zs}|_\eta \tag{B.2.4}$$

I do note, however, that the third and sixth terms on the right hand side of equation (B.2.1) will be large near the banks.

B.3 Cross-Stream Momentum Conservation Equation

I write the depth-averaged conservation of momentum in the cross-stream, or n, direction:

$$\frac{\rho}{1-nC}\frac{\partial}{\partial s}UVh + \rho\frac{\partial}{\partial n}V^2h - \frac{\rho}{1-nC}(U^2 - V^2)hC = -\rho gh\frac{\partial E}{\partial n}$$

$$\dots + \frac{1}{1-nC}\frac{\partial}{\partial s}\tau_{ns}h + \frac{\partial}{\partial n}\tau_{nn}h + \frac{1}{1-nC}(\tau_{ss} - \tau_{nn})hC + \frac{1}{1-nC}\tau_{ns}|_\eta\frac{\partial\eta}{\partial s}$$

$$\dots + \tau_{nn}|_\eta\frac{\partial\eta}{\partial n} - \tau_{zn}|_\eta \tag{B.3.1}$$

Substituting the scaling relations of the first section and canceling like terms, I have:

$$\frac{1}{1-\hat{n}\hat{C}}\frac{H}{b}\frac{\partial}{\partial\hat{s}}\hat{U}\hat{V}\hat{h} + \frac{H}{b}\frac{\partial}{\partial\hat{n}}\hat{V}^2\hat{h} - \frac{1}{1-\hat{n}\hat{C}}\frac{H}{b}(\hat{U}^2 - \hat{V}^2)\hat{h}\hat{C} = -C_f\hat{h}\frac{\partial}{\partial\hat{n}}\hat{E}$$

$$\dots + \frac{1}{1-\hat{n}\hat{C}}\frac{H^2}{b^2}\frac{\partial}{\partial\hat{s}}\hat{\tau}_{ns}\hat{h} + \frac{H^2}{b^2}\frac{\partial}{\partial\hat{n}}\hat{\tau}_{nn}\hat{h} + \frac{1}{1-\hat{n}\hat{C}}\frac{H^2}{b^2}(\hat{\tau}_{ss} - \hat{\tau}_{nn})\hat{h}\hat{C}$$

$$\dots + \frac{1}{1-\hat{n}\hat{C}}\frac{H^2}{b^2}\hat{\tau}_{ns}|_\eta\frac{\partial}{\partial\hat{s}}\hat{\eta} + \frac{H^2}{b^2}\hat{\tau}_{nn}|_\eta\frac{\partial}{\partial\hat{n}}\hat{\eta} - \hat{\tau}_{zn}|_\eta \tag{B.3.2}$$

As in the previous section, I throw out terms of $O(\varepsilon^2)$, though I note again that the third and sixth terms on the right hand side of equation (B.3.1) will be large near the banks. Reverting to dimensional coordinates, I have:

$$\frac{\rho}{1-nC}\frac{\partial}{\partial s}UVh + \rho\frac{\partial}{\partial n}V^2h - \frac{\rho}{1-nC}(U^2-V^2)hC = -\tau_{zn}\Big|_\eta \qquad \text{(B.3.3)}$$

B.4 Continuity of Mass Equation

I write the depth-averaged equation for continuity of mass:

$$\frac{1}{1-nC}\frac{\partial}{\partial s}Uh + \frac{\partial}{\partial n}Vh - \frac{VhC}{1-nC} = 0 \qquad \text{(B.4.1)}$$

Without carrying through the steps, I note that all terms are of $O(\varepsilon)$ such that I retain all terms.

B.5 Special Cases

It is worthwhile at this point to examine some special cases alluded to in the previous sections.

In the straight section, or cross-over, between meander bends and other transitions from small to large curvature, curvature is small, but the downstream rate of change of curvature and, therefore, the lateral flow velocity are large. In such cases, it is appropriate to drop all terms and parts of terms proportional to curvature. Thus, I have, for downstream momentum conservation,

$$\rho\frac{\partial}{\partial s}U^2h + \rho\frac{\partial}{\partial n}UVh = -\tau_{zs}\Big|_\eta \qquad \text{(B.5.1)}$$

for cross-stream momentum conservation,

$$\rho\frac{\partial}{\partial s}UVh + \rho\frac{\partial}{\partial n}V^2h = -\tau_{zn}\big|_\eta \tag{B.5.2}$$

and for continuity,

$$\frac{\partial}{\partial s}Uh + \frac{\partial}{\partial n}Vh = 0 \tag{B.5.3}$$

In this case, the convective acceleration terms are dominant.

On the other hand, within bends where curvature is large but approximately constant, convective accelerations and terms proportional to lateral flow velocity will be small, and I am left with only the centrifugal force term in the lateral momentum equation:

$$\frac{\rho}{1-nC}U^2hC = \tau_{zn}\big|_\eta \tag{B.5.4}$$

Therefore, the bed topography depends only on curvature and primary hydraulic properties of the flow.

Recall the caveat I made about the terms proportional to lateral changes in depth and bed elevation, that these terms are large near the banks in general and, especially, near the outside bank (i.e., next to the pool). Adding back these terms, I have, for the downstream momentum equation,

$$\frac{\rho}{1-nC}\frac{\partial}{\partial s}U^2h + \rho\frac{\partial}{\partial n}UVh - \frac{2\rho}{1-nC}UVhC = -\tau_{zs}\big|_\eta + \frac{\partial}{\partial n}\tau_{ns}h + \tau_{ns}\big|_\eta\frac{\partial\eta}{\partial n} \tag{B.5.5}$$

for the lateral momentum equation,

$$\frac{\rho}{1-nC}\frac{\partial}{\partial s}UVh + \rho\frac{\partial}{\partial n}V^2h - \frac{\rho}{1-nC}(U^2-V^2)hC = -\tau_{zn}\big|_\eta + \frac{\partial}{\partial n}\tau_{nn}h + \tau_{nn}\big|_\eta\frac{\partial\eta}{\partial n} \tag{B.5.6}$$

and the continuity equation is unchanged.

Using the chain rule, I break down these "bank" terms:

$$\frac{\partial}{\partial n}\tau_{ns}h = h\frac{\partial \tau_{ns}}{\partial n} + \tau_{ns}\frac{\partial h}{\partial n} \qquad (B.5.7)$$

at the bank, the second term on the right hand side of equation (B.5.7) is dominant. Thus, I have

$$\frac{\partial}{\partial n}\tau_{ns}h\bigg|_{\pm\frac{b}{2}} = \left(\tau_{ns}\frac{\partial h}{\partial n}\right)\bigg|_{\pm\frac{b}{2}} \qquad (B.5.8)$$

Similarly, from the lateral momentum equation, I have

$$\frac{\partial}{\partial n}\tau_{nn}h\bigg|_{\pm\frac{b}{2}} = \left(\tau_{nn}\frac{\partial h}{\partial n}\right)\bigg|_{\pm\frac{b}{2}} \qquad (B.5.9)$$

I may now re-write the downstream and lateral momentum equations to include the bank terms:

$$\frac{\rho}{1-nC}\frac{\partial}{\partial s}U^2h + \rho\frac{\partial}{\partial n}UVh - \frac{2\rho}{1-nC}UVhC = -\tau_{zs}\big|_{\eta} + \left(\tau_{ns}\frac{\partial h}{\partial n}\right)\bigg|_{\pm\frac{b}{2}} + \left(\tau_{ns}\big|_{\eta}\frac{\partial \eta}{\partial n}\right)\bigg|_{\pm\frac{b}{2}} \qquad (B.5.10)$$

$$\frac{\rho}{1-nC}\frac{\partial}{\partial s}UVh + \rho\frac{\partial}{\partial n}V^2h - \frac{\rho}{1-nC}(U^2-V^2)hC = -\tau_{zn}\big|_{\eta}$$

$$\ldots + \left(\tau_{nn}\frac{\partial h}{\partial n}\right)\bigg|_{\pm\frac{b}{2}} + \left(\tau_{nn}\big|_{\eta}\frac{\partial \eta}{\partial n}\right)\bigg|_{\pm\frac{b}{2}} \qquad (B.5.11)$$

Appendix C

Magnitude of Lateral Momentum Transfer

To assess the magnitude of the lateral momentum transfer, I compare it to the bed shear stress for the special case of a channel following a sine-generated curve,

$$\phi(s) = \omega \sin \frac{2\pi s}{M} \tag{C.0.1}$$

where ϕ is the downstream direction angle; ω is the maximum angle; and M is the meander wavelength.

The average bottom stress integrated over the channel width and an incremental downstream distance is

$$dF_z = \rho C_f U^2 b \, ds \tag{C.0.2}$$

Then, from equations (C.0.2) and (4.13), the ratio of the cross-stream and bottom "forces" is

$$\frac{dF_n}{dF_z} = \frac{\pi^4\left(\frac{1}{H} - \frac{2}{b}\right)H^2 b^3 K^2 \omega^2 \sin^2 \frac{2\pi s}{M}}{M^4 C_f} \tag{C.0.3}$$

where the transverse slope parameter, K, is derived from equation (A.1.5) (here I neglect the effect of form drag; see *Ikeda*, 1989, and equation (A.1.5)). I then find the leading term of the series expansion of this force ratio at the point of maximum lateral momentum transfer, $s=M/4$, to get, neglecting higher order terms,

$$\frac{dF_n}{dF_z} \sim \frac{H b^3 \Psi \omega^2}{\Psi_{cr} C_f^2 M^4} \tag{C.0.4}$$

I now assign the value, ε, to small numbers of similar magnitude: H/b, b/M, Ψ_{cr}/Ψ; and ε^2

to C_f. Then the ratio in equation (C.0.4) is $O(\omega^2)$.

Appendix D

River Meandering Model Based on Linearized Flow Equations

The linearized flow equation (LFE) model assumes bank shear stress and channel migration are proportional to the near-bank flow velocity perturbation. The form of the velocity perturbation in *Johannesson and Parker* [1989c] is:

$$u_{b1} = \chi_{20} U b C(s) + \frac{C_f U b^2}{H}\left[\chi_{20}\left(\frac{U^2}{gH} + 2\right) - 1\right] e^{\frac{-2C_f s}{H}} \int_0^s C(s') e^{\frac{2C_f s'}{H}} ds'$$

$$\dots + \frac{C_f U b}{H}(K + A_s) e^{\frac{-2C_f s}{H}} \int_0^s C(s') e^{\frac{2C_f s'}{H}} ds'$$

(D.0.1)

$$A_s = \frac{181}{\chi_1}\left(\frac{2H}{b}\right)^2\left(2\chi^2 + \frac{4\chi}{5} + \frac{1}{15}\right), \ \delta = \frac{\chi_1^2\left(\chi + \frac{1}{4}\right)}{\left(\frac{\chi^2}{12} + \frac{11\chi}{360} + \frac{1}{504}\right)}$$

(D.0.2)

$$\chi_{20} = \frac{1}{\chi_1^3}\left(\chi^3 + \chi^2 + \frac{2\chi}{5} + \frac{2}{35}\right), \ \chi_1 = \frac{0.077}{\sqrt{C_f}}, \ \chi = \frac{0.077}{\sqrt{C_f}} - \frac{1}{3}$$

(D.0.3)

My version of the LFE uses equation (D.0.1), where I have made one simplification. To make the LFE model more directly comparable to the TSRM model, which uses local curvature to determine the bed topography, I substituted local curvature, *C*, for the effective curvature integral in *Johannesson and Parker* [1989c]. A.D. Howard [personal communication, 1996] reports that the use of this integral has an insignificant effect on model behavior.

References

Ahnert, F., 1976. Brief description of a comprehensive three-dimensional process-response model of landform development, in *Quantitative Slope Models*, ed. by F Ahnert, *Z. Geomorph.*, Supp. 25, p. 29.

Andrews, E.D., 1981. Measurement and computation of bed-material discharge in a shallow sand-bed stream, Muddy Creek, Wyoming, *Water Resour. Res.*, 17(1), 131-141.

Andrews, E.D., 1982. Bank stability and channel width adjustment, East Fork River, Wyoming, *Water Resour. Res.*, 18(4), 1184-1192.

Andrle, R., 1994. The angle measure technique: A new method for characterizing the complexity of geomorphic lines, *Mathematical Geol.*, 26, 83-97.

Andrle, R. 1996. Measuring channel planform of meandering rivers, *Physical Geog.*, 17(3), 270-281.

Beaumont, C., P. Fullsack, and J. Hamilton, 1992. Erosional control of active compressional orogens, in *Thrust Tectonics*, ed. by McClay, K.R., New York, Chapman and Hall, pp. 1-18.

Beauvais, A.A., and D.R. Montgomery, 1996. Influence of valley type on the scaling properties of river planforms, *Water Resour. Res.*, 32(5), 1441-1448.

Beck, S., 1983. Mathematical modeling of meander interaction, in *River Meandering*, Proceedings of the conference rivers 1983, ASCE, New Orleans, Oct. 24-26, pp. 932-941.

Begin, Z.B., 1981. Stream curvature and bank erosion: A model based on the momentum equation, *J. Geol.*, 89, 497-504.

Beven, K.J., and M.J. Kirkby, 1979. A physically-based variable contributing area model of basin hydrology, *Hydrol. Sci. Bull.*, 24(1), 43-69.Black, T., and D.R. Montgomery, 1991. Sediment transport by burrowing mammals, Marin County, California, *Earth Surf. Proc. Landf.*, 16, 163-172.

Black, T.A., and D.R. Montgomery, 1991. Sediment transport by burrowing mammals, Marin County, California, *Earth Surf. Proc. and Landf.*, 16(2), 163-172.

Blondeaux, P., and G. Seminara, 1985. A unified bar-bend theory of river meanders, *J. Fluid Mech.*, 157, 449-470.

Brakenridge, G.R., J.C. Knox, E.D. Paylor II, and F.J. Magilligan, 1994. Radar remote sensing aids study of the Great Flood of 1993, *EOS, Trans. A.G.U.*, 75(45), 521-527.

Bras, R.L., 1990. *Hydrology: An Introduction to Hydrologic Science*, Addison-Wesley Publishing Co., Inc., Reading, Mass.

Braun, J., and M. Sambridge, 1994. Dynamical Lagrangian Remeshing (DLR): A new

algorithm for solving large strain deformation problems and its application to fault-propagation folding, *Earth and Plan. Sci. Let.*, 124(1/4), 211-.

Braun, J., and M. Sambridge, 1997. Modelling landscape evolution on geological time scales: a new method based on irregular spatial discretization, *Basin Research*, 9(1), 27-52.

Brice, J., 1974. Meandering pattern of the White River in Indiana--an analysis, in *Fluvial Geomorphology*, ed. by M. Morisawa, S.U.N.Y., Binghamton, pp. 178-200.

Brown, P.J.C., 1995. Three examples of incremental Delaunay triangulation algorithms for terrain modelling, *http://www.cl.cam.ac.uk/users/pjcb2/Publications/ delaunaysurvey/delaunaysurvey.html*.

Bruinsma, R., 1990. The statistical mechanics of meandering. *J. Phys. France*, 51(9) 829-845.

Carson, M.A., and M.J. Kirkby, 1972, *Hillslope Form and Process*, Cambridge University Press, 475 pp.

Chase, C.G., 1992. Fluvial landsculpting and the fractal dimension of topography, *Geomorphology*, 5, 39-57.

Chow, V.T., 1959. *Open-Channel Hydraulics*, McGraw-Hill Book Company, New York, 680 pp.

Cordova, J.R., I. Rodriguez-Iturbe, and P. Vaca, 1982. On the development of drainage networks, in *Recent developments in the explanation and prediction of erosion and sediment yield*, ed. by D.E. Wallings, Exeter, U.K., 19-30.

Crosato, A., 1990. Simulation of meandering river processes, Communications on hydraulic and geotechnical engineering, Rep. no. 90-3, Delft U. of Tech, 104 pp.

Davis, W.M., 1909. *Geographical Essays*, Ginn, Boston, 777 pp.

Dietrich, W. E., and J. D. Smith, 1983. Influence of the point bar on flow through curved channels, *Water Resour. Res.*, 19(5), 1173-1192.

Dietrich, W. E., and J. D. Smith, 1984. Bed load transport in a river meander, *Water Resour. Res.*, 20(10), 1355-1380.

Dietrich, W. E., and P. Whiting, 1989. Boundary shear stress and sediment transport in river meanders of sand and gravel, in *River Meandering*, ed. by S. Ikeda and G. Parker (Water resources monograph: 12), Am. Geophys. Union, Washington, pp. 1-50.

Dietrich, W.E., C.J. Wilson, D.R. Montgomery, and J. McKean, 1993. Analysis of erosion thresholds, channel networks, and landscape morphology using a digital terrain model, *J. Geol.*, 101, 259-278.

Dietrich, W.E., Wilson, C.J., Montgomery, D.R., McKean, J., and Bauer, R., 1992. Erosion thresholds and land surface morphology, *Geology*, 20, 675-679.

Droste, C., 1996. Observability of parameters in meander migration models, American Geophysical Union 1996 Spring Meeting.

Du, C., 1996. An algorithm for automatic Delaunay triangulation of arbitrary planar domains, *Adv. Eng. Software*, 27(1-2), 21-26.

Dunne, T., and B.F. Aubry, 1986. Evaluation of Horton's theory of sheetwash and rill erosion on the basis of field experiments, in *Hillslope Processes*, ed. by A.D. Abrahams, Allen & Unwin, Boston, 31-53.

Eagleson, P.S., 1978. Climate, soil, and vegetation: 2. The distribution of annual precipitation derived from observed storm sequences, *Water Resour. Res.*, 14, 713-721.

Engelund, F., and F. Hansen, 1967. A monograph on sediment transport in alluvial streams, in *Teknisk Verlag: Copenhagen, Denmark*, Technical University of Denmark, 63 pp.

Ferguson, R.I., 1976. Disturbed periodic model for river meanders, *Earth Surf. Proc.*, 1, 337-347, summarized in *Howard and Hemberger* [1991].

Ferguson, R.I., P.E. Ashmore, P.J. Ashworth, C. Paola, and K.L. Prestegaard, 1992. Measurements in a braided river chute and lobe 1. Flow pattern, sediment transport, and channel change, *Water Resour. Res.*, 28(7), 1877-1886.

Furbish, D.J., 1991. Spatial autoregressive structure in meander evolution, *Geol. Soc. of Am. Bull.*, 103, 1576-1589.

Garcia, M. H., L. Bittner, and Y. Niño, 1994. Mathematical modeling of meandering streams in Illinois: A tool for stream management and engineering, Civ. Eng. Studies Hydraulic Engineering Series No. 43, Urbana, IL, 49 pp.

Gasparini, N.M., G.E. Tucker, R.L. Bras, and S.T. Lancaster, 1997. Downstream fining: A drainage basin perspective, American Geophysical Union 1997 Fall Meeting (abstract).

Gasparini, N.M., G.E. Tucker, and R.L. Bras, 1998. *Modeling transport of multiple grain sizes in the landscape*, Master's Thesis, Dept. of Civil and Environmental Engineering, Massachusetts Institute of Technology.

Gilbert, G.K., 1877. *Report on the Geology of the Henry Mountains*, U.S. Geographical and Geological Survey, Washington, D.C., 160 pp.

Gilbert, G.K., 1909. The convexity of hilltops, *J. Geology*, 17, 344-350.

Gilley, J.E., W.J. Elliot, J.M. Laflen, and J.R. Simanton, 1993. Critical shear stress and critical flow rates for initiation of rilling, *J. Hydrology*, 142, 251-271.

Gomez, B., 1993. Roughness of stable, armored gravel beds, *Water Resour. Res.*, 29(11), 3631-3642.

Gomez, B., 1994. Effects of particle shape and mobility on stable armor development, *Water Resour. Res.*, 30(7), 2229-2239.

Govers, G., 1992. Evaluation of transporting capacity formulae for overland flow, in *Overland Flow*, ed. by A.J. Parsons and A.D. Abrahams, Chapman & Hall, New York, 243-273.

Guibas, L.J., and J. Stolfi, 1985. Primitives for the manipulation of general subdivisions

and the computation of Voronoi diagrams, *ACM Trans. on Graphics*, 4(2), 74-123.

Hack, J.T., 1957. Studies of longitudinal stream profiles in Virginia and Maryland, *U.S.G.S. Prof. Paper 294-B*.

Hack, J.T., 1960. Interpretation of erosional topography in humid temperature regions, *Am. J. Sci.*,258-A, 80-97.

Hasegawa, K., 1989. Studies on qualitative and quantitative prediction of meander channel shift, in *River Meandering*, ed. by G. Parker and S. Ikeda (Water resources monograph: 12), Am. Geophys. Union, Washington, pp. 215-235.

Hey, R.D., and C.R. Thorne, 1986. Stable channels with mobile gravel beds, *J. Hydraul. Eng.*, 112(8), 671-689.

Hickin, E.J., 1974. The development of meanders in natural river-channels, *Am. J. Sci.*, 274(4), 414-442.

Hickin, E.J., 1984. Vegetation and river channel dynamics, *Canadian Geog.*, 28(2), 111-126.

Hoey, T.B., and R. Ferguson, 1994. Numerical simulation of downstream fining by selective transport in gravel bed rivers: Model development and illustration, *Water Resour. Res.*, 30(7), 2251-2260.

Hooke, J.M., 1995. River channel adjustment to meander cutoffs on the River Bollin and River Dane, northwest England, *Geomorphology*, 14(3), 235-253.

Hooke, R. Le B., 1975. Distribution of sediment transport and shear stress in a meander bend, *J. Geol.*, 83(5), 543-565.

Hopson, T., and J.D. Smith, 1997. Bank erosion in meandering rivers, American Geophysical Union Fall 1997 Meeting, San Francisco.

Howard, A.D., 1971. Simulation model of stream networks by headward growth and branching, *Geographical Analysis*, 3(10), 29-50.

Howard, A.D., 1990. Theoretical model of optimal drainage networks, *Water Resour. Res.*, 26, 2107-2117.

Howard, A.D., 1992. Modelling channel migration and floodplain development in meandering streams, In: *Lowland Floodplain Rivers* (P.A. Carling and G.E. Petts, eds.), Chichester, John Wiley & Sons, p. 1-42.

Howard, A.D., 1994. A detachment-limited model of drainage basin evolution, *Water Resour. Res.*, 30(7), 2261-2285.

Howard, A.D., 1996. Modelling channel evolution and floodplain morphology, In: *Floodplain Processes*, ed. by M. G. Anderson, D. E. Walling, and P. D. Bates, John Wiley and Sons, Ltd., Chichester, pp. 16-62.

Howard, A.D., 1997. Simulation of gully erosion and bistable landforms, *Proceedings of the Conference on Landscapes Disturbed by Channel Incision*, in press.

Howard, A.D., 1998. Modeling gully development due to vegetation disturbance, American Geophysical Union Spring 1998 Meeting, Boston.

Howard, A.D., and A.T. Hemberger, 1991. Multivariate characterization of meandering, *Geomorphology*, 4, 161-186.

Howard, A.D., and T.R. Knutson, 1984. Sufficient conditions for river meandering: A simulation approach, *Water Resour. Res.*, 20(11), 1659-1667.

Howard, A.D., and C.F. McLane, III, 1988. Erosion of cohesionless sediment by groundwater seepage, *Water Resour. Res.*, 24(10), 1659-1674.

Ijjasz-Vasquez, E.J., R.L. Bras, and G.E. Moglen, 1992. Sensitivity of a basin evolution model to the nature of runoff production and to initial conditions, *Water Resour. Res.*, 28, 2733-2741.

Ijjasz-Vasquez, E.J., R.L. Bras, and I. Rodriguez-Iturbe, 1993. Form, scales and optimality in the basin landscape and its channel network, *Ralph M. Parsons Lab. Rep. no. 339*, M.I.T. Dept. of Civ. & Env. Eng., Cambridge, 181 pp.

Ijjasz-Vasquez, E., and R.L. Bras, 1995. Scaling regimes of local slope versus contributing area in digital elevation models, *Geomorphology*, 12(4), 299-311.

Ikeda, S., 1989. Sediment transport and sorting at bends, in *River Meandering*, ed. by S. Ikeda and G. Parker (Water resources monograph: 12), Am. Geophys. Union, Washington, pp. 103-126.

Ikeda, S., G. Parker, and K. Sawai, 1981. Bend theory of river meanders. Part 1. Linear development, *J. Fluid Mech.*, 112, 363-377.

Ikeda, S., M. Yamasaka, and M. Chiyoda, 1987. Bed topography and sorting in bends, *J. Hydraul. Eng.*, 113(2), 190-206.

Imran, J., and G. Parker, 1997. Flow in meandering submarine and subaerial channels, American Geophysical Union 1997 Fall Meeting.

Johannesson, H., and G. Parker, 1985. Computer simulated migration of meandering rivers in Minnesota, Project Report No. 242, St. Anthony Falls Hydraulic Laboratory, Minneapolis, MN, 82 pp.

Johannesson, H., and G. Parker, 1989a. Linear theory of river meanders, in *River Meandering*, ed. by S. Ikeda and G. Parker (Water resources monograph: 12), Am. Geophys. Union, Washington, pp. 181-214.

Johannesson, H., and G. Parker, 1989b. Secondary flow in mildly sinuous channel, *J. Hydraul. Eng.*, 115(3), 289-308.

Johannesson, H., and G. Parker, 1989c. Velocity redistribution in meandering rivers, *J. Hydraul. Eng.*, 115(8), 1019-1039.

Johnson, W., and B. Logan, 1990. Geoarchaeology of the Kansas River basin, central Great Plains, in *Archaeological Geology of North America*, ed. by N.P. Lasca and J. Donahue, Geological Society of America, Centennial Special Volume 4, Boulder, 267-299.

Julien, P.Y., and M. Frenette, 1985. Modeling of rainfall erosion, *J. Hydraul. Eng.*, 111(10), 1344-1359.

Kinoshita, R., 1987. Investigation on alluvial actions in a flood and experimental study on an optimum designed channel with complex cross section, Report for "Studies on control of flood flows in alluvial rivers and improvement of the safety for river training", Grant-in-Aid for Developmental Scientific Research of MESG (Principal Investigator Tsutomu Kishi), in Japanese, summarized in *Hasegawa* [1989].

Kirkby, M.J., 1971. Hillslope process-response models based on the continuity equation, in *Slopes, Forms and Processes*, Institute of British Geographers, Special Publication No. 3.

Kirkby, M.J., 1986. A two-dimensional simulation model for slope and stream evolution, in *Hillslope Processes*, ed. by A.D. Abrahams, Winchester, Mass., Allen and Unwin, pp. 203-222.

Kirkby, M.J., 1989. A model to estimate the impact of climatic change on hillslope and regolith form, *Working Pap. 522*, School of Geography, University of Leeds, Leeds, 36 pp. and figures.

Kirkby, M.J., 1994. Thresholds and instability in stream head hollows: A model of magnitude and frequency for wash processes, in *Process Models and Theoretical Geomorphology*, ed. by M.J. Kirkby, New York, John Wiley and Sons, Inc., pp. 295-314.

Koltermann, C.E., and S.M. Gorelick, 1992. Paleoclimatic signature in terrestrial flood deposits, *Science*, 256, 1775-1782.

Komar, P.D., 1987a. Selective gravel entrainment and the empirical evaluation of flow competence, *Sedimentology*, 34, 1165-1176.

Komar, P.D., 1987b. Selective entrainment by a current from a bed of mixed sizes--a reanalysis, *J. Sed. Petrology*, 57(2), 203-211.

Kooi, H., and C. Beaumont, 1994. Escarpment evolution on high-elevation rifted margins; insights derived from a surface processes model that combines diffusion, advection, and reaction, *J. Geophys. Res.*, 99, 12,191-12,209.

Laguna, A., and J.V. Giraldez, 1993. The description of soil erosion through a kinematic wave model, *J. Hydrol.*, 145(1-2), 65-82.

Lancaster, S.T. and R.L. Bras, 1995. Modeling alluvial sedimentation with a landscape evolution model, American Geophysical Union 1995 Spring Meeting, Baltimore.

Lancaster, S.T., R.L. Bras, and K.X. Whipple, 1996. Simulation of river meandering over long distances and times: A physically based model, American Geophysical Union Spring 1996 Meeting, Baltimore.

Langbein, W.B., and L.B. Leopold, 1966, River meanders—theory of minimum variance, *U. S. Geol. Surv. Prof. Pap. 422-H*, 15pp.

Lathrap, D.W., 1968. Aboriginal occupation and changes in river channel on the central Ucayali, Peru, *American Antiquity*, 33(1), 62-79.

Leopold, L.B., and T. Maddock, Jr.,1953. The hydraulic geometry of stream channels and some physiographic implications, *U.S. Geol. Surv. Prof. Pap.*, 252, 57pp.

Leopold, L.B., and M.G. Wolman, 1957, River channel patterns: Braided, meandering and straight, *U.S. Geol. Surv. Prof. Pap., 282-B*, 85pp.

Leopold, L.B., and M.G. Wolman, 1960. River meanders, *Bull. Geol. Soc. Am.*, 71, 769-794.

Leopold, L.B., M.G. Wolman, and J.P. Miller, 1964. *Fluvial Processes in Geomorphology*, W. H. Freeman and Co., San Francisco, 522 pp.

Lobeck, A.K., 1939. *Geomorphology: An Introduction to the Study of Landscapes*, McGraw-Hill Book Co., Inc., New York, 731 pp.

Lomb, N.R., 1976. *Astrophysics and Space Science*, 39, 447-462, cited in *Press, et al.* [1997], pp. 569-577.

Lorenz, E.N., 1963. Deterministic nonperiodic flow, *J. Atmos. Sci.*, 20, 130-141.

Masek, J.G., and D.L. Turcotte, 1993. A diffusion-limited aggregation model for the evolution of drainage networks, *Earth and Plan. Sci. Lett.*, 119(3), 379-386.

Matsushita, M., and S. Ouchi, 1989. On the self-affinity of various curves, *Physica D*, 38, 246-251.

McCuen, R. H., 1985, *Statistical Methods for Engineers,* Prentice-Hall, Englewood Cliffs, NJ, 439 pp.

McKean, J.A., W.E. Dietrich, R.C. Finled, J.R. Southon, and M.W. Caffee, 1993. Quantification of soil production and downslope creep rates from cosmogenic ^{10}Be accumulations on a hillslope profile, *Geol.*, 21, 343-346.

McKenney, R., R.B. Jacobson, and R.C. Wertheimer, 1995. Woody vegetation and channel morphogenesis in low-gradient, gravel-bed streams in the Ozarks Region, Missouri and Arkansas, *Geomorphology*, 13, 175-198.

Meritts, D.J., K.R. Vincent, and E.E. Wohl, 1994. Long river profiles, tectonism, and eustasy: A guide to interpreting fluvial terraces, *J. Geophys. Res.,* 99(B7), 14,031-14,050.

Mertes, Leal A.K., 1997. Documentation and significance of the perirheic zone on inundated floodplains, *Water Resour. Res.*, 33(7), 1749-1762.

Moglen, G., and R.L. Bras, 1994. Simulation of observed topography using a physically-based basin evolution model, *Ralph M. Parsons Lab. Tech. Rep. No. 340*, (Ph.D. thesis) M.I.T. Dept. of Civ. & Env. Eng., Cambridge, 227 pp.

Moglen, G., and R.L. Bras, 1995. The effect of spatial heterogeneities on geomorphic expression in a model of basin evolution, *Water Resour. Res.*, 31(10), 2613-2623.

Montgomery, D.R., 1994. Valley incision and the uplift of mountain peaks, *J. Geophys. Res.*, 99(B7), 13,913-13,921.

Montgomery, D.R., and W.E. Dietrich, 1988. Where do channels begin? *Nature*, 336, 232-234.

Montgomery, D.R. and W.E. Dietrich, 1989. Source areas, drainage density, and channel

initiation, *Water Resour. Res.*, 25(8), 1907-1918.

Montgomery, D.R. and W.E. Dietrich, 1992. Channel initiation and the problem of landscape scale, *Science*, 255, p. 826.

Montgomery, D.R., and W.E. Dietrich, 1994. A physically based model for the topographic control on shallow landsliding, *Water Resour. Res.*, 30(4), 1153-1171.

Montgomery, D.R., and E. Foufoula-Georgiou, 1993. Channel network source representation using digital elevation models, *Water Resour. Res.*, 29(12), 3925-3934.

Mosselman, E., 1995. A review of mathematical models of river planform changes, *Earth Surf. Proc. and Landforms*, 20, 661-670.

Murray, A.B, and C. Paola, 1994. A cellular model of braided rivers, *Nature*, 371(6492), 54-57.

Murray, A.B., and C. Paola, 1996. A new quantitative test of geomorphic models, applied to a model of braided streams, *Water Resour. Res.*, 32(8), 2579-2587.

Nanson, G.C., and E.J. Hickin, 1983. Channel migration and incision on the Beatton River, *J. Hydraul. Eng.*, 109, 327-337.

Nanson, G.C., and E.J. Hickin, 1986. A statistical analysis of bank erosion and channel migration in Western Canada, *GSA Bull.*, 97(4), 497-504.

Nelson, J.M., and J.D. Smith, 1989a. Flow in meandering channels with natural topography, in *River Meandering*, ed. by S. Ikeda and G. Parker (Water resources monograph: 12), Am. Geophys. Union, Washington, pp. 69-102.

Nelson, J.M., and J.D. Smith, 1989b. Evolution and stability of erodible channel beds, in *River Meandering*, ed. by S. Ikeda and G. Parker (Water resources monograph: 12), Am. Geophys. Union, Washington, pp. 321-378.

Odgaard, A. J., 1982. Bed characteristics in alluvial channel bends, *J. Hydraul. Div.*, ASCE, 108(HY11), 1268-1281.

Odgaard, A. J., 1986. Meander flow model. I: Development, *J. Hydraul. Eng.*, 112(12), 1117-1136.

Odgaard, A.J., 1987. Streambank erosion along two rivers in Iowa, *Water Resour. Res.*, 23, 1225-1236.

O'Loughlin, E.M., 1986. Prediction of surface saturation zones in natural catchments, *Water Resour. Res.*, 22, 794-804.

Paola, C., P.L. Hellert, and C.L. Angevine, 1992. The large-scale dynamics of grain-size variation in alluvial basins, 1: Theory, *Basin Res.*, 4, 73-90.

Parker, G., 1983. Theory of meander bend deformation, in *River Meandering*, Proceedings of the conference rivers 1983, ASCE, New Orleans, Oct. 24-26, pp. 722-733.

Parker, G., 1990. Surface-based bedload transport relation for gravel rivers, *J. Hydraul. Res.*, 28(4), 417-436.

Parker, G., 1996. Some speculations on the relation between channel morphology and channel-scale flow structures, in *Coherent Flow Structures in Open Channels*, ed. by P.J. Ashworth and J.L. Bennet, John Wiley and Sons, pp. 429-432.

Parker, G., and E. D. Andrews, 1986. On the time development of meander bends, *J. Fluid Mech.*, 162, 139-156.

Parker, G., P. Diplas, and J. Akiyama, 1983. Meander bends of high amplitude, *J. Hydraul. Eng.*, 109(10), 1323-1337.

Parker, G., and H. Johannesson, 1989. Observations on several recent theories of resonance and overdeepening in meandering channels, in *River Meandering*, ed. by S. Ikeda and G. Parker (Water resources monograph: 12), Am. Geophys. Union, Washington, pp. 379-416.

Parker, G., K. Sawai, and S. Ikeda, 1982. Bend theory of river meanders. Part 2. Nonlinear deformation of finite-amplitude bends, *J. Fluid Mech.*, 115, 303-314.

Parsons, A.J., A.D. Abrahams, and J.W. Wainwright, 1994, On determining resistance to interrill overland flow, *Water Resour. Res.*, 30(12), 3515-3521.

Pederson, D.T., and J.F. Cornwall, 1998. The role of groundwater sapping in river channel evolution, American Geophysical Union Spring 1998 Meeting, Boston.

Pizzuto, J.E., 1987. Sediment diffusion during overbank flows, *Sedimentology*, 34(2), 301-317.

Pizzuto, J.E., and T.S. Meckelnburg, 1989. Evaluation of a linear bank erosion equation, *Water Resour. Res.*, 25, 1005-1013.

Press, W.H., S.A. Teukolsky, W.T. Vetterling, and B.P. Flannery, 1997. *Numerical Recipes in Fortran 77: The Art of Scientific Computing, Second Edition* (Vol. 1 of Fortran Numerical Recipes), Cambridge University Press, New York, 940 pp.

Prestegaard, K.L., 1983, Variables influencing water-surface slopes in gravel-bed streams at bankfull stage, *Geol. Soc. Am. Bull.*, 94, 673-678.

Quinn, P., K. Bevin, P. Chevallier, and O. Planchon, 1991. The prediction of hillslope flowpaths for distributed hydrological modelling using digital terrain models, in *Advances in Hydrological Processes, Terrain Analysis and Distributed Modelling in Hydrology*, ed. by K.J. Bevin and I.D. Moore, John Wiley and Sons, New York, 63-83.

Rinaldo, A., W.E. Dietrich, R. Rigon, G.K. Vogel, and I. Rodriguez-Iturbe, 1995. Geomorphological signatures of varying climate, *Nature*, 374(6523), 632-635.

Rodriguez-Iturbe, I.; A. Rinaldo; R. Rigon; R.L. Bras; A. Marani; and E. Ijjasz-Vasquez; 1992. Energy dissipation, runoff production, and the three-dimensional structure of river basins. *Water Resour. Res.*, 28(4) 1095-1103.

Rosenbloom, N.A., and R.S. Anderson, 1994. Hillslope and channel evolution in a marine terraced landscape, Santa Cruz, California, *J. Geophys. Res.*, 99(B7), 14,013-14,029.

Schumm, S.A., 1967. Meander wavelength of alluvial rivers, *Science*, 157, 1549-1550.

Schumm, S.A., 1993. River response to baselevel change: Implications for sequence stratigraphy, *J. Geology*, 101, 279-294.

Schumm, S.A., M.P. Mosley, and W.E. Weaver, 1987. *Experimental Fluvial Geomorphology*, John Wiley & Sons, New York, 412 pp.

Scott and Gravlee, 1968. Flood surge on the Rubicon River, California--hydrology, hydraulics, and boulder transport, *USGS Prof. Pap. 422-M*.

Seminara, G., and M. Tubino, 1989. Alternate bars and meandering: Free, forced and mixed interactions, in *River Meandering*, ed. by S. Ikeda and G. Parker (Water resources monograph: 12), Am. Geophys. Union, Washington, pp. 267-320.

Seminara, G., and M. Tubino, 1992. Weakly nonlinear theory of regular meanders, *J. Fluid Mech.*, 244, 257-288.

Singh, V.P., and R.R. Regl, 1983. Analytical solutions of kinematic equations for erosion on a plane I. Rainfall of indefinite duration, *Adv. Wat. Resour.*, 6, 2-10.

Slingerland, R., J.W. Harbaugh, and K. Furlong, 1994. *Simulating Clastic Sedimentary Basins*, PTR Prentice Hall, Englewood Cliffs, 220 pp. and diskette.

Smith, C.E., 1998. Modeling high sinuosity meanders in a small flume, *Geomorphology*, in press.

Smith, J.D., and S.R. McLean, 1984. A model for flow in meandering streams, *Water Resour. Res.*, 20(9), 1301-1315.

Smith, T.R., and F.P. Bretherton, 1972. Stability and the conservation of mass in drainage basin evolution, *Water Resour. Res.*, 8, 1506-1529.

Stølum, H.-H., 1996. River meandering as a self-organization process, *Science*, 271, 1710-1713.

Sun, T., P. Meakin, T. Jøssang, and K. Schwarz, 1996. A simulation model for meandering rivers, *Water Resour. Res.*, 32(9), 2937-2954.

Tarboton, D.G., R.L. Bras, and I. Rodriguez-Iturbe, 1991. On the extraction of channel networks from digital elevation data. *Hydrol. Processes* 5, 81-100.

Tarboton, D.G., R.L. Bras, and I. Rodriguez-Iturbe, 1992. A physical basis for drainage density, *Geomorphology*, 5, 59-76.

Tetzlaff, D.M., and J.W. Harbaugh, 1989. *Simulating Clastic Sedimentation*, Van Nostrand Rheinhold, New York, 202 pp.

Thorne, S.D., and D.J. Furbish, 1995. Influences of coarse bank roughness on flow within a sharply curved river bend, in *Predicting Process from Form*, ed. by P.J. Whiting and D.J. Furbish, spec. issue of *Geomorphology*, 12(3), 241-257.

Tucker, G.E., 1996. *Modeling the large-scale interaction of climate, tectonics, and topography*, Pennsylvania State University Earth System Science Center Technical Report no. 96-003, University Park, PA.

Tucker, G.E., and R.L. Slingerland, 1994. Erosional dynamics, flexural isostasy, and long-lived escarpments: a numerical modeling study, *J. Geophys. Res.*, 99, 12,229-12,243.

Tucker, G.E., and R.L. Slingerland, 1996. Predicting sediment flux from fold and thrust belts, *Basin Research*, 8, 329-349.

Tucker, G.E., and R.L. Slingerland, 1997. Drainage basin response to climate change, *Water Resour. Res.*, 33(8), 2031-2047.

Tucker, G.E., and R.L. Bras, 1998. Hillslope processes, drainage density, and landscape morphology, *Water Resour. Res.* in press.

Weldon, R.J., 1994. The nature of fluvial terraces and their use in climate and tectonic studies, *G.S.A., Abstracts with Programs*, 26(7), 1994, p. A-239.

Whiting, P.J., and W.E. Dietrich, 1993a. Experimental constraints on bar migration through bends: Implications for meander wavelength selection, *Water Resour. Res.*, 29(4), 1091-1102.

Whiting, P.J., and W.E. Dietrich, 1993b. Experimental studies of bed topography and low patterns in large-amplitude meanders 1. Observations, *Water Resour. Res.*, 29(11), 3605-3614.

Whiting, P. J., and W. E. Dietrich, 1993c. Experimental studies of bed topography and flow patterns in large-amplitude meanders 2. Mechanisms, *Water Resour. Res.*, 29(11), 3615-3622.

Wilcock, P.R., and B.W. McArdell, 1993. Surface-based fractional transport rates: Mobilization thresholds and partial transport of a sand-gravel sediment, *Water Resour. Res.*, 29(4), 1297-1312.

Willgoose, G., R.L. Bras, and I. Rodriguez-Iturbe, 1989, A physically based channel network and catchment evolution model, *Ralph M. Parsons Lab. Tech Rep. No. 322*, M.I.T. Dept. of Civ. & Env. Eng., Cambridge, 464 pp.

Willgoose, G., R.L. Bras, and I. Rodriguez-Iturbe, 1991. A physically based coupled network growth and hillslope evolution model, 1, theory, *Water Resour. Res.*, 27, 1671-1684.

Yang, C.T., and C.C.S. Song, 1979a. Theory of minimum rate of energy dissipation, *J. Hydraul. Div., ASCE*, 105(HY7), 769-784.

Yang, C.T., and C.C.S. Song, 1979b. Dynamic adjustments of alluvial channels, in *Adjustments of the Fluvial System*, ed. by D.D. Rhodes and G.P. Williams, Proc., 10th Ann. Bing. Geomorphology Symp., Kendall/Hunt Pub. Co., Dubuque, pp. 55-67.

Yen, C., and S. Ho, 1990. Bed evolution in channel bends, *J. Hydraul. Eng.*, 116(4), 544-562.

Young, R., and I. McDougall, 1993. Long-term landscape evolution: Early Miocene and Modern rivers in southern New South Wales, Australia, *J. Geol.*, 101, 35-49.

Zhou, J., H.H. Chang, and D. Stow, 1993. A model for phase lag of secondary flow in river meanders, *J. Hydrol.*, 146(1-4), 73-88.